UNIVERSIDAD DE CHILE
FACULTAD DE CIENCIAS FÍSICAS Y MATEMÁTICAS
DEPARTAMENTO DE GEOLOGÍA

PERMIAN–TRIASSIC PLUTONISM IN THE CHILEAN FRONTAL ANDES (28°–28°30'S): A KEY EVIDENCE OF THE GEODYNAMIC EVOLUTION OF THE SOUTHWESTERN MARGIN OF PANGEA AND ITS IMPLICATIONS TO THE ANDEAN OROGENESIS

TESIS PARA OPTAR AL GRADO DE MAGÍSTER EN CIENCIAS,
MENCIÓN GEOLOGÍA
MEMORIA PARA OPTAR AL TÍTULO DE GEÓLOGO

ÁLVARO FELIPE DEL REY HERNÁNDEZ-GONZÁLEZ

PROFESOR GUÍA:
Dr. rer.nat. KATJA DECKART

PROFESOR CO-GUÍA:
Dr. CÉSAR ARRIAGADA

MIEMBROS DE LA COMISIÓN:
Dr. FRANCISCO HERVÉ
Dr. VÍCTOR MAKSAEV

SANTIAGO DE CHILE
2016

RESUMEN DE LA TESIS PARA OPTAR AL TÍTULO DE: Geólogo y grado de Magister en Ciencias, Mención Geología
POR: Álvaro Felipe Del Rey Hernández-González
FECHA: Agosto, 2016
PROFESORA GUÍA: Dr. rer.nat. Katja Deckart

PERMIAN–TRIASSIC PLUTONISM IN THE CHILEAN FRONTAL ANDES (28°–28°30'S): A KEY EVIDENCE OF THE GEODYNAMIC EVOLUTION OF THE SOUTHWESTERN MARGIN OF PANGEA AND ITS IMPLICATIONS TO THE ANDEAN OROGENESIS

Traditionally, late Permian–Triassic magmatism has been attributed to a period characterized by intense extensional conditions. Several hypotheses have been proposed to explain such levels of crustal extension, including cessation of subduction and slab break-off. Nevertheless, all those ideas explain magmatism only locally and fail in giving a regional tectonic framework for all the magmatism of this period along the Chilean–Argentinian continental margin. Likewise, they do not provide a clear idea of how that setting changed into the Andean subduction at the beginning of Jurassic and even they do not give genetical relations to the coeval igneous activity observed along the margin. This research provides new insights for the late Paleozoic–Triassic plutonism of the Chilean Frontal Andes using new U–Pb in zircon ages (SHRIMP II, LA-ICPMS); O, Lu–Hf, Sm–Nd, Rb–Sr and Re–Os isotopes and geochemical major and trace element analyses. A detailed comparison with coeval units ranging from 21° to 40°S allows presenting a new regional tectonic model for that period and its link with the Andean Orogenesis.

Results indicate that plutonism shows a continuous trend from continental-like contributions (latest early Carboniferous) towards more mantle-like signatures (Triassic). Despite its continuity, it is possible to separate units with or without mantle-like signatures at ca. 270 Ma (middle Permian) by using $\delta^{18}O$ isotope ratios. In addition, Nb–Ta troughs and positive Pb anomalies indicate subduction-related magmatism during the entire period. In general, εNd_i and $^{87}Sr/^{86}Sr_i$ signatures suggest a lower continental crust source with variable degrees of crustal components.

Latest early Carboniferous–middle Permian magmatism is characterized by high $\delta^{18}O$ ($\delta^{18}O>6.5$ ‰) and low εHf_i ($\varepsilon Hfi<0$) values, and it is predominantly metaluminous, calc-alkaline to high-K calc-alkaline, and mostly I-type. These characteristics depicts plutons formed as subduction-related magmas emplaced in a normal to thickened continental crust where they acquired the input of continental-like material and/or the influence of sediments. The simultaneous occurrence of the San Rafael orogenic event (ca. 284 Ma to 276 Ma) allows describing an orogenic setting for the magmatism: the Gondwanide Orogeny, linked to the assembling of Pangea supercontinent. South of 31°S, the absence of magmatism younger than 300 Ma in the Chilean territory can be explained by the progressive slab shallowing through time that eventually developed a flat slab segment (in Chile) during most of early Permian (300–290 Ma). This process not only hindered magmatism in Chile but also displaced it eastwards, to the Argentinian territory where subduction-related I-type suits can be seen from at least 33° to 36°S.

Middle Permian–Triassic magmatism presents lower $\delta^{18}O$ ($\delta^{18}O<6.5$ ‰) and more positive εHf_i (εHf_i = -3 to +3), and it is predominantly peraluminous, calc-alkaline to high-K calc-alkaline, and I-, S- and A-type. Overall, it shows trace element patterns of thinned continental crust. West-to-east geochemical zoning, i.e. increasing I-type volcanic arc granitoids westwards and increasing A-type within plate granites eastwards (at least between 28°–28°30'S in the Chilean Frontal Andes) allows inferring extensional conditions in a subduction zone caused by slab rollback and resulting in orogenic collapse. Slab rollback triggered intense extension and related magmatism in the backarc region respecting the previous latest early Carboniferous–middle Permian arc. Part of the magmatism occurred due to anatexis of a thinned lower continental crust, which melted because of accumulation of underplating basalts after decompression during the orogenic collapse, at the same time with typical subduction-related magmatism. Analogously from the previous period, south 31°S extensional-related magmatism was displaced inland (towards Argentina) due to slab shallowing, flat slab and prevailing slab rollback conditions. The reason behind the slab rollback extensional condition falls in particularly low subducting plate velocity while Pangea supercontinent was fully assembled.

When Pangea started its break-up (ca. 200 Ma), increase in the subducting plate velocity terminated the slab rollback conditions. Igneous activity was displaced westwards, towards Chilean territory, possibly in association with slab steepening, occurring primarily within the mantle wedge overlying the subducted slab thus explaining the transition between Triassic–Jurassic igneous activity, i.e. the onset of the Andean Orogenesis.

RESUMEN DE LA TESIS PARA OPTAR AL TÍTULO DE: Geólogo y grado de Magister en Ciencias, Mención Geología
POR: Álvaro Felipe Del Rey Hernández-González
FECHA: Agosto, 2016
PROFESORA GUÍA: Dr. rer.nat. Katja Deckart

PLUTONISMO DEL PÉRMICO Y TRIÁSICO EN LOS ANDES FRONTALES CHILENOS (28°–28°30'S): EVIDENCIA CLAVE DE LA EVOLUCIÓN GEODINÁMICA DEL MARGEN SUROESTE DE PANGEA Y SUS IMPLICANCIAS EN LA OROGÉNESIS ANDINA

Tradicionalmente, el magmatismo del Pérmico tardío–Triásico ha sido atribuido a un periodo caracterizado por intensas condiciones extensionales. Varias hipótesis han sido propuestas para explicar la extensión continental observada, incluyendo el cese de la subducción y desprendimiento del *slab*. No obstante, todas aquellas ideas sólo explican el magmatismo de manera local y fallan en dar un marco tectónico regional para todo el magmatismo de aquel periodo a lo largo del margen continental chileno–argentino. Asimismo, tampoco entregan una explicación clara de cómo aquella configuración tectónica cambió y dio origen a la subducción Andina al comienzo del Jurásico, ni tampoco entregan relaciones genéticas con el resto de la actividad ígnea coetánea observada a lo largo del margen. Esta investigación aporta nuevas perspectivas para el plutonismo del Paleozoico tardío–Triásico de la Cordillera Frontal Chilena usando nuevas edades U–Pb en zircón (SHRIMP II, LA-ICPMS); isotopos de O, Lu–Hf, Sm–Nd, Rb–Sr y Re–Os; y análisis geoquímicos de elementos mayores y trazas. Una detallada comparación con unidades coetáneas que extienden desde los 21° hasta los 40°S permite presentar un nuevo modelo a escala regional para aquel periodo de tiempo, a la vez de su conexión con la Orogénesis Andina.

Los resultados indican que el plutonismo estudiado presenta una tendencia continua desde elevados niveles de influencia continental (Carbonífero medio) hacia signaturas más mantélicas (Triásico). A pesar de su continuidad, es posible separar la actividad ígnea entre unidades con o sin afinidades mantélicas hace 270 Ma (Pérmico medio) usando valores isotópicos de $\delta^{18}O$. Además, anomalías negativas de Nb–Ta en conjunto con anomalías positivas de Pb, permiten inferir magmatismo de subducción durante todo el periodo estudiado. Por su parte, signaturas de εNd_i y $^{87}Sr/^{86}Sr_i$ evidencian una fuente proveniente de la corteza continental inferior la cual se vio afectada por diversos componentes corticales.

El magmatismo del Carbonífero medio–Pérmico tardío se encuentra caracterizado por valores altos de $\delta^{18}O$ ($\delta^{18}O>6.5‰$) y bajos de εHf_i ($\varepsilon Hfi<0$); es predominantemente metaluminoso, calco-alcalino a calco-alcalino de alto K y mayoritariamente del tipo I. Estas características describen plutones formados a partir de magmas relacionados con subducción, los cuales se emplazaron en una corteza continental de espesor normal a engrosado, lugar donde adquirieron el aporte de material cortical y/o la influencia de sedimentos. La simultánea ocurrencia del evento orogénico San Rafael (aprox. 284–276 Ma) permite describir un ambiente orogénico para el magmatismo: la Orogénesis Gondwánica, proceso ligado a la formación del supercontinente de Pangea. Al sur de los 31°S, la ausencia de magmatismo posterior a los 300 Ma en el territorio chileno puede ser explicada a partir de la progresiva somerización del *slab*, la cual eventualmente terminó con el establecimiento de un segmento de *flat slab* (en Chile) durante gran parte del Pérmico temprano (300–290 Ma). Este proceso no solo restringió el magmatismo en Chile, al mismo tiempo lo desplazó hacia el este, hacia territorio argentino, en donde magmatismo tipo I relacionado a subducción puede ser observado entre 33° y 36°S.

El magmatismo del Pérmico medio–Triásico presenta valores bajos de $\delta^{18}O$ ($\delta^{18}O<6.5‰$) y más positivos de εHf_i (εHf_i = -3 to +3); y es predominantemente peraluminoso, calco-alcalino a calco-alcalino de alto K, y del tipo I, S y A. En términos generales, sus patrones de elementos traza evidencian condiciones de corteza continental adelgazada. Zonación química Oeste–Este (i.e., granitoides de arco del tipo I ocurren en mayor abundancia hacia el Oeste, mientras que granitos de intraplaca del tipo A más hacia el Este en los Andes Frontales Chilenos, 28°–28°30'S) permiten inferir condiciones extensionales en un ambiente de subducción causado por *slab rollback* con consecuente colapso del orógeno. La condición de *slab rollback* provocó extensión intensa y su relacionado magmatismo en la región de tras arco con respecto al arco magmático previo (Carbonífero medio–Pérmico medio). Parte del consiguiente magmatismo se produjo debido a anatexis de una corteza continental inferior adelgazada, la cual se fundió debido a la acumulación de basaltos formados después de la descompresión causada durante el colapso del orógeno; al mismo tiempo con magmatismo asociado a subducción. De manera análoga al periodo anterior, el magmatismo extensional al sur de los 31°S fue desplazado hacia el continente (hacia Argentina) debido a una somerización del *slab*, o *flat slab*, al mismo tiempo de preponderantes condiciones de *slab rollback*. La razón detrás la extensión producto de *rollback* recae en bajas velocidades de subducción durante el periodo del supercontinente Pangea.

Cuando Pangea comenzó su desmembramiento (ca. 200 Ma), un aumento en la velocidad de subducción finalizó las condiciones de *slab rollback*. La consiguiente actividad ígnea fue desplazada hacia el Oeste (en territorio chileno), en posible asociación con un aumento en el ángulo de subducción, ocurriendo principalmente en la cuña mantélica sobreyaciente al *slab*. Finalmente, este proceso explicaría la transición entre el magmatismo Triásico y Jurásico, es decir, al momento del inicio de la Orogénesis Andina.

A mis padres,
Carmen Gloria y Nelson

Gracias por todo

ACKNOWLEDGMENTS

This research was financed by the Servicio Nacional de Geología y Minería (SERNAGEOMIN) project Plan Nacional de Geología (Geological Map 'Iglesia Colorada – Cerro El Potro'), the Masters fellowship of the Comisión Nacional de Investigación Científica y Tecnológica – CONICYT (grant no. 221320626), Dr. Katja Deckart private research resources, and additional funding provided by the Departamento de Postgrado y Postítulo, Universidad de Chile. The one-year academic exchange at the University of Ghent, Belgium, was fully funded by the Erasmus Mundus Action 2 – EMA2 Mundus Lindo (2012-2658) scholarship grant.

The present work could not have been possible without the encouragement and help of several people. I am deeply grateful to my supervisor, Dr. Katja Deckart, whose guidance and confidence in me, allow me to successfully carry on this work and grow as a scientist. I thank Dr. César Arriagada and Dr. Fernándo Martínez for trusting in me for the project, and Dr. Marc de Batist (University of Ghent) for having chosen me for the academic exchange. Also, I am grateful to Dr. Mark Fanning for the analytical work (U-Pb, Lu-Hf and O) and help during my internship at the ANU. I also would like to thank Dr. Robert Pankhurst, whose insightful comments successfully helped me to publish the main hypothesis of this research.

TABLE OF CONTENT

LIST OF FIGURES

LIST OF TABLES

INTRODUCTION

Chile is situated, from a geological perspective, at an important active continental margin, which has been subject of abundant investigation and debate. Its related protracted magmatism evidences the tectonic evolution along the southwestern margin of South America since about 320 Ma (Lower Pennsylvanian) until present day.

Traditionally, the geodynamic evolution has been divided into several tectonic cycles (Charrier et al., 2007), each one representing specific types of magmatism and tectonic regimes. Early Paleozoic history has been explained through a collisional model (Ramos, 1988), which indicates that the southwestern part of South America registered a tectonic history dominated by the progressive accretion of allochthonous and/or para-autochthonous terranes. According to that, the last stages of the Paleozoic collision involves the amalgamation of the Chilenia terrane at the western margin of Gondwana during Devonian times (Ramos et al., 1986; Álvarez et al., 2011) and the Patagonia terrane (from ca. 40°S southwards) at the southwestern margin in the early Permian (Ramos, 2008). From there, the Gondwanian tectonic cycle (latest early Carboniferous–late Permian) has been defined as an active subduction-related magmatic arc along the Chilean margin. Extensional conditions prevailed during this period with the exception of the San Rafael compressive orogenic deformation in middle Permian (Llambias and Sato, 1990). Later, the Pre–Andean tectonic cycle (late Permian–early Jurassic) corresponds to a period characterized by the cessation of subduction, the development of abundant and widely distributed felsic magmatism, and a paleo-geography dominated by NNW–SSE orientated extensional basins (e.g., Charrier et al., 2007, and references therein). Progressive extension towards the end of this period together with felsic magmatism has been interpreted as products of orogenic collapse and slab break-off (Mpodozis and Kay, 1990, 1992). Finally, the Andean tectonic cycle (early Jurassic–present) established the beginning of the long-lasting subduction-related magmatism along the Chilean margin since the renewal of subduction in the Pliensbachian (middle Lower Jurassic) (e.g., Charrier et al., 2007, and references therein). Typical Andean arc magmas were generated during this period in an almost uninterrupted way to present day. Despite the definition of these tectonic cycles, a comprehensive tectonic model for most of the Pre–Andean cycle is still missing, and the precise links with the processes that occurred before and after (i.e., Gondwanian and Andean subduction) are not clearly defined.

Late Carboniferous–Triassic plutonism is widespread along the entire Chilean–Argentinian border (21°–40°S) and comprises the Chilean Frontal Andes batholiths (28°–31°S), a series of important granitoids in the understanding of the tectonic setting controlling this magmatism. Notwithstanding its areal extension and geological relevance, still several important issues remain unaddressed. In this sense, how this magmatism

originated and how is it related to the coeval units along the Chilean margin, are the main questions trying to be answered in this research work. Consequently, the answer of which tectonic mechanism relating the transition between Permo–Triassic magmatism and the one produced during the Jurassic Andean tectonic cycle is also given. Therefore, this study is focused on the petrology of plutonic igneous rocks emplaced during late Paleozoic–Triassic times and its tectonic implications.

Here, new U–Pb (SHRIMP II, LA-ICPMS) zircon ages, together with O, Lu–Hf, Rb–Sr, Sm–Nd and Re–Os isotopic composition and major and trace whole-rock geochemical analysis are presented to unravel the petrogenetic processes controlling the formation of several units from part of the Chilean Frontal Andes (Montosa–El Potro batholiths, 28°–28°30'S). Isotopic and geochemical comparisons with coeval units ranging from 25°S to 40°S along the Chilean–Argentinian border allowed extending the hyphotesis and establishing a regional-scale comprehensive tectonic model.

This thesis consists in two main chapters; each one representing separated manuscripts, one published in Gondwana Research (chapter 1) and the other prepared for publication in Earth–Science Reviews. Both received the comments from Dr. Katja Deckart, Dr. César Arriagada and Dr. Fernando Martínez. Chapter 1: “Resolving the paradigm of the late Paleozoic–Triassic Chilean magmatism: Isotopic approach” broadly proposes a new tectonic model for most of the latest early Carboniferous–Triassic magmatism along the Chilean margin using U–Pb (SHRIMP II) in zircon, and O and Lu–Hf systematics performed by Dr. Mark Fanning at the Australian National University. Chapter 2: “Middle Permian–Triassic plutonism in the Chilean Frontal Andes (28°–28°30'S): a record of the evolution of the southwestern margin of Pangea” is currently in preparation for submission to Earth–Science Reviews and basically consists in supporting the model previously described using comprehensive major and trace geochemical analysis plus Rb–Sr, Sm–Nd and Re–Os isotopes, and additional U–Pb (LA-ICPMS) in zircon ages. Sampling and methodologies occupied are described within each chapter.

STATE OF THE ART

The Permian–Triassic tectonic models

The Permian–Triassic period in Chile comprises part of the defined Gondwanan tectonic cycle (late Devonian – earliest Permian) and the Pre-Andean tectonic cycle (latest Permian – earliest Jurassic) (e.g., Charrier et al., 2007). For the first one, it has been proposed (north of 33°S in Chile) an active subduction-related magmatic arc during Carboniferous times, which expanded and migrated towards the foreland during early Permian times, associated with the San Rafael orogenic deformation (Charrier et al., 2014).

On the other hand, the Pre-andean has been traditionally defined as a period of arrested or very slow subduction during which extensional conditions prevailed following deformation of the late Permian deposits. Accordingly, the end of this period has been defined as marked by resumption or more intense subduction activity along the continental margin and development of the early Jurassic magmatic arc (Charrier et al., 2014). The extensional conditions during the Pre-Andean favoured the development of widely distributed felsic magmatism along the Chilean-Argentinian margin that resulted predominantly from intense crustal melting (e.g., Kay et al., 1989; Mpodozis and Kay, 1992, among others). The magmatism of this period includes the Frontal Andes batholiths north of 33°S: the Elqui plutonic complex, a series of plutonic and subvolcanic units comprised in the late Lopingian to Middle Triassic age group (264-242 Ma) of Hervé et al. (2014), the equivalent of the Ingaguás superunit of Mpodozis and Kay (1990, 1992), which in turn represents the intrusive equivalent of the felsic upper Choiyoi group (Nasi et al., 1985; Mpodozis and Kay, 1990). Also, Norian and younger Triassic ages have also been obtained along the Chilean coast (Gana, 1991; Parada et al., 1999; Vásquez and Franz, 2008). All these widely distributed plutonic units and related volcanic ones demonstrate the vast regional extension of the late Permian-Triassic magmatism, which also includes units in the Argentinian Frontal Andes (e.g., Gregori and Benedini, 2013) and the Choiyoi province in Argentina (e.g., Kleiman and Japas, 2009).

Despite its extension and somewhat similar petrological characteristics - which allow for example, the definition of equivalent units from north of Chile (28°-31°S, Mpodozis and Kay, 1992) with the Choiyoi province in Argentina (36°-40°S, Kleiman and Japas, 2009) - different tectonic models have been proposed in order to explain the crustal derived extensional-related magmatism.

For the Chilean Frontal Andes, the traditional tectonic model belong to Mpodozis and Kay (1992), which interprets late Permian to Triassic units as best explained as post-collisional granitoids - after the accretion of the

unidentified ‘X terrene’ -, formed in conjunction with melting of a thinned and relaxing crust by underplated basalts. Gravitational collapse of the inactive slab (slab detachment) and loss of the mantle lithosphere and possibly the lower crust are proposed as the possible factors that could have produced the required decompressional mantle melting and crustal extension.

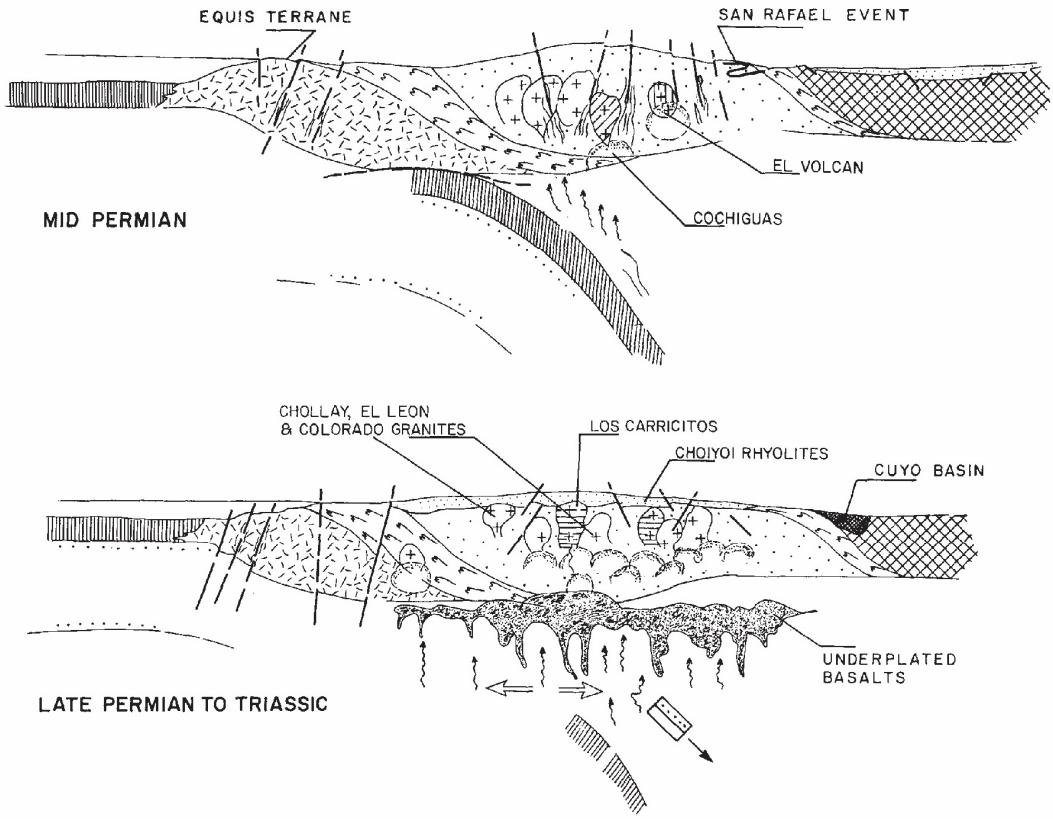

Fig. 0.1 Evolution of the central Andean Gondwana margin from mid Permian to the Triassic after Mpodozis and Kay (1992). Mid Permian: approach and oblique collision of the Equis terrane resulted in thickening of the crust. Final collision resulted in uplift and shortening deformation in the foreland (San Rafael event). Late Permian to early Jurassic: subduction-related magmatism ended. A combination of slab collapse and lithospheric (mantle and crustal) delamination was associated with decompressional mantle melting.

Additionally, for the Choiyoi province in Argentina (34°-36°S) the voluminous felsic magmatims of the upper Choiyoi is interpreted as major crustal melting associated with a thermal raise through a thinning crust. This thermal raise is related to the end of subduction due to slab detachment and post-orogenic extensional collapse, at the same time associated with clockwise rotations of continental blocks in relation to the margin which produced the shut of subduction and subsequent gravitational collapse of the oceanic plate and extension of the San Rafael Orogen (Kleiman and Japas, 2009).

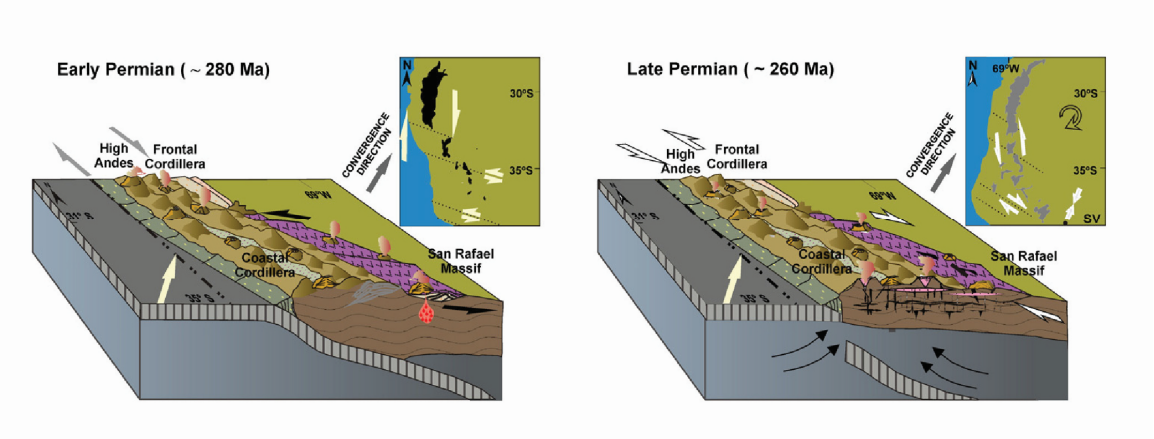

Fig. 0.2 Permian evolution of the SW Gondwana margin between 30° and 35°S in South America after Kleiman and Japas (2009). Early Permian: south of 34°S the margin is curved. Progressive shallowing of the oceanic plate resulted in inland arc migration with inception of volcanic eruptions syntectonically with the San Rafael orogeny. Late Permian: continental dextral clockwise block rotations situated the margin near parallel to the direction of convergence, north of 36°S. This caused the cessation of subduction and the extensional collapse of the orogen. Slab removal allowed astenospheric upwelling, concurrent profuse melting of the crust and the inception of the upper Choiyoi volcanism.

Although the cause for the cessation of subduction has been attributed to different mechanism in the previous models (Figs. 0.1 and 0.2), this idea –cessation of subduction- has also been previously suggested (Kay et al., 1989; Llambías and Sato, 1995; Franzese and Spalletti, 2001) thus becoming arguably the most known overall hypothesis for the late Permian–Triassic period.

Nevertheless, other works have shown geochemical and geochronological results suggesting that subduction-related magmatism indeed occurred during Permian-Triassic times. In particular, for the Coastal range and Chilean Frontal Andes (ca. 25°-26°S) Permian-Triassic plutonic complexes are interpreted as magmas from volcanic arc origin, indicating a stable geodynamic situation, i.e., continuous subduction, since early Permian time (Brown, 1991).

Moreover, for the Coastal range between 34°-37°S (west of the Choiyoi province in Argentina), Upper Triassic to Lower Jurassic plutonic units (225-197 Ma) have been explained as subduction-related arc magmas under extensional conditions in a tectonic regime of oblique subduction (Vásquez et al., 2011). Extension of the continental plate occurred under slab steepening regime, which generated crustal thinning close to the trench and generation of subcontinental mantle-derived magmas by decompression (Vásquez et al., 2011).

For the 34°-36°S section it seems models for Triassic magmatism are incompatible, proposing opposing ideas: ongoing subduction versus cessation of it. The same happens north, although it could be argued that Triassic

subduction-related units are located farther north (25°-26°S) than the ones defined as non-subduction related (28°-31°S). Nevertheless, these different scenarios make the overall tectonic setting for Permian–Triassic times a subject of much debate.

Furthermore, a recent work (Kato and Godoy, 2015) considers middle to late Triassic north-south trending near vertical shear zones (between 26°-42°S in coastal Chile) as consistent with large scale dextral transpression (or possible transform movement) during highly oblique NNE-SSW convergence along the Pre-Andean margin (sharing some similarities with the presently active San Andreas transform system of California), which would be in agreement with the general hiatus of regional subduction-related magmatism during middle to late Triassic, in opposition to the identified arc-related plutonism both at 26°S (Brown, 1991) and 34°-36°S (Vásquez et al., 2011) during Triassic times.

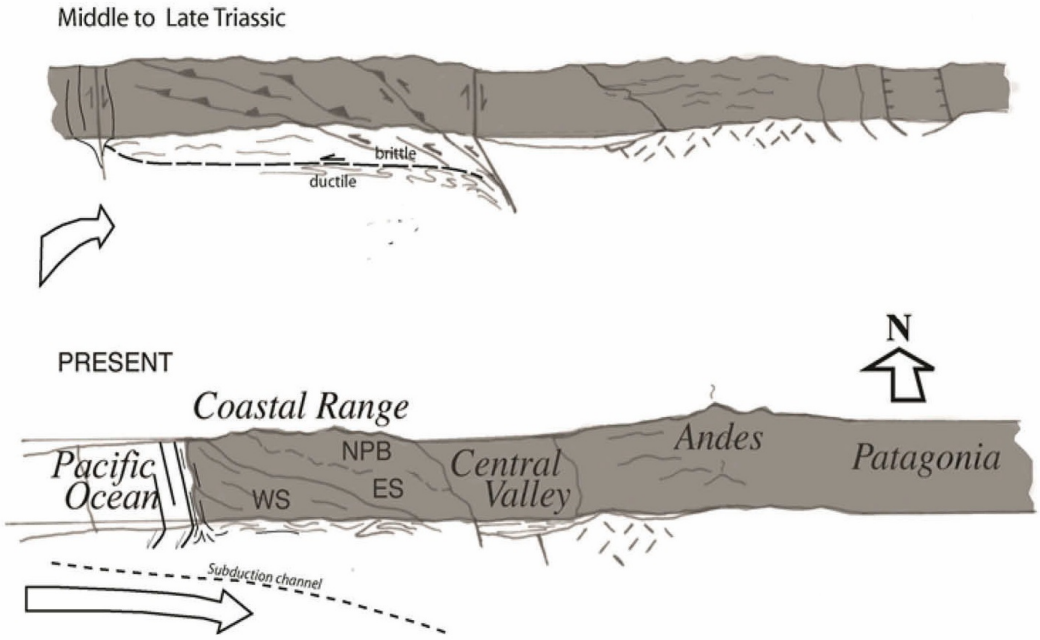

Fig. 0.3 Development of a possible transform (transpressional) zone within the context of the evolving South American margin after Kato and Godoy (2015). Middle to Late Triassic: transitional (post-Gondwanan/pre-Andean) uplift and dextral translation offsetting and modifying margin. Jurassic to present: Andean subduction. WS, Western Series; ES, Eastern Series; NPB, North Patagonia batholith/Nahuelbuta Range.

Regardless of its similarities and despite the fact sometimes late Permian–Triassic magmatism is treated as the Choiyoi province (extending from 23°S to 42°S in Chile and Argentina) (e.g., Kleiman and Japas, 2009), there is not a consensus concerning the tectonic regime in which this magmatism occurred. Furthermore, the discussion of subduction versus cease of subduction is still a subject in which scientific agreement has not been reached yet.

CHAPTER 1

Resolving the paradigm of the late Paleozoic–Triassic Chilean magmatism: Isotopic approach

A. del Rey[a, *], K. Deckart[a, b], C. Arriagada[a], F. Martínez[a]

[a]Departamento de Geología, Universidad de Chile, Santiago, Chile
[b]Advanced Mining Technology Centre (AMTC), Universidad de Chile, Santiago, Chile.

*Corresponding author (alvherna@ing.uchile.cl)

Gondwana Research, Volume 37, September 2016, Pages 172-181

Abstract

The Andean orogenic cycle and its subduction-related magmatism along the southwestern margin of South America began during the early Jurassic after an accretionary history throughout Paleozoic times. The Chilean and Argentinian Frontal Andes batholiths, together with the Coastal Batholith, represent most of the pre-Andean orogenic cycle plutonism. However, how late Paleozoic-Triassic magmatism occurred along this margin and its transition to the Andean orogenic cycle still remains unclear. Here we present a geodynamic model using all the available published Lu–Hf and oxygen isotopic data ranging from latitudes 28° to 40°S, together with 5 new Hf–O data and U-Pb zircon ages from the Chilean Frontal Andes. Data indicate that subduction began at least in the latest early Carboniferous and was continuous throughout the late Paleozoic–Triassic period. Isotopic and geochronological results show a continuous magmatic trend, from high $\delta^{18}O$ values (continental) to mantle-like signatures, as the rocks get younger. Between latest early Carboniferous and earliest middle Permian, magmas formed in a subduction-related arc during the Gondwanide Orogeny. Later, throughout middle Permian to Triassic, magmatism occurred in a slab rollback extensional setting, triggered by low subducting plate velocities while Pangea was essentially in a static reference mode. There is no evidence for cessation of subduction during the Triassic and its renovation in the early Jurassic as previous work suggested. Therefore, we propose that Andean subduction has been a continuous

tectonic process since Paleozoic times, whose initial geodynamic evolution was directly related to the Gondwanide Orogeny as part of the Pangea Assembly. Slab rollback, as well as shallowing and steepening of the subduction angle were among the triggers for the change in the type of magmatism observed among these rocks.

Keywords: Pangea assemblage, U–Pb geochronology, O–Hf isotopes, Zircon, Andean orogenic cycle

1.1 Introduction

Although it is one of the Earth's main plate boundaries, a complete comprehensive tectonic model for the paleo-South American southwestern margin in Chile does not exist. Specifically, the late Paleozoic–Triassic magmatism in Chile still has several important issues that remain unaddressed. First of all, how are these rocks related genetically along the Chilean margin (particularly from 28° to 40°S)? Second – and most important – in what tectonic setting did they originate? Traditionally, the geodynamic evolution has been explained through a collisional model (Ramos, 1988), which indicates that the southwestern part of South America registered a tectonic history dominated by the progressive accretion of allochthonous and/or para-autochthonous terranes. According to that model, the last stage of the Paleozoic collision involves the amalgamation of the Chilenia terrane at the western margin of Gondwana during Devonian times (Ramos et al., 1986; Álvarez et al., 2011) and the Patagonia terrane at the southwestern margin in the early Permian (Ramos, 2008). The eastward subduction of the paleo-Pacific oceanic plate under the Chilenia continental basement was responsible for the latest early Carboniferous–early Permian calc-alkaline I-type magmatism, now observed in the north-central Chilean and Argentinian Frontal Andes. Subsequently, during the Permian–Triassic period, calc-alkaline to transitional A-type granites were related to rifting (Mpodozis and Kay, 1992), which is associated with the Choiyoi province (23°S to 42°S in Chile and Argentina (Kay et al., 1989; Kleiman and Japas, 2009)). Based on these ideas, the change in the tectonic setting and thus its magmatism, has been interpreted as a consequence of a cessation in subduction after the accretion of an exotic, unidentified, ‘terrane X’ on the western side of Chilenia during the middle Permian (Mpodozis and Kay, 1992). This hypothetic collision was responsible for the cessation of subduction and therefore, formed the trigger for rifting conditions (extension due to slab collapse and lithospheric delamination). Re-establishment of subduction along the Chilean margin in the earliest Jurassic marked the initiation of the Andean orogenic cycle, which has continued without interruption to the present day (e.g. in Patagonia (Hervé et al., 2007)).

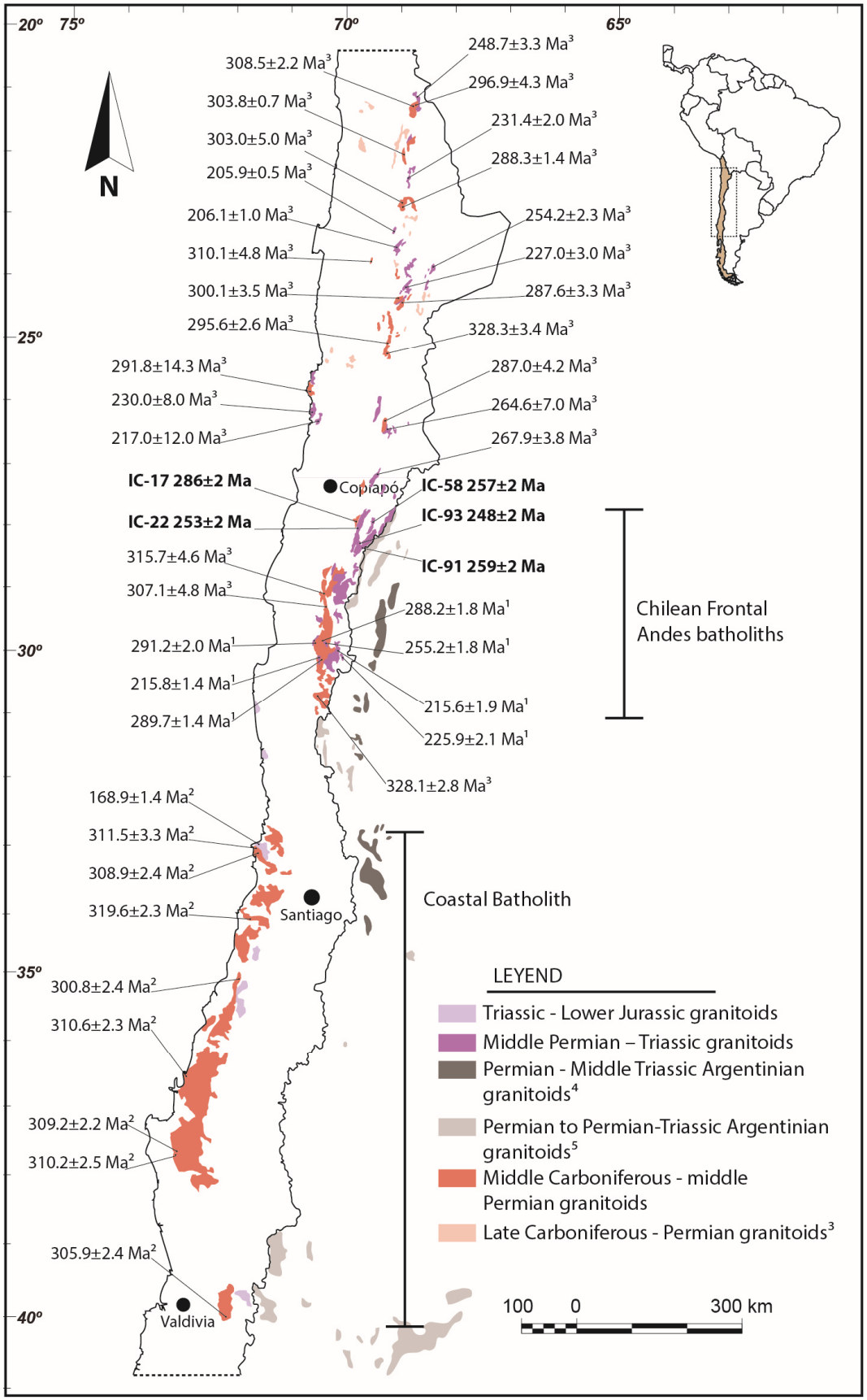
20º
75º
70º
65º
25º
30º
35º
40º
N
248.7±3.3 Ma3
308.5±2.2 Ma3
296.9±4.3 Ma3
303.8±0.7 Ma3
231.4±2.0 Ma3
303.0±5.0 Ma3
288.3±1.4 Ma3
205.9±0.5 Ma3
206.1±1.0 Ma3
254.2±2.3 Ma3
310.1±4.8 Ma3
227.0±3.0 Ma3
300.1±3.5 Ma3
287.6±3.3 Ma3
295.6±2.6 Ma3
328.3±3.4 Ma3
291.8±14.3 Ma3
287.0±4.2 Ma3
230.0±8.0 Ma3
264.6±7.0 Ma3
217.0±12.0 Ma3
267.9±3.8 Ma3
IC-17 286±2 Ma
Copiapó
IC-58 257±2 Ma
IC-22 253±2 Ma
IC-93 248±2 Ma
315.7±4.6 Ma3
IC-91 259±2 Ma
307.1±4.8 Ma3
288.2±1.8 Ma1
291.2±2.0 Ma1
255.2±1.8 Ma1
215.8±1.4 Ma1
215.6±1.9 Ma1
289.7±1.4 Ma1
225.9±2.1 Ma1
328.1±2.8 Ma3
Chilean Frontal
Andes batholiths
168.9±1.4 Ma2
311.5±3.3 Ma2
308.9±2.4 Ma2
319.6±2.3 Ma2
Santiago
Coastal Batholith
300.8±2.4 Ma2
310.6±2.3 Ma2
309.2±2.2 Ma2
310.2±2.5 Ma2
305.9±2.4 Ma2
Valdivia
LEYEND
Triassic - Lower Jurassic granitoids
Middle Permian – Triassic granitoids
Permian - Middle Triassic Argentinian granitoids4
Permian to Permian-Triassic Argentinian granitoids5
Middle Carboniferous - middle Permian granitoids
Late Carboniferous - Permian granitoids3
100 0 300 km

Fig. 1.1 Geographical distribution of the Chilean Frontal Andes late Paleozoic – Triassic batholiths and the Coastal Batholith (from ca. 20°S to 40°S). The location of the samples and their U–Pb crystallization ages are indicated (IC-17, IC-22, IC-58, IC-91, IC-93, this work; 1, Hervé et al. (2014); 2, Deckart et al. (2014); 3, Maksaev et al. (2014)). Tera Wasserburg concordia and age probability density plots of the analyzed samples are given in Fig. 1.2. Sample groups 1 and 2 have Hf–O isotopic data associated with the U–Pb ages (Fig. 1.3). Argentinian late Paleozoic–Triassic batholiths are also shown (4, Gregori & Benedini (2013); 5, SEGEMAR (2012)).

However, the tectonic process controlling the magmatism linking the Paleozoic accretionary history and the Jurassic Andean orogenic cycle is not clearly understood. Complete absence of geological evidence for the 'terrane X' and the remaining question whether subduction was renewed or intensified at the beginning of the Jurassic (Charrier et al., 2014) make the late Paleozoic–Triassic Chilean magmatism a crucial source of evidence. Moreover, there is no previous work relating all the intrusive units from that period of time (at least from 28° to 40°S). On the contrary, it has been suggested that units north and south of 33°S are genetically unrelated (Charrier et al., 2014; Hervé et al., 2014), arguing that the emplacement ages differ considerably between southern and northern plutons. Here we use all the available published Lu–Hf and oxygen isotopic data ranging from latitudes 28° to 40°S, together with 5 new Hf–O data and U–Pb zircon ages from the Montosa–El Potro Batholith (28°-28°30'S) in the Chilean Frontal Andes (Fig. 1.1) to propose a new tectonic scenario, and thus challenge previous models by demonstrating a continuous magmatic evolution from the latest early Carboniferous to latest Triassic with a noticeable change in the middle Permian.

1.2 Materials and methods

The studied zircon grains are from 5 rock samples belonging to the Montosa–El Potro Batholith (28° to 28°30'S), which is part of the Chilean Frontal Andes (Fig. 1.1). Zircon grains were separated from 2 kg whole rock samples using standard techniques: grinding, Gemini table, heavy liquids and Frantz separation followed by final hand picking under a binocular microscope. Separating work was undertaken in the mineral separating facility of the Geology Department, University of Chile.

U–Th–Pb analyses were undertaken using a sensitive high-resolution ion microprobe (SHRIMP II) for defining the $^{206}Pb/^{238}U$ ages following standard procedures (Williams, 1998). Between 15 and 17 grains were analyzed in each sample to characterize the age variation present. Weighted mean $^{206}Pb/^{238}U$ ages were calculated and the uncertainties are reports as 95% confidence limits.

$\delta^{18}O$ analyses were carried out using a sensitive high resolution ion microprobe (SHRIMP SI) and electron gun for charge compensation (Ickert et al. 2008) in the exact same spots were the U–Pb analyses were obtained with

SHRIMP II. Calculated $\delta^{18}O$ values were normalized relative to an FC1 weighted mean $\delta^{18}O$ value of +5.61 ‰ .

Lu–Hf analyses were completed using laser ablation multi-collector inductively coupled plasma mass spectrometry (Neptune LA-MC-ICPMS) coupled with a HelEx 193 nm ArF Excimer laser ablation system (Eggins et al., 2005). Laser ablation analyses were done on the spots previously used for U–Pb and oxygen isotopes.

U–Pb, oxygen and Lu–Hf analytical labwork was undertaken at the Research School of Earth Sciences of the Australian National University in Canberra, Australia. Detailed analytical methods are found in Supplementary information.

1.3 Results and discussion

1.3.1 Chilean Frontal Andes (28°–28°30'S) results

Isotopic and geochronological analyses are summarized in Table 1. Full geochronological and isotopic data are provided in Supplementary data.

U–Pb zircon age determinations are summarized as follows (Fig. 1.2): La Estancilla pluton sample (IC-17) yielded a weighted mean $^{206}Pb/^{238}U$ age of 286 ± 2 Ma (MSWD = 1.17); Montosa sample (IC-22), 253 ± 2 Ma (MSWD = 0.81); El León sample (IC-58), 257 ± 2 Ma (MSWD = 0.97); Chollay sample (IC-91), 259 ± 2 Ma (MSWD = 0.94); and El Colorado sample (IC-93), 248 ± 2 Ma (MSWD = 1.17). Accordingly, La Estancilla pluton corresponds to Artinskian (early Permian) whilst the other 4 samples are very close to the Permian–Triassic boundary (according to the 2016 IUGS International Chronostratigraphic Chart). All obtained ages can be confidently interpreted as igneous crystallization ages.

εHf_i values among the 5 units are generally overlapping (La Estancilla pluton: between -3.8 and +1.2; Montosa: between -3.2 and +1.6; El León: between -2.5 and +2.0; Chollay: between -1.3 and +2.8), with only one sample showing more positive values (El Colorado: between -2.7 and +4.7). There is not a noticeable variation within the εHf_i signatures among the units (most values range approximately from -3.0 to +3.0). On the other hand, La Estancilla pluton shows noticeable higher $\delta^{18}O$ values (approximately over 6.5‰, with $\delta^{18}O$ ranging from 6.6 ‰ to 7.5 ‰) compared to the other units (mainly below 6.5‰, with $\delta^{18}O$ ranging from 5.5 ‰ to 6.7 ‰ for Montosa; from 5.5 ‰ to 6.4 ‰ for El León; from 4.8 ‰ to 6.4 ‰ for Chollay; and from 4.4 ‰ to 6.0 ‰ for El Colorado).

Calculated two-stage Depleted Mantle model ages (T_{DM2}) range from 1.1 to 1.5 Ga (Mesoproterozoic) for La Estancilla pluton; from 1.1 to 1.4 Ga (Mesoproterozoic) for Montosa; from 1.1 to 1.3 Ga (Mesoproterozoic) for El León; from 1.0 to 1.3 Ga (Mesoproterozoic) for Chollay; and from 0.9 to 1.4 Ga (early Neoproterozoic–Mesoproterozoic) for El Colorado. These ages show a significant crustal residence time with inferred separation from a depleted mantle source during Mesoproterozoic times.

The 5 granitoid samples corresponding to a north-to-south distance along the Montosa–El Potro Batholith of ca. 50 km record a range in crystallization ages between 286 Ma and 248 Ma (early Permian to early Triassic). Isotopic εHf_i values do not show a considerable difference among the samples and range from -3.8 to +4.7, whereas $\delta^{18}O$ indicates a considerable difference between the oldest sample (IC-17) and the rest of them (IC-22, IC-58, IC-91 and IC-93): values range between 6.6 ‰ and 7.5 ‰ ; and 4.4 ‰ and 6.7 ‰ respectively. The new data largely fill a previous apparent 'gap' in the trend of Fig. 1.3 (between the Coastal Batholith and the Frontal Andes Batholith) making it now continuous from latest early Carboniferous to Triassic.

1.3.2 Hf–O isotopic signatures and U–Pb geochronological interpretations

Results indicate a clear and continuous trend from high values of $\delta^{18}O$ to mantle-like signatures with lower $\delta^{18}O$, as the rocks get younger (from ca. 9.3 ‰ during latest early Carboniferous to ca. 4.4 ‰ and lower in the late Triassic, Fig. 1.3). Despite its continuity, it is possible to separate units with or without 'mantle zircon values' at ca. 270 Ma (middle Permian). High values of $\delta^{18}O$ ($\delta^{18}O > 6.5$ ‰) indicate a continental crustal to supracrustal component (Taylor and Sheppard, 1986; Pietranik et al., 2013), and low εHf_i ($\varepsilon Hf_i < 0$), the addition of non-radiogenic continental crust-like material (Kemp et al., 2007). This isotopic signature is observed in both the Frontal Andes and the Coastal Range, with zircon isotope values of different samples completely superimposed (Fig. 1.3). This allows us to distinguish a stage from at least 325 Ma to 270 Ma (late Mississippian–middle Permian) in which magmas formed with a crustal component, and one from 270 Ma to 210 Ma (middle Permian–late Triassic) in which the magmas are dominated by mantle components. Another important feature is the fact that two-stage Depleted Mantle Model Age (T_{DM2}) calculations yielded Mesoproterozoic ages for all these samples, indicating that a component of the magmas from which the zircons crystallized had a significant residence time and therefore the magmatic arc formed on continental crust. Part or all of the continental crust-like material required for the high $\delta^{18}O$ values could correspond to sediments transported deep into the mantle wedge by the subducting slab (Gerya and Meilick, 2011) or the isotopic signature could have been acquired

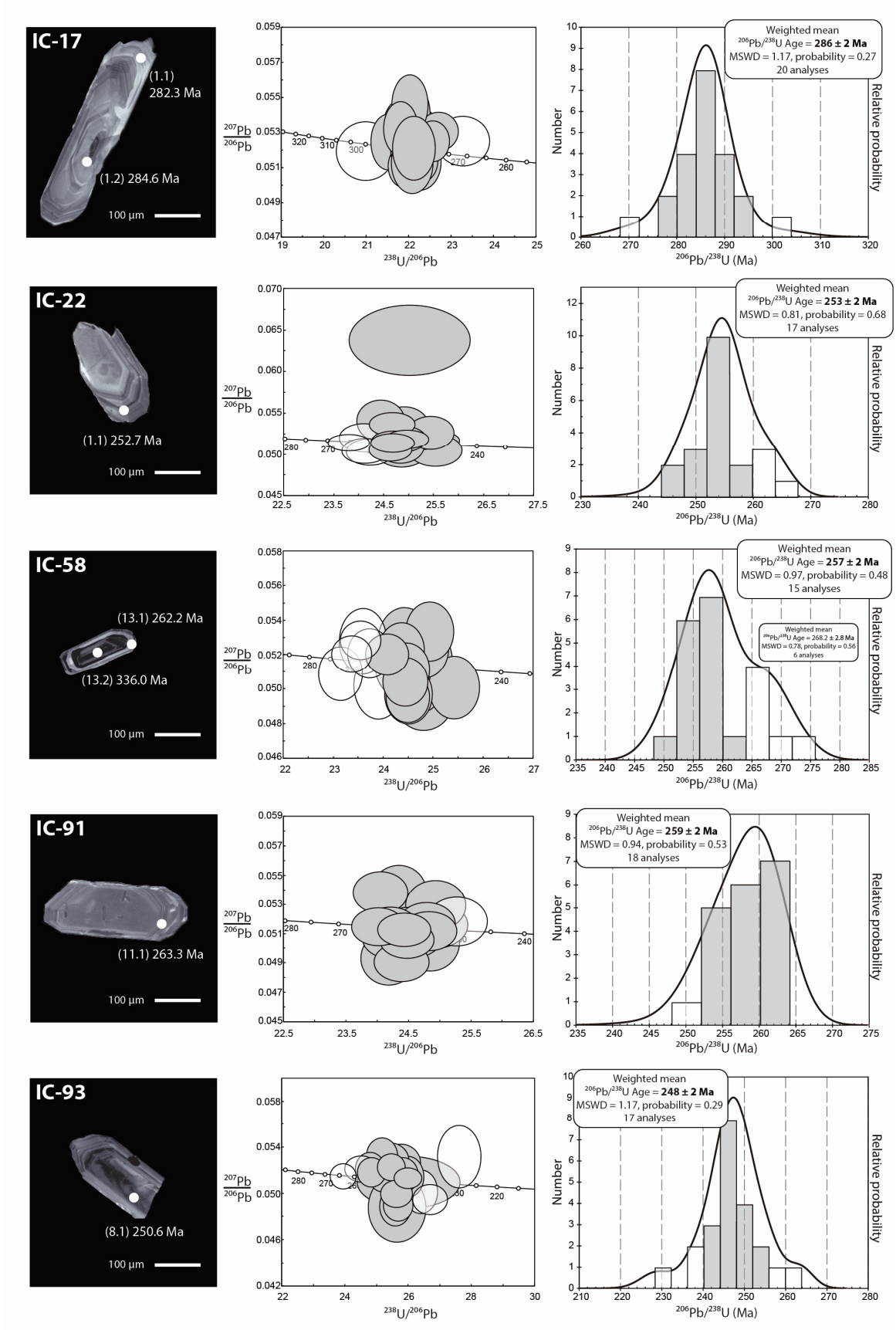
IC-17
(1.1)
282.3 Ma
(1.2) 284.6 Ma
100 µm
Weighted mean
$^{206}Pb/^{238}U$ Age = **286 ± 2 Ma**
MSWD = 1.17, probability = 0.27
20 analyses
IC-22
(1.1) 252.7 Ma
100 µm
Weighted mean
$^{206}Pb/^{238}U$ Age = **253 ± 2 Ma**
MSWD = 0.81, probability = 0.68
17 analyses
IC-58
(13.1) 262.2 Ma
(13.2) 336.0 Ma
100 µm
Weighted mean
$^{206}Pb/^{238}U$ Age = **257 ± 2 Ma**
MSWD = 0.97, probability = 0.48
15 analyses
Weighted mean
$^{206}Pb/^{238}U$ Age = 268.2 ± 2.8 Ma
MSWD = 0.78, probability = 0.56
6 analyses
IC-91
(11.1) 263.3 Ma
100 µm
Weighted mean
$^{206}Pb/^{238}U$ Age = **259 ± 2 Ma**
MSWD = 0.94, probability = 0.53
18 analyses
IC-93
(8.1) 250.6 Ma
100 µm
Weighted mean
$^{206}Pb/^{238}U$ Age = **248 ± 2 Ma**
MSWD = 1.17, probability = 0.29
17 analyses
$^{207}Pb/^{206}Pb$
$^{238}U/^{206}Pb$
Number
Relative probability
$^{206}Pb/^{238}U$ (Ma)

Fig. 1.2 Geochronological analyses. Cathodoluminescence images of representative zircon grains along Tera–Wasserburg Concordia and age probability density plots (95% confidence limits) for each sample. IC-17: La Estancilla pluton; IC-22: Montosa; IC-58: El León; IC-91: Chollay; and IC-93: El Colorado.

through crustal contamination as the plutons were emplaced in the upper parts of the continental crust. Thus, the O–Hf compositions indicate a deep source of magmas, either affected by assimilation processes during magma ascent or with the influence of material acquired at depth, in the subcontinental mantle wedge.

The younger rocks of this study (<270Ma) show markedly different $\delta^{18}O$ compositions to the rocks described above. They show $\delta^{18}O < 6.5$ ‰ (Fig. 1.3), along with a wider range of εHf_i values (mostly from -3 to +3). The $\delta^{18}O$ data (4.9 to 6.5 ‰) indicate mantle source magmas from which the zircons crystallized with no ingestion of continental crust or supracrustal material (units fall completely within the mantle zircon range; taken from Valley et al. (1998)) or minor participation of the latter ($\delta^{18}O$ slightly above the mantle zircon limit). In the case of εHf_i values, although they are very concordant, they show a tendency from less to more radiogenic as the rocks get younger. Positive εHf_i values indicate a more mantle-derived influence (Valley et al., 1998; Pietranik et al., 2013) (Fig. 1.3), which could reflect the addition of juvenile material in a foreland region (Dahlquist et al., 2013). Nevertheless, the overlap of isotopic data and ages does not allow a more specific differentiation among these samples and thus the differences can be attributed to variations in the magma source and/or in the magmatic differentiation processes. On the other hand, low $\delta^{18}O$ values (between 3.5 and 5.5 ‰) with positive εHf_i ratios (ca. +3 to +7) could be related to a subcontinental mantle source of magmas with assimilation of high temperature altered continental rocks or oceanic crust (Bindeman and Valley, 2001; Monani and Valley, 2001; Bolhar et al., 2008).

Table 1.1 Summarized U–Pb SHRIMP II in zircon ages, initial εHf_i and $\delta^{18}O$ values for zircon spots from Montosa–El Potro Batholith.

Sample/Unit	Geographical coordinates	Lithology	$^{206}Pb/^{238}U$ Age (Ma)	Initial εHf_i	$\delta^{18}O$ (‰) (range/average)	T_{DM2} Hf (Ga)
IC-17/La Estancilla pluton	28°00′14″S 69°53′05″W	Hbl-bt tonalite	286 ± 2	-3.8 to +1.2	6.6–7.5/6.9	1.1–1.5
IC-22/Montosa	28°05′34″S 69°50′57″W	Hbl-bt tonalite	253 ± 2	-3.2 to +1.6	5.5–6.7/6.1	1.1–1.4
IC-58/El León	28°01′06″S 69°32′19″W	Bt-hbl monzogranite	257 ± 2	-2.5 to +2.0	5.5–6.4/6.1	1.1–1.3
IC-91/Chollay	28°28′17″S 69°43′25″W	Bt-hbl syenogranite	259 ± 2	-1.3 to +2.8	4.8–6.4/5.5	1.0–1.3
IC-93/El Colorado	28°24′38″S 69°47′11″W	Bt syenogranite	248 ± 2	-2.7 to +4.7	4.4–6.0/5.3	0.9–1.4

Notes: Lithologies were determined using petrographic descriptions, before the geochemical analyses.
T_{DM2}: Two-stage Depleted Mantle Model Age.

Some zircons, although showing mantle-like $\delta^{18}O$ values and εHf_i between +2 and -2, are from highly differentiated rocks (i.e. granites). This

signature is normally a characteristic of mafic igneous rocks and can be observed in arc magmas contaminated by sediments, since the O-isotope signature is relatively insensitive to mixing with arc-subducted sediments (Nebel et al., 2011). Melting of old mafic crust, even with limited proportions of sediments, can produce mantle-like $\delta^{18}O$ signatures without a real involvement of mantle material (Clemens et al., 2011; Villaros et al., 2012; Pietranik et al., 2013). This means that the rocks emplaced during the middle Permian–Triassic could have involved melting of an old, thinned, mafic crust (e.g., IC-93, IC-91, Fig. 1.3) with more or less continental crust

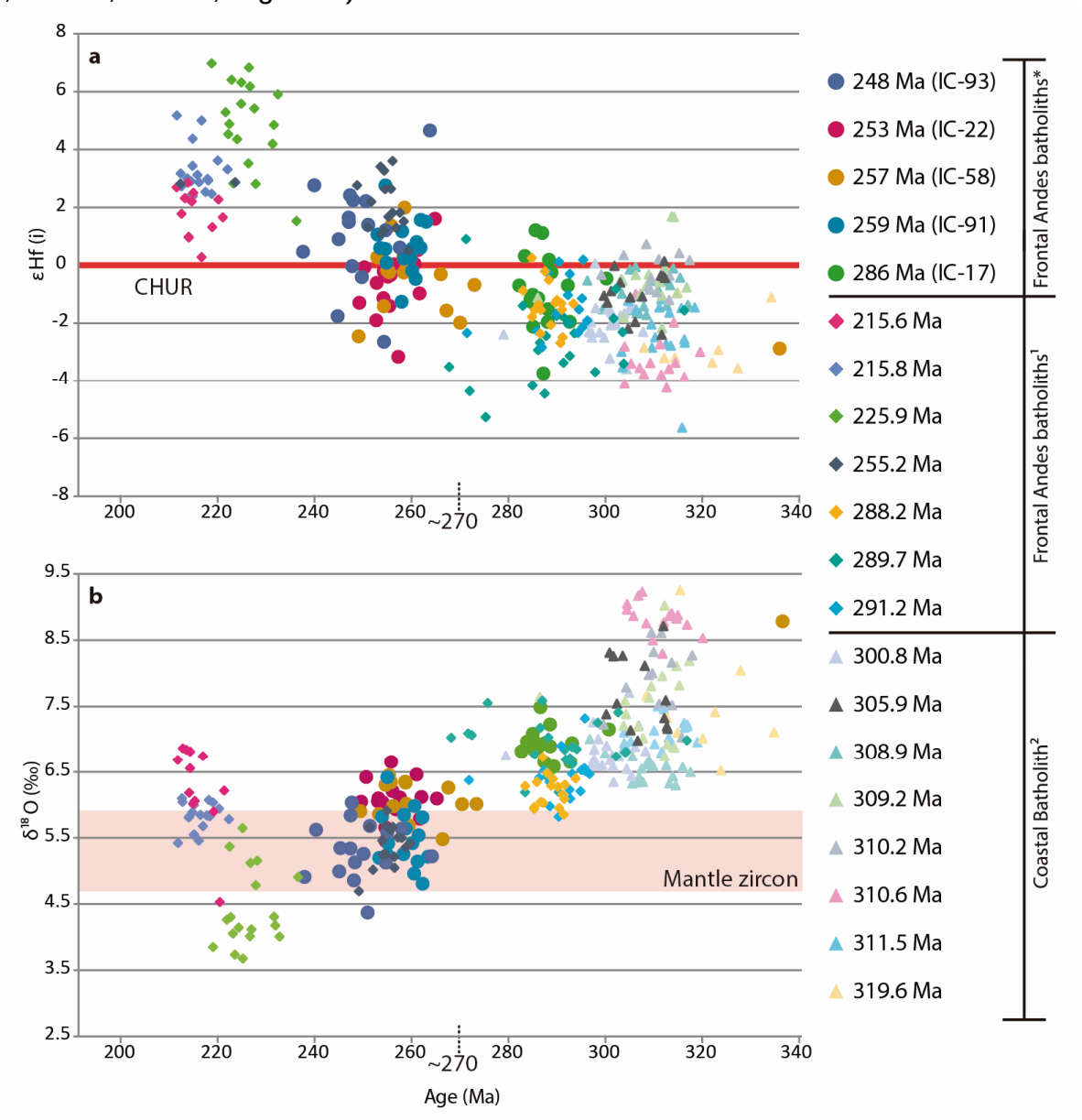

Fig. 1.3 Progressive isotopic evolution. a. Initial εHf_i vs Age (Ma) diagram; b. $\delta^{18}O$ vs Age (Ma) diagram for the samples from the Chilean Frontal Andes (*this work); its continuation (1, Hervé et al. (2014)); and the Coastal Batholith (2, Deckart et al. (2014)). Samples extend from 20°S to 40°S. A clear and continuous trend in the magmatism from high values of $\delta^{18}O$ to mantle-like signatures can be seen. At ca. 270 Ma (middle Permian), isotopic signatures (especially with $\delta^{18}O$) indicate the evolution from continent-derived characteristics to mantle-like signatures revealing variations in the tectonic setting (see section 3.2). Mantle zircon $\delta^{18}O$ range is taken from Valley et al. (1998).

material involvement (e.g., IC-22, IC-58, Fig. 1.3). The newly formed magmas inherited mantle-like $\delta^{18}O$ values from the mafic crust (lower continental crust) and some of them were slightly contaminated with a continental crust component. The resulting rocks were more differentiated but preserved mantle-like $\delta^{18}O$ signatures. It can be postulated that this occurred in a thinned continental crust context – possibly due to an extensional setting.

Higher $\delta^{18}O$ samples could have resulted from subduction-related magmatism in a normal-to-thickened continental crust, with involvement of continental crust to supracrustal material. Such a tectonic setting has been proposed for the Coastal Batholith (Deckart et al., 2014), which in consequence could define a single magmatic belt together with the Frontal Cordillera batholiths. U–Pb zircon ages from previous works (e.g., Maksaev et al., 2014) (Fig. 1.1) allow us to identify continuous plutonism from 328 to 300 Ma along the entire belt between 21°S and 40°S. There was protracted plutonism from 328 to ca. 270 Ma north of 33°S in Chile, but subduction-related granitoids younger than 300 Ma are absent to the south. Furthermore, a single inherited zircon core from a 257 Ma sample (at around 28°S with mantle-like $\delta^{18}O$) yielded ca. 336 Ma and $\delta^{18}O$ and εHf_i values of 8.76 ‰ and -2.88 respectively, showing the same isotopic signatures as the rocks from the older units here analyzed. Despite that it may be arguable that it is only one zircon core, it still shows the same isotopic composition as the coeval zircon grains and therefore, it can give a glimpse of older rocks forming under the same tectonic conditions.

Although previous work (Charrier et al., 2014; Hervé et al., 2014) defined four magmatic groups ranging from latest early Carboniferous to late Triassic based on age clusters, their geochemical and isotopic characteristics are coherent with the two groups described here and also coincide with major episodes of volcanism (Maksaev et al., 2014). Rocks younger than middle Permian (<270Ma) show a more juvenile isotopic composition whereas the older ones (i.e. latest early Carboniferous–early Permian), represent rocks syntectonically emplaced into thickened crust.

1.3.3 Magma genesis and geodynamic evolution

1.3.3.1 Pre–middle Permian

The Andean margin of Gondwana can be considered as an accretionary orogeny (Vaughan and Pankhurst, 2008). Between Silurian and Devonian periods, the Chilenia terrane accreted onto the western Pacific margin of Gondwana (Ramos et al., 1986; Bahlburg and Hervé, 1997) (Fig. 1.4a). Convergence in this segment may have started between ca. 343 and 310 Ma (Willner et al., 2012). Orogenic deformation due to changes in the intensity of plate convergence during that period marks the commencement of a major

subduction cycle (Ramos and Alemán, 2000). Subsequently, from latest early Carboniferous to earliest middle Permian, high $\delta^{18}O$ isotopic signature plutons were emplaced in a subduction-related compressional setting, possibly as the roots of the magmatic arc beneath the Chilenia basement (Fig. 1.4b). This orogenic deformation corresponds to the Gondwanide Orogeny, which is also part of the end of the Terra Australis Orogen, starting with Rodinia break-up at ca. 630–530 Ma (Cawood, 2005). It includes the San Rafael event (ca. 284 Ma to 276 Ma), a compressional episode marked by intense folding and thrusting (Llambias and Sato, 1990) observed in the Argentinian Frontal Cordillera. In this tectonic configuration, isotopic data suggest a crustal to supracrustal component in the magmas and/or the influence of mature sediments transported through the subducted slab, given the increased $\delta^{18}O$ values and negative εHf_i, the latter indicating the input of less radiogenic, continental-like material.

This orogenic event was the result of a major global plate reorganization: the assembly of Pangea (Cawood, 2005), which occurred between ca. 320 and 280 Ma (Li and Powell, 2001) and was contemporaneous with the high $\delta^{18}O$ magmatism described above. In other words, all the magmatism from latest early Carboniferous to earliest middle Permian was emplaced in a subduction setting under orogenic conditions during the Gondwanide Orogeny as a consequence of the subduction of the Pantalassa Oceanic Plate under the southwestern margin of the assembling Pangea (Fig. 1.4b).

1.3.3.2 Post–middle Permian

After ca. 270 Ma and once Pangea was fully assembled, a new post-orogenic extensional setting was configured. Due to Pangea being in a static reference mode (Vilas and Valencio, 1978) or with arrested continental drift (Charrier et al., 2014) and in consequence, with ceasing or very low subduction velocities (Charrier et al., 2014), a new geodynamic scenario was configured. A low subducting plate velocity promotes a relatively steady hinge retreat (Schellart, 2005) resulting in backarc extension. Additionally, a plate rollback velocity greater than the movement of the continent towards the trench – which in the case of Pangea can be considered arrested – can also trigger backarc extension (Grocott and Taylor, 2002). This tectonic setting can be seen in two active continental margins today: East Asia and the Mediterranean (Schellart, 2005). Generalized extension at the southwestern margin of Pangea affected pre-existing zones of weakness (Charrier et al., 2014), particularly the hanging walls of sutures between the Paleozoic accreted terranes (Mpodozis and Ramos, 2008; Ramos, 2009). This resulted in the development of several NW-SE basins whose deposits are generally marine to continental from the coast to their inland prolongations (Charrier et al., 2014), including the rift-related bimodal sequences of the Choiyoi province (Kay et al., 1989). Moreover, considering at around 40°S the southernmost limit of the accreted Chilenia terrane (Ramos, 2009) and thus the area of the lateral

slab edge, rapid rollback can be expected there (Schellart et al., 2007; Schellart, 2008). This results in significant upper plate extension within 1800 km of the lateral slab edge (Schellart et al., 2007) that can explain the increasing extensional-related magmatism and depocentres of the Triassic-earliest Jurassic rift systems towards 40°S (between 22° and 40°S ≈ 2000 km).

Slab rollback extension promoted the conditions for the mantle-like $\delta^{18}O$ and progressively higher εHf_i magmatism. As the continental crust thinned (orogenic collapse), decompression triggered melting in the mantle. Large amounts of juvenile basaltic magmas accumulated below the continental crust (underplating) providing sufficient heat for melting of the old thinned mafic crust and thus, new melts inherited mantle-like $\delta^{18}O$ signatures but relatively low εHf_i. This configuration lasted at least from 270 Ma to 210 Ma according to $\delta^{18}O$ and εHf_i signatures (Fig. 1.4b). However, the presence of bimodal magmatism (from 20°S to 31°S) until the late Triassic (ca. 205 Ma (Maksaev et al., 2014)) suggests that the slab rollback extensional setting was continuous throughout middle Permian and Triassic times. This scenario is coherent with slab rollback during early Carboniferous in the Eastern Sierras Pampeanas, Argentina (Alasino et al., 2012), thus making it a relatively continuous process (except for the San Rafael compressional event) which progressed westwards to the Chilean Frontal Andes, and ultimately defined the tectonic configuration during middle Permian–Triassic. εHf_i values reported here are within the range of previous results (Dahlquist et al., 2013, 2016), supporting the idea of addition of variable amounts of juvenile material in a foreland extensional region.

South of 31°S, progressive slab shallowing from ca. 300 to 290 Ma displaced the magmatism eastwards. Permian-Triassic plutonism was not developed in the Chilean margin but is present in Argentina. The shallower slab setting was not uniform from 31°S to 40°S; it was gradually shallower from 31°S to 36°S, completely flat between 36°S and 39°S and again shallower from 39°S to 40°S (Kleiman and Japas, 2009) (Fig. 1.5). This segmentation explains the presence of subduction-related magmatism (ca. 276 Ma), which later changed into a transitional, post-orogenic crust-derived middle Permian (273–262 Ma) to Triassic bimodal magmatism in Argentina (Gregori and Benedini, 2013) (Fig. 1.5), in agreement with the isotopic interpretations presented here. Notwithstanding a shallower oceanic plate, arrested continental drift and slow subduction velocity prevailed. Thus, slab rollback extension was still present south of 31°S during middle Permian–Triassic times. In addition, scarce late Triassic anorogenic extensional-related A-type granites within the Coastal Batholith Range (Vásquez and Franz, 2008) can be linked to this tectonic setting as magmatism produced by crustal melting due to orogenic collapse. The results indicate a common setting for all the middle Permian–late Triassic magmatism from 20°S to 40°S: post-orogenic backarc extensional conditions due to slab rollback.

1.3.3.3 Overall geodynamic evolution

The latest early Carboniferous–middle Permian high $\delta^{18}O$ granitoids, as well as the middle Permian-Triassic extension-related plutonic complexes, formed a continuous magmatic belt at least between 20°S and 40°S. The magmatism progressively and almost uninterruptedly evolved from a continental-derived source towards mantle-like signatures from latest early Carboniferous to late Triassic as a response to the tectonic changes before, during and after Pangea assembly (Fig. 1.4). First, subduction of the paleo-Pacific oceanic plate (Panthalassa Ocean) under the western margin of paleo-South America (southwestern margin of Gondwana) was the cause of the crust-derived magmatism, which was syntectonic with compressional deformation of the San Rafael Tectonic Event during the Gondwanide Orogeny. Subsequently, and throughout the existence of Pangea as a supercontinent (after ca. 270 Ma), low subduction velocity triggered steady backarc extension and related magmatism due to hinge retreat. Progressive slab shallowing from 31°S southward (starting ca. 300–290 Ma), shifted magmatism inland. This tectonic configuration remained continuous until the latest Triassic, when the initial break-up of the Pangea Supercontinent took place (ca. 200 Ma (Deckart et al., 1998; Veevers, 2005; Torsvik and Cocks, 2013)). Changes of the plate dynamics from the static mode of Pangea towards an increased convergence rate of the newly re-established Gondwana (with higher subduction velocity) concluded slab rollback extension and thus, its magmatism in the backarc region. Because of the new conditions, and possibly in association with steepening of the oceanic subducting plate, magmatism was displaced westwards (i.e. trenchward), occurring primarily within the mantle wedge overlying the subducted slab (Pankhurst et al., 1988). This tectonic evolution is coherent with the presence of the early–late Jurassic magmatic arc in the Coastal Range (Charrier et al., 2014), stretching from southern Peru to central Chile (Mpodozis and Ramos, 2008). The locus of plutonism jumped to the Coastal Range from the east by the beginning of the Jurassic in an almost non-magmatic episode (scarce presence of latest Triassic–earliest Jurassic plutons: ca. 205–200 Ma), which is comparable to the jump of the magmatism from the Coastal Range to the High Andes (west to east) during Cenozoic times (Parada et al., 2007). The magmatism (between 195 and 155 Ma) occurred in an extensional intra-arc basin due to sinistral movement in a high-stress regime with oblique convergence (Parada et al., 2007).

Finally, the continuous north to south latest early Carboniferous–Triassic magmatic belt was displaced from east to west by Mesozoic extension and basin development (Parada et al., 2007), while the corresponding South American continent was essentially static in a mantle reference framework (Brown, 1991). The displacement of the magmatic belt can be seen at ca. 31°–32°S (Fig. 1.1), corresponding to the Coastal Batholith and the Frontal Andes batholiths, as well as by the occurrence of late Paleozoic–Triassic plutonic

rocks in the Coastal Range and Frontal Andes at 26°S (Brown, 1991) (Fig. 1.1).

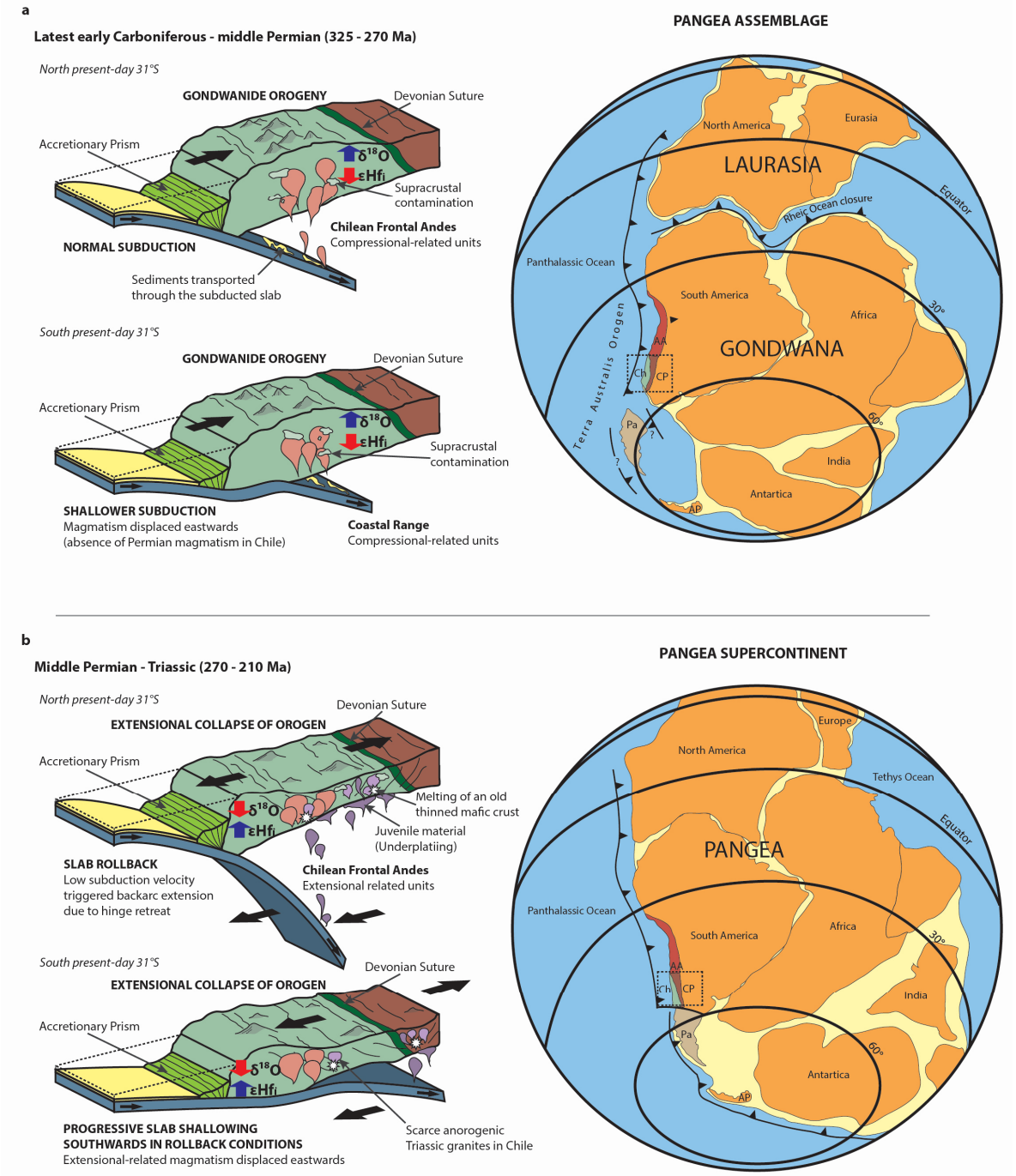

Fig. 1.4 Tectonic model. a. Latest early Carboniferous to earliest middle Permian: low values of εHf_i (ca. +1 to -4) with high $\delta^{18}O$ (ca. >6.5 ‰) indicate an elevated supracrustal component and the addition of less radiogenic continental-like material; magmas formed in a subduction-related continental arc during the Gondwanide Orogeny. b. Middle Permian to Triassic: a wider range of εHf_i values (ca. +3 to -3) with relatively low, mantle-like $\delta^{18}O$ (ca. 4.0–6.5‰) indicate magmas inheriting lower $\delta^{18}O$ values from the melting of an old thinned mafic crust. The higher positive values of εHf_i can be related to the influence of new juvenile material in the source of some magma; magmas formed in a slab rollback extensional setting. AA, Arequipa–Antofalla; CP, Cuyania–Precordillera; Ch, Chilenia; Pa, Patagonia; AP, the Antartic Peninsula. Global reconstruction based on previous work (Keppie and Ramos, 1999; Torsvik and Cocks, 2013).

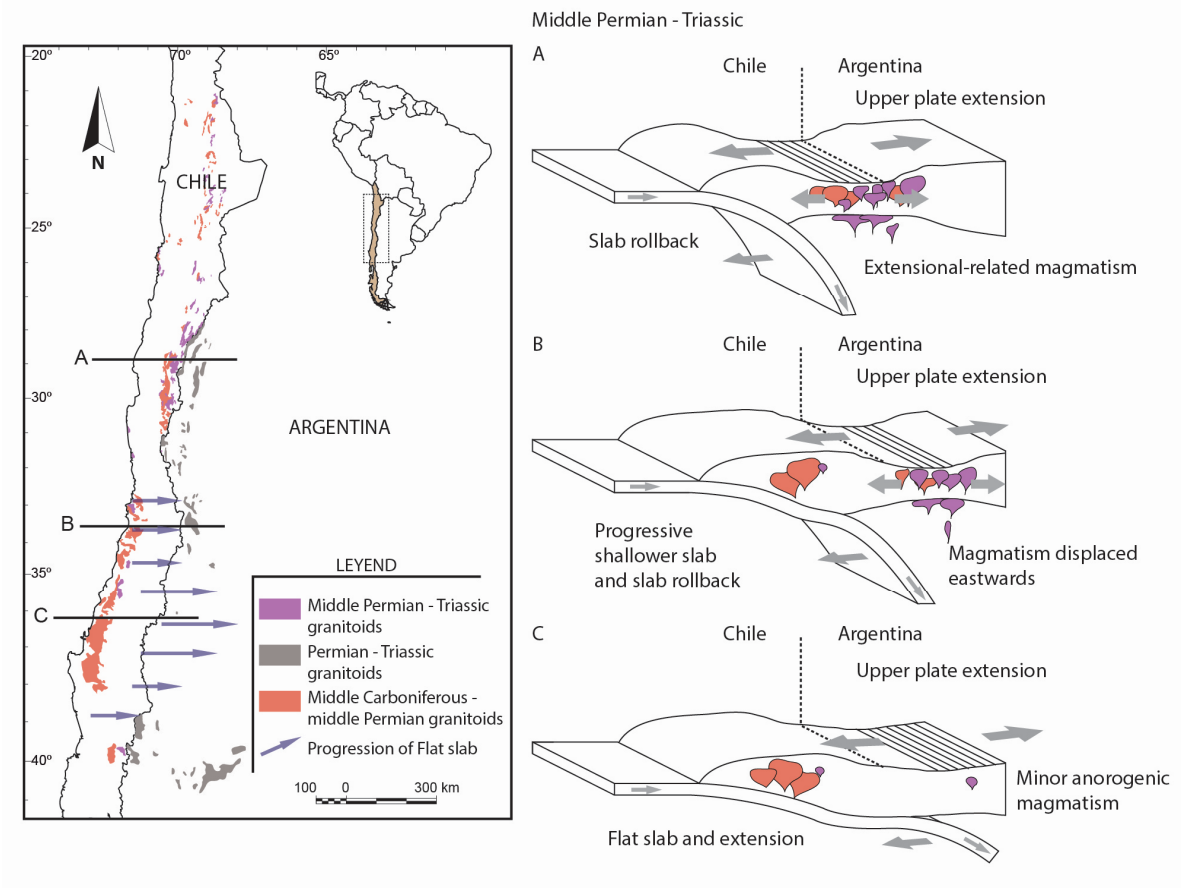

Fig. 1.5 Permian – Triassic flat slab evolution. The displacement of the Permian–Triassic magmatism eastwards south of 31°S can be explained by progressive slab shallowing and final flat-slab segmentation. It became gradually shallower from 31°S to 36°S, completely flat between 36°S and 39°S and again shallower from 39°S to 40°S. Section A shows extension-related magmatism without slab shallowing. Section B, progressively shallower slab (southward) shifted magmatism eastward (to Argentina). Section C shows the complete flat slab segment and low magmatic activity. Post-orogenic granitoids in the flat slab section can be attributed to crustal melting due to orogenic collapse (decompression) during the extensional period (middle Permian–Triassic). In sections: orange units represent latest early Carboniferous–middle Permian subduction-related magmatism; purple units, slab rollback middle Permian–Triassic extensional-related magmatism. Permian–Triassic units in Argentina (SEGEMAR, 2012; Gregori and Benedini, 2013) (gray on map) correspond to both subduction- and extension-related magmatism, in agreement with the timing of the tectonic evolution proposed here.

1.4 Conclusions

We propose that tectonic conditions from the latest early Carboniferous to late Triassic and the continuity of magmatism, strongly supported by the geological records, are the results of the subduction-related convergent evolution of the paleo-Pacific border of Pangea since the Terra Australis Orogen until its break-up (i.e. 200 Ma (Deckart et al., 1998), among others). Furthermore, the progressive evolution from an orogenic compressional setting with expansion of magmatism to later slab shallowing (with flat slab in the southern region), extension, orogenic collapse and slab steepening, allows us to re-define the Andean orogenic cycle (at least between latitudes 20°S and

40°S), as a continuous subduction-related process since the latest early Carboniferous to the present day. Consequently, its roots are linked to the Terra Australis Orogen. The sequence of events is in agreement with the idealized tectonic evolution of an Andean orogenic cycle (Ramos, 2009) where the angle of subduction is the key factor controlling magma-mixing processes (Pankhurst et al., 1988). In addition to that, the expected westward retreat of the arc at the beginning of the Jurassic due to the end of slab rollback also fits the idealized model. There is no reason to consider cessation of subduction during the late Permian/Triassic and its renovation in the early Jurassic (Mpodozis and Kay, 1992; Franzese and Spalletti, 2001), and therefore the existence of the hypothetic 'terrane X' (Mpodozis and Kay, 1992). The Andean orogenic cycle due to the subduction of the Pacific/paleo-Pacific oceanic plate underneath South America/paleo-South America has been a continuous process since the late Paleozoic. The major differences observed since that period are the prevailing global geodynamic conditions. While Pangea was being assembled, those conditions were different enough (compared to the traditionally defined Andean orogenic cycle; e.g. Charrier et al. (2014)) to produce noticeable changes in the magmatism (i.e. extreme extensional conditions due to low subducting plate velocities and slab rollback). Analogue models (Schellart, 2008) demonstrate that low subduction velocities trigger backarc extension due to hinge retreat. Also, Jurassic intrusions are located in a belt from 20°S to 36°S, ending at the beginning of the flat-slab segment (also present in the eastern margin of the Southern Patagonian batholith south of 48°S; Hervé et al. (2007)). The Paleozoic accretionary history of the south-western margin of Gondwana (up to 40°S) was completely finished by latest early Carboniferous and was followed by the Andean subduction, a continuous process since Paleozoic times and not from the early Jurassic as previously thought (e.g. Mpodozis and Kay, 1992; Charrier et al., 2014). Distinctive magmatism during the mid Permian–Triassic was due to Pangea assembly, a unique and global event that conditioned geodynamic processes worldwide. Moreover, the presence of a rift-related belt of magmatism in Peru and Bolivia from the late Permian–middle Jurassic (Sempere et al., 2002) allows us to speculate the idea of the continuity of the Andean orogenic cycle northward to 8°S -20°S. Nevertheless, more evidence is required to confirm this hypothesis. The new tectonic model proposed here, unravels the paradigm of the latest early Carboniferous–Triassic magmatism in Chile and provides an argument for an uninterrupted convergent plate margin setting for the vast late Paleozoic–early Mesozoic magmatism in Chile and Argentina. This model also shows how global geodynamics (i.e. assemblage and break-up of supercontinents) are a key factor in the occurrence of certain type of magmatism (rifting-related A-type granites; e.g., Mpodozis and Kay (1992)) which otherwise can be considered 'odd' if analyzed only from a local point of view.

Acknowledgements

We thank Juan Vargas and Roberto Valles (Universidad de Chile) for the zircon separation; Dr. Mark Fanning (ANU) for the Lu–Hf, O and U–Pb analytical work at the ANU; and Drs. Jacobus Le Roux and Gregory De Pascale (Universidad de Chile) for the English language corrections. The authors would like to acknowledge the constructive comments and discussions by Robert Pankhurst during revision of the manuscript. This research was funded by the Servicio Nacional de Geología y Minería (SERNAGEOMIN) project Plan Nacional de Geología (Geological Map 'Iglesia Colorada – Cerro El Potro') and the Masters fellowship of the Comisión Nacional de Investigación Científica y Tecnológica – CONICYT (grant no. 221320626). Additional funding was provided by the Departamento de Postgrado y Postítulo, Universidad de Chile. This work is part of the M.Sc. thesis of the principal author.

Supplementary data

Full SHRIMP U-Pb geochronological and O-Hf isotopic data are given in Appendix A. Supplementary data to this article can be found online at http://dx.doi.org/10.1016/j.gr.2016.06.008.

References

Alasino, P.H., Dahlquist, J.A., Pankhurst, R.J., Galindo, C., Casquet, C., Rapela, C.W., Larrovere, M.A., Fanning, C.M., 2012. Early Carboniferous sub- to mid-alkaline magmatism in the Eastern Sierras Pampeanas, NW Argentina: A record of crustal growth by the incorporation of mantle-derived material in an extensional setting. Gondwana Res. 22, 992–1008. doi:10.1016/j.gr.2011.12.011

Álvarez, J., Mpodozis, C., Arriagada, C., Astini, R., Morata, D., Salazar, E., Valencia, V.A., Vervoort, J.D., 2011. Detrital zircons from late Paleozoic accretionary complexes in north-central Chile (28°-32°S): Possible fingerprints of the Chilenia terrane. J. South Am. Earth Sci. 32, 460–476. doi:10.1016/j.jsames.2011.06.002

Bahlburg, H., Hervé, F., 1997. Geodynamic evolution and tectonostratigraphic terranes of northwestern Geodynamic evolution and tectonostratigraphic terranes of northwestern Argentina and northern Chile. Geol. Soc. Am. Bull. 109, 869–884. doi:10.1130/0016-7606(1997)109<0869

Bindeman, I.N., Valley, J.W., 2001. Low-delta O-18 rhyolites from Yellowstone: Magmatic evolution based on analyses of zircons and individual phenocrysts. J. Petrol. 42, 1491–1517. doi:10.1093/petrology/42.8.1491

Bolhar, R., Weaver, S.D., Whitehouse, M.J., Palin, J.M., Woodhead, J.D., Cole, J.W., 2008. Sources and evolution of arc magmas inferred from coupled O and Hf isotope systematics of plutonic zircons from the Cretaceous Separation Point Suite (New Zealand). Earth Planet. Sci. Lett. 268, 312–

324. doi:10.1016/j.epsl.2008.01.022
Brown, M., 1991. Comparative geochemical interpretation of Permian-Triassic plutonic complexes of the Coastal Range and Altiplano (25°30’ to 26°30'S), northern Chile. Geol. Soc. Am. 265.
Cawood, P.A., 2005. Terra Australis Orogen: Rodinia breakup and development of the Pacific and Iapetus margins of Gondwana during the Neoproterozoic and Paleozoic. Earth-Science Rev. 69, 249–279. doi:10.1016/j.earscirev.2004.09.001
Charrier, R., Ramos, V.A., Tapia, F., Sagripanti, L., 2014. Tectono-stratigraphic evolution of the Andean Orogen between 31° and 37° S (Chile and Western Argentina). Geol. Soc. London, Spec. Publ. 399, 13–61. doi:10.1144/SP399.20
Clemens, J.D., Stevens, G., Farina, F., 2011. The enigmatic sources of I-type granites: The peritectic connexion. Lithos 126, 174–181. doi:10.1016/j.lithos.2011.07.004
Dahlquist, J.A., Pankhurst, R.J., Gaschnig, R.M., Rapela, C.W., Casquet, C., Alasino, P.H., Galindo, C., Baldo, E.G., 2013. Hf and Nd isotopes in Early Ordovician to Early Carboniferous granites as monitors of crustal growth in the Proto-Andean margin of Gondwana. Gondwana Res. 23, 1617–1630. doi:10.1016/j.gr.2012.08.013
Dahlquist, J.A., Pankhurst, R.J., Rapela, C.W., Basei, M.A.S., Alasino, P.H., Saavedra, J., Baldo, E.G., Murra, J.A., da Costa Campos Neto, M., 2016. The Capilla del Monte pluton, Sierras de Córdoba, Argentina: the easternmost Early Carboniferous magmatism in the pre-Andean SW Gondwana margin. Int. J. Earth Sci. doi:10.1007/s00531-015-1249-0
Deckart, K., Féraud, G., Marques, L.S., Bertrand, H., 1998. New time constraints on dyke swarms related to the Paraná-Etendeka magmatic province, and subsequent South Atlantic opening, southeastern Brazil. J. Volcanol. Geotherm. Res. 80, 67–83. doi:10.1016/S0377-0273(97)00038-3
Deckart, K., Hervé, F., Fanning, M., Ramírez, V., Calderón, M., Godoy, 2014. U-Pb Geochronology and Hf-O Isotopes of zircons from the Pennsylvanian Coastal Batholith, South-Central Chile. Andean Geol. 41, 49–82. doi:10.5027/andgeoV41n1-a03
Eggins, S.M., Grün, R., McCulloch, M.T., Pike, A.W.G., Chappel, J., Kinsley, L., Mortimer, G., Shelley, M., Murray-Wallace, C. V., Spötl, C., Taylor, L., 2005. In situ U-series dating by laser-ablation multi-collector ICPMS; new prospects for Quaternary geochronology. Quat. Sci. Rev. 24, 2523–2538.
Franzese, J.R., Spalletti, L. a., 2001. Late triassic- Early jurassic continental extension in SouthWestern Gondwana: Tectonic segmentation and pre-break-up rifting. J. South Am. Earth Sci. 14, 257–270. doi:10.1016/S0895-9811(01)00029-3
Gerya, T. V., Meilick, F.I., 2011. Geodynamic regimes of subduction under an active margin: Effects of rheological weakening by fluids and melts. J. Metamorph. Geol. 29, 7–31. doi:10.1111/j.1525-1314.2010.00904.x
Gregori, D., Benedini, L., 2013. The Cordon del Portillo Permian magmatism,

Mendoza, Argentina, plutonic and volcanic sequences at the western margin of Gondwana. J. South Am. Earth Sci. 42, 61–73. doi:10.1016/j.jsames.2012.07.010

Grocott, J., Taylor, G.K., 2002. Magmatic arc fault systems, deformation partitioning and emplacement of granitic complexes in the Coastal Cordillera, north Chilean Andes (25°30'S to 27°00'S). J. Geol. Soc. London. 159, 425–442. doi:10.1144/0016-764901-124

Hervé, F., Fanning, C.M., Calderón, M., Mpodozis, C., 2014. Early Permian to Late Triassic batholiths of the Chilean Frontal Cordillera (28°-31°S): SHRIMP U-Pb zircon ages and Lu-Hf and O isotope systematics. Lithos 184-187, 436–446. doi:10.1016/j.lithos.2013.10.018

Hervé, F., Pankhurst, R.J., Fanning, C.M., Calderón, M., Yaxley, G.M., 2007. The South Patagonian batholith: 150 my of granite magmatism on a plate margin. Lithos 97, 373–394. doi:10.1016/j.lithos.2007.01.007

Ickert, R.B., Hiess, J., Williams, I.S., Holden, P., Ireland, T.R., Lanc, P., Schram, N., Foster, J.J., Clement, S.W., 2008. Determining high precision, in situ, oxygen isotope ratios with a SHRIMP II: analyses of MPI-DING silicate-glass reference materials and zircon from contrasting granites. Chem. Geol. 257, 114–128.

Kay, S.M., Ramos, V.A., Mpodozis, C., Sruoga, P., 1989. Late Paleozoic to Jurassic silicic magmatism at the Gondwana margin : Analogy to the Middle Proterozoic in North America? Geol. Soc. Am. 17, 324–328. doi:10.1130/0091-7613(1989)017<0324

Kemp, A.I.S., Hawkesworth, C.J., Foster, G.L., Paterson, B.A., Woodhead, J.D., Hergt, J.M., Gray, C.M., Whitehouse, M.J., 2007. Magmatic and crustal differentiation history of granitic rocks from Hf-O isotopes in zircon. Science (80-.). 315, 980–983. doi:10.1126/science.1136154

Keppie, J.D., Ramos, V.A., 1999. Odyssey of terranes in the Iapetus and Rheic oceans during the Paleozoic. Geol. Soc. Am. 336, 267–276.

Kleiman, L.E., Japas, M.S., 2009. The Choiyoi volcanic province at 34°S-36°S (San Rafael, Mendoza, Argentina): Implications for the Late Palaeozoic evolution of the southwestern margin of Gondwana. Tectonophysics 473, 283–299. doi:10.1016/j.tecto.2009.02.046

Li, Z.X., Powell, C.M., 2001. An outline of the palaeogeographic evolution of the Australasian region since the beginning of the Neoproterozoic. Earth Sci. Rev. 53, 237–277. doi:10.1016/S0012-8252(00)00021-0

Llambias, E.J., Sato, A.M., 1990. El Batolito de Colangüil (29-31°S) Cordillera Frontal de Argentina: estructura y marco tectónico. Rev. Geol. Chile 17, 89–108.

Maksaev, V., Munizaga, F., Tassinari, C., 2014. Timing of the magmatism of the paleo-Pacific border of Gondwana: U-Pb geochronology of Late Paleozoic to Early Mesozoic igneous rocks of the north Chilean Andes between 20° and 31°S. Andean Geol. 41, 447–506. doi:10.5027/andgeoV41n3-a01

Monani, S., Valley, J.W., 2001. Oxygen isotope ratios of zircon: Magma genesis of low δ18O granites from the British Tertiary igneous province, western

Scotland. Earth Planet. Sci. Lett. 184, 377–392. doi:10.1016/S0012-821X(00)00328-9
Mpodozis, C., Kay, S.M., 1992. Late Paleozoic to Triassic evolution of the Gondwana margin: evidence from Chilean Frontal cordilleran batholiths (28°S to 31°S). Geol. Soc. Am. Bull. 104, 999–1014. doi:10.1130/0016-7606(1992)104<0999:LPTTEO>2.3.CO;2
Mpodozis, C., Ramos, V.A., 2008. Tectónica jurásica en Argentina y Chile: extensión, subducción oblicua, rifting, deriva y colisiones? Rev. la Asoc. Geológica Argentina 63, 481–497.
Nebel, O., Vroon, P.Z., van Westrenen, W., Iizuka, T., Davies, G.R., 2011. The effect of sediment recycling in subduction zones on the Hf isotope character of new arc crust, Banda arc, Indonesia. Earth Planet. Sci. Lett. 303, 240–250. doi:10.1016/j.epsl.2010.12.053
Pankhurst, R., Hole, M., Brook, M., 1988. Isotope evidence for the origin of Andean granites. Trans. R. Soc. Edinb. Earth Sci. 79, 123–133.
Parada, M.A., López-Escobar, L., Oliveros, V., Fuentes, F., Morata, D., Calderón, M., Aguirre, L., Féraud, G., Espinoza, F., Moreno, H., Figueroa, O., Muñoz Ravo, J., Troncoso Vásquez, R., Stern, C.R., 2007. Andean magmatism, in: Moreno, T., Gibson, W. (Eds.), The Geology of Chile. The Geological Society, London, pp. 115–146.
Pietranik, A., Słodczyk, E., Hawkesworth, C.J., Breitkreuz, C., Storey, C.D., Whitehouse, M., Milke, R., 2013. Heterogeneous zircon cargo in voluminous Late Paleozoic rhyolites: Hf, O isotope and Zr/Hf records of plutonic to volcanic magma evolution. J. Petrol. 54, 1483–1501. doi:10.1093/petrology/egt019
Ramos, V.A., 1988. The tectonics of the Central Andes; 30° to 33°S latitude. Geol. Soc. Am. 31–54. doi:10.1130/SPE218-p31
Ramos, V.A., 2008. Patagonia: A Paleozoic continent adrift? J. South Am. Earth Sci. 26, 235–251. doi:10.1016/j.jsames.2008.06.002
Ramos, V.A., 2009. Anatomy and global context of the Andes: Main geologic features and the Andean orogenic cycle. Geol. Soc. Am. Mem. 204, 31–65. doi:10.1130/2009.1204(02)
Ramos, V.A., Alemán, A., 2000. Tectonic evolution of the Andes, in: Cordani, U.G., Milani, E.J., Thomaz Filha, A., Campos, D.A. (Eds.), Tectonic Evolution of South America. 31st International Geological Congress. Rio de Janeiro, pp. 635–685.
Ramos, V.A., Jordan, T.E., Allmendinger, R.W., Mpodozis, C., Kay, S.M., Cortés, J.M., Palma, M., 1986. Paleozoic terranes of the Central Argentine-Chilean Andes. Tectonics 5, 855–880. doi:10.1029/TC005i006p00855
Schellart, W.P., 2005. Influence of the subducting plate velocity on the geometry of the slab and migration of the subduction hinge. Earth Planet. Sci. Lett. 231, 197–219. doi:10.1016/j.epsl.2004.12.019
Schellart, W.P., 2008. Overriding plate shortening and extension above subduction zones: A parametric study to explain formation of the Andes Mountains. Bull. Geol. Soc. Am. 120, 1441–1454. doi:10.1130/B26360.1
Schellart, W.P., Freeman, J., Stegman, D.R., Moresi, L., May, D., 2007.

Evolution and diversity of subduction zones controlled by slab width. Nature 446, 308–311. doi:10.1038/nature05615
SEGEMAR, 2012. Sistema de Información Geográfica del Servicio Geológico Minero Argentino [WWW Document]. URL sig.segemar.gov.ar.
Sempere, T., Carlier, G., Soler, P., Fornari, M., Carlotto, V., Jacay, J., Arispe, O., Néraudeau, D., Cárdenas, J., Rosas, S., Jiménez, N., 2002. Late Permian-Middle Jurassic lithospheric thinning in Peru and Bolivia, and its bearing on Andean-age tectonics. Tectonophysics 345, 153–181. doi:10.1016/S0040-1951(01)00211-6
Taylor, H., Sheppard, S., 1986. Igneous rocks; I, Processes of isotopic fractionation and isotopic systematics. Rev. Mineral. Geochemistry 16, 227–271.
Torsvik, T.H., Cocks, L.R.M., 2013. Gondwana from top to base in space and time. Gondwana Res. 24, 999–1030. doi:10.1016/j.gr.2013.06.012
Valley, J.W., Kinny, P.D., Schulze, D.J., Spicuzza, M.J., 1998. Zircon megacrysts from kimberlite: oxygen isotope variability among mantle melts. Contrib. to Mineral. Petrol. 133, 1–11. doi:10.1007/s004100050432
Vásquez, P., Franz, G., 2008. The Triassic Cobquecura Pluton (Central Chile): An example of a fayalite-bearing A-type intrusive massif at a continental margin. Tectonophysics 459, 66–84. doi:10.1016/j.tecto.2007.11.067
Vaughan, A.P.M., Pankhurst, R.J., 2008. Tectonic overview of the West Gondwana margin. Gondwana Res. 13, 150–162. doi:10.1016/j.gr.2007.07.004
Veevers, J.J., 2005. Edge tectonics (trench rollback, terrane export) of Gondwanaland-Pangea synchronized by supercontinental heat. Gondwana Res. 8, 449–456. doi:10.1016/S1342-937X(05)71147-3
Vilas, J.F., Valencio, D.A., 1978. Paleomagnetism of South American and African rocks and the age of the South Atlantic. Rev. Bras. Geociências 8, 3–10.
Villaros, A., Buick, I.S., Stevens, G., 2012. Isotopic variations in S-type granites: An inheritance from a heterogeneous source? Contrib. to Mineral. Petrol. 163, 243–257. doi:10.1007/s00410-011-0673-9
Williams, I.S., 1998. U–Th–Pb geochronology by ion microprobe, in: McKibben, M.A., Shanks, W.C., Ridley, W.I. (Eds.), Reviews in Economic Geology. pp. 1–35.
Willner, A.P., Massone, H.-J., Ring, U., Sudo, M., Thomson, S.N., 2012. P–T evolution and timing of a late Palaeozoic fore-arc system and its heterogeneous Mesozoic overprint in north-central Chile (latitudes 31–32°S). Geol. Mag. 149, 177–207. doi:10.1017/S0016756811000641

In Chapter 1, a new tectonic model was hypothesized for the late Paleozoic–Triassic Chilean–Argentinian border from 28° to 40°S by using new isotopic (O-Hf) and geochronological data (SHRIMP II) and its comparison with previously published data. The results show an overall continuous shift from crustal to mantle-like compositions with time. These compositional variations were interpreted as the result from the interplay between subduction angle, slab rollback, subduction velocity and convergence rate within a broadly continuous subduction regime, in opposition with previous explanations. The following Chapter 2 takes this model and completes it by adding detailed petrogenetic interpretations of the studied units using mayor and trace geochemical analyses, plus more isotopic (Nd-Sr) and geochronological evidences (LA-ICPMS). The results further support the proposed model in Chapter 1 and re-establishes the 270 Ma limit for the crustal towards mantle-like shift seen in the magmatism through the geochemical comparison of coeval units along the Chilean–Argentinian border. The final tectonic model provides a more realistic scenario than previous ideas (e.g., interrupted subduction) thus assisting in the resolution of the paradigm of the late Paleozoic–Triassic magmatism.

CHAPTER 2

Middle Permian–Triassic plutonism in the Chilean Frontal Andes (28°–28°30'S): A record of the evolution of the southwestern margin of Pangea

A. del Rey[a, *], K. Deckart[a, b], C. Arriagada[a], F. Martínez[a]

[a]Departamento de Geología, Universidad de Chile, Santiago, Chile
[b]Advanced Mining Technology Centre (AMTC), Universidad de Chile, Santiago, Chile.

*Corresponding author (alvherna@ing.uchile.cl)

For submission to Earth–Science Reviews

Abstract

The Chilean Frontal Andes batholiths (28°–31°S) represent part of the extensive late Paleozoic–Triassic magmatism along the southwestern margin of South America. Traditionally and despite its importance, a fair consensus regarding the tectonic model controlling the magmatism and its link to the Andean subduction has not been reached. Here we present new LA-ICPMS U–Pb in zircon ages, geochemical and isotope analysis, which indicate that latest early Carboniferous–middle Permian dioritic to granodioritic plutonism occurred in a subduction-related orogenic cycle emplaced into normal to thickened crust. Middle Permian–Triassic granitic magmatism originated in a subduction-related slab rollback extensional setting with increasing thinning towards Triassic times. During this period, longitudinal geochemical variations show predominance of coeval I-type volcanic arc magmatism to the west with increasing transitional to A-type igneous activity with within plate affinities eastwards, in concordance with progressive extension in the backarc region. Multielement variation patterns show clear subduction characteristics and εNd_i–$^{87}Sr/^{86}Sr_i$ values between +2.1 and -12.2, and 0.703 and 0.708 respectively, a lower continental crust source. Together, isotopic and geochemical data allow inferring anatexis of lower crust as the main mechanism producing magmas, the one caused by decompression and subsequent accumulation of underplating basalts after orogenic collapse. A comparison with other igneous units along

the Chilean–Argentinian border allows extending this model from at least 21° to 40°S. Exceptionally low subducting velocities during the transitory state of Pangea (middle Permian–Triassic) triggered intense extension in a subduction setting. Subduction of the paleo-Pacific oceanic plate beneath paleo-South America has been a continuous process since early Carboniferous onwards. There is no period of time without subduction before the onset of the Andean as previous models suggested.

Keywords: Chilean Frontal Andes, Permian–Triassic magmatism, Element geochemistry and Sr–Nd isotopes, LA-ICPMS U–Pb in zircon, Andean subduction, Slab rollback

2.1 Introduction

Despite its importance, late Paleozoic and early Mesozoic magmatism along the southwestern margin of South America is still not completely understood. This protracted igneous activity extends from the Cordillera de Marañón in central Peru (Chew et al., 2007; Miskovic and Schaltegger, 2009) to units in Bolivia (Sempere et al., 2002), the Chilean Precordillera (20°–24°S, Munizaga et al. (2008)), the Cordillera de Domeyko (24°–27°S; Mpodozis et al. (1993)), the Chilean Frontal Andes (28°–31°S, also known as Chilean Frontal Cordillera; Mpodozis and Cornejo, 1988; Mpodozis and Kay, 1992; Pankhurst et al., 1996; among others) and the Coastal Cordillera (33°–38°S, Deckart et al., 2014; Parada, 1990; Vásquez et al., 2011) in Chile. In Argentina, it extends to the Argentinian Frontal Cordillera (33°S, Gregori and Benedini, 2013), the San Rafael Block (34°–36°S; (Kleiman and Japas, 2009; Rocha-Campos et al., 2011), and La Pampa province (38°S, Kay et al., 1989). Several tectonic models have been proposed for different localities showing that this geological period has been the subject of much debate. In particular, a well-known model for the Chilean Frontal Andes consider rocks formed during Carboniferous to early Permian as magmatism related to a first stage of subduction followed by a second stage (late Permian–Triassic) of post-collisional magmatism after to the accretion of a hypothetical terrane during middle Permian ('X terrane', Mpodozis and Kay, 1992). The later associated with cessation of subduction and subsequent orogenic collapse. Nevertheless, considering the extension of magmatism and the unproved existence of the terrane, new hypotheses seem necessary. On the other hand, a more recent regional-scale tectonic model has been proposed (Del Rey et al., 2016), which indicates that plutonism occurred first as subduction-related magmatism with continental crust influence (latest early Carboniferous–middle Permian) associated with the Gondwanide Orogeny, and it was directly followed by intense subduction-related extensional conditions due to slab rollback (middle Permian–Triassic) that triggered magmatism with mantle-like isotopic signatures.

Here we present new Rb–Sr, Sm–Nd and Re–Os isotopic systematics; LA-ICPMS U–Pb in zircon ages; and major and trace element whole-rock geochemical analysis for rock samples from a part of the Chilean Frontal Andes (28°-28°30'S). A comparison with other late Paleozoic–Triassic plutonic rocks from Chile and Argentina is also made. The analysed data allow us to evaluate the origin of the vast magmatic event thus providing more detail to its geodynamic evolution and supporting the model proposed by Del Rey et al. (2016).

2.2 Geological setting

The Chilean Frontal Andes (28°–31°S) possesses a series of batholiths that can be divided into several units. From north to south, these batholiths are named Montosa–El Potro, Chollay and Elqui–Limarí (Nasi et al., 1985; Mpodozis and Kay, 1992). According to their geochronological and geochemical characteristics, units have been divided between Elqui and Ingaguás complexes (Mpodozis and Cornejo, 1988; Mpodozis and Kay, 1992; Nasi et al., 1990, 1985; Parada, 1988, 1990; among others). The Elqui Complex (Carboniferous–early Permian) is constituted by the Elqui and Montosa batholiths, which are composed by several granitoid units named Guanta, Montosa, Cochiguás and El Volcán. Compositionally, they correspond to diorites, tonalities, granodiorites and granites; calc-alkaline and I- to S-types. Guanta unit corresponds to the most basic granitoid (tonalities and granodiorites) whilst Montosa is slightly more differentiated. Both units are metaluminous, I-type and present relatively flat HREE patterns. On the other hand, Cochiguás unit correspond to granodiorites and monzogranites sometimes with primary white mica, peraluminous, I- to S- types and with steep HREE patterns. El Volcán unit consist in the most differentiated plutons of the Elqui Complex: granodiorites and granites with primary white mica, S-type and relatively flat HREE patterns (Mpodozis and Kay, 1992). The Ingaguás Complex (Permian–Trassic) – which is included in the Choiyoi province (Kay et al., 1989) – is constituted by the Limarí, El Potro and Chollay batholiths, and they include Los Carricitos, Chollay, El León and El Colorado units, along with gabbroic stocks (La Laguna Gabbros) (Nasi et al., 1985). Overall, these units correspond to hyper siliceous granitoids, calc-alkaline to transitional and S- to A-types (Mpodozis and Kay, 1992). Los Carricitos unit consists in peraluminous granodiorites, S-type and with relatively steep LREE and HREE patterns, whilst Chollay, El León and El Colorado, are highly differentiated calc-alkaline to transitional A-type granites. Particularly, Chollay unit is represented mainly by monzogranites, El León by granites, and El Colorado by granites and porphyritic rhyolites. These three units have relatively flat HREE patterns and large negative Eu anomalies (Mpodozis and Kay, 1992). In Argentina the equivalent to this complex corresponds to the Colangüil Batholith, which is

composed by leucocratic granodiorites and granites (Llambias and Sato, 1990).

Traditionally, the Elqui Complex has been interpreted as the product of subduction-related magmatism caused by the subduction of the paleo-Pacific oceanic plate beneath Gondwana after Chilenia accretion in a normal to thickened crust (Mpodozis and Kay, 1990, 1992). Consequently, the Ingaguás Complex has been considered as generated during the cessation of the subduction after the San Rafael orogenic event, which triggered extensional conditions during most of the Permian–Triassic time (Llambias and Sato, 1990; Mpodozis and Kay, 1990, 1992).

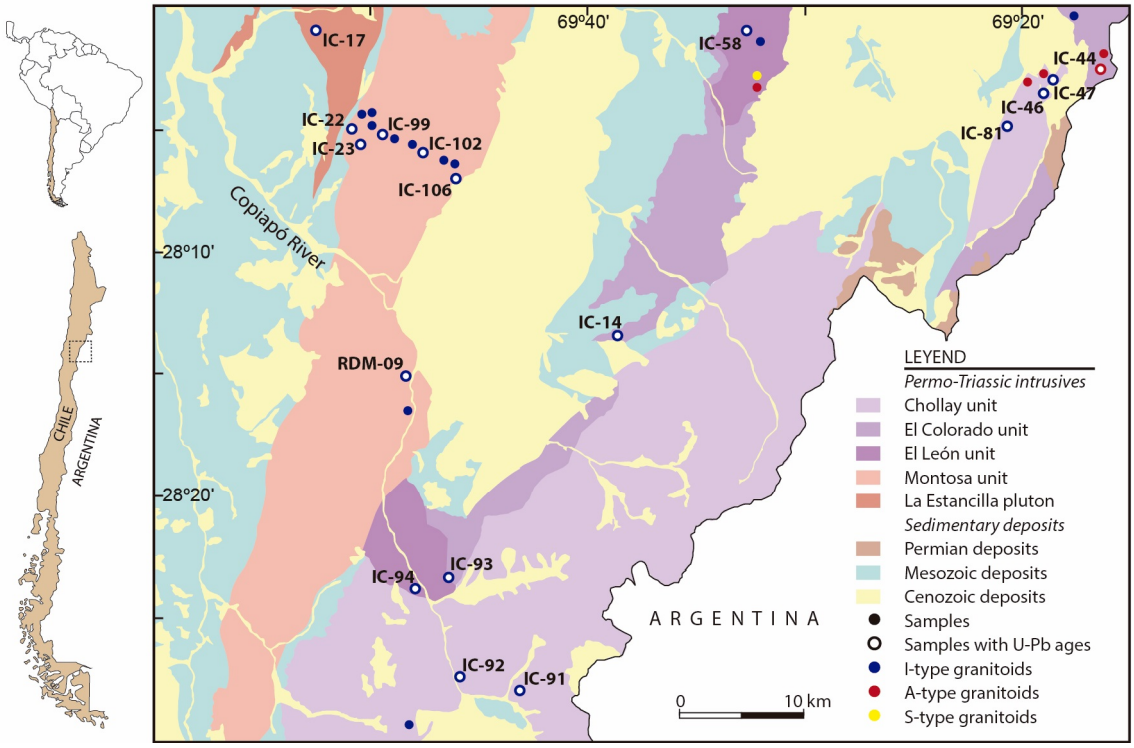

Fig. 2.1 Simplified geological map of the Chilean Frontal Andes (28°-28°30'S). Late Paleozoic–Triassic intrusives, the location of analysed samples and Paleozoic, Mesozoic and Cenozoic sedimentary deposits are shown (after Martínez et al., 2015). The Montosa–El Potro Batholith is constituted by La Estancilla pluton and Montosa, El León, El Colorado and Chollay units. All samples have geochemical analyses. Only dated samples have their identification shown in the map. Only one sample can be defined as S-type, the rest are I-type with slight S-type characteristics according to Chappell and White (2001). Samples IC-17, -22, -58, -91 and -93 were SHRIMP U–Pb dated (Del Rey et al., 2016), the rest were dated using LA-ICPMS.

2.3 Sampling and analytical methods

The rocks studied here correspond to 33 samples from the Montosa–El Potro Batholith, including La Estancilla pluton, Montosa, Chollay, El León and El Colorado units (Fig. 2.1). Thin section petrographic descriptions were made for each sample. Whole-rock compositions were analysed by Fusion-ICP (mayor elements plus Sc, Be, V, Sr, Zr, Ba) and Fusion-ICPMS (trace

elements) at Actlabs using several international and internal standards to assure data quality (Code 4LITHORES (11+) Major Elements Fusion ICP(WRA)/Trace Elements Fusion ICPMS(WRA4B2). The analytical precision was <9% 2σ and accuracy mostly better than 3%.

Zircon (LA-ICPMS U–Pb) and magnetite (ID-TIMS Re–Os) grains were separated from 2 kg whole-rock samples (11 and 5 samples for zircons and magnetites, respectively) using standard techniques at the Sample Preparation Laboratory (University of Chile), as grinding, Gemini table, heavy liquids and Frantz separation, followed by a final hand picking under binocular microscope.

LA-ICPMS U–Pb in zircon geochronology has been undertaken in 11 representative samples of the different rock units in addition to the 5 previously dated (Del Rey et al., 2016). Analyses were carried out using a Thermo Xseries QICPMS coupled to a Resonetics Resolution M050 Excimer laser following the analytical protocol after Solari et al. (2010). The laser ablation spots were 23 μm. U–Pb reference grain and uncertainties were obtained as in Paton et al. (2010). $^{207}Pb/^{206}Pb$ ratios, ages and errors were calculated according to Petrus and Kamber (2012). Weighted mean $^{206}Pb/^{238}U$ ages have been calculated and the uncertainties are reported at 95% confidence limits. Analytical work was performed at the Laboratory of Isotopic Studies (LEI) of the Geoscience Centre of the National Autonomous University of Mexico (UNAM).

Re–Os analyses were performed using Negative Thermal Ion Mass Spectrometer (NTIMS-VG54 MS) following the standard procedure described in Creaser et al. (1991). Magnetite grains were loaded in Carius tubes (Shirey and Walker, 1995). Re and Os spikes and 16 ml of Aqua Regia were added and kept under cold conditions to avoid evaporation and early chemical reaction, then sealed. Afterwards, the tubes were place into an oven at 240°C overnight. Os was separated from the solution in a two-stage distillation process (Nägler and Frei, 1997), then purified and loaded with $Ba(OH)_2$ on a Pt filament. Re was separated after Os by using the remaining acid solution. After drying, the solution was re-dissolved in 0.1 HNO_3. Re was extracted and purified by using AG1-X8 (100-200 mesh) resins. Subsequently, Re was loaded with $Ba(SO)_4$ on Pt filaments. The analytical work was performed at the Arizona Geochronology Centre of the University of Arizona.

Sr and Nd isotopic analyses were performed on 17 dated samples (11 in this work and 6 previously dated) using Thermo Neptune Plus Multicollector ICPMS following the previous protocols of Gómez-Tuena et al. (2013, 2011, 2003). Nd isotopic compositions of samples and standards were measured in ca. 200 ppb solutions, and Sr isotopes were determined using solutions diluted to ca. 300 ppb concentrations. Analyses of samples and standards consist of 70–100 static measurement cycles, with each cycle measured in ca. 4 s

integrations. Beam intensities of 5 V/ppm and 100 V/ppm were routinely achieved for ^{88}Sr and ^{142}Nd, respectively, using wet plasma and a 100 µL/mm free aspirating nebulizer. The interference-corrected $^{87}Sr/^{86}Sr$ ratios were exponentially normalized for mass bias to $^{86}Sr/^{88}Sr = 0.1194$ and corrected to a NBS-987 standard ratio of $^{87}Sr/^{86}Sr = 0.710230$. Nd isotopic ratios were measured statically using the entire collector array in order to monitor all relevant isotopic species and the potentially critical isobaric interference of Sm. The calculated $^{143}Nd/^{144}Nd$ ratios were exponentially normalized for mass bias to $^{146}Nd/^{144}Nd = 0.72190$, and then corrected to a JNdi standard value of $^{143}Nd/^{144}Nd = 0.512115$. Sr and Nd analytical work was performed at the Laboratory of Isotopic Studies (LEI) of the Geoscience Centre of the National Autonomous University of Mexico (UNAM).

2.4 Results

Isotopic and geochronological results, including prior age data –together with sample locations – are summarized in Table 2.1. Weighted mean age histograms are given for each dated sample (Fig. 2.2). Full geochronological, major and trace element data and petrographic descriptions are given in the Supplementary data.

2.4.1 U–Pb in zircon geochronology

The analysed samples represent crystallization ages from Guadalupian (late Permian) to Upper Triassic. New U–Pb dates ranging from 264.2 ± 1.6 to 244.4 ± 1.6 Ma for Montosa; from 247.7 ± 1.2 to 215.6 ± 1.4 Ma for Cholloy; and from 260.9 ± 1.5 to 249.9 ± 1.6 Ma for El Colorado were obtained. No new ages were analysed for El León and La Estancilla pluton units. Considering previous geochronological data (Table 2.1) and according to the 2016 IUGS International Chronostratigraphic Chart, La Estancilla pluton corresponds to Cisularian (early Permian); El Colorado to Guadalupian (middle Permian)–Lower Triassic; El León to Lopingian (late Permian)–Middle Triassic; Chollay to Lopingian (late Permian)–Upper Triassic; and Montosa to Guadalupian (middle Permian)–Middle Triassic. Overall, the Montosa–El Potro Batholith (Fig. 2.1) can be defined from Cisuralian (early Permian) to Upper Triassic. Weighted mean age and MSWD can be seen in Fig. 2.2.

2.4.2 Whole-rock geochemistry

Geochemical analyses for the dated samples are shown in Table 2.2. A geochemical classification summary for all samples is given in Supplementary data.

Table 2.1 Summarized geochemical classification, U–Pb in zircon ages and initial εNd_i, $^{87}Sr/^{86}Sri$ and γOs_i values from the Montosa–El Potro Batholith.

Sample	Geographical coordinates	Lithology[1]	S-I-A type	ASI	(Eu/Eu*)	$(La/Yb)_N$	$^{206}Pb/^{238}U$ Age (Ma)	εNd_i	$(^{87}Sr/^{86}Sr)_i$	γOs_i
La Estancilla pluton										
IC-17	28°00'13.82"S 69°53'05.22"W	Hbl-bt tonalite	I-type	0.93	0.89	7.6	286.0 ± 2.0[a]	+2.09	0.705279	-
Montosa										
IC-22	28°05'03.45"S 69°50'57.01"W	Hbl-bt tonalite	I-type	0.97	0.66	9.0	253.0 ± 2.0[a]	-2.13	0.703985	125-140
IC-23	28°05'03.08"S 69°50'48.21"W	Bt syenogranite	I-type, slightly S-type	1.03	0.83	28.0	264.2 ± 1.6	-1.36		1056-1290
IC-99	28°05'17.06"S 69°49'05.87"W	Bt-Hbl tonalite	I-type	1.00	1.21	16.5	253.3 ± 1.5	-0.51	0.704599	-
IC-102	28°05'49.90"S 69°47'40.70"W	Bt porphyritic rhyolite	I-type	1.02	0.61	9.5	251.9 ± 1.6	+6.17	0.707463	-
IC-106	28°07'01.23"S 69°45'44.49"W	Bt-Hbl granodiorite	I-type, slightly S-type	1.06	0.53	14.9	244.4 ± 1.6	+10.04		-
RdM-09	28°15'11.26"S 69°48'07.86"W	Bt syenogranite	I-type	1.02	0.72	22.6	253.6 ± 1.4	-2.64	0.708028	-
El León										
IC-58	28°01'05.74"S 69°32'18.92"W	Bt-Hbl monzogranite	I-type	1.02	0.45	8.3	257.0 ± 2.0[a]	-2.87	0.707902	447
IC-94	28°23'41.59"S 69°47'40.90"W	Syenogranite	I-type	1.04	1.14	5.5	243.9 ± 2.1[b]	-2.60	0.708099	-
El Colorado										
IC-14	28°13'53.00"S 69°39'47.32"W	Bt monzogranite	I-type	1.04	0.68	11.2	249.9 ± 1.6	-2.09	0.705693	-
IC-44	28°03'20.83"S 69°16'53.23"W	Hbl-bt porph. rhyolite	A-type	1.03	0.11	3.9	260.9 ± 1.5	-2.64		-
IC-93	28°24'37.53"S 69°47'10.99"W	Bt syenogranite	I-type	1.02	0.58	9.2	248.0 ± 2.0[a]	-0.92	0.706140	409-423
Chollay										
IC-46	28°03'30.12"S 69°18'54.18"W	Bt syenogranite	I-type	1.03	0.19	2.2	247.7 ± 1.2	+0.29		-
IC-47	28°02'49.99"S 69°18'37.11"W	Afs granite	I-type, slightly S-type	1.03	0.40	7.9	244.9 ± 0.9	-0.73		-
IC-81	28°04'29.05"S 69°21'39.16"W	Bt monzogranite	I-type	0.98	0.43	12.0	242.0 ± 1.0	-1.64	0.705923	-
IC-91	28°28'16.69"S 69°43'25.13"W	Hbl-bt syenogranite	I-type	0.98	0.62	8.5	259.0 ± 2.0[a]	-12.17	0.705090	23-37
IC-92	28°27'33.04"S 69°45'54.60"W	Porphyritic quartz latite	I-type	1.00	0.45	7.8	215.6 ± 1.4	-1.18	0.703301	-

Notes: Afs: alkali feldspar; Bt: biotite; Hbl: hornblende.
Aluminium Saturation Index, ASI: A/CNK = $Al_2O_3/(CaO+Na_2O+K_2O)$ (molar).
Detailed isotopic calculations for εNd_i–$(^{87}Sr/^{86}Sr)_i$ and γOs_i are in Tables 2.3 and 2.4 respectively.
i = isotopic initial ratios calculated using the obtained U–Pb ages.
$(La/Yb)_N$, N: normalized to chondrite, McDonough and Sun (1995).
[1]Lithologies were obtained after petrographic descriptions (Supplementary data)
[a]Age from Del Rey et al. (2016).
[b]Age from Martínez et al. (2016).

Table 2.2 Geochemical data for the dated samples from the Montosa–El Potro Batholith.

Unit	*La Estancilla*	*El Colorado*			*El León*		*Chollay*		
Sample	*IC-17*	*IC-14*	*IC-44*	*IC-93*	*IC-58*	*IC-94*	*IC-46*	*IC-47*	*IC-81*
wt.%									
SiO_2	59.87	68.19	76.78	73.54	71.23	76.19	78.45	76.19	72.07
Al_2O_3	16.46	15.69	12.18	13.40	14.10	12.63	12.03	12.11	13.73
Fe_2O_3(T)	6.68	3.35	1.68	1.80	3.18	0.69	1.00	1.57	2.91
MnO	0.10	0.07	0.04	0.03	0.06	0.01	0.02	0.04	0.06
MgO	3.12	0.95	0.16	0.38	0.88	0.07	0.03	0.19	0.55
CaO	6.14	2.86	0.33	1.16	2.26	0.67	0.30	0.87	1.46
Na_2O	2.73	4.27	4.05	3.98	3.31	3.70	3.57	2.97	3.88
K_2O	1.85	2.66	4.17	4.12	3.98	4.48	4.89	4.89	4.57
TiO_2	0.90	0.48	0.13	0.22	0.36	0.11	0.10	0.19	0.37
P_2O_5	0.14	0.16	0.04	0.06	0.10	0.04	0.03	0.05	0.11
LOI	1.89	0.61	0.78	1.42	0.84	1.02	0.51	1.55	0.54
Total	99.87	99.28	100.3	100.1	100.3	99.62	100.9	100.6	100.2
ppm									
Sc	17	6	2	3	7	3	2	3	5
Be	2	2	3	3	2	1	6	4	4
V	156	51	11	26	52	11	9	13	29
Co	16	4	<1	2	5	<1	<1	1	3
Cu	20	<10	<10	10	<10	<10	<10	<10	<10
Zn	60	<30	60	<30	40	<30	<30	30	30
Ga	17	17	17	14	15	12	15	14	18
Ge	1.7	1.7	1.1	2.0	1.9	1.8	2.2	1.8	2.0
Rb	85	89	194	126	168	132	347	239	185
Sr	297	247	30	115	199	64	27	40	140
Y	14.8	24.5	47.9	16.1	24.9	18	37.1	23.5	35.7
Zr	139	210	193	103	137	54	84	115	225
Nb	5.1	7.4	14.3	7.8	6.8	5.1	25.7	12.3	16
Cs	3.8	1.7	5.3	1.9	4.1	1.9	5	3.8	4.1
Ba	323	818	201	657	793	846	101	365	559
La	17.9	42.1	30.6	27.2	34.7	16.6	18.2	34.7	69
Ce	35.6	77.8	62.2	52.1	68.3	32.7	49.1	65.9	133
Pr	4.10	8.76	8.06	5.80	7.64	3.72	4.95	7.47	14.3
Nd	15.7	31.8	30.5	19.4	26.6	12.9	17.6	25.7	47.4
.Sm	3.28	6.22	7.29	3.57	5.36	2.73	4.31	4.76	7.96
Eu	0.94	1.28	0.27	0.63	0.88	0.39	0.26	0.59	1.00
Gd	3.02	4.96	7.26	2.86	4.45	2.48	4.09	3.87	5.93
Tb	0.48	0.83	1.41	0.50	0.75	0.47	0.91	0.69	1.00
Dy	2.72	4.63	8.38	2.79	4.20	2.96	5.85	4.05	5.90
Ho	0.55	0.89	1.82	0.56	0.90	0.62	1.35	0.86	1.20
Er	1.50	2.59	5.02	1.67	2.60	1.82	4.25	2.53	3.52
Tm	0.25	0.41	0.87	0.30	0.45	0.32	0.80	0.46	0.63
Yb	1.61	2.56	5.37	2.01	2.86	2.05	5.75	3.01	3.91
Lu	0.23	0.34	0.74	0.31	0.42	0.29	0.81	0.43	0.57
Hf	3.2	4.7	6.1	2.9	3.9	1.8	3.3	3.5	5.6
Ta	0.6	0.93	1.81	1.2	1.12	0.84	5.26	1.77	2.01
Tl	0.55	0.57	2.62	0.72	1.16	0.84	2.48	2.73	1.24
Pb	12	11	16	10	12	14	19	13	17
Th	8.93	10.0	25.2	11.9	16.9	8.17	38.7	19.7	24.9
U	2.09	1.42	4.65	2.31	3.8	1.51	6.49	3.01	3.90

Notes: Major element oxides and trace elements were analysed by Actlabs Canada.
Mayor elements plus Sc, Be, V, Sr, Zr and Ba were analysed using FUS-ICP and trace elements using FUS-ICPMS.
Total iron as Fe_2O_3.

Table 2.2 (continued)

Unit	*Chollay*		*Montosa*					
Sample	*IC-91*	*IC-92*	*IC-22*	*IC-23*	*IC-99*	*IC-102*	*IC-106*	*RdM-09*
wt.%								
SiO_2	68.80	75.38	68.82	78.31	68.87	70.88	67.25	78.46
Al_2O_3	14.71	12.70	14.88	11.85	15.06	13.07	14.64	11.96
Fe_2O_3(T)	3.76	2.44	4.20	0.97	4.31	2.40	4.25	1.05
MnO	0.06	0.02	0.06	0.01	0.08	0.06	0.09	0.03
MgO	0.98	0.13	1.27	0.14	1.33	0.63	1.33	0.13
CaO	2.58	0.71	3.44	0.68	3.81	1.68	2.44	0.83
Na_2O	3.82	4.41	3.28	2.69	3.94	3.78	3.77	3.72
K_2O	3.69	3.85	3.37	5.40	1.49	3.26	2.91	3.78
TiO_2	0.48	0.25	0.49	0.12	0.50	0.30	0.55	0.11
P_2O_5	0.15	0.06	0.13	0.03	0.18	0.09	0.15	0.03
LOI	1.78	0.78	0.81	0.62	0.69	2.25	1.54	0.26
Total	100.8	100.7	100.7	100.8	100.3	98.39	98.93	100.4
ppm								
Sc	8	4	10	3	8	5	12	1
Be	3	3	2	<1	2	2	2	1
V	66	20	76	14	74	32	84	13
Co	5	2	6	<1	6	3	7	<1
Cu	<10	10	<10	<10	<10	<10	<10	<10
Zn	40	<30	<30	<30	60	<30	40	<30
Ga	16	17	16	11	17	14	17	12
Ge	1.8	1.6	1.7	1.9	1.5	1.4	1.9	1.7
Rb	133	81	157	106	57	117	85	69
Sr	235	55	245	86	303	65	338	37
Y	19.5	22.9	21.7	5.9	9.9	21	19.1	5.8
Zr	184	242	200	76	162	144	160	72
Nb	7.2	5.8	7.8	0.8	0.9	6	5.2	< 0.2
Cs	3.8	1.1	8.3	1.5	1.9	2.4	2.3	0.7
Ba	727	683	846	1101	728	552	1176	218
La	29.7	33	31	33.7	28.1	32.7	45.1	19.9
Ce	63.2	64.7	62.6	60.6	49.9	63.6	84.8	38.5
Pr	7.51	7.3	7.1	6.22	5.21	7.11	8.87	4.33
Nd	27.2	25.9	25.6	19.3	17.4	25	30	14.5
Sm	4.71	4.89	4.87	2.68	2.7	4.44	4.99	2.38
Eu	0.89	0.67	0.98	0.62	0.96	0.83	1.09	0.36
Gd	3.72	4.03	4.04	1.68	2	3.63	3.99	1.64
Tb	0.62	0.7	0.68	0.22	0.31	0.64	0.61	0.21
Dy	3.5	4.02	3.83	1.15	1.74	3.66	3.44	1.05
Ho	0.72	0.86	0.76	0.22	0.35	0.73	0.69	0.21
Er	2.09	2.62	2.2	0.63	1.02	2.11	1.98	0.59
Tm	0.37	0.43	0.37	0.10	0.19	0.36	0.30	0.09
Yb	2.39	2.9	2.36	0.82	1.16	2.36	2.07	0.6
Lu	0.35	0.43	0.33	0.13	0.18	0.34	0.29	0.09
Hf	4.5	6	4.6	2.7	3.8	4.1	4.1	1.8
Ta	0.95	0.85	1.21	0.34	0.25	0.89	0.52	0.3
Tl	0.93	0.88	0.86	0.61	0.34	0.61	0.45	0.57
Pb	17	<5	11	12	7	8	13	16
Th	16.6	10.3	18.8	10.6	4.49	12.6	9.94	16.1
U	2.03	2.65	3.86	1.49	1.3	2.32	1.85	0.98

Notes: Major element oxides and trace elements were analysed by Actlabs Canada.
Mayor elements plus Sc, Be, V, Sr, Zr and Ba were analysed using FUS-ICP and trace elements using FUS-ICPMS.
Total iron as Fe_2O_3.

Rocks analysed here represent compositions ranging from diorites to granites (petrographic descriptions in Supplementary data). Samples are calc-alkaline to high-K calc-alkaline, metaluminous to weakly peraluminous and present clear I-type characteristics with some samples showing transition to A-type and others with slight S-type tendencies (according to Chappell and White (2001) and references therein) (Fig. 2.3). Multielement variation diagrams of trace elements and REE normalized to primitive mantle and chondrite (McDonough and Sun, 1995) respectively, display a relatively similar pattern for all the intrusives (middle Permian–late Triassic) (Fig. 2.4). The rocks are enriched in incompatible elements showing negative Sr, P, Ti and Ba anomalies, Nb–Ta troughs and positive Pb anomalies. Most samples have negative Eu anomalies and relatively flat REE patterns.

The oldest sample, La Estancilla pluton (286.0 ± 2.0 Ma, early Permian, Del Rey et al. (2016)) is of dioritic composition (SiO_2 = 59.9%), calc-alkaline, metaluminous (Aluminun Saturation Index, ASI = 0.93) and I-type (Fig. 2.3). In primitive mantle-normalized multielement diagrams it shows no Ti anomaly, negative Ba and P, Nb–Ta troughs, and positive Pb anomaly. It has relatively flat REE patterns (ca. $(La/Yb)_N$ = 7.6) and almost absent Eu anomaly (Eu/Eu*=0.89) (Fig. 2.4).

Montosa unit (middle Permian–Middle Triassic) shows the largest compositional range, ranging from diorites to granites continuously through granodiorites (SiO_2 = 56–78%). All diorites – together with some granodiorites – are metaluminous (ASI between 0.87 and 1.00), whereas all granites and most granodiorites are weakly peraluminous (ASI between 1.02 and 1.06). Samples are calc-alkaline and I-type with some showing slight S-type characteristics (Fig 3). According to the new ages obtained, geochemical variability is coeval among the analysed samples, occurring mostly during late Permian and early Triassic. Multielement diagrams indicate negative Sr, P, Ti and Nb–Ta troughs, and positive Pb. The unit presents two general groups of REE patterns: relatively flat ($(La/Yb)_N$ = 6.0–14.9) and steep ($(La/Yb)_N$=16.5–52.1) (Fig. 2.4). Typically, they do not have very pronounced negative Eu anomalies (Eu/Eu* = 0.53–0.89, with an Eu/Eu* average of 0.82) with some samples showing absence or slightly positive values (Eu/Eu* = 0.92–1.21).

El León unit (late Permian–Middle Triassic) is granitic (SiO_2 = 71–76%), high-K calc-alkaline and weakly (ASI between 1.02 and 1.10) to strongly (only one sample ASI = 1.14) peraluminous. Most samples are I-type with one showing slight A-type characteristics and another S-type affinities (Fig. 2.3). Multielement diagrams show negative Sr, P and Ti anomalies, somewhat negative Ba (one sample positive), positive Pb anomalies and Nb–Ta troughs. It has relatively flat REE patterns ($(La/Yb)_N$ = 5.5–15.1) and fairly negative Eu anomalies (Eu/Eu* = 0.44–0.63) (Fig. 2.4).

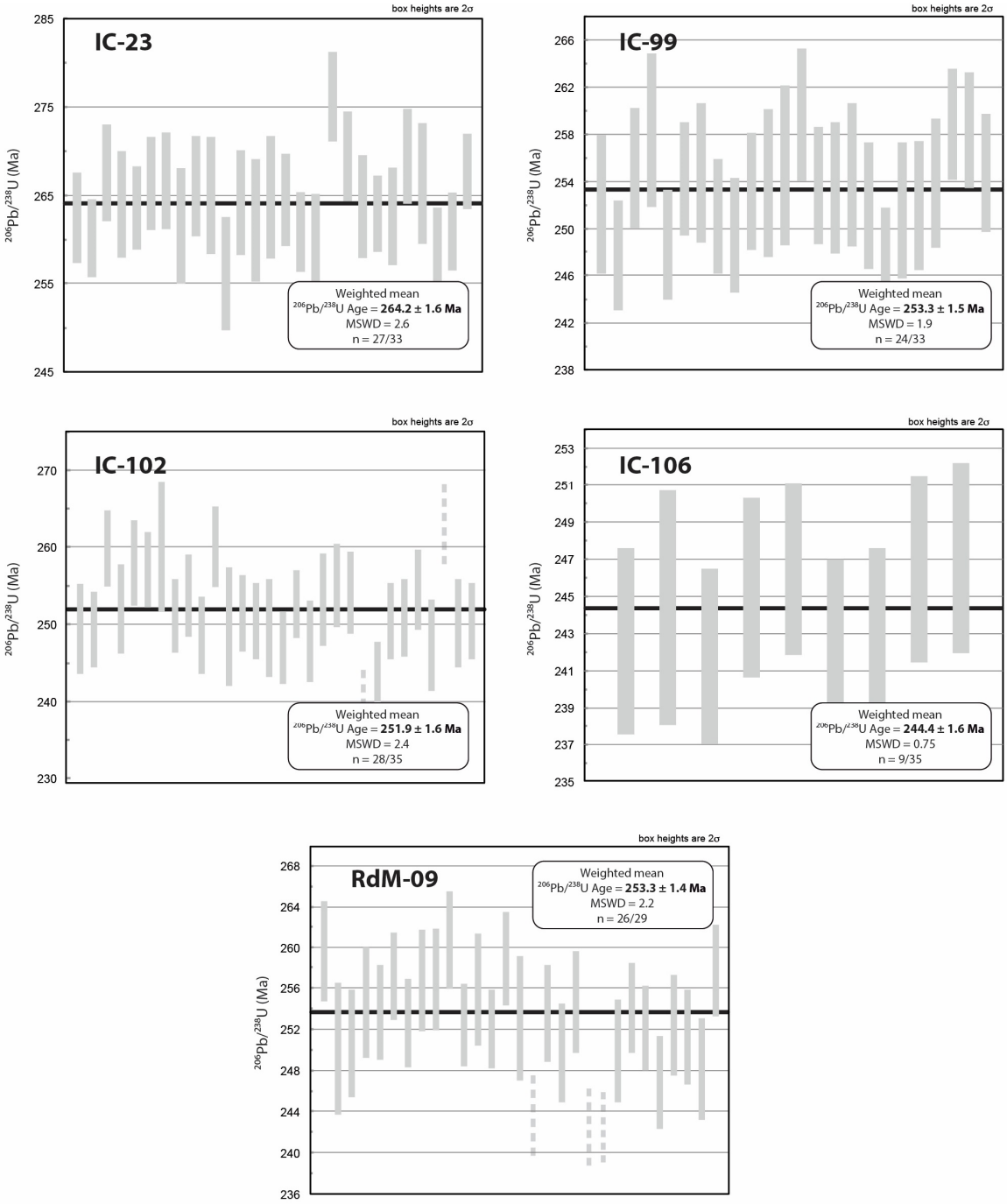

Fig. 2.2 Geochronological analyses. Weighted mean age histograms for each sample. Montosa: IC-23, IC-99, IC-102, IC-106, RdM-09. Location of analysed samples is shown in Fig. 2.1.

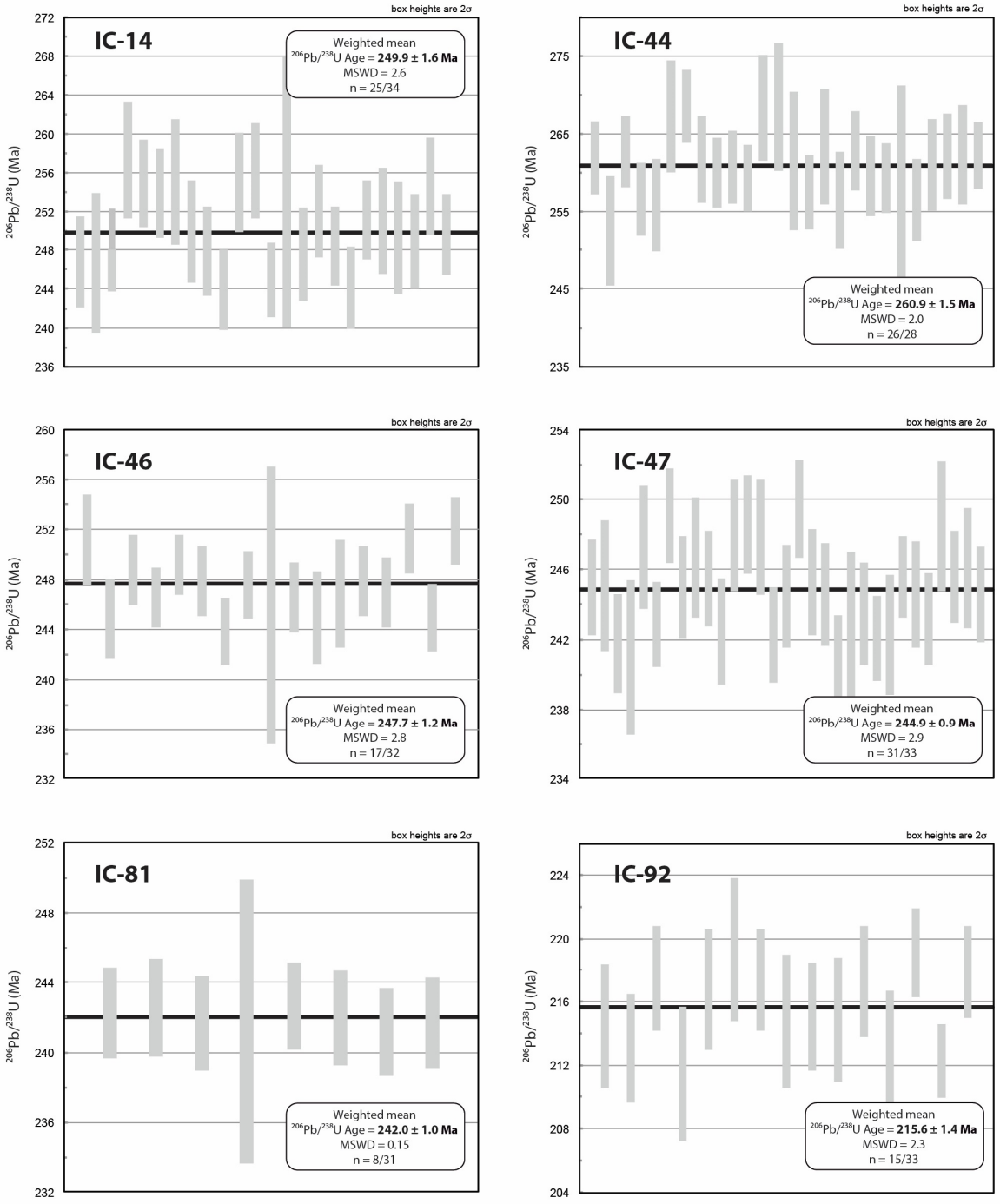

Fig. 2.2 Geochronological analyses (continued). Weighted mean age histograms for each sample. El Colorado: IC-14, IC-44; Chollay: IC-46, IC-47, IC-81, IC-92. Location of analysed samples is shown in Fig. 2.1.

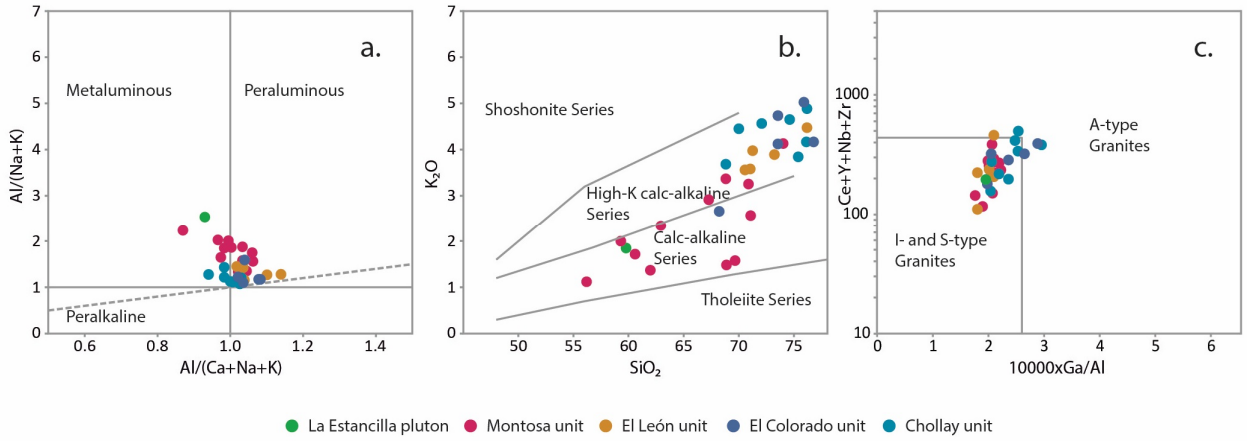

Fig. 2.3 Classification diagrams. a. A/CNK vs. A/NK diagram indicating that samples are divided between metaluminous and peraluminous. El León and El Colorado units are strictly peralumnious, and La Estancilla, metaluminous. b. Peccerillo and Taylor (1976) diagram displaying a calc-alkaline to high-K calc-alkaline trend typical of continental magmatic arcs. Units Montosa and La Estancilla can be defined as calc-alkaline, whereas El León, Chollay and El Colorado as high-K calc-alkaline. c. 10,000×Ga/Al vs. Ce+Nb+Zr+Y granite discrimination diagram (Whalen et al., 1987). Only few samples from El León, Chollay and El Colorado plot in the A-type granites area.

Chollay unit (late Permian–Middle Triassic) presents a granitic composition (SiO_2 = 69–78%), high-K calc-alkaline and metaluminous to weakly peraluminous (ASI between 0.94 and 1.03). Samples are mostly I-type with lesser A-type, and one with slight S-type characteristics (Fig. 2.3). It is worth mentioning that a sample from late Triassic shows a metaluminous and I-type composition. Regarding the multielement diagrams, the intrusive presents negative Sr, P, Ti and Ba anomalies with Nb–Ta troughs and positive Pb anomaly. It has relatively flat REE patterns ($(La/Yb)_N$ = 2.2–12.0) and pronounced negative Eu anomalies (Eu/Eu* = 0.12–0.62) (Fig. 2.4).

El Colorado unit (middle Permian–early Triassic) presents a granitic to granodioritic composition, and is high-K calc-alkaline and weakly peraluminous (ASI between 1.02 and 1.08). Samples are I- and A-type with one showing slight S-type tendencies (Fig. 2.3). Multielement diagrams show negative Ba, Sr, P and Ti anomalies, Nb–Ta troughs and positive Pb. It has relatively flat REE patterns ($(La/Yb)_N$ = 3.9–11.2) and the most pronounced negative Eu anomalies (Eu/Eu* = 0.11–0.68) (Fig. 2.4).

2.4.3 Whole-rock Rb–Sr and Sm–Nd isotopic data

All $^{87}Sr/^{86}Sr$ and $^{143}Nd/^{144}Nd$ analysed samples (12 and 17, respectively) have assigned new U–Pb in zircon ages or they have been previously dated (Table 2.1). Initial εNd_i values and Sr-isotope ratios were calculated at the given U–Pb in zircon age for each sample. The obtained ratios range from +9.9 to -12.2 for εNd_i, and from 0.703 to 0.708 for $^{87}Sr/^{86}Sr_i$. Unfortunately, due to extremely low Sr levels in comparison to Rb, not all the samples could be isotopically analysed (Table 2.3).

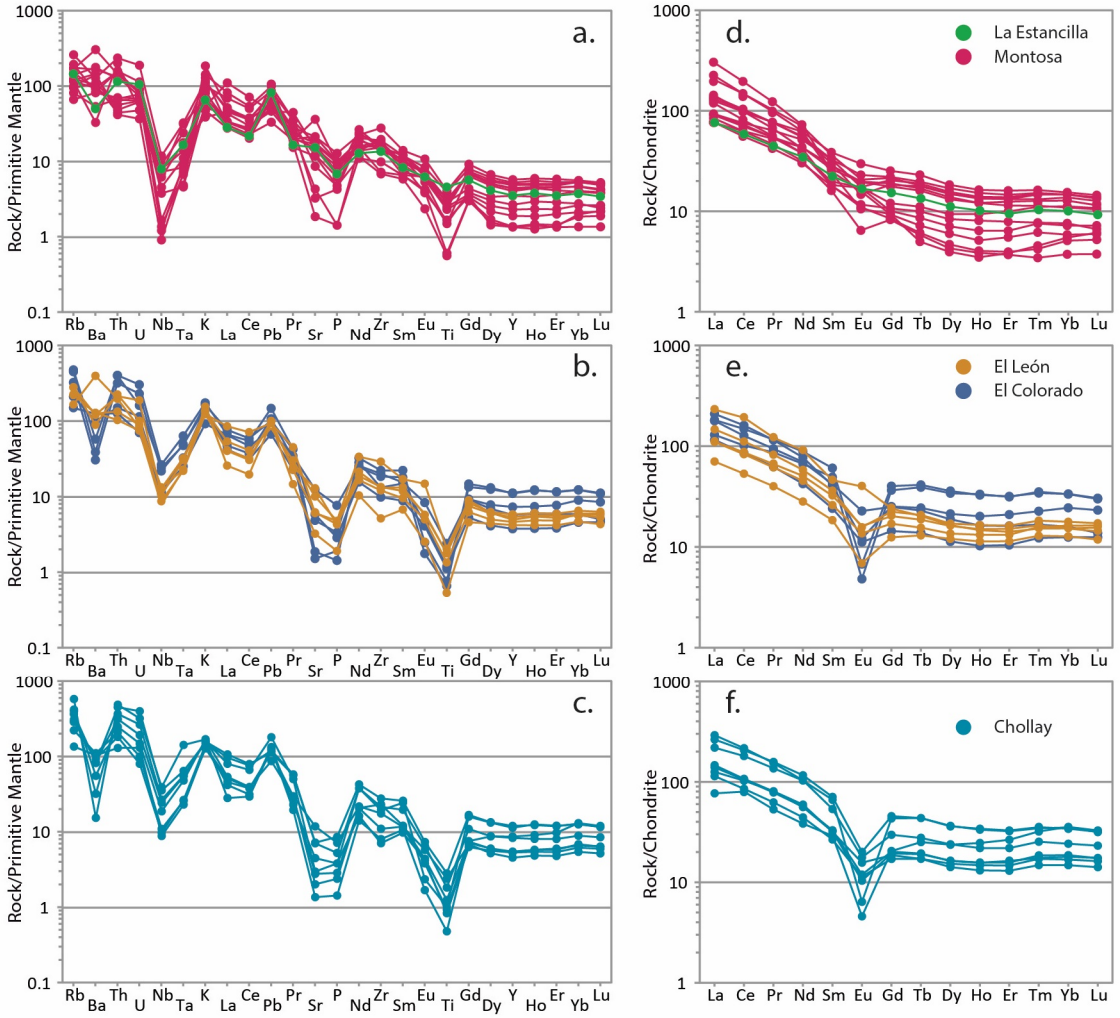

Fig. 2.4 Trace element diagrams. Primitive mantle-normalised multielement variation diagrams of trace elements (a, b, c), and chondrite-normalised REE plots (d, e, f) (after McDonough and Sun, 1995) for units from the Montosa–El Potro Batholith: La Estancilla pluton (ca. 286 Ma), Montosa (264-244 Ma), El León (257-244 Ma), El Colorado (261-248 Ma), and Chollay (259-216 Ma). Ages taken from Table 2.1.

La Estancilla pluton presents εNd_i = +2.1 and $^{87}Sr/^{86}Sr_i$ = 0.705, indicating a less evolved source of magmas compared with the rest of the units. El Colorado shows εNd_i values between -2.6 and -0.9 and $^{87}Sr/^{86}Sr$ = 0.706. El León, εNd_i between -2.9 and -2.9 and $^{87}Sr/^{86}Sr_i$ = 0.708. Chollay present the most negative εNd_i value of -12.2 starting from +0.3 and $^{86}Sr/^{87}Sr_i$ values between 0.703 and 0.706. Lastly, Montosa presents the most positive εNd_i value of +9.9, starting from -2.6 and with $^{87}Sr/^{86}Sr_I$ between 0.704 and 0.708. No clear relation between these isotopic values and individual ages can be observed. On the other hand, an evident lower continental crust signature predominates during early Permian–late Triassic.

Table 2.3 Sm–Nd and Rb–Sr isotopic data for the U–Pb dated samples from the Montosa–El Potro Batholith.

Sample	SiO_2 (wt.%)	Age (Ma)	Sm (ppm)	Nd (ppm)	$^{147}Sm/^{144}Nd$	$(^{143}Nd/^{144}Nd)_{today}$	$(^{143}Nd/^{144}Nd)_i$	$CHUR_i$	εNd_i	Rb (ppm)	Sr (ppm)	$^{87}Rb/^{86}Sr$	$(^{87}Sr/^{86}Sr)_{today}$	$(^{87}Sr/^{86}Sr)_i$
La Estancilla pluton														
IC-17	59.87	286[a]	3.28	15.7	0.126	0.512612	0.512377	0.512270	+2.09	85	297	0.8281	0.708645	0.705279
Montosa														
IC-22	68.82	253[a]	4.87	25.6	0.115	0.512393	0.512203	0.512312	-2.13	157	245	1.8543	0.710667	0.703985
IC-23	78.31	264	2.68	19.3	0.084	0.512372	0.512227	0.512296	-1.36	106	86	3.5665	-	
IC-99	68.87	253	2.7	17.4	0.093	0.512440	0.512284	0.512310	-0.51	57	303	0.5443	0.706574	0.704599
IC-102	70.88	252	4.44	25.0	0.107	0.512806	0.512630	0.512314	+6.17	117	65	5.2085	0.726127	0.707463
IC-106	67.25	244	4.99	30.0	0.100	0.512993	0.512827	0.512313	+10.04	85	338	0.7277	-	
RdM-09	78.46	254	2.38	14.5	0.099	0.512340	0.512176	0.512311	-2.64	69	37	5.3962	0.727496	0.708028
El León														
IC-58	71.23	257[a]	5.36	26.6	0.121	0.512364	0.512160	0.512307	-2.87	168	199	2.4428	0.716826	0.707902
IC-94	76.19	244[b]	2.73	12.9	0.127	0.512394	0.512189	0.512322	-2.60	132	64	5.9681	0.728907	0.708099
El Colorado														
IC-14	68.19	250	6.22	31.8	0.118	0.512403	0.512213	0.512319	-2.09	89	247	1.0426	0.709363	0.705693
IC-44	76.78	261	7.29	30.5	0.144	0.512415	0.512176	0.512311	-2.64	194	30	18.7119	-	
IC-93	73.54	248[a]	3.57	19.4	0.111	0.512451	0.512271	0.512319	-0.92	126	115	3.1704	0.717329	0.706140
Chollay														
IC-46	78.45	248	4.31	27.2	0.104	0.512573	0.512334	0.512319	+0.29	347	27	37.1881	-	
IC-47	76.19	245	4.76	17.6	0.147	0.512464	0.512285	0.512323	-0.73	239	40	17.2893	-	
IC-81	72.07	242	7.96	47.4	0.101	0.512404	0.512246	0.512330	-1.64	185	140	3.8237	0.718922	0.705923
IC-91	68.80	259[a]	4.71	25.7	0.112	0.511858	0.511682	0.512305	-12.17	133	235	1.6377	0.711113	0.705090
IC-92	75.38	216	4.89	25.9	0.114	0.512461	0.512300	0.512360	-1.18	81	55	4.2615	0.716368	0.703301

Notes: The decay constant used in the calculation is $\lambda^{147}Sm = 6.54\times10^{-12}$ year^{-1} and $\lambda^{87}Rb = 1.42\times10^{-11}$ year^{-1} (Steiger and Jäger, 1977).
εNd values were calculated relative to a chondrite isotopic initial ratios using present day values $(^{143}Nd/^{144}Nd)^{today}_{CHUR} = 0.512638$; $(^{143}Sm/^{144}Nd)^{today}_{CHUR} = 0.1967$ (Jacobsen and Wasserburg, 1980).
i = isotopic initial ratios calculated using the obtained U–Pb ages.
For samples IC-44, -46, -47, and -23, ICPMS $(^{87}Sr/^{86}Sr)_i$ values were unable to obtain due to extremely low Sr values relative to Rb.
Sample IC-106 was not reported by the laboratory.
[a]Age from Del Rey et al. (2016).
[b]Age from Martínez et al. (2016).

2.4.4 Re–Os in magnetite isotopic data

Most of γOs_i analysed samples have been previously dated (Del Rey et al., 2016) and one has a new U–Pb in zircon age (Table 2.1). The obtained initial ratios (γOs_i) are: Montosa, +125 to +1290; El León, +447; Chollay, +23 to +37; and El Colorado, +409 to +423 (Table 2.4). There is an apparent trend of increasingly lower γOs_i values, as the rocks get younger. However, more analysis must be performed to assert this tendency.

Table 2.4 Re–Os in magnetite isotopic data for some of the U–Pb dated samples from the Montosa–El Potro Batholith.

Magnetite grain	Age (Ma)	Re (ppb)	^{187}Re (ppb)	Os (ppb)	^{187}Os (ppb)	$^{187}Re/^{188}Os$	$^{187}Os/^{188}Os$	$(^{187}Os/^{188}Os)_i$	$(\gamma Os)_i$
Montosa									
IC-22-mt-2	253[a]	0.187	0.117	0.043	0.002	21.60	0.376	0.285	125
IC-22-mt-3	253[a]	0.117	0.073	0.050	0.002	11.64	0.352	0.302	140
IC-23-mt-1	264	0.308	0.193	0.037	0.007	48.64	1.674	1.459	1056
IC-23-mt-2	264	0.170	0.107	0.032	0.006	31.41	1.893	1.755	1290
El León									
IC-58-mt-2	257[a]	0.915	0.573	0.046	0.006	108.92	1.158	0.691	447
El Colorado									
IC-93-mt-2	248[a]	2.361	1.478	0.520	0.046	23.71	0.741	0.642	409
IC-93-mt-3	248[a]	1.684	1.054	0.521	0.046	16.85	0.730	0.660	423
Chollay									
IC-91-mt-2	259[a]	0.556	0.348	0.224	0.006	12.12	0.207	0.155	23
IC-91-mt-3	259[a]	0.472	0.296	0.168	0.005	13.76	0.232	0.173	37

Notes: The decay constant used in the calculation is $\lambda^{187}Re = 1.666\times10^{-11}$ year^{-1} (Smoliar et al., 1996).
γOs values were calculated relative to primitive mantle peridotites using present day values $(^{187}Re/^{188}Os)^{today}_{PM} = 0.3924$; $(^{187}Os/^{188}Os)^{today}_{PM} = 0.1262$ (Walker et al., 2002).
i = isotopic initial ratios calculated using the obtained U–Pb ages.
[a]Age from Del Rey et al. (2016).

2.5 Discussions

2.5.1 Timing and the source for the Frontal Andes magmatism

New geochronological results indicate that the analysed rock units were emplaced in magmatic pulses, with a peak between Guadalupian (middle Permian)–Middle Triassic (264.2 ± 1.6–242.0 ± 1.0 Ma) and minor activity during Upper Triassic (215.6 ± 1.4 Ma) (Table 2.1). Nevertheless and despite the different pulses, protracted magmatism from latest early Carboniferous–late Triassic (328.1 ± 2.8–215.6 ± 1.9 Ma) has been described for the Chilean Frontal Andes (Maksaev et al., 2014) thus samples are in agreement continuous magmatic activity between middle Permian-to-late Triassic.

La Estancilla pluton

Geochemical and isotopically, the oldest sample corresponding to the La Estancilla pluton (286.0 ± 2.0 Ma, Del Rey et al., 2016) displays one of the least evolved characteristics. This is, dioritic composition and εNd_i = +2.1 and

$^{87}Sr/^{86}Sr_i$ = 0.705 (Fig. 2.5a). It also shows a distinct trace element composition with absence of Eu, Sr and Ti anomalies, indicating no major fractionation of plagioclase thus possibly greater depths of the source (emplaced into normal thickness crust). It also shows positive Pb and negative Nb–Ta anomalies, indicating subduction-related arc magmas.

Montosa, El León, Chollay and El Colorado units

The rest of the samples display a wider compositional range (diorite to granites) and I-type with minor S-, and A-type affinities. The clear contemporaneity of the rocks does not allow to effectively differentiating periods regarding major geochemical characteristics. Additionally, most units display quite similar patterns in the multielement variation diagrams, showing similar element anomalies. Particularly, all units present negative Nb–Ta and positive Pb anomalies (normalized to primitive mantle), which is characteristic of subduction-related arc magmas (e.g., Pearce and Peate, 1995)).

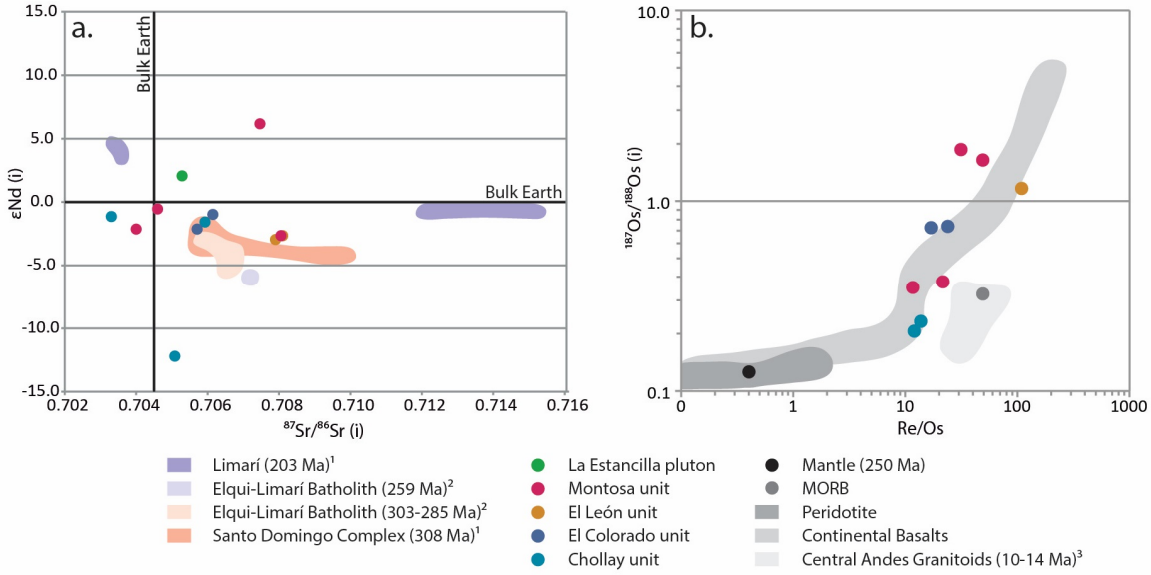

Fig. 2.5 Isotopic composition diagrams. a. Sr–Nd initial isotope composition diagram for the units from the Montosa–El Potro Batholith. A comparison is made with coeval units along the Chilean border (ca. 28º–34ºS). Late Carboniferous–middle Permian units (La Estancilla, Elqui–Limarí Batholith and Santo Domingo Complex) apparently show a trend from higher initial $^{87}Sr/^{86}Sr$ ratios (Santo Domingo Complex) – indicating higher upper crustal involvement – towards less evolved signatures (La Estancilla pluton), which overlap with part of the middle Permian–Triassic units. Most of the herewith-studied samples present εNd_i values close to zero, indicating a lower continental crust source with minimum contribution from evolved crustal material. In particular, the steeper trend for Chollay unit indicates older, low Rb/Sr sources, also associated with deeper continental crust. Middle Permian–Triassic units showing an increased trend towards higher initial $^{87}Sr/^{86}Sr$ ratios (El León, Montosa, Elqui–Limarí Batholith) indicate higher contributions from evolved material but not exceptionally large as in Limarí. The latter also presents samples towards a more primitive mantle-like source, evidencing a major hybrid magmatic episode (bimodal magmatism) in agreement with an extensional tectonic regime and melting throughout the crustal section. Overall, a trend from upper crustal involvement towards a more disperse source (mix between mantle-like and continental sources) can be seen from late Carboniferous to Trassic. b. Re/Os ratio versus Os initial isotope composition for the units from the Montosa–El Potro Batholoth, plus a variety of terrestial rocks data contained in the Woods Hole Re–Os database (Blusztajn

et al., 2000) for comparison. Again, a mix between mantle-like and continental sources can be seen during middle Permian-Triassic. Specific age for each analysed sample can be obtained from Table 2.3 and 2.4 for Sr–Nd and Re–Os respectively. 1, Parada et al. (1999); 2, Mpodozis and Kay (1992); 3, Deckart et al. (2010).

Montosa displays some differences compared to the other units and its variability has been previously attributed to source region variations, phase accumulation and minor phase fractionation (Mpodozis and Kay, 1992). This unit shows slight to absent negative Eu anomalies and relatively flat ($(La/Yb)_N$ = 6.0–14.9) to steep ($(La/Yb)_N$ = 16.5–52.1) REE patterns, with less pronounced negative Sr and Ti anomalies, indicating a less prominent role of plagioclase fractionation. Moreover, the steepest REE patterns ($(La/Yb)_N$ = 22.6 to 52.1) plus no Eu anomaly and high LREE indicate higher pressures i.e., melts generated in a thicker crust. In some samples, slight concave-up REE patterns supports amphibole fractionation. Montosa also presents the strongest negative Nb–Ta anomalies, indicating subduction zone magma affinities, probably with a source from the shallow parts of the subduction zone (Baier et al., 2008). Overall less peraluminosity and less enrichment in incompatible elements (U, Th and Pb) indicate lesser magma differentiation than the rest of the units. εNd_i values (+9.0 to -2.6) are in agreement with lesser magma differentiation by continental contamination and, together with $^{87}Sr/^{86}Sr_i$ (0.704–0.708) also show lower continental crust affinities (Fig. 2.5a). This unit is also clearly I-type that together with its weakly peraluminous character indicate magmas derived from the melting of metaluminous source materials during partial melting of the crust at pressures below the garnet stability field (Chappell et al., 2012).

El León, El Colorado and Chollay show strong negative Eu anomalies together with negative Sr, Ba (specially for El Colorado and Chollay) and Ti anomalies; and relatively flat REE patterns ($(La/Yb)_N$ = 2.2–15.1), pointing to fractionation of plagioclase or retention in the source suggesting low pressure melting and differentiation in a garnet-free source/residuum under a possible thinned crust. These units are mostly weakly peraluminous (apart from some metaluminous rocks from Chollay) and present enrichment in incompatible elements (mainly U, Th and Pb) displaying crustal contributions and/or high amounts of magmatic differentiation by partial melting-fractionation. Compared with La Estancilla pluton and Montosa, these units show higher K content (high-K calc-alkaline versus calc-alkaline) and overall higher enrichment in trace elements. Particularly Chollay and El Colorado are the most enriched ones, followed by El León. Negative εNd_i for all these samples, plus moderate $^{87}Sr/^{86}Sr_i$ values evidence a lower continental crust signature (Fig. 2.5a).

El Colorado and Chollay show stronger transitional to A-type characteristics suggesting emplacement in an extensional regime; either continental back-arc, post-collisional extension or within plate scenario (e.g., Eby, 1992; Whalen et al., 1996), and they mostly correspond to magmas

derived from melting of continental crust with or without mantle input (A2-type, Eby, 1992) (Fig. 2.6a).

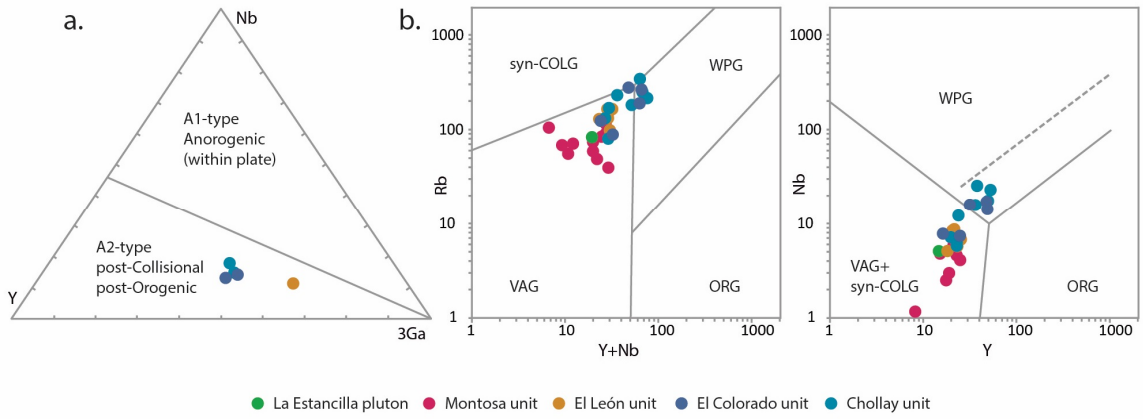

Fig. 2.6 Tectonic discrimination diagrams. a. Y–Nb–3Ga diagram (Eby, 1992) showing that all the A-type samples from the Montosa–El Potro Batholith plot in the volcanic arc and post-orogenic tectonic setting (A2-type, crustal derived). b. Tectonic discrimination Y+Nb vs. Rb and Y vs. Nb diagrams (Pearce et al., 1984). Most samples plot in the volcanic arc granite field (La Estancilla, Montosa and El León units) and some show transitional features towards within-plate granites (Chollay and El Colorado units). VAG: volcanic arc granites; WPG: within-plate granites; syn-COLG: syn-collision granites; ORG: ocean ridge granites.

Disregarding the almost coevalness of the samples, a geographical distinction can be made. According to Fig. 2.1, Montosa unit corresponds to the western batholith whereas El León, Chollay and El Colorado to the eastern. In fact, only Montosa unit presents steeper REE patterns and the clear absence of Eu anomalies suggest a westward increase in crustal thickness (i.e. towards the shallow parts of the subduction zone). However, a lower pressure magma source is most probably also present in the suite (evidenced by the flatter REE patterns), indicating magmagenesis in possibly different levels of the continental crust. This explains the broader geochemical variations and the strongest negative Nb–Ta anomalies seen in this unit i.e., Montosa was emplaced in the shallower part of the subducting slab. In addition, El Colorado and Chollay showing A-type characteristics suggests that this signature increase eastwards whereas I-type, westward. Also, these units present the most negative Eu anomalies, whereas El León intermediate values compared to Montosa (the least negative). Regarding trace element enrichment, a similar pattern can be seen: the further inland, the higher overall enrichment in trace elements (Fig. 2.4).

Beside the initial $^{143}Nd/^{144}Nd_i$–$^{87}Sr/^{86}Sr_i$ lower continental crust signatures observed in the rocks, εNd_i values close to zero (Table 2.3) indicate a minimum contribution from evolved crustal material (e.g., Alasino et al., 2012). Compared to previous work, the samples studied here show similar values among most of latest Carboniferous/Triassic plutonism (Fig. 2.5a), and they are considerably more continental-like than Jurassic–Cretaceous magmatism (Parada et al., 1999, 2002).

In the case of Re–Os, according to Woods Hole Re-Os database (Blusztajn et al., 2000), $^{187}Os/^{188}Os_i$ values lower than 0.2 ($\gamma Os<+5$) represent mantle-like signatures (i.e. peridotite, MORB signatures; Tejada et al. (2013)) (Fig. 2.5b). Arc volcanic rocks tend to have very low Os concentrations (Borg et al., 2000; Hart et al., 2002; Woodland et al., 2002), thus increasing Re/Os and γOs_i values. According to this, the herewith-obtained data indicate a more mantle-like signature or influence, as the rocks get younger (Table 2.4). Moreover, Re–Os systematics is the most sensitive isotope system for detecting young mafic crust in orogenic systems (Johnson et al., 1996), meaning that lower γOs_i values, such as in Chollay (γOs_i = 23–37) imply a more direct mantle influence or source. On the other hand, the oldest Re–Os analysed sample, Montosa (264.2±1.6 Ma) shows the highest γOs_i values (γOs_i = 1056–1290) as well as absence of Eu anomaly, possibly indicating a deeper level source with major crustal contributions and/or fractional crystallization in absence of mantle influence. Nevertheless, between latest Permian and early Triassic a more mixed source can be described, with some samples showing higher crustal signatures (e.g., Montosa, El León and El Colorado) and others more mantle-like affinities (e.g., Chollay).

Summarizing, all the studied samples present clear subduction-related arc magma characteristics and variable amounts of continental crust contributions. Most of REE patterns evidence low-pressure garnet-free sources, where plagioclase played a major role (fractionation or retention in the source). However, steeper REE patterns can be seen in the western batholith (Montosa unit) suggesting and increase in the thickness of the crust westwards. Furthermore, the presence of transitional to A-type granites decreases westward (Fig. 2.1 at ca. 28°S). Generally, according to εNd_i and $^{87}Sr/^{86}Sr_i$ almost all samples present lower continental crust signatures, apart from the slightly more primitive signature for La Estancilla pluton (ca. 286.0 ± 2.0 Ma, Del Rey et al., 2016) and some Montosa samples (samples IC-102 and IC-106, Table 2.3).

2.5.2 Geodynamic setting and evolution

In their tectonic context, rocks range from VAG-type (Volcanic Arc Granites) to WPG-type (Within Plate Granites) according to Pearce et al. (1984) (Fig. 2.6b). La Estancilla, Montosa and El León units can be characterized as VAG while Chollay and El Colorado as a combination between VAG and WPG. According to the geochronological results, the different tectonic scenarios are coeval for the analysed samples. It is worth mentioning that the youngest dated rock (Chollay unit, 215.6±1.4 Ma) presents VAG affinities, which together with its subduction-related multielement anomalies and metaluminous I-type character indicates that subduction was active during late Triassic.

The clear coevalness of intrusive units, VAG and WPG mixed scenario and the presence of A-type intrusives allow to infer a tectonic setting where rocks were emplaced in high temperature conditions (presence of A-type granites, Whalen et al. (1987)) into a thinned continental crust (overall relatively flat REE patterns and negative Eu anomalies) with volcanic arc activity. The described characteristics depict a tectonic scenario which could consists in a convergent margin with subduction zone and predominant extensional conditions, the latter being the responsible for the thinned continental crust and high temperatures (allowing the emplacement of A-type granites). Long lasting and strong enough extension must have existed in order to produce continental thinning and in consequence, within plate affinities. In addition, the west-to-east differences observed in the multielement and REE patterns together with A-type characteristics can also be seen relative to VAG and WPG. This is, Montosa presents exclusively volcanic arc granitoids whereas the eastern units increasing within plate tendencies. All these characteristics could indicate that the thickness of the continental crust varied longitudinally, i.e. progressive lithospheric thinning eastwards, allowing in the same manner the participation of more juvenile material in those magmas (Fig. 2.7). Higher trace element and K enrichment eastwards could point out higher magma differentiation in the same pattern.

Regarding the A-type granites, it should be noted that the original definition proposed by Loiselle and Wones (1979) refers to this type of granite as characterized by emplacement in a rift zone or stable continental block, hence ‘anorogenic’. Nevertheless, a more recent work by King et al. (1997) considers the tectonic definition of ‘anorogenic’ A-type confusing and too broad, thus separating aluminous (metaluminous to weakly peraluminous) A-type granites from peralkaline associations (rift-related). Consequently, all the herewith-studied A-type samples can be re-defined as aluminous A-type according to their characteristic. King et al. (1997) results indicate that the aluminous A-type granites differ greatly from the peralkaline counterpart, being produced by combined partial melting-fractionation from source compositions such as lower crustal (that can overlap in composition with I-type sources) but with limited availability of H_2O and relatively low oxygen fugacity during high temperature partial melting. Such high temperatures required may have been reached by mantle upwelling or mafic magma influx in a localized area; and the source region could be either very localized or separated from other granite source regions vertically in the crust. These tectonic implications are coherent with slab rollback extensional conditions and point to melting of a lower crust source. In addition, Cordilleran I-type rocks have been explained by multiple episodes of partial melting of a basaltic underplate accompanied by crystal and/or restite fractionation from the resulting magmas (Chappell and Stephens, 1988), therefore the overall tectonic scenario for the Montosa–El Potro Batolith can be described as magmas generated by partial melting of a basaltic underplate and a metaluminous lower crust in a subduction-related extensional setting.

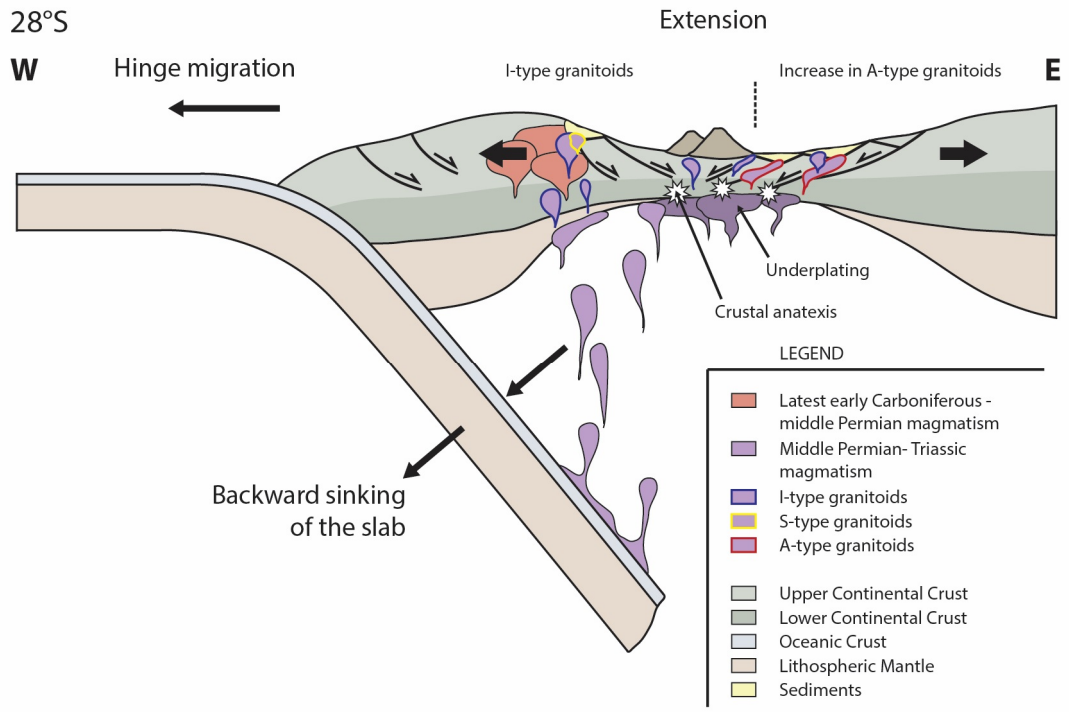

Fig. 2.7 Paleogeographic model. Schematic cross-sections through Chilean–Argentinian Frontal Andes (at. ca. 28°S) during middle Permian–Triassic subduction-related extensional setting with increasing thinning of continental crust towards the late Triassic. West to east geochemical zoning indicates decreasing crustal thickness eastwards, in the same manner with increasing magma differentiation (higher overall enrichment in trace elements in the east) and A-type magmatism. Towards the west, the closer to the shallower part of the subducting slab is evidenced in stronger negative Nb–Ta anomalies, I-type magmas and trace element patterns indicating thicker crust. Middle Permian–Triassic magmas are due to anatexis of mafic to intermediate lower continental crust and subduction-derived. I-, S-, and A-type magmas are all from middle Permian–Triassic (lilac coloured).

These geodynamic conditions are in agreement with the model proposed by Del Rey et al. (2016), where an extensional setting occurred inboard from a subduction zone by slab rollback. The foundering slab creates a gravitational potential well into which the orogen (the one associated with the San Rafael event) collapses (Lister and Forster, 2009), creating the extensional conditions. During the ongoing hinge retreat, strong crustal thinning causes decompression of the asthenosphere with subsequent underplating basalts accumulation and final anatexis of lower continental crust (granite formation) (Collins, 2002), at the same time with melts derived from the subducted slab (Fig. 2.7).

This explains why stronger subduction-related signatures can be seen in the west at the same time of more mantle-like transitional magmatism inland. A similar setting was described for the early Carboniferous in the Eastern Sierras Pampeanas (27°30'–30°S, Alasino et al., 2012) with an evolution from A-type granitoids inland towards I-type to the west with time. The absence of early Carboniferous rocks in the Chilean territory could lead to the

interpretation of westward migration of the arc under slab rollback conditions, which ultimately conditioned the tectonic setting for the late Carboniferous onwards. The continuous extensional conditions due to slab rollback from early Carboniferous to Triassic shifted to compression only during the Gondwanide Orogeny (late Carboniferous–middle Permian, Cawood, 2005) which includes the San Rafael event (ca. 284 to 276 Ma, Llambias and Sato, 1990). Regardless of that, a coherent evolution of westward migration of the arc can be defined from early to late Carboniferous.

In relation with the isotopic and geochronologic data presented by Del Rey et al. (2016), it may be confusing that rocks younger than ca. 270 Ma are more mantle-like although their geochemical data indicate higher continental crust affinities. Considering all the presented characteristics, most middle Permian–Triassic rocks were formed due to melting of a mafic crust, more precisely, lower mafic continental crust, thus the observed $\delta^{18}O$ mantle-like signatures in zircon grains (Del Rey et al., 2016) are inherited (Clemens et al., 2011; Villaros et al., 2012; Pietranik et al., 2013) as they are a characteristic of mafic igneous rocks (Nebel et al., 2011). Because of this, anatexis and fractional crystallization are the main processes producing highly evolved granitic suits (in opposition to crustal contamination/assimilation), with only minor participation of continental crust material. Most peraluminous granitoids were originated by crustal anatexis of the lower continental crust, reaching the needed high temperatures through the mechanism of underplating. Generally, lower continental crust can be considered to be of mafic to intermediate composition (e.g., Hacker et al., 2015; Rudnick and Fountain, 1995), and various works interpret highly evolved calc-alkaline granites (such as most of late Permian–Triassic) as products of melting of biotite ± hornblende bearing intermediate compositional rocks in the mid to lower crust (e.g. Whitney, 1988). If such rocks have a metaluminuos character (as indicated in, for example, Chappell et al., 2012), they could be the required protolith for most of the weakly peraluminous I-type granites observed in the batholiths.

2.5.3 Coeval magmatism along the southwestern margin of South America (25°–37°S)

Considering previous published data from Chile and Argentina (Fig. 2.8), a comparison has been made with that and the model proposed here. Hence, the ca. 270 Ma boundary has been used to separate units according to the hypothesis.

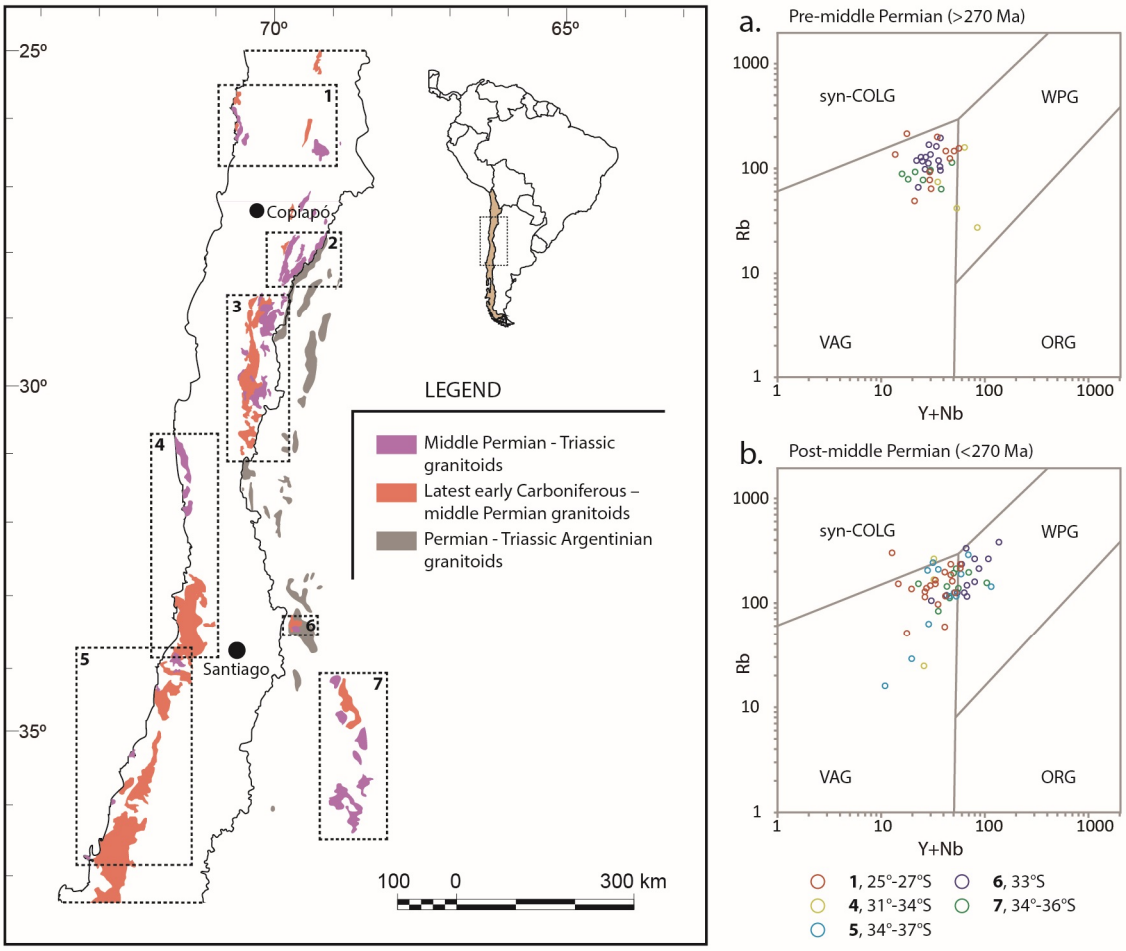

Fig. 2.8 Geographical distribution of the late Paleozoic–Triassic igneous rocks from the Chilean–Argentinian border (from ca. 25°S to 37°S). Areas are the following studies: 1, Brown (1991); 2, this work (Fig. 2.6b); 3, Mpodozis and Kay (1992); 4, Parada et al. (1999); 5, Vásquez et al. (2011); 6, Gregori and Benedini (2013); and 7, Kleiman and Japas (2009). Units are separated according to the 270 Ma limit defined by Del Rey et al. (2016) (latest early Carboniferous–middle Permian and middle Permian–Triassic) and then plotted into the Y+Nb vs. Rb discrimination diagram by Pearce et al. (1984) (a and b plots). Units from this work are plotted in Fig. 2.6b. Mpodozis and Kay (1992) samples are not in the diagram because the lacked Y and Nb, but they are considered the southern prolongation of Montosa–El Potro Batholith. a. Pre–middle Permian units plot almost exclusively in the VAG field, which together with the published studies, indicate subduction related magmatism in a typical arc setting. b. Post–middle Permian units show transitional features from VAG towards WPG, correspondingly with the middle Permian–Triassic units herewith studied. In the same manner, some units are predominantly VAG (1 and 4 in the map), while others show intermediate features between VAG and WPG (5, 6 and 7), which may be due to its relative paleogeographical position in the subduction-related slab rollback extensional setting as seen in Fig. 2.7.

Pre–middle Permian

Older than ca. 270 Ma units (and younger than Lower Pennsylvanian) correspond to the following: in Chile, La Estancilla pluton (ca. 286 Ma, Del Rey et al. (2016)); Guanta (ca. 310-297 Ma, Mpodozis and Kay (1992)), Santo Domingo Complex (308 Ma, Parada et al. (1999)) and Cifuncho, Pan de Azúcar and Doña Inés Chica (ca. 292-270 Ma, Brown (1991)). In Argentina, Cerro

Punta Blanca (ca. 276 Ma, Gregori and Benedini (2013)) and Lower Choiyoi (ca. 281 Ma, Kleiman and Japas (2009)).

Overall these units are predominantly metaluminous, calc-alkaline to high-K calc-alkaline and mostly I- and S-types. According to the granite tectonic discrimination diagrams (Pearce et al., 1984) (Fig. 2.8a), all units fall within the VAG field. In particular, Guanta is interpreted as subduction-related granitoids (Mpodozis and Kay, 1992), Santo Domingo Complex as orogenic magmatism (Parada et al., 1999); Cifuncho, Pan de Azúcar and Doña Inés Chica as subduction-related magmatism (Brown, 1991); Cerro Punta Blanca as subduction-related (Gregori and Benedini, 2013) and Lower Choiyoi as arc related magmatism (Kleiman and Japas, 2009). At the same time, almost all units are predominantly granodiorites with minor tonalites and granites (except the volcano-sedimentary Lower Choiyoi).

The similarities among all these units are also in agreement with the model proposed by Del Rey et al. (2016), reinforcing the idea that early/late Carboniferous–middle Permian magmatism is subduction-related and formed a latitudinal continuous belt between at least 21°–40°S (considering also coeval units between 26° and 21°S as in Maksaev et al., (2014) and the southernmost limit of the Coastal Batholith, Deckart et al., (2014)).

Post–middle Permian

In Chile, middle Permian–Triassic units are the following: El Colorado, Chollay, El León, Montosa (this work); the Ingaguás Complex (Mpodozis and Kay, 1992); Limarí Complex (203 Ma, Parada et al. (1999); Triassic granitoids of the Coastal Cordillera between 34° and 37°S (ca. 224–197 Ma, Vásquez et al. (2011)); and Chañaral, Cerros del Vetado, Corral del Alambre, Pedernales and La Ola complexes (ca. 257–212 Ma, Brown (1991)). In Argentina, Cerro Bayo and Cerro Punta Negra (ca. 262 and 234 Ma respectively, Gregori and Benedini (2013)), and Upper Choiyoi (intrusive units 265 Ma, Kleiman and Japas (2009)).

Overall, these suits are predominantly weakly peraluminous, calc-alkaline to high-K calc-alkaline and I- and S-type with clear transitional signatures to A-type. The granite discrimination diagram (Pearce et al., 1984) (Fig. 2.8b) shows an evident mix between VAG and WPG affinities, with some units being mostly WPG (e.g. El Colorado, Cerro Punta Negra). One unit in specific, Cerro Bayo (262 Ma, Gregori and Benedini, 2013) shows clear transitional signatures between VAG and WPG.

As with the units described here, middle Permian–Triassic magmatism presents higher amounts of variability, reflected in the contemporaneity of I, S- and A-type granotoids emplaced in both VAG and WPG scenarios. The Ingaguás Complex is interpreted as rocks formed due to anatexis of a thinner

crust (Mpodozis and Kay, 1992); the Limarí Complex as crustal-derived (Parada et al., 1999); the Triassic granitoids of the Coastal Cordillera as plutons emplaced in a extensional subduction-related setting with mantle and crustal sources (Vásquez et al., 2011); Chañaral, Cerros del Vetado, Corral del Alambre, Pedernales and La Ola complexes as subduction-related magmatism (Brown, 1991); Cerro Bayo and Cerro Punta Negra as the result of a transition between subduction-related and intraplate extension-related magmatism (Gregori and Benedini, 2013); and Upper Choiyoi as transitional to intraplate post-orogenic extension-related magmatism (Kleiman and Japas, 2009). In addition, all the available data of A-type rocks from this period (i.e., Upper Choiyoi (Kleiman and Japas, 2009) and Chilean Triassic granitoids (Vásquez and Franz, 2008; Vásquez et al., 2011)) can be described as aluminous A-type, in the same way as the A-type granites herewith studied, thus allowing to infer the same tectonic implications for such rocks in the Chilean Frontal Andes (28°–28°30'S), in the Coastal Cordillera (34°–37°S) and in the Choiyoi province (34°–36°S, Argentina).

Again, the described characteristics are coherent with the proposed model in which middle/late Permian–Triassic magmatism occurred under extensional conditions with important contributions of crustal melts in a subduction setting. Observed bimodal magmatism in this period (e.g. Kleiman and Japas, 2009; Maksaev et al., 2014; Vásquez et al., 2011) is also coherent with strong rollback extensional conditions, and explains the presence of mafic mantle-derived units (e.g., Triassic gabbroic stocks of the Cobquecura Pluton, ca. 36°S; Vásquez et al. (2011)). Differently from the pre–middle Permian period, this magmatism occurred eastwards, linked to the development of several NW–SE to NNW–SSE basins (e.g., Charrier et al., 2014).

Analogously to the latest early Carboniferous–middle Permian, these units formed a latitudinal belt that was progressively displaced eastwards south of 31°S, possibly due to slab shallowing and final flat slab subduction at ca. 36°S (Kleiman and Japas, 2009; Del Rey et al., 2016). This process not only displaced late Permian–Triassic magmatism but also the previous subduction-related plutonism further inland (Del Rey et al., 2016), evidenced by, for example, Cerro Bayo and Lower Choiyoi.

2.5.4 Tectonic model: how Pangea supercontinent played a key role in the changes of magmatism

The Carboniferous–Triassic magmatism along the southwestern margin of South America (21°–40°S) evidences changes in the tectonic conditions at ca. 270 Ma (Del Rey et al., 2016) the most important one corresponding to the shift from normal to thickened crust during latest early Carboniferous–middle Permian to thinned continental crust with increasing and more extensive extensional conditions towards late Triassic/earliest Jurassic.

Along this entire period, subduction-related signatures can be seen in almost all the samples (such as Nb–Ta troughs and positive Pb anomaly in, for example, Upper Choiyoi; and Nb–Ta troughs in Cerro Bayo), evidencing that subduction was a continuous process from at least latest early Carboniferous to latest Triassic and continued during Jurassic, in opposition to the postulated cessation of subduction from late Permian to the early Jurassic (e.g., Charrier, 1979; Charrier et al., 2014; Kleiman and Japas, 2009; Mpodozis and Kay, 1992). In addition, Willner et al. (2005) has shown that detectable accretion activity as a result of long-term basal underplating in the accretionary prism in central Chile lasted for 100 Myr during the interval 320–224 Ma, hence continuous subduction during that period of time, in agreement with the model herewith presented. After this time the late Palaeozoic accretion system remained inactive despite continuing subduction at the convergent margin (Willner et al., 2005). This model also explains why VAG signatures are dominant during the entire period of time

Considering all the gathered geochemical and isotope data, the general tectonic evolution can be described as follows: latest early Carboniferous–middle Permian subduction-related magmatism was emplaced in a normal to thickened continental crust and acquired the input of continental-like material. Continued middle Permian–Triassic subduction-related magmatism was emplaced in a progressively thinned crust as consequence of unusually enforced extensional conditions that can be attributed to a hypothetical slab rollback setting. This setting allowed the formation of magmatism with within plate affinities in a possible backarc region at the same time as arc magmas being emplaced due to the typical subduction mechanism (Fig. 2.7). The same significant change in the igneous activity from volcanic arc to within plate magmatism has been described for the San Rafael Block in Argentina from ca. 281 Ma to 251 Ma (Rocha-Campos et al., 2011).

South of 31°S the absence of Permian magmatism in Chile (but present in Argentina) can be explained by a progressive slab shallowing that displaced magmatism and slab rollback extension eastwards (Del Rey et al., 2016). The same magmatic shift can be seen in the Argentinian Frontal Andes (Cordón del Portillo, ca. 33°–34°S, Gregori and Benedini (2013)) and the San Rafael Massif (34°–36°S, Kleiman and Japas (2009)). Regarding slab shallowing, a flat slab segment was developed (at least at 31°–32°S) during most of the early Permian (ca. 300–290 Ma, García-Sansegundo et al. (2014)). This reinforces the idea that in Chile, a flat o very shallow segment from 31° to 40°S hindered magmatism during early Permian (Del Rey et al., 2016). Furthermore, the possible subduction of an ocean ridge (or plume-influenced ridge) between 34°–39°S (Hyppolito et al., 2014) could explain the final complete flat slab at ca. 36°–37°S (proposed by Kleiman and Japas, 2009). In addition, the less voluminous Chilean Triassic magmatism between 34° and 37°S (compared to middle Permian–Triassic magmatism in the Chilean Frontal Andes) has also been interpreted as subduction-related magmatism emplaced in a extensional

setting (Vásquez et al., 2011), likewise the entire middle Permian–Triassic magmatism herewith described. This also points to the fact that middle Permian–early Triassic rollback extension occurred mostly inland (in Argentinian territory) and increased until it reached Chilean territory towards the end of Triassic, probably in association with a progressively steeper slab, which allowed the emplacement of the late Triassic extension-related units in the south of Chile (e.g., Vásquez et al. 2011). Progressive steepening of the slab towards the end of Triassic along the entire margin (21°–40°S) also helps to explains the presence of early-to-late Jurassic magmatism in the Chilean Coastal Range (Charrier et al., 2014), thus the westward jump of the plutonism from the Frontal Andes.

The geochemical, isotopic and geochronological characteristics of all the units allow to identify one continued late Paleozoic–Triassic magmatic belt from at least 21°S to 40°S. South of 31°S, the Coastal Batholith west displacement regarding the Chilean Frontal Andes, as late Paleozoic–Triassic plutonic outcrops occur in both, the Frontal Andes and the costal range north of 31°S, have been attributed to Mesozoic and Cenozoic extension (e.g. Brown, 1991; Pankhurst et al., 1988; Parada et al., 2007). However and in contrast, recent work (Muñoz et al., 2015) using inherited zircon crystals found in Neogene–Quaternary igneous rocks (at ca. 34 °S, Frontal Andes), suggests the existence of two parallel but separated batholith swaths of late Paleozoic age north and south of 33°S. The two oldest inherited grains of ca. 305 Ma are used to imply the existence of a basement of that age beneath the surface. Nevertheless, it could be argued that those ages do not represent crystallization ages and they could be part of the zircon grains of rocks crystallized ca. 295 Ma (within the interval of the Frontal Cordillera as a whole; Sato et al. (2015) and references therein); or they could be detrital zircon grains that were incorporated during the ascend of the Neogene–Quaternary magmas. Their isotopic εHf_i and $\delta^{18}O$ signatures are similar to the pre–middle Permian group defined by this work and Del Rey et al. (2016) and their geographical location allows inferring provenance from the Frontal Composite Batholiths in Argentina, if ca. 295 Ma is assumed as crystallization age (Cordón del Portillo, Gregori and Benedini, 2013), in agreement with the herewith proposed model. Moreover, in Argentina, Sato et al. (2015) interpreted the presence of detrital zircon grains of ca. 297 Ma in the San Rafael basin (around 34°S) as probably from the Frontal Cordillera region. In addition, considering that ca. 305 Ma is very well represented along the Coastal Cordillera, it is also likely that the oldest zircon grains found by Muñoz et al. (2015) are from that source.

Post–middle Permian–Triassic extensional-related magmatism occurred eastwards, linked to several NW–SE to NNW–SSE basin development with fast subsidence (Charrier, 1979; Franzese and Spalletti, 2001). Those orientations were at least partly inherited from late Paleozoic structures, particularly the hanging walls of the sutures of the Paleozoic accreted terranes (Mpodozis and

Ramos, 2008; Ramos, 2009), the last one accreted being Chilenia in Devonian times (e.g., Álvarez et al., 2011; Charrier et al., 2014).

Previous explanations given to the extensional conditions are: rifting related to the first stage of Pangea break-up (Charrier, 1979), hypothetical dextral strike-slip movements (Rapela and Pankhurst, 1992), orogenic collapse and slab break-off after the accretion of an hypothetic terrane (north 33°S, Mpodozis and Kay, 1992), cessation of subduction together with dextral strike-slip movements parallel to the continental margin (Franzese and Spalletti, 2001), and continental dextral rotations with subsequent slab break-off and orogenic collapse (south 31°S, Kleiman and Japas, 2009). Various works (e.g., Charrier et al., 2014, 2007; Gana, 1991) indicate cessation of subduction between latest Permian and earliest Jurassic time. Yet all these ideas are uncertain determining the area of extension, they lack of a comprehensive model for coeval extensional-related units along the margin (e.g., south 31°S, Kleiman and Japas, 2009), and some are only hypothetical (e.g., 'X terrane', Mpodozis and Kay, 1992).

Considering the dimension of the middle Permian–Triassic magmatic belt and similar extensional characteristics (transitional to aluminous A-type granites, WPG affinities, subduction-related signatures) among all the described units, the previous, traditional justifications seem unlikely or at least fail in giving a regional scale explanation for the entire magmatism.

The hypothesis presented here and supporting the previous regional model (Del Rey et al., 2016) explains the vast magmatism as a whole. Extension in a subduction setting due to slab rollback and steepening (also proposed locally for the south 31°S Chilean Triassic granitoids by Vásquez et al. (2011)) explains the observed continuity of subduction during the Triassic and the backarc location of the transitional to within plate magmatism. Also, in highly extended regions widespread occurrence of high temperature metamorphism, migmatisation and anatexis is expected (Lister and Forster, 2009) hence explaining the origin of most of the aluminous A-type granites. In a more global scale, during middle Permian–Triassic times Pangea supercontinent was fully assembled and in a possible static reference mode (Vilas and Valencio, 1978), greatly decreasing subduction velocities thus enhancing rollback extension in the backarc region (Schellart, 2005). It can be argued that units possess some distinct features when compared to each other, however those variations can be explained on a more local scale. The major geodynamic process controlling magmatism along the southwestern margin of South America (previously Gondwana/Pangea) is and has been the subduction of the paleo-Pacific oceanic plate beneath the paleo-South American plate. In other words, the Andean subduction has been a continuous process since early Carboniferous onwards, in opposition to arrested subduction during Triassic (e.g., Charrier et al., 2014; Mpodozis and Kay, 1992, 1990; among others). The only mechanism differing the Pre–Andean

(Lopingian (late Permian)–late Lower Jurassic) from the Andean subduction (late Lower Jurassic–present, Charrier et al., 2014) are the convergent rates or subduction velocities, which triggered all herein presented structural and magmatic changes. The regional convergent continental active margin conditions are the key factor controlling the magmatism.

2.6 Conclusions

Whole-rock geochemical composition, together with geochronological data show that the Chilean Frontal Andes batholiths (28°–28°30'S) crystallized from a calc-alkaline, I-, S-, and transitional to aluminous A-type magmas during most of middle Permian–Triassic. Isotopic data evidences a lower continental crust source with minor degrees of crustal contribution and important partial melting-fractionation. A comparison with other coeval plutonic units allows the following general regional conclusions:

i. Latest early Carboniferous–middle Permian magmatism originated in a subduction-related orogenic setting with normal to thickened crust. I- and S-type calc-alkaline dioritic, tonalitic and granodioritic magmas were emplaced forming a continuous north to south belt from at least 21°S to 40°S. Isotopic data demonstrate crustal contributions. This magmatism occurred during the Gondwanide Orogeny.

ii. Middle Permian–Triassic magmatism occurred in a subduction-related slab rollback extensional setting with increasing thinning of continental crust towards Triassic. Most magmas originated due to melting of lower continental crust with variable degrees of crustal contribution but undeniable minor than previous units according to the isotopic data (mainly zircon $\delta^{18}O$ isotopes, based on Del Rey et al. (2016)). Magmatism and extension occurred inland, in the backarc region relative to the latest early Carboniferous–middle Permian arc. Vast extensional conditions were triggered by slab rollback under very low subduction velocities throughout Pangea as a supercontinent.

iii. West-to-east geochemical zonation (observed in the Chilean Frontal Andes) shows coeval I-type magmatism to the west with increasing transitional to aluminous A-type igneous activity and crustal thinning to the east. These characteristics depict intense extensional conditions in the backarc region under a subduction-related tectonic setting.

iv. Subduction of the paleo-Pacific oceanic plate beneath paleo-South America has been a continuous process since early Carboniferous and throughout Triassic–Jurassic times until present day. In other words, there is no period of time without subduction between the end of Gondwana and the beginning of the Andean subduction cycle. Therefore,

the Andean subduction has its roots linked to the Gondwanide Orogeny as part of the Terra Australis Orogen (Cawood, 2005). The transitory Pangea stage of continental tectonics (Stampfli et al., 2013) was the key to the magmatic changes observed during middle Permian–Triassic times along the southwestern margin of paleo-South America (i.e., unusually low subducting velocities).

In general, despite minor differences among intrusive units ranging from 21° to 40°S during Carboniferous–Triassic, the hypothesis proposed by Del Rey et al. (2016) can be further supported by the herewith presented geochemical data, providing a simple yet complete explanation for the subduction-related magmatism occurring along the Chilean–Argentinian border.

Acknowledgements

We thank J. Vargas and R. Valles (Universidad de Chile) for the zircon and magnetite separation, O. Pérez Arvizu for the preparation and measurement of Rb–Sr and Sm–Nd samples (LEI, UNAM) and J. Kirk for Os isotope analyse of magnetite (University of Arizona). This research was funded by the Servicio Nacional de Geología y Minería (SERNAGEOMIN) project Plan Nacional de Geología (Geological Map 'Iglesia Colorada – Cerro El Potro'), private research resources supplied by K. Deckart and the Masters fellowship of the Comisión Nacional de Investigación Científica y Tecnológica – CONICYT (grant no. 221320626). This work is part of the M.Sc. thesis of the principal author.

Supplementary data

Full LA-ICPMS U-Pb geochronological, major and trace element data and summarized petrographic descriptions are given in Appendix B.

References

Alasino, P.H., Dahlquist, J.A., Pankhurst, R.J., Galindo, C., Casquet, C., Rapela, C.W., Larrovere, M.A., Fanning, C.M., 2012. Early Carboniferous sub- to mid-alkaline magmatism in the Eastern Sierras Pampeanas, NW Argentina: A record of crustal growth by the incorporation of mantle-derived material in an extensional setting. Gondwana Res. 22, 992–1008. doi:10.1016/j.gr.2011.12.011

Álvarez, J., Mpodozis, C., Arriagada, C., Astini, R., Morata, D., Salazar, E., Valencia, V.A., Vervoort, J.D., 2011. Detrital zircons from late Paleozoic accretionary complexes in north-central Chile (28°-32°S): Possible

fingerprints of the Chilenia terrane. J. South Am. Earth Sci. 32, 460–476. doi:10.1016/j.jsames.2011.06.002
Baier, J., Audétat, A., Keppler, H., 2008. The origin of the negative niobium tantalum anomaly in subduction zone magmas. Earth Planet. Sci. Lett. 267, 290–300.
Blusztajn, J., Hart, S.R., Ravizza, G., Dick, H.J.B., 2000. Platinum-group elements and Os isotopic characteristics of the lower oceanic crust. Chem. Geol. 168, 113–122.
Borg, L.E., Brandon, A.D., Clynne, M.A., Walker, R.J., 2000. Re-Os isotopic systematics of primitive lavas from the Lassen region of the Cascade arc, California. Earth Planet. Sci. Lett. 177, 301–317. doi:10.1016/S0012-821X(00)00051-0
Brown, M., 1991. Comparative geochemical interpretation of Permian-Triassic plutonic complexes of the Coastal Range and Altiplano (25°30' to 26°30'S), northern Chile. Geol. Soc. Am. 265.
Cawood, P.A., 2005. Terra Australis Orogen: Rodinia breakup and development of the Pacific and Iapetus margins of Gondwana during the Neoproterozoic and Paleozoic. Earth-Science Rev. 69, 249–279. doi:10.1016/j.earscirev.2004.09.001
Chappell, B.W., Bryant, C.J., Wyborn, D., 2012. Peraluminous I-type granites. Lithos 153, 142–153. doi:10.1016/j.lithos.2012.07.008
Chappell, B.W., Stephens, W.E., 1988. Origin of infracrustal (I-type) granite magmas. Trans. R. Soc. Edinb. Earth Sci. 79, 71–86. doi:10.1017/S0263593300014139
Chappell, B.W., White, A.J.R., 2001. Two contrasting granite types: 25 years later. Aust. J. Earth Sci. 48, 489–499.
Charrier, R., 1979. El Triásico en Chile y regiones adyacentes de Argentina: Una reconstrucción paleogeográfica y paleoclimática. Comunicaciones 26, 1–37.
Charrier, R., Pinto, L., Rodríguez, M.P., 2007. Tectonostratigraphic evolution of the Andean orogen in Chile, in: Moreno, T., Gibson, W. (Eds.), The Geology of Chile. The Geological Society, London, pp. 21–114.
Charrier, R., Ramos, V.A., Tapia, F., Sagripanti, L., 2014. Tectono-stratigraphic evolution of the Andean Orogen between 31° and 37° S (Chile and Western Argentina). Geol. Soc. London, Spec. Publ. 399, 13–61. doi:10.1144/SP399.20
Chew, D.M., Schaltegger, U., Kosler, J., Whitehouse, M.J., Gutjahr, M., Spikings, R.A., Miskovic, A., 2007. U-Pb geochronologic evidence for the evolution of the Gondwanan margin of the north-central Andes. Bull. Geol. Soc. Am. 119, 697–711. doi:10.1130/B26080.1
Clemens, J.D., Stevens, G., Farina, F., 2011. The enigmatic sources of I-type granites: The peritectic connexion. Lithos 126, 174–181. doi:10.1016/j.lithos.2011.07.004
Collins, W.J., 2002. Hot orogens, tectonic switching, and creation of continental crust. Geology 30, 535–538. doi:10.1130/0091-7613(2002)030<0535:HOTSAC>2.0.CO;2

Creaser, R.A., Papanastassiou, D.A., Wasserburg, G.J., 1991. Negative Thermal Ion Mass-Spectrometry of Osmium, Rhenium, and Iridium. Geochim. Cosmochim. Acta 55, 397–401. doi:10.1016/0016-7037(91)90427-7

Deckart, K., Godoy, E., Bertens, A., Jerez, D., Saeed, A., 2010. Barren Miocene granitoids in the Central Andean metallogenic belt , Chile : Geochemistry and Nd-Hf and U-Pb isotope systematics 37, 1–31.

Deckart, K., Hervé, F., Fanning, M., Ramírez, V., Calderón, M., Godoy, 2014. U-Pb Geochronology and Hf-O Isotopes of zircons from the Pennsylvanian Coastal Batholith, South-Central Chile. Andean Geol. 41, 49–82. doi:10.5027/andgeoV41n1-a03

Del Rey, A., Deckart, K., Arriagada, C., Martínez, F., 2016. Resolving the paradigm of the late Paleozoic–Triassic Chilean magmatism: Isotopic approach. Gondwana Res. doi:10.1016/j.gr.2016.06.008

Eby, G.N., 1992. Chemical subdivision of the A-type granitoids:Petrogenetic and tectonic implications. Geology 20, 641–644. doi:10.1130/0091-7613(1992)020<0641:CSOTAT>2.3.CO;2

Franzese, J.R., Spalletti, L. a., 2001. Late triassic- Early jurassic continental extension in SouthWestern Gondwana: Tectonic segmentation and pre-break-up rifting. J. South Am. Earth Sci. 14, 257–270. doi:10.1016/S0895-9811(01)00029-3

Gana, P., 1991. Magmatismo bimodal del Triasico Superior-Jurasico Inferior, en la Cordillera de la Costa, Provincias de Elqui y Llmari, Chile. Rev. Geológica Chile 18, 55–67.

García-Sansegundo, J., Farias, P., Heredia, N., Gallastegui, G., Charrier, R., Rubio-Ordóñez, A., Cuesta, A., 2014. Structure of the Andean Palaeozoic basement in the Chilean coast at 31°30’ S: Geodynamic evolution of a subduction margin. J. Iber. Geol. 40, 293–308. doi:10.5209/rev_JIGE.2014.v40.n2.45300

Gómez-Tuena, A., Díaz-Bravo, B., Vásquez-Duarte, A., Pérez-Arvizu, O., Mori, L., 2013. Andesite petrogenesis by slab-derived plume pollution of a continental rift. in Gómez-Tuena, A., Straub, S.M and Zellmer, G.F. (editors). Orogenic Andesites and Crustal Growth. Geological Society, London, Special Publications. En prensa. Geol. Soc. London 385.

Gómez-Tuena, A., Lagatta, A., Langmuir, C.H., Goldstein, S.L., Ortega-Gutiérrez, F., Carrasco-Núñez, G., 2003. Temporal control of subduction magmatism in the Eastern Trans-Mexican Volcanic Belt: mantle sources, slab contributions and crustal contamination. Geochemistry, Geophys. Geosystems 4.

Gómez-Tuena, A., Mori, L., Goldstein, S.L., Pérez-Arvizu, O., 2011. Magmatic diversity of western Mexico as a function of metamorphic transformations in the subducted oceanic plate. Geochim. Cosmochim. Acta 75, 213–241.

Gregori, D., Benedini, L., 2013. The Cordon del Portillo Permian magmatism, Mendoza, Argentina, plutonic and volcanic sequences at the western margin of Gondwana. J. South Am. Earth Sci. 42, 61–73. doi:10.1016/j.jsames.2012.07.010

Hacker, B.R., Kelemen, P.B., Behn, M.D., 2015. Continental Lower Crust. Annu. Rev. Earth Planet. Sci. 43, 167–205. doi:10.1146/annurev-earth-050212-124117

Hart, G.L., Johnson, C.M., Shirey, S.B., Clynne, M.A., 2002. Osmium isotope constraints on lower crustal recycling and pluton preservation at Lassen Volcanic Center, CA. Earth Planet. Sci. Lett. 199, 269–285. doi:10.1016/S0012-821X(02)00564-2

Hyppolito, T., Juliani, C., García-Casco, A., Meira, V.T., Bustamante, A., Hervé, F., 2014. The nature of the Palaeozoic oceanic basin at the southwestern margin of Gondwana and implications for the origin of the Chilenia terrane (Pichilemu region, central Chile). Int. Geol. Rev. 56, 1097–1121.

Jacobsen, S.B., Wasserburg, G.J., 1980. Sm-Nd isotopic evolution of chondrites. Earth Planet. Sci. Lett. 50, 139–155.

Johnson, C.M., Shirey, S.B., Barovich, K.M., 1996. New approaches to crustal evolution studies and the origin of granitic rocks: what can the Lu-Hf and Re-Os isotope systems tell us? Trans. R. Soc. Edinb. Earth Sci. 87, 339–352.

Kay, S.M., Ramos, V.A., Mpodozis, C., Sruoga, P., 1989. Late Paleozoic to Jurassic silicic magmatism at the Gondwana margin : Analogy to the Middle Proterozoic in North America? Geol. Soc. Am. 17, 324–328. doi:10.1130/0091-7613(1989)017<0324

King, P.L., White, A.J.R., Chappell, B.W., Allen, C.M., 1997. Characterization and Origin of Aluminous A-type Granites from the Lachlan Fold Belt , Southeastern Australia 38, 371–391.

Kleiman, L.E., Japas, M.S., 2009. The Choiyoi volcanic province at 34°S-36°S (San Rafael, Mendoza, Argentina): Implications for the Late Palaeozoic evolution of the southwestern margin of Gondwana. Tectonophysics 473, 283–299. doi:10.1016/j.tecto.2009.02.046

Lister, G., Forster, M., 2009. Tectonic mode switches and the nature of orogenesis. Lithos 113, 274–291. doi:10.1016/j.lithos.2008.10.024

Llambias, E.J., Sato, A.M., 1990. El Batolito de Colangüil (29-31°S) Cordillera Frontal de Argentina: estructura y marco tectónico. Rev. Geol. Chile 17, 89–108.

Loiselle, M.C., Wones, D.R., 1979. Characteristics and origin of anorogenic granites. Geol. Soc. Am. Abstr. 11, 468.

Maksaev, V., Munizaga, F., Tassinari, C., 2014. Timing of the magmatism of the paleo-Pacific border of Gondwana: U-Pb geochronology of Late Paleozoic to Early Mesozoic igneous rocks of the north Chilean Andes between 20° and 31°S. Andean Geol. 41, 447–506. doi:10.5027/andgeoV41n3-a01

Martínez, F., Arriagada, C., Peña, M., Deckart, K., Charrier, R., 2016. Tectonic styles and crustal shortening of the Central Andes “Pampean” flat-slab segment in northern Chile (27-29°S). Tectonophysics.

Martínez, F., Peña, M., Arriagada, C., 2015. Geología de las áreas Iglesia Colorada - Cerro del Petro y Cerro Mondaquita, Región de Atacama. Cart.

Geológica Chile Serie Geol, 179–180.
McDonough, W.F., Sun, S.S., 1995. Composition of the Earth. Chem. Geol. 120, 223–253.
Miskovic, A., Schaltegger, U., 2009. Crustal growth along a non-collisional cratonic margin: A Lu-Hf isotopic survey of the Eastern Cordilleran granitoids of Peru. Earth Planet. Sci. Lett. 279, 303–315. doi:10.1016/j.epsl.2009.01.002
Mpodozis, C., Cornejo, P., 1988. Hoja Pisco Elqui, IV Región de Coquimbo. Cart. Geológica Chile 68, 164.
Mpodozis, C., Kay, S.M., 1990. Provincias magmaticas acidas y evolucion tectonica de Gondwana andes chilenos (28-31°S). Rev. Geol. Chile 17, 153–180. doi:10.5027/andgeoV17n2-a03
Mpodozis, C., Kay, S.M., 1992. Late Paleozoic to Triassic evolution of the Gondwana margin: evidence from Chilean Frontal cordilleran batholiths (28°S to 31°S). Geol. Soc. Am. Bull. 104, 999–1014. doi:10.1130/0016-7606(1992)104<0999:LPTTEO>2.3.CO;2
Mpodozis, C., Marinovic, N., Smoje, I., Cuitiño, L., 1993. Estudio Geológico-Estructural de la Cordillera de Domeyko entre Sierra Limón Verde y Sierra Mari- posas, Región de Antofagasta. Serv. Nac. Geol. y Minería, Inf. Regist. IR-93-04 282.
Mpodozis, C., Ramos, V.A., 2008. Tectónica jurásica en Argentina y Chile: extensión, subducción oblicua, rifting, deriva y colisiones? Rev. la Asoc. Geológica Argentina 63, 481–497.
Munizaga, F., Maksaev, V., Fanning, C.M., Giglio, S., Yaxley, G., Tassinari, C.C.G., 2008. Late Paleozoic-Early Triassic magmatism on the western margin of Gondwana: Collahuasi area, Northern Chile. Gondwana Res. 13, 407–427. doi:10.1016/j.gr.2007.12.005
Muñoz, M., Charrier, R., Sigoña, P., Fanning, C.M., 2015. The Paleozoic Basement beneath the Mesozoic Cover of the Andean Principal Cordillera in Central Chile (34°00'-34°30'S): Tracks from Inherited Zircon Crystals. IV Congr. Geológico Chil. "Geología para el siglo XXI."
Nägler, T.F., Frei, R., 1997. Plug in osmium distillation. Schweizer Mineral. und Petrogr. Mitteilungen 77, 123–127.
Nasi, C., Moscoso, R., Maksaev, V., 1990. Hoja Guanta, Regiones de Atacama y Coquimbo. Cart. Geológica Chile 67, 140.
Nasi, C., Mpodozis, C., Cornejo, P., Moscoso, R., Maksaev, V., 1985. El Batolito Elqui-Limarí (Paleozoico Superior-Triásico): características petrográficas, geoquímicas y significado tectónico. Rev. Geológica Chile 77–111.
Nebel, O., Vroon, P.Z., van Westrenen, W., Iizuka, T., Davies, G.R., 2011. The effect of sediment recycling in subduction zones on the Hf isotope character of new arc crust, Banda arc, Indonesia. Earth Planet. Sci. Lett. 303, 240–250. doi:10.1016/j.epsl.2010.12.053
Pankhurst, R., Hole, M., Brook, M., 1988. Isotope evidence for the origin of Andean granites. Trans. R. Soc. Edinb. Earth Sci. 79, 123–133.
Pankhurst, R., Millar, I., Hervé, F., 1996. A Permo-Carboniferous U-Pb age

for part of the Guanta Unit of the Elqui-Limari Batholith at Rio del Transito, Northern Chile. Rev. Geol. Chile 23, 35–42 ST–A Permo–Carboniferous U–Pb age for par.
Parada, M.A., 1990. Granitoid plutonism in central Chile and its geodynamic implications; A review. Geol. Soc. Am. Spec. Pap. 241, 51–66.
Parada, M.A., Larrondo, P., Guiresse, C., Roperch, P., 2002. Magmatic Gradients in the Cretaceous Caleu Pluton (Central Chile): Injections of Pulses from a Stratified Magma Reservoir. Gondwana Res. 307–324. doi:10.1016/S1342-937X(05)70725-5
Parada, M.A., López-Escobar, L., Oliveros, V., Fuentes, F., Morata, D., Calderón, M., Aguirre, L., Féraud, G., Espinoza, F., Moreno, H., Figueroa, O., Muñoz Ravo, J., Troncoso Vásquez, R., Stern, C.R., 2007. Andean magmatism, in: Moreno, T., Gibson, W. (Eds.), The Geology of Chile. The Geological Society, London, pp. 115–146.
Parada, M.A., Nyström, J.O., Levi, B., 1999. Multiple sources for the Coastal Batholith of central Chile (31 – 34° S): geochemical and Sr – Nd isotopic evidence and tectonic implications. Lithos 46, 505–521. doi:10.1016/S0024-4937(98)00080-2
Parada, M. a, 1988. Pre-Andean peraluminous and metaluminous leucogranitoid suites in the High Andes of central Chile. J. South Am. Earth Sci. 1, 211–221. doi:10.1016/0895-9811(88)90039-9
Paton, C., Woodhead, J.D., Hellstrom, J.C., Hergt, J.M., Greig, A., Maas, R., 2010. Improved laser ablation U–Pb zircon geochronology through robust downhole fractionation correction. Geochemistry Geophys. Geosystems 11.
Pearce, J.A., Harris, N.B.W., Tindle, A.G., 1984. Trace Element Discrimination Diagrams for the Tectonic Interpretation of Granitic Rocks 25, 956–983.
Pearce, J.A., Peate, D.W., 1995. Tectonic implications of Volcanic Arc Magmas. Annu. Rev. Earth Planet. Sci. 23, 251–285. doi:DOI: 10.1146/annurev.ea.23.050195.001343
Peccerillo, A., Taylor, S.R., 1976. Geochemistry of Eocene Calc-Alkaline Volcanic Rocks from the Kastamonu Area, Northern Turkey. Contrib. to Mineral. Petrol. 81, 63–81.
Petrus, J.A., Kamber, B.S., 2012. VizualAge: A Novel Approach to Laser Ablation ICP-MS U-Pb Geochronology Data Reduction. Geostand. Geoanalytical Res. 36, 247–270.
Pietranik, A., Słodczyk, E., Hawkesworth, C.J., Breitkreuz, C., Storey, C.D., Whitehouse, M., Milke, R., 2013. Heterogeneous zircon cargo in voluminous Late Paleozoic rhyolites: Hf, O isotope and Zr/Hf records of plutonic to volcanic magma evolution. J. Petrol. 54, 1483–1501. doi:10.1093/petrology/egt019
Ramos, V.A., 2009. Anatomy and global context of the Andes: Main geologic features and the Andean orogenic cycle. Geol. Soc. Am. Mem. 204, 31–65. doi:10.1130/2009.1204(02)
Rapela, C.W., Pankhurst, R.J., 1992. The granites of northern Patagonia and

the Gastre Fault System in relation to the break-up of Gondwana. Geol. Soc. London, Spec. Publ. 68, 209–220.
Rocha-Campos, A.C., Basei, M.A., Nutman, A.P., Kleiman, L.E., Varela, R., Llambias, E., Canile, F.M., da Rosa, O. de C.R., 2011. 30million years of Permian volcanism recorded in the Choiyoi igneous province (W Argentina) and their source for younger ash fall deposits in the Paraná Basin: SHRIMP U–Pb zircon geochronology evidence. Gondwana Res. 19, 509–523. doi:10.1016/j.gr.2010.07.003
Rudnick, R.L., Fountain, D.M., 1995. Nature and Composition of the Continental Crust : a Lower Crustal Perspective 267–309. doi:10.1029/95RG01302
Sato, A.M., Llambías, E.J., Basei, M.A.S., Castro, C.E., 2015. Three stages in the Late Paleozoic to Triassic magmatism of southwestern Gondwana, and the relationships with the volcanogenic events in coeval basins. J. South Am. Earth Sci. 63, 48–69. doi:10.1016/j.jsames.2015.07.005
Schellart, W.P., 2005. Influence of the subducting plate velocity on the geometry of the slab and migration of the subduction hinge. Earth Planet. Sci. Lett. 231, 197–219. doi:10.1016/j.epsl.2004.12.019
Sempere, T., Carlier, G., Soler, P., Fornari, M., Carlotto, V., Jacay, J., Arispe, O., Néraudeau, D., Cárdenas, J., Rosas, S., Jiménez, N., 2002. Late Permian-Middle Jurassic lithospheric thinning in Peru and Bolivia, and its bearing on Andean-age tectonics. Tectonophysics 345, 153–181. doi:10.1016/S0040-1951(01)00211-6
Shirey, S.B., Walker, R.J., 1995. Carius Tube Digestion for Low-Blank Rhenium-Osmium Analysis. Anal. Chem. 67, 2136–2141. doi:10.1021/ac00109a036
Smoliar, M.I., Walker, R.J., Morgan, J.W., 1996. Re–Os ages of group IIA, IIIA, IVA, and IVB iron meteorites. Science (80-.). 271, 1099–1102.
Solari, L.A., Gómez-Tuena, A., Bernal, J.P., Pérez-Arvizu, O., Tanner, M., 2010. U-Pb zircón geochronology by an integrated LAICPMS microanalytical workstation: achievements in precision and accuracy. Geostand. Geoanalytical Res. 34, 5–18.
Stampfli, G.M., Hochard, C., Vérard, C., Wilhem, C., vonRaumer, J., 2013. The formation of Pangea. Tectonophysics 593, 1–19. doi:10.1016/j.tecto.2013.02.037
Steiger, R.H., Jäger, E., 1977. Subcommission of geochronology: convention on the use of decay constants in geo- and cosmochronology. Earth Planet. Sci. Lett. 1.
Tejada, M.L.G., Suzuki, K., Hanyu, T., Mahoney, J.J., Ishikawa, a., Tatsumi, Y., Chang, Q., Nakai, S., 2013. Cryptic lower crustal signature in the source of the Ontong Java Plateau revealed by Os and Hf isotopes. Earth Planet. Sci. Lett. 377–378, 84–96. doi:10.1016/j.epsl.2013.07.022
Vásquez, P., Franz, G., 2008. The Triassic Cobquecura Pluton (Central Chile): An example of a fayalite-bearing A-type intrusive massif at a continental margin. Tectonophysics 459, 66–84. doi:10.1016/j.tecto.2007.11.067
Vásquez, P., Glodny, J., Franz, G., Frei, D., Romer, R., 2011. Early Mesozoic

Plutonism of the Cordillera de la Costa (34°–37°S), Chile: Constraints on the Onset of the Andean Orogeny. J. Geol. 119, 159–184.
Vilas, J.F., Valencio, D.A., 1978. Paleomagnetism of South American and African rocks and the age of the South Atlantic. Rev. Bras. Geociências 8, 3–10.
Villaros, A., Buick, I.S., Stevens, G., 2012. Isotopic variations in S-type granites: An inheritance from a heterogeneous source? Contrib. to Mineral. Petrol. 163, 243–257. doi:10.1007/s00410-011-0673-9
Walker, R.J., Horan, M.F., Morgan, J.W., Becker, H., Grossman, J.N., Rubin, A.E., 2002. Comparative 187Re–187Os systematics of chondrites: implications regarding early solar system processes. Geochim. Cosmochim. Acta 66, 4187–4201.
Whalen, J.B., Currie, K.L., Chappell, B.W., 1987. A-type granites: geochemical characteristics, discrimination and petrogenesis. Contrib. to Mineral. Petrol. 95, 407–419. doi:10.1007/BF00402202
Whalen, J.B., Jenner, G.A., Longstafe, Frederick, J., Robert, F., Gariepy, C., 1996. Geochemical and Isotopic (O, Nd, Pb and Sr) Constraints on A-type Granite Petrogenesis Based on the Topsails Igneous Suite, Newfoundland Appalachians. J. Petrol. 37, 1463–1489. doi:10.1093/petrology/37.6.1463
Whitney, J.A., 1988. The origin of granite: The role and source of water in the evolution of granitic magmas. Bull. Geol. Soc. Am. 100, 1886–1897. doi:10.1130/0016-7606(1988)100<1886:TOOGTR>2.3.CO;2
Willner, A.P., Thomson, S.N., Kröner, A., Wartho, J.A., Wijbrans, J.R., Hervé, F., 2005. Time markers for the evolution and exhumation history of a Late Palaeozoic paired metamorphic belt in North-Central Chile (34°-35°30′S). J. Petrol. 46, 1835–1858. doi:10.1093/petrology/egi036
Woodland, S.J., Pearson, D.G., Thirlwall, M.F., 2002. A platinum group element and Re-Os isotope investigation of siderophile element recycling in subduction zones: Comparison of Grenada, Lesser Antilles arc, and the Izu-Bonin arc. J. Petrol. 43, 171–198. doi:10.1093/petrology/43.1.171

CONCLUSIONS

The presented results allow to propose a comprehensive tectonic model for the latest early Carboniferous–Triassic magmatism, as well as its links with the Andean subduction. The broad comparison with coeval units along the Chilean–Argentinian margin reveals a common tectonic setting for most of the late Paleozoic–early Mesozoic southwestern margin of paleo-South America. The use of several isotopic systems, together with traditional geochemical analysis allows deciphering a specific tectonic model for the magmagenesis, providing a geodynamic scenario to a period of much debate of the Chilean Geology.

Chronologically, the tectonic evolution along the southwestern margin of paleo-South America can be described as follows:

Latest early Carboniferous–middle Permian (325–270 Ma)

After the accretion of Chilenia during Devonian times, the paleo-Chilean margin was completed from ca. 18°S down to ca. 40°S and followed by convergence that started in the early Carboniferous. Throughout this period, the subduction of the paleo-Pacific oceanic plate beneath the continental crust generated calc-alkaline, mostly metaluminous, I-type magmatism from at least 21°S to 40°S in a volcanic arc setting. The generated magmas acquired continental-like material and/or the influence of sediments, and they were emplaced into a normal to thickened continental crust. During this time, the San Rafael event (early–middle Permian) – a compressional episode – allows depicting an overall orogenic scenario and magmatism: the Gondwanide Orogeny, ultimately linked to the Terra Australis Orogen and the assembling of Pangea supercontinent. South of 31°S, the absence of magmatism younger than 300 Ma in Chilean territory can be explained by the progressive slab shallowing through time that eventually developed a flat slab segment (in Chile) during most of early Permian (300–290 Ma). This process not only hindered magmatism in Chile but also displaced it eastwards, to the Argentinian territory, where subduction-related I-type suits can be seen from at least 33° to 36°S.

Middle Permian–Triassic (270–200 Ma)

From 270 Ma, and after Pangea supercontinent was fully assembled, important and progressive tectonic changes conditioned magmatism along the Chilean–Argentinian border. The most striking difference is the continuous trend from higher continental-like contributions (form the previous period) towards more mantle-like signatures. In addition, this period is characterized by a broader composition of magmas, ranging from dioritic to granitic (the later predominant) with calc-alkaline to high-K calk-alkaline and mostly peraluminous characterisitics. I-, S- and A-type granitoids can be seen along

the margin and they show a mixture between volcanic arc and within plate affinities. Plutons present subduction-related signatures and evidence thinned continental crust conditions during Triassic. Geographically, these rocks exhibit a geochemical west–to–east zoning. This is, increasing I-type volcanic arc granitoids westwards and increasing A-type within plate granites eastwards (at least between 28°–28°30'S in the Chilean Frontal Andes). The described characteristics are in accord with extensional conditions in a subduction zone, caused by hypothetical slab rollback and resulting in orogenic collapse. In this scenario, intense extension occurred in the backarc region respecting the previous latest early Carboniferous–middle Permian arc, allowing the emplacement of silicic A-type magmas in the backarc at the same time with subduction-derived I-type suits to the west. Part of the magmatism (e.g. A-type units) occurred due to anatexis of a thinned lower continental crust, which melted because of accumulation of underplating basalts, at the same time with traditional subduction-related Cordilleran magmatism. With this model, there is no need for cessation of subduction or slab break-off as previous work have suggested for explaining the intense and vast extensional conditions. The key factor controlling this process falls in the subducting plate velocity, which in this period was particularly low (while Pangea was assembled) thus triggering strong extension in the continental crust.

Analogously from the previous period, south 31°S extensional-related magmatism was displaced inland (Argentina) due to slab shallowing and prevailing slab rollback. The occurrence of scarce Triassic extensional subduction-related A-type granitoids in the Chilean margin can be explained as progressive thinning of the continental crust and steepening of the slab, which eventually reached Chilean territory (advancing from Argentina) and caused the related magmatism in the same way as north 31°S.

Latest Triassic–earliest Jurassic (ca. 200 Ma)

As Pangea started its break-up, increase in the subducting plate velocity terminated the slab rollback conditions. Therefore, intense extension and related magmatism no longer occurred inland. Igneous activity was displaced westards, towards Chilean territory, in association with slab steepening, occurring primarily within the mantle wedge overlying the subducted slab. The westward movement of the magmatism respecting the Permo–Triassic units is coherent with the presence of early–to–late Jurassic magmatic arc in the Chilean coastal range, thus explaining the transition between Triassic–Jurassic igneous activity.

The described tectonic model points out the progressive evolution from an orogenic compressional setting with expansion of magmatism to later slab shallowing (with flat slab in the southern region), extension, orogenic collapse and slab steepening. This series of events shares a very similar pattern with the defined idealized tectonic evolution of the Andean Orogenic Cycle, thus

permitting the proposition of extending the beginning of this process to early Carboniferous (and not from early Jurassic as considered by previous works). The differences observed between Triassic–Jurassic magmatism do not necessarily require a complete change in the geodynamic processes. Overall scenarios could be the same, but the occurrence of an unusual yet important variation could trigger unexpected changes in the magmatism and tectonic regime, i.e., Pangea supercontinent (and its related very low subducting velocities) was the main factor controlling the magmatic changes observed during middle Permian–Triassic times along the southwestern margin of paleo-South America.

Regardless of that, a more general and conclusive statement can be suggested: subduction is, and has been an uninterrupted, continuous process since early Carboniferous times. There is no reason to consider cessation of subduction during the late Permian/Triassic and its renovation in the early Jurassic as previously thought. The proposed tectonic model provides a new hypothesis to resolve the paradigm of the late Paleozoic–Triassic magmatism in Chile and postulates a coherent argument for an uninterrupted active convergent margin along the southwestern border of South America.

BIBLIOGRAPHY

Álvarez, J., Mpodozis, C., Arriagada, C., Astini, R., Morata, D., Salazar, E., Valencia, V.A., Vervoort, J.D., 2011. Detrital zircons from late Paleozoic accretionary complexes in north-central Chile (28°-32°S): Possible fingerprints of the Chilenia terrane. J. South Am. Earth Sci. 32, 460–476. doi:10.1016/j.jsames.2011.06.002

Brown, M., 1991. Comparative geochemical interpretation of Permian-Triassic plutonic complexes of the Coastal Range and Altiplano (25°30' to 26°30'S), northern Chile. Geol. Soc. Am. 265.

Charrier, R., Pinto, L., Rodríguez, M.P., 2007. Tectonostratigraphic evolution of the Andean orogen in Chile, in: Moreno, T., Gibson, W. (Eds.), The Geology of Chile. The Geological Society, London, pp. 21–114.

Charrier, R., Ramos, V.A., Tapia, F., Sagripanti, L., 2014. Tectono-stratigraphic evolution of the Andean Orogen between 31° and 37° S (Chile and Western Argentina). Geol. Soc. London, Spec. Publ. 399, 13–61. doi:10.1144/SP399.20

Franzese, J.R., Spalletti, L. a., 2001. Late triassic- Early jurassic continental extension in SouthWestern Gondwana: Tectonic segmentation and pre-break-up rifting. J. South Am. Earth Sci. 14, 257–270. doi:10.1016/S0895-9811(01)00029-3

Gana, P., 1991. Magmatismo bimodal del Triasico Superior-Jurasico Inferior, en la Cordillera de la Costa, Provincias de Elqui y Llmari, Chile. Rev. Geológica Chile 18, 55–67.

Gregori, D., Benedini, L., 2013. The Cordon del Portillo Permian magmatism, Mendoza, Argentina, plutonic and volcanic sequences at the western margin of Gondwana. J. South Am. Earth Sci. 42, 61–73. doi:10.1016/j.jsames.2012.07.010

Hervé, F., Fanning, C.M., Calderón, M., Mpodozis, C., 2014. Early Permian to Late Triassic batholiths of the Chilean Frontal Cordillera (28°-31°S): SHRIMP U-Pb zircon ages and Lu-Hf and O isotope systematics. Lithos 184-187, 436–446. doi:10.1016/j.lithos.2013.10.018

Kato, T.T., Godoy, E., 2015. Middle to late Triassic mélange exhumation along a pre-Andean transpressional fault system : Coastal Chile (26 °-42 ° S). Int. Geol. Rev. doi:10.1080/00206814.2014.1002119

Kay, S.M., Ramos, V.A., Mpodozis, C., Sruoga, P., 1989. Late Paleozoic to Jurassic silicic magmatism at the Gondwana margin : Analogy to the Middle Proterozoic in North America? Geol. Soc. Am. 17, 324–328. doi:10.1130/0091-7613(1989)017<0324

Kleiman, L.E., Japas, M.S., 2009. The Choiyoi volcanic province at 34°S-36°S (San Rafael, Mendoza, Argentina): Implications for the Late Palaeozoic evolution of the southwestern margin of Gondwana. Tectonophysics 473, 283–299. doi:10.1016/j.tecto.2009.02.046

Llambias, E.J., Sato, A.M., 1990. El Batolito de Colangüil (29-31°S) Cordillera Frontal de Argentina: estructura y marco tectónico. Rev. Geol. Chile 17, 89–108.

Llambías, E.J., Sato, A.M., 1995. El batolito de Colangüil: transición entre orogénesis y anorogénesis. Rev. la Asoc. Geológica Argentina 50, 111–131.

Mpodozis, C., Kay, S.M., 1990. Provincias magmaticas acidas y evolucion tectonica de Gondwana andes chilenos (28-31°S). Rev. Geol. Chile 17, 153–180. doi:10.5027/andgeoV17n2-a03

Mpodozis, C., Kay, S.M., 1992. Late Paleozoic to Triassic evolution of the Gondwana margin: evidence from Chilean Frontal cordilleran batholiths (28°S to 31°S). Geol. Soc. Am. Bull. 104, 999–1014. doi:10.1130/0016-7606(1992)104<0999:LPTTEO>2.3.CO;2

Nasi, C., Mpodozis, C., Cornejo, P., Moscoso, R., Maksaev, V., 1985. El Batolito Elqui-Limarí (Paleozoico Superior-Triásico): características petrográficas, geoquímicas y significado tectónico. Rev. Geológica Chile 77–111.

Parada, M.A., Nyström, J.O., Levi, B., 1999. Multiple sources for the Coastal Batholith of central Chile (31 – 34° S): geochemical and Sr – Nd isotopic evidence and tectonic implications. Lithos 46, 505–521. doi:10.1016/S0024-4937(98)00080-2

Ramos, V.A., 1988. The tectonics of the Central Andes; 30° to 33°S latitude. Geol. Soc. Am. 31–54. doi:10.1130/SPE218-p31

Ramos, V.A., 2008. Patagonia: A Paleozoic continent adrift? J. South Am. Earth Sci. 26, 235–251. doi:10.1016/j.jsames.2008.06.002

Ramos, V.A., Jordan, T.E., Allmendinger, R.W., Mpodozis, C., Kay, S.M., Cortés, J.M., Palma, M., 1986. Paleozoic terranes of the Central Argentine-Chilean Andes. Tectonics 5, 855–880. doi:10.1029/TC005i006p00855

Vásquez, P., Franz, G., 2008. The Triassic Cobquecura Pluton (Central Chile): An example of a fayalite-bearing A-type intrusive massif at a continental margin. Tectonophysics 459, 66–84. doi:10.1016/j.tecto.2007.11.067

Vásquez, P., Glodny, J., Franz, G., Frei, D., Romer, R., 2011. Early Mesozoic Plutonism of the Cordillera de la Costa (34°–37°S), Chile: Constraints on the Onset of the Andean Orogeny. J. Geol. 119, 159–184.

APPENDIX A

Full SHRIMP U-Pb geochronological and O-Hf isotopic data

Table A.1 U–Pb SHRIMP age for zircon spots from Montosa–El Potro Batholith samples.

Spot	U (ppm)	Th (ppm)	Th/U	$^{206}Pb^*$ (ppm)	$^{204}Pb/^{206}Pb$	f_{206} (%)	Total				Radiogenic		Age (Ma)	
							$^{238}U/^{206}Pb$	±	$^{207}Pb/^{206}Pb$	±	$^{206}Pb/^{238}U$	±	$^{206}Pb/^{238}U$	±
IC-17 / La Estancilla pluton														
1.1	138	67	0.48	5.3	-	0.10	22.32	0.28	0.0527	0.0011	0.0448	0.0006	282.3	3.6
1.2	146	86	0.59	5.7	0.000432	0.27	22.10	0.28	0.0541	0.0011	0.0451	0.0006	284.6	3.5
2.1	224	98	0.44	8.7	-	0.17	22.08	0.26	0.0533	0.0009	0.0452	0.0005	285.0	3.4
3.1	150	105	0.70	5.8	-	<0.01	22.27	0.34	0.0513	0.0011	0.0449	0.0007	283.4	4.3
4.1	314	147	0.47	12.4	-	0.15	21.78	0.25	0.0533	0.0010	0.0458	0.0005	288.9	3.3
5.1	123	103	0.84	5.0	-	<0.01	20.98	0.46	0.0520	0.0011	0.0477	0.0011	300.3	6.5
6.1	190	113	0.59	7.5	-	0.01	21.87	0.26	0.0521	0.0009	0.0457	0.0006	288.2	3.5
7.1	201	133	0.66	8.0	-	0.08	21.54	0.26	0.0528	0.0009	0.0464	0.0006	292.3	3.4
8.1	240	134	0.56	9.2	-	<0.01	22.30	0.26	0.0514	0.0008	0.0449	0.0005	282.9	3.3
8.2	208	135	0.65	7.7	0.000201	0.11	23.30	0.42	0.0525	0.0009	0.0429	0.0008	270.6	4.8
9.1	594	241	0.41	23.3	-	0.07	21.93	0.24	0.0526	0.0005	0.0456	0.0005	287.2	3.1
10.1	149	91	0.61	6.0	0.000030	0.04	21.52	0.27	0.0525	0.0011	0.0464	0.0006	292.7	3.7
11.1	323	285	0.88	12.2	0.000054	0.16	22.72	0.31	0.0531	0.0007	0.0439	0.0006	277.2	3.7
12.1	189	152	0.80	7.3	-	<0.01	22.21	0.27	0.0519	0.0009	0.0450	0.0006	283.9	3.4
13.1	139	75	0.54	5.4	-	0.33	22.04	0.28	0.0546	0.0011	0.0452	0.0006	285.1	3.6
14.1	315	287	0.91	12.4	-	<0.01	21.90	0.25	0.0511	0.0008	0.0457	0.0005	288.1	3.3
15.1	299	264	0.88	11.7	0.000059	0.01	21.96	0.25	0.0521	0.0010	0.0455	0.0005	287.0	3.3
16.1	206	118	0.57	8.0	0.000143	0.07	22.02	0.27	0.0526	0.0009	0.0454	0.0006	286.2	3.4
17.1	181	102	0.57	7.1	-	0.15	21.82	0.27	0.0533	0.0010	0.0458	0.0006	288.4	3.5
18.1	277	153	0.55	10.5	0.000086	0.08	22.58	0.26	0.0525	0.0008	0.0442	0.0005	279.1	3.2
19.1	234	181	0.77	9.1	-	<0.01	22.09	0.33	0.0513	0.0012	0.0453	0.0007	285.6	4.2
20.1	183	103	0.56	7.1	-	0.02	22.14	0.34	0.0521	0.0012	0.0452	0.0007	284.8	4.3

Notes: Uncertainties given at the one σ level.
Error in Temora reference zircon calibration was 0.34% for the analytical session (not included in above errors but required when comparing data from different mounts).
f_{206}% denotes the percentage of ^{206}Pb that is common Pb.
Correction for common Pb for the U/Pb data has been made using the measured $^{238}U/^{206}Pb$ and $^{207}Pb/^{206}Pb$ ratios following Tera and Wasserburg (1972) as outlined in Williams (1998).

Table A.1 (continued)

Spot	U (ppm)	Th (ppm)	Th/U	$^{206}Pb^*$ (ppm)	$^{204}Pb/^{206}Pb$	f_{206} (%)	Total $^{238}U/^{206}Pb$	±	Total $^{207}Pb/^{206}Pb$	±	Radiogenic $^{206}Pb/^{238}U$	±	Age (Ma) $^{206}Pb/^{238}U$	±
IC-22 / Montosa														
1.1	343	206	0.60	11.8	-	0.09	24.99	0.28	0.0520	0.0007	0.0400	0.0005	252.7	2.8
2.1	60	39	0.65	2.1	0.000267	<0.01	24.88	0.38	0.0512	0.0017	0.0402	0.0006	254.0	3.9
3.1	228	148	0.65	7.9	0.000238	0.31	24.70	0.30	0.0538	0.0009	0.0404	0.0005	255.1	3.0
4.1	433	293	0.68	15.6	0.000128	<0.01	23.84	0.27	0.0516	0.0007	0.0419	0.0005	264.9	2.9
5.1	261	140	0.54	8.8	0.000146	0.20	25.45	0.30	0.0527	0.0013	0.0392	0.0005	247.9	2.9
6.1	418	253	0.60	14.6	0.000074	<0.01	24.66	0.28	0.0507	0.0009	0.0406	0.0005	256.5	2.9
6.2	143	140	0.99	4.9	0.000971	1.58	25.04	0.79	0.0638	0.0028	0.0393	0.0013	248.5	7.8
7.1	151	142	0.94	5.1	0.000423	0.15	25.22	0.34	0.0524	0.0012	0.0396	0.0005	250.3	3.4
8.1	161	116	0.72	5.7	-	0.09	24.15	0.32	0.0521	0.0011	0.0414	0.0006	261.4	3.5
9.1	361	252	0.70	12.5	0.000046	0.02	24.71	0.28	0.0515	0.0008	0.0405	0.0005	255.7	2.9
10.1	279	286	1.02	9.5	-	0.08	25.34	0.45	0.0518	0.0009	0.0394	0.0007	249.3	4.4
11.1	177	109	0.62	6.2	0.000085	0.35	24.47	0.31	0.0542	0.0017	0.0407	0.0005	257.3	3.3
12.1	296	176	0.60	10.3	-	0.05	24.73	0.29	0.0517	0.0009	0.0404	0.0005	255.5	3.0
13.1	239	167	0.70	8.3	0.000123	0.12	24.83	0.30	0.0523	0.0014	0.0402	0.0005	254.2	3.1
14.1	134	72	0.53	4.5	-	<0.01	25.55	0.35	0.0506	0.0013	0.0392	0.0005	247.7	3.3
15.1	161	128	0.79	5.6	0.000080	0.28	24.93	0.32	0.0535	0.0016	0.0400	0.0005	252.8	3.3
16.1	205	166	0.81	7.1	0.000194	0.09	24.89	0.31	0.0520	0.0010	0.0401	0.0005	253.7	3.2
17.1	218	157	0.72	7.7	0.000165	<0.01	24.16	0.30	0.0506	0.0010	0.0414	0.0005	261.7	3.2
18.1	192	137	0.71	6.8	0.000544	<0.01	24.26	0.31	0.0504	0.0011	0.0413	0.0005	260.7	3.3
19.1	213	255	1.19	7.4	0.000147	<0.01	24.86	0.31	0.0512	0.0014	0.0402	0.0005	254.3	3.2
20.1	191	91	0.48	6.6	-	0.08	24.82	0.31	0.0519	0.0017	0.0403	0.0005	254.4	3.2

Notes: Uncertainties given at the one σ level.
Error in Temora reference zircon calibration was 0.34% for the analytical session (not included in above errors but required when comparing data from different mounts).
f_{206}% denotes the percentage of ^{206}Pb that is common Pb.
Correction for common Pb for the U/Pb data has been made using the measured $^{238}U/^{206}Pb$ and $^{207}Pb/^{206}Pb$ ratios following Tera and Wasserburg (1972) as outlined in Williams (1998).

Table A.1 (continued)

Spot	U (ppm)	Th (ppm)	Th/U	$^{206}Pb^*$ (ppm)	$^{204}Pb/^{206}Pb$	f_{206} (%)	Total $^{238}U/^{206}Pb$	±	Total $^{207}Pb/^{206}Pb$	±	Radiogenic $^{206}Pb/^{238}U$	±	Age (Ma) $^{206}Pb/^{238}U$	±
IC-58 / El León														
1.1	131	124	0.95	4.4	0.000269	<0.01	25.41	0.33	0.0501	0.0012	0.0394	0.0005	249.1	3.3
2.1	150	115	0.77	5.2	0.000179	0.14	24.82	0.32	0.0524	0.0011	0.0402	0.0005	254.3	3.2
3.1	123	81	0.65	4.3	0.000251	<0.01	24.80	0.39	0.0495	0.0012	0.0404	0.0006	255.4	4.0
4.1	143	109	0.76	5.0	0.000191	<0.01	24.46	0.41	0.0513	0.0012	0.0409	0.0007	258.3	4.3
5.1	429	293	0.68	15.8	0.000129	0.05	23.36	0.26	0.0521	0.0007	0.0428	0.0005	270.1	3.0
6.1	249	181	0.73	8.7	-	<0.01	24.43	0.30	0.0505	0.0009	0.0410	0.0005	258.9	3.1
7.1	195	142	0.73	6.8	0.000186	<0.01	24.46	0.30	0.0512	0.0010	0.0409	0.0005	258.4	3.2
8.1	142	140	0.98	5.2	0.000339	0.15	23.59	0.31	0.0528	0.0012	0.0423	0.0006	267.2	3.5
9.1	167	116	0.69	5.9	0.000222	<0.01	24.50	0.32	0.0497	0.0011	0.0409	0.0005	258.4	3.3
10.1	67	55	0.82	2.3	0.000232	0.01	24.78	0.40	0.0514	0.0018	0.0404	0.0007	255.0	4.1
11.1	122	102	0.84	4.3	-	0.17	24.42	0.36	0.0527	0.0013	0.0409	0.0006	258.3	3.7
12.1	220	152	0.69	8.0	-	0.07	23.72	0.29	0.0521	0.0009	0.0421	0.0005	266.0	3.2
13.1	295	58	0.20	10.5	0.000099	0.07	24.07	0.28	0.0521	0.0008	0.0415	0.0005	262.2	3.1
13.2	658	197	0.30	30.3	-	<0.01	18.69	0.22	0.0532	0.0005	0.0535	0.0006	336.0	3.9
14.1	122	88	0.72	4.2	0.000426	<0.01	24.72	0.33	0.0506	0.0013	0.0405	0.0006	255.8	3.4
15.1	110	75	0.68	3.8	-	<0.01	24.84	0.34	0.0506	0.0014	0.0403	0.0006	254.7	3.5
16.1	287	142	0.50	10.1	0.000002	<0.01	24.49	0.29	0.0496	0.0010	0.0409	0.0005	258.6	3.0
17.1	194	159	0.82	6.8	0.000127	0.11	24.36	0.30	0.0523	0.0010	0.0410	0.0005	259.1	3.2
18.1	186	173	0.93	6.9	-	<0.01	23.14	0.29	0.0509	0.0010	0.0433	0.0005	273.0	3.4
18.2	389	244	0.63	14.2	-	0.16	23.54	0.27	0.0529	0.0007	0.0424	0.0005	267.8	3.0
19.1	166	110	0.66	5.7	0.000092	0.26	24.92	0.32	0.0534	0.0011	0.0400	0.0005	252.9	3.2
20.1	114	66	0.58	4.1	-	<0.01	23.90	0.33	0.0503	0.0013	0.0419	0.0006	264.7	3.6

Notes: Uncertainties given at the one σ level.
Error in Temora reference zircon calibration was 0.34% for the analytical session (not included in above errors but required when comparing data from different mounts).
f_{206}% denotes the percentage of ^{206}Pb that is common Pb.
Correction for common Pb for the U/Pb data has been made using the measured $^{238}U/^{206}Pb$ and $^{207}Pb/^{206}Pb$ ratios following Tera and Wasserburg (1972) as outlined in Williams (1998).

Table A.1 (continued)

Spot	U (ppm)	Th (ppm)	Th/U	$^{206}Pb^*$ (ppm)	$^{204}Pb/^{206}Pb$	f_{206} (%)	Total $^{238}U/^{206}Pb$	±	Total $^{207}Pb/^{206}Pb$	±	Radiogenic $^{206}Pb/^{238}U$	±	Age (Ma) $^{206}Pb/^{238}U$	±
IC-91 / Chollay														
1.1	171	98	0.57	5.9	0.000311	0.21	24.93	0.32	0.0530	0.0011	0.0400	0.0005	253.0	3.2
2.1	276	171	0.62	9.8	0.000007	<0.01	24.30	0.29	0.0509	0.0010	0.0412	0.0005	260.2	3.1
2.2	379	151	0.40	62.0	0.000038	0.16	5.25	0.06	0.0784	0.0005	0.1902	0.0022	1122.5	11.8
3.1	296	247	0.83	10.4	-	<0.01	24.47	0.29	0.0507	0.0008	0.0409	0.0005	258.5	3.0
4.1	185	114	0.62	6.4	-	<0.01	24.84	0.31	0.0505	0.0013	0.0403	0.0005	254.7	3.2
5.1	235	166	0.71	8.3	0.000243	<0.01	24.22	0.30	0.0508	0.0009	0.0413	0.0005	261.1	3.2
6.1	282	219	0.78	9.8	0.000093	<0.01	24.82	0.30	0.0512	0.0009	0.0403	0.0005	254.7	3.0
7.1	228	132	0.58	8.0	0.000099	<0.01	24.48	0.30	0.0514	0.0010	0.0408	0.0005	258.1	3.1
8.1	316	209	0.66	11.2	-	0.02	24.21	0.28	0.0516	0.0008	0.0413	0.0005	260.9	3.0
9.1	243	168	0.69	8.4	0.000078	0.05	24.91	0.35	0.0516	0.0010	0.0401	0.0006	253.6	3.5
10.1	196	117	0.60	6.9	-	<0.01	24.51	0.35	0.0508	0.0010	0.0408	0.0006	258.0	3.6
11.1	299	206	0.69	10.7	-	<0.01	24.01	0.28	0.0515	0.0008	0.0416	0.0005	263.0	3.1
12.1	256	174	0.68	9.1	0.000152	0.30	24.05	0.29	0.0539	0.0009	0.0415	0.0005	261.9	3.1
13.1	235	133	0.57	8.3	0.000241	<0.01	24.18	0.29	0.0494	0.0012	0.0415	0.0005	261.9	3.2
14.1	238	142	0.60	8.3	0.000083	0.05	24.79	0.30	0.0517	0.0010	0.0403	0.0005	254.8	3.1
15.1	278	169	0.61	9.8	-	<0.01	24.38	0.29	0.0491	0.0009	0.0411	0.0005	259.8	3.1
16.1	186	84	0.45	6.3	-	0.09	25.27	0.32	0.0519	0.0011	0.0395	0.0005	250.0	3.2
17.1	238	159	0.67	8.4	0.000124	0.30	24.34	0.30	0.0538	0.0013	0.0410	0.0005	258.8	3.1
18.1	128	90	0.71	4.7	0.004249	6.54	23.51	0.60	0.1036	0.0091	0.0397	0.0011	251.3	7.0
19.1	405	266	0.66	14.2	0.000088	<0.01	24.42	0.28	0.0513	0.0007	0.0409	0.0005	258.7	2.9
20.1	366	342	0.93	12.9	0.000056	<0.01	24.28	0.38	0.0512	0.0008	0.0412	0.0006	260.3	4.0

Notes: Uncertainties given at the one σ level.
Error in Temora reference zircon calibration was 0.34% for the analytical session (not included in above errors but required when comparing data from different mounts).
f_{206}% denotes the percentage of ^{206}Pb that is common Pb.
Correction for common Pb for the U/Pb data has been made using the measured $^{238}U/^{206}Pb$ and $^{207}Pb/^{206}Pb$ ratios following Tera and Wasserburg (1972) as outlined in Williams (1998).

Table A.1 (continued)

Spot	U (ppm)	Th (ppm)	Th/U	$^{206}Pb^*$ (ppm)	$^{204}Pb/^{206}Pb$	f_{206} (%)	Total $^{238}U/^{206}Pb$	±	Total $^{207}Pb/^{206}Pb$	±	Radiogenic $^{206}Pb/^{238}U$	±	Age (Ma) $^{206}Pb/^{238}U$	±
IC-93 / El Colorado														
1.1	710	1169	1.65	23.5	0.000060	0.04	25.97	0.29	0.0514	0.0006	0.0385	0.0004	243.4	1.1
1.2	152	180	1.18	5.0	0.000201	<0.01	26.01	1.08	0.0510	0.0015	0.0385	0.0016	243.3	1.2
2.1	134	154	1.14	4.5	0.000269	0.04	25.58	0.35	0.0514	0.0013	0.0391	0.0005	247.1	2.1
3.1	171	153	0.90	5.8	-	0.14	25.28	0.33	0.0523	0.0012	0.0395	0.0005	249.8	3.1
4.1	643	962	1.50	22.0	-	0.05	25.17	0.28	0.0516	0.0009	0.0397	0.0004	251.1	4.1
4.2	416	289	0.70	14.0	-	0.14	25.46	0.29	0.0523	0.0008	0.0392	0.0005	248.0	4.2
5.1	465	445	0.96	16.7	0.000066	<0.01	23.94	0.27	0.0515	0.0007	0.0418	0.0005	263.8	5.1
6.1	253	247	0.98	8.5	-	0.21	25.44	0.38	0.0529	0.0010	0.0392	0.0006	248.0	6.1
7.1	417	298	0.71	14.0	0.000065	<0.01	25.63	0.33	0.0500	0.0008	0.0391	0.0005	247.1	7.1
8.1	247	246	1.00	8.4	0.000132	0.25	25.16	0.33	0.0533	0.0010	0.0396	0.0005	250.6	8.1
9.1	364	384	1.05	12.6	0.000131	0.07	24.83	0.29	0.0519	0.0008	0.0402	0.0005	254.3	9.1
10.1	230	158	0.69	7.7	-	0.20	25.76	0.41	0.0527	0.0011	0.0387	0.0006	245.0	10.1
11.1	70	41	0.59	2.3	-	<0.01	25.64	0.60	0.0488	0.0019	0.0391	0.0009	247.3	11.1
12.1	249	138	0.56	8.6	0.000167	0.11	24.79	0.31	0.0522	0.0009	0.0403	0.0005	254.7	12.1
19.1	77	60	0.78	2.4	0.000398	0.31	27.61	0.45	0.0532	0.0018	0.0361	0.0006	228.7	19.1
13.1	173	114	0.66	5.7	-	0.05	25.98	0.34	0.0515	0.0012	0.0385	0.0005	243.3	13.1
14.1	305	273	0.90	9.8	-	<0.01	26.68	0.36	0.0495	0.0009	0.0376	0.0005	237.6	14.1
15.1	419	364	0.87	14.7	0.000157	0.10	24.50	0.34	0.0522	0.0007	0.0408	0.0006	257.6	15.1
16.1	166	100	0.60	5.6	0.000440	<0.01	25.59	0.33	0.0490	0.0011	0.0392	0.0005	247.8	16.1
17.1	138	108	0.79	4.5	-	<0.01	26.39	0.35	0.0502	0.0012	0.0379	0.0005	240.0	17.1
18.1	242	164	0.68	8.1	-	<0.01	25.68	0.31	0.0491	0.0009	0.0390	0.0005	246.9	18.1
20.1	232	140	0.60	7.7	-	0.07	25.82	0.33	0.0516	0.0010	0.0387	0.0005	244.8	20.1

Notes: Uncertainties given at the one σ level.
Error in Temora reference zircon calibration was 0.34% for the analytical session (not included in above errors but required when comparing data from different mounts).
f_{206}% denotes the percentage of ^{206}Pb that is common Pb.
Correction for common Pb for the U/Pb data has been made using the measured $^{238}U/^{206}Pb$ and $^{207}Pb/^{206}Pb$ ratios following Tera and Wasserburg (1972) as outlined in Williams (1998).

Table A.2 Lu–Hf and O results for zircon spots from Montosa–El Potro Batholith samples.

Spot	Age (Ma)	±	$^{18}O/^{16}O$	± (10^{-7})	$\delta^{18}O$ (‰)	± 2σ	$^{176}Hf/^{177}Hf$	± 2σ (10^{-6})	$^{176}Lu/^{177}Hf$	± 2σ (10^{-6})	εHf_{today}	εHf_i	± 2σ	T_{DM2} (Ga)*
IC-17 / La Estancilla pluton														
1.1	282.3	3.6	0.0020406	3	6.81	0.32	0.282590	36	0.00045	2	-6.9	-0.7	1.3	1.3
1.2	284.6	3.5	0.0020411	1	7.08	0.30	0.282577	46	0.00075	6	-7.4	-1.2	1.6	1.3
2.1	285.0	3.4	0.0020406	3	6.82	0.32	0.282582	40	0.00098	36	-7.2	-1.0	1.4	1.3
3.1	283.4	4.3	0.0020409	2	6.96	0.31	0.282623	47	0.00141	93	-5.7	0.3	1.7	1.2
4.1	288.9	3.3	0.0020401	1	6.58	0.30	0.282603	52	0.00127	11	-6.4	-0.3	1.8	1.2
5.1	300.3	6.5	0.0020412	1	7.14	0.30	0.282587	41	0.00072	25	-7.0	-0.5	1.5	1.3
6.1	288.2	3.5	0.0020407	1	6.89	0.30	0.282563	39	0.00044	15	-7.9	-1.5	1.4	1.3
7.1	292.3	3.4	0.0020402	1	6.65	0.30	0.282584	36	0.00050	4	-7.1	-0.7	1.3	1.3
9.1	287.2	3.1	0.0020408	1	6.94	0.30	0.282502	48	0.00066	19	-10.0	-3.8	1.7	1.5
10.1	292.7	3.7	0.0020408	1	6.93	0.30	0.282552	67	0.00118	99	-8.2	-2.0	2.4	1.4
13.1	285.1	3.6	0.0020408	1	6.94	0.30	0.282550	44	0.00083	21	-8.3	-2.1	1.6	1.4
14.1	288.1	3.3	0.0020414	1	7.22	0.30	0.282552	42	0.00068	43	-8.2	-2.0	1.5	1.4
15.1	287.0	3.3	0.0020402	1	6.65	0.30	0.282644	46	0.00153	22	-5.0	1.1	1.6	1.2
16.1	286.2	3.4	0.0020419	2	7.48	0.30	0.282576	29	0.00064	39	-7.4	-1.2	1.0	1.3
17.1	288.4	3.5	0.0020400	1	6.55	0.30	0.282613	45	0.00077	14	-6.1	0.2	1.6	1.2
19.1	285.6	4.2	0.0020407	1	6.86	0.30	0.282650	72	0.00198	170	-4.8	1.2	2.6	1.1
20.1	284.8	4.3	0.0020406	2	6.84	0.32	0.282573	36	0.00053	5	-7.5	-1.3	1.3	1.3
IC-22 / Montosa														
1.1	252.7	2.8	0.0020390	1	6.05	0.30	0.282575	43	0.00059	2	-7.43	-1.91	1.52	1.31
3.1	255.1	3.0	0.0020395	1	6.28	0.30	0.282616	35	0.00056	13	-5.98	-0.40	1.24	1.22
4.1	264.9	2.9	0.0020391	0	6.09	0.30	0.282668	34	0.00086	26	-4.14	1.60	1.20	1.10
6.1	256.5	2.9	0.0020388	1	5.93	0.30	0.282631	33	0.00133	22	-5.45	0.03	1.17	1.19
7.1	250.3	3.4	0.0020398	1	6.42	0.30	0.282630	47	0.00095	24	-5.48	-0.07	1.66	1.20
8.1	261.4	3.5	0.0020385	1	5.78	0.30	0.282638	49	0.00054	9	-5.20	0.52	1.73	1.17
9.1	255.7	2.9	0.0020393	2	6.20	0.31	0.282618	36	0.00075	21	-5.91	-0.35	1.27	1.22
10.1	249.3	4.4	0.0020390	1	6.04	0.30	0.282596	54	0.00095	200	-6.68	-1.30	1.91	1.27
11.1	257.3	3.3	0.0020391	2	6.10	0.31	0.282542	81	0.00174	29	-8.59	-3.17	2.87	1.40
12.1	255.5	3.0	0.0020402	2	6.65	0.30	0.282591	46	0.00136	13	-6.86	-1.41	1.63	1.29
13.1	254.2	3.1	0.0020382	1	5.65	0.30	0.282596	33	0.00065	7	-6.68	-1.14	1.17	1.27
15.1	252.8	3.3	0.0020391	1	6.09	0.30	0.282612	40	0.00071	5	-6.12	-0.62	1.42	1.23
16.1	253.7	3.2	0.0020390	2	6.03	0.31	0.282649	47	0.00185	38	-4.81	0.52	1.66	1.16
17.1	261.7	3.2	0.0020391	2	6.11	0.31	0.282598	48	0.00107	58	-6.61	-0.98	1.70	1.26
18.1	260.7	3.3	0.0020398	1	6.45	0.30	0.282625	56	0.00055	29	-5.66	0.04	1.98	1.20
19.1	254.3	3.2	0.0020378	2	5.45	0.30	0.282627	51	0.00166	32	-5.59	-0.21	1.80	1.21

Notes: Oxygen isotope ratios normalised relative to FC1 = 5.61 ‰ .
The decay constant used in the calculation is $\lambda\,^{176}Lu = 1.865 \times 10^{-11}$ $year^{-1}$ (Söderlund et al., 2004).
$(^{176}Hf/^{177}Hf)_{CHUR} = 0.282785$ and $(^{176}Lu/^{177}Hf)_{CHUR} = 0.0336$ (Bouvier et al., 2008).
Present day depleted mantle values $(^{176}Hf/^{177}Hf)^{today}_{DM} = 0.283225$; $(^{176}Lu/^{177}Hf)^{today}_{DM} = 0.0385$ (Vervoort and Blichert-Toft, 1999).
Bulk earth $(^{176}Lu/^{177}Hf)_{BE} = 0.015$ (Goodge and Vervoort, 2006).
i = isotopic initial ratios calculated using the obtained U-Pb ages.
T_{DM2}: Two-stage Depleted Mantle Model Age.

Table A.2 (continued)

Spot	Age (Ma)	±	$^{18}O/^{16}O$	± (10^{-7})	$\delta^{18}O$ (‰)	± 2σ	$^{176}Hf/^{177}Hf$	± 2σ (10^{-6})	$^{176}Lu/^{177}Hf$	± 2σ (10^{-6})	εHf_{today}	εHf_i	± 2σ	T_{DM2} (Ga)*
IC-58 / El León														
1.1	249.1	3.3	0.0020387	1	5.90	0.30	0.282565	54	0.00132	24	-7.78	-2.46	1.91	1.35
2.1	254.3	3.2	0.0020395	2	6.30	0.31	0.282589	47	0.00086	12	-6.93	-1.42	1.66	1.28
3.1	255.4	4.0	0.0020396	2	6.34	0.30	0.282621	49	0.00073	8	-5.80	-0.24	1.73	1.21
4.1	258.3	4.3	0.0020396	1	6.34	0.30	0.282638	49	0.00148	39	-5.20	0.29	1.73	1.18
5.1	270.1	3.0	0.0020389	1	6.00	0.30	0.282563	44	0.00079	3	-7.85	-1.99	1.56	1.33
8.1	267.2	3.5	0.0020394	2	6.25	0.30	0.282579	46	0.00128	65	-7.28	-1.57	1.63	1.30
9.1	258.4	3.3	0.0020396	2	6.33	0.31	0.282619	45	0.00076	6	-5.87	-0.25	1.59	1.21
10.1	255.0	4.1	0.0020398	1	6.44	0.30	0.282624	59	0.00093	27	-5.69	-0.18	2.09	1.21
12.1	266.0	3.2	0.0020378	1	5.47	0.30	0.282614	55	0.00104	15	-6.05	-0.31	1.95	1.22
13.2	336.0	3.9	0.0020446	2	8.77	0.31	0.282500	46	0.00126	91	-10.08	-2.88	1.63	1.44
14.1	255.8	3.4	0.0020389	2	5.97	0.31	0.282667	38	0.00088	21	-4.17	1.37	1.34	1.11
16.1	258.6	3.0	0.0020389	1	6.01	0.30	0.282684	59	0.00113	31	-3.57	1.99	2.09	1.07
17.1	259.1	3.2	0.0020383	1	5.68	0.30	0.282623	44	0.00081	61	-5.73	-0.11	1.56	1.21
18.1	273.0	3.4	0.0020389	2	6.01	0.31	0.282599	38	0.00097	16	-6.58	-0.68	1.34	1.25
19.1	252.9	3.2	0.0020386	1	5.85	0.30	0.282637	52	0.00070	6	-5.23	0.27	1.84	1.18
IC-91 / Chollay														
1.1	253.0	3.2	0.0020373	2	5.19	0.31	0.282662	49	0.00133	20	-4.35	1.05	1.73	1.13
2.1	260.2	3.1	0.0020368	1	4.95	0.30	0.282620	42	0.00085	23	-5.83	-0.20	1.49	1.21
2.2	1122.0	12.0	0.0020372	1	5.14	0.30	0.282172	50	0.00097	9	-21.68	2.76	1.77	1.71
3.1	258.5	3.0	0.0020382	2	5.63	0.31	0.282633	36	0.00084	14	-5.38	0.23	1.27	1.18
4.1	254.7	3.2	0.0020373	2	5.24	0.31	0.282706	52	0.00070	13	-2.79	2.75	1.84	1.02
5.1	261.1	3.2	0.0020380	1	5.53	0.30	0.282648	38	0.00095	12	-4.84	0.80	1.34	1.15
6.1	254.7	3.0	0.0020397	0	6.41	0.30	0.282645	59	0.00093	19	-4.95	0.56	2.09	1.16
7.1	258.1	3.1	0.0020386	1	5.84	0.30	0.282659	38	0.00068	61	-4.46	1.17	1.34	1.12
8.1	260.9	3.0	0.0020371	2	5.14	0.31	0.282612	40	0.00091	6	-6.12	-0.47	1.42	1.23
9.1	253.6	3.5	0.0020385	1	5.81	0.30	0.282646	39	0.00079	8	-4.92	0.59	1.38	1.16
10.1	258.0	3.6	0.0020374	3	5.25	0.32	0.282595	54	0.00164	67	-6.72	-1.26	1.91	1.28
11.1	263.0	3.1	0.0020373	2	5.21	0.30	0.282666	39	0.00083	10	-4.21	1.50	1.38	1.11
12.1	261.9	3.1	0.0020385	3	5.80	0.34	0.282641	33	0.00076	2	-5.09	0.60	1.17	1.16
13.1	261.9	3.2	0.0020365	1	4.80	0.30	0.282670	55	0.00112	40	-4.07	1.57	1.95	1.10
14.1	254.8	3.1	0.0020377	2	5.41	0.31	0.282631	51	0.00082	4	-5.45	0.08	1.80	1.19
15.1	259.8	3.1	0.0020377	1	5.41	0.30	0.282634	43	0.00111	14	-5.34	0.25	1.52	1.18
20.1	260.3	4.0	0.0020389	3	5.97	0.32	0.282644	55	0.00129	31	-4.99	0.58	1.95	1.16

Notes: Oxygen isotope ratios normalised relative to FC1 = 5.61 ‰ .
The decay constant used in the calculation is $\lambda\,^{176}Lu = 1.865 \times 10^{-11}$ year^{-1} (Söderlund et al., 2004).
$(^{176}Hf/^{177}Hf)_{CHUR} = 0.282785$ and $(^{176}Lu/^{177}Hf)_{CHUR} = 0.0336$ (Bouvier et al., 2008).
Present day depleted mantle values $(^{176}Hf/^{177}Hf)^{today}_{DM} = 0.283225$; $(^{176}Lu/^{177}Hf)^{today}_{DM} = 0.0385$ (Vervoort and Blichert-Toft, 1999).
Bulk earth $(^{176}Lu/^{177}Hf)_{BE} = 0.015$ (Goodge and Vervoort, 2006).
i = isotopic initial ratios calculated using the obtained U-Pb ages.
T_{DM2}: Two-stage Depleted Mantle Model Age.

Table A.2 (continued)

Spot	Age (Ma)	±	$^{18}O/^{16}O$	± (10^{-7})	$\delta^{18}O$ (‰)	± 2σ	$^{176}Hf/^{177}Hf$	± 2σ (10^{-6})	$^{176}Lu/^{177}Hf$	± 2σ (10^{-6})	εHf_{today}	εHf_i	± 2σ	T_{DM2} (Ga)*
IC-93 / El Colorado														
2.1	247.1	3.4	0.0020375	1	5.33	0.30	0.282686	81	0.00213	54	-3.50	1.65	2.87	1.09
3.1	249.8	3.3	0.0020374	2	5.25	0.31	0.282622	46	0.00123	13	-5.76	-0.41	1.63	1.22
4.1	251.1	2.8	0.0020382	2	5.67	0.31	0.282712	79	0.00969	150	-2.58	1.39	2.80	1.10
5.1	263.8	3.0	0.0020373	2	5.21	0.32	0.282758	52	0.00151	15	-0.95	4.65	1.84	0.91
6.1	248.0	3.6	0.0020371	1	5.12	0.30	0.282697	70	0.00099	45	-3.11	2.24	2.48	1.05
7.1	247.1	3.2	0.0020386	1	5.83	0.30	0.282677	62	0.00112	43	-3.82	1.49	2.19	1.09
8.1	250.6	3.2	0.0020356	1	4.36	0.30	0.282702	62	0.00257	200	-2.94	2.21	2.19	1.05
9.1	254.3	3.0	0.0020371	2	5.12	0.31	0.282562	68	0.00249	67	-7.89	-2.65	2.41	1.36
10.1	245.0	3.9	0.0020376	0	5.34	0.30	0.282662	74	0.00126	30	-4.35	0.89	2.62	1.13
11.1	247.3	5.8	0.0020390	2	6.03	0.31	0.282701	60	0.00072	110	-2.97	2.41	2.12	1.04
12.1	254.7	3.1	0.0020380	1	5.58	0.30	0.282671	70	0.00253	100	-4.03	1.21	2.48	1.12
14.1	237.6	3.2	0.0020367	1	4.90	0.30	0.282656	52	0.00165	21	-4.56	0.46	1.84	1.15
15.1	257.6	3.6	0.0020382	1	5.63	0.30	0.282653	72	0.00265	300	-4.67	0.61	2.55	1.16
16.1	247.8	3.2	0.0020366	1	4.85	0.30	0.282637	69	0.00190	36	-5.23	-0.04	2.44	1.19
17.1	240.0	3.2	0.0020381	0	5.61	0.30	0.282719	86	0.00154	54	-2.33	2.76	3.04	1.01
20.1	244.8	3.1	0.0020368	2	4.98	0.31	0.282592	75	0.00236	29	-6.82	-1.77	2.65	1.30

Notes: Oxygen isotope ratios normalised relative to FC1 = 5.61 ‰ .
The decay constant used in the calculation is $\lambda\,^{176}Lu = 1.865x10^{-11}$ $year^{-1}$ (Söderlund et al., 2004).
$(^{176}Hf/^{177}Hf)_{CHUR} = 0.282785$ and $(^{176}Lu/^{177}Hf)_{CHUR} = 0.0336$ (Bouvier et al., 2008).
Present day depleted mantle values $(^{176}Hf/^{177}Hf)^{today}_{DM} = 0.283225$; $(^{176}Lu/^{177}Hf)^{today}_{DM} = 0.0385$ (Vervoort and Blichert-Toft, 1999).
Bulk earth $(^{176}Lu/^{177}Hf)_{BE} = 0.015$ (Goodge and Vervoort, 2006).
i = isotopic initial ratios calculated using the obtained U-Pb ages.
T_{DM2}: Two-stage Depleted Mantle Model Age.

APPENDIX B

Full LA-ICPMS U-Pb geochronological, major and trace element data and summarized petrographic descriptions

Table B.1 LA-ICPMS U–Pb in zircon data of El Colorado unit from the Montosa–El Potro Batholith.

Sample				Corrected Ratios									Corrected Ages (Ma)							
Zircon grain	U (ppm)	Th (ppm)	Th/U	$^{207}Pb/^{206}Pb$	±2σ abs	$^{207}Pb/^{235}U$	±2σ abs	$^{206}Pb/^{238}U$	±2σ abs	$^{208}Pb/^{232}Th$	±2σ abs	Rho	$^{206}Pb/^{238}U$	±2σ	$^{207}Pb/^{235}U$	±2σ	$^{207}Pb/^{206}Pb$	±2σ	Best Age (Ma)	±2σ
IC-14 / El Colorado																				
Zircon_071	166	76	0.45	0.0702	0.0082	0.362	0.052	0.03732	0.00085	0.0169	0.0026	0.83	236.2	5.3	312	37	910	200	236	5
Zircon_072	229	169	0.73	0.0532	0.0052	0.283	0.030	0.03903	0.00076	0.0130	0.0018	0.22	246.8	4.7	253	24	360	150	247	5
Zircon_073	220	118	0.54	0.0543	0.0045	0.289	0.027	0.03900	0.00120	0.0120	0.0017	0.49	246.7	7.2	258	22	340	120	247	7
Zircon_074	230	275	1.20	0.0508	0.0044	0.277	0.026	0.03923	0.00069	0.0121	0.0017	0.01	248.0	4.3	248	20	304	99	248	4
Zircon_075	132	63	0.48	0.0615	0.0077	0.347	0.047	0.04073	0.00096	0.0147	0.0022	0.28	257.3	6.0	302	33	680	170	257	6
Zircon_076	443	397	0.90	0.0533	0.0043	0.290	0.026	0.04034	0.00072	0.0128	0.0018	0.37	254.9	4.5	258	20	340	110	255	5
Zircon_077	246	252	1.02	0.0541	0.0048	0.293	0.028	0.04017	0.00075	0.0125	0.0017	0.20	253.9	4.6	260	22	340	110	254	5
Zircon_078	179	249	1.39	0.0572	0.0088	0.316	0.049	0.04040	0.00110	0.0128	0.0018	0.18	255.0	6.5	282	34	480	220	255	7
Zircon_079	144	90	0.63	0.0650	0.0110	0.349	0.068	0.03953	0.00085	0.0178	0.0028	0.33	249.9	5.3	302	46	710	240	250	5
Zircon_080	204	191	0.94	0.0518	0.0045	0.296	0.029	0.04175	0.00071	0.0135	0.0019	0.28	263.7	4.4	263	23	270	130	264	4
Zircon_081	179	201	1.12	0.0541	0.0052	0.277	0.031	0.03676	0.00081	0.0127	0.0018	0.12	232.7	5.0	247	24	440	110	233	5
Zircon_082	1415	1299	0.92	0.0511	0.0040	0.262	0.022	0.03750	0.00100	0.0108	0.0015	0.38	237.6	6.4	236	18	250	110	238	6
Zircon_083	231	167	0.72	0.0581	0.0051	0.310	0.029	0.03921	0.00074	0.0125	0.0017	0.20	247.9	4.6	274	22	490	120	248	5
Zircon_084	405	365	0.90	0.0561	0.0045	0.292	0.026	0.03855	0.00066	0.0122	0.0017	0.04	243.9	4.1	260	20	500	150	244	4
Zircon_085	144	169	1.18	0.0567	0.0060	0.325	0.036	0.04035	0.00083	0.0137	0.0019	0.19	255.0	5.1	284	27	540	150	255	5
Zircon_086	243	144	0.59	0.0685	0.0064	0.382	0.039	0.04054	0.00079	0.0160	0.0022	0.60	256.2	4.9	328	27	880	130	256	5
Zircon_087	584	328	0.56	0.0498	0.0040	0.270	0.023	0.03872	0.00061	0.0117	0.0016	0.58	244.9	3.8	242	20	220	110	245	4
Zircon_088	602	265	0.44	0.0533	0.0043	0.307	0.028	0.04173	0.00075	0.0146	0.0020	0.63	263.6	4.7	271	21	320	130	264	5
Zircon_089	99	66	0.67	0.0750	0.0250	0.440	0.320	0.04230	0.00310	0.0245	0.0069	0.28	267.0	19.0	360	120	1090	340	267	19
Zircon_090	423	254	0.60	0.0517	0.0043	0.267	0.024	0.03756	0.00066	0.0119	0.0016	0.36	237.7	4.1	240	19	290	110	238	4
Zircon_091	99	72	0.72	0.0580	0.0300	0.320	0.250	0.04020	0.00230	0.0327	0.0070	0.07	254.0	14.0	280	120	640	400	254	14
Zircon_092	204	130	0.64	0.0706	0.0067	0.379	0.040	0.03916	0.00078	0.0156	0.0022	0.43	247.6	4.8	325	29	940	150	248	5
Zircon_093	365	295	0.81	0.0516	0.0046	0.286	0.028	0.03987	0.00078	0.0127	0.0018	0.26	252.0	4.8	255	22	310	110	252	5
Zircon_095	224	173	0.77	0.0526	0.0048	0.289	0.027	0.03929	0.00066	0.0131	0.0018	0.18	248.4	4.1	257	21	430	100	248	4
Zircon_096	488	810	1.66	0.0567	0.0050	0.301	0.028	0.03859	0.00067	0.0122	0.0017	0.06	244.1	4.2	267	23	490	120	244	4
Zircon_097	136	90	0.66	0.0712	0.0082	0.406	0.054	0.04140	0.00110	0.0160	0.0025	0.20	261.4	6.9	345	36	930	180	261	7
Zircon_098	350	291	0.83	0.0513	0.0043	0.277	0.025	0.03972	0.00067	0.0126	0.0017	0.20	251.1	4.1	248	20	243	80	251	4
Zircon_099	302	280	0.93	0.0652	0.0055	0.340	0.030	0.03794	0.00068	0.0128	0.0018	0.20	240.0	4.2	297	23	790	120	240	4
Zircon_100	154	233	1.51	0.0508	0.0046	0.279	0.027	0.03970	0.00089	0.0123	0.0017	0.04	251.0	5.5	250	21	370	150	251	6
Zircon_101	281	186	0.66	0.0521	0.0045	0.283	0.026	0.03944	0.00093	0.0134	0.0019	0.31	249.3	5.8	252	21	308	99	249	6
Zircon_102	395	436	1.10	0.0497	0.0042	0.273	0.025	0.03937	0.00079	0.0120	0.0017	0.14	248.9	4.9	245	19	260	120	249	5
Zircon_103	245	142	0.58	0.0537	0.0047	0.294	0.027	0.04028	0.00080	0.0140	0.0020	0.11	254.6	5.0	261	22	355	98	255	5
Zircon_104	1293	1119	0.87	0.0503	0.0041	0.275	0.023	0.03948	0.00068	0.0125	0.0017	0.21	249.6	4.2	247	19	200	130	250	4
Zircon_105	311	359	1.15	0.0528	0.0082	0.289	0.050	0.03971	0.00079	0.0144	0.0021	0.20	251.0	4.9	257	36	310	220	251	5

Notes: U and Th concentrations are calculated employing an external standard zircon as in Paton et al. (2010). 2σ uncertainties propagated according to Paton et al. (2010). $^{207}Pb/^{206}Pb$ ratios, ages and errors are calculated according to Petrus and Kamber (2012). Analyzed spots were 23 micrometers, using an analytical protocol modified from Solari et al. (2010). Data measured employing a Thermo Xseries QICPMS coupled to a Resonetics, Resolution M050 excimer laser workstation.

Table B.1 (continued)

Sample				Corrected Ratios								Corrected Ages (Ma)							
Zircon grain	U (ppm)	Th (ppm)	Th/U	$^{207}Pb/^{206}Pb$	±2σ abs	$^{207}Pb/^{235}U$	±2σ abs	$^{206}Pb/^{238}U$	±2σ abs	$^{208}Pb/^{232}Th$	±2σ abs Rho	$^{206}Pb/^{238}U$	±2σ	$^{207}Pb/^{235}U$	±2σ	$^{207}Pb/^{206}Pb$	±2σ	Best Age (Ma)	±2σ
IC-44 / El Colorado																			
Zircon_036	190	78	0.41	0.0536	0.0047	0.304	0.029	0.04148	0.00071	0.0131	0.0019 0.20	262.0	4.4	271	23	420	110	262	4
Zircon_037	293	208	0.71	0.0780	0.0140	0.414	0.095	0.04000	0.00110	0.0221	0.0035 0.06	252.6	6.8	351	57	1140	200	253	7
Zircon_038	393	167	0.42	0.0538	0.0043	0.303	0.027	0.04160	0.00070	0.0135	0.0019 0.19	262.8	4.3	271	21	386	87	263	4
Zircon_039	660	640	0.97	0.0611	0.0088	0.369	0.061	0.04428	0.00097	0.0147	0.0021 0.74	279.3	6.0	318	42	640	220	279	6
Zircon_040	307	187	0.61	0.0521	0.0045	0.290	0.027	0.04063	0.00071	0.0122	0.0017 0.19	256.7	4.4	260	21	293	98	257	4
Zircon_042	161	122	0.76	0.0522	0.0050	0.290	0.030	0.04049	0.00093	0.0131	0.0018 0.22	255.9	5.7	261	22	330	120	256	6
Zircon_043	90	69	0.77	0.0660	0.0110	0.383	0.070	0.04230	0.00110	0.0192	0.0033 0.14	267.3	6.9	346	44	1030	150	267	7
Zircon_044	604	282	0.47	0.0581	0.0051	0.338	0.033	0.04254	0.00071	0.0162	0.0023 0.22	268.6	4.4	296	25	500	130	269	4
Zircon_047	553	308	0.56	0.0550	0.0130	0.313	0.090	0.04144	0.00086	0.0191	0.0036 0.07	261.8	5.3	276	58	430	300	262	5
Zircon_048	286	136	0.48	0.0518	0.0042	0.291	0.026	0.04117	0.00068	0.0130	0.0018 0.18	260.1	4.2	259	21	280	120	260	4
Zircon_049	620	393	0.63	0.0548	0.0053	0.312	0.035	0.04128	0.00070	0.0148	0.0021 0.17	260.8	4.4	275	26	430	170	261	4
Zircon_050	698	291	0.42	0.0514	0.0041	0.289	0.025	0.04106	0.00065	0.0127	0.0017 0.20	259.4	4.0	258	19	270	120	259	4
Zircon_051	46	34	0.74	0.0657	0.0075	0.378	0.046	0.04250	0.00110	0.0139	0.0020 0.03	268.4	6.5	331	33	810	140	268	7
Zircon_052	90	88	0.98	0.0557	0.0081	0.320	0.046	0.04250	0.00130	0.0139	0.0020 0.47	268.5	7.9	280	34	600	210	269	8
Zircon_053	44	31	0.70	0.0558	0.0081	0.315	0.047	0.04140	0.00140	0.0126	0.0019 0.23	261.6	8.6	273	36	620	160	262	9
Zircon_055	293	128	0.44	0.0516	0.0042	0.290	0.026	0.04076	0.00072	0.0131	0.0018 0.08	257.6	4.5	260	20	297	93	258	5
Zircon_058	156	55	0.36	0.0650	0.0160	0.370	0.110	0.04170	0.00110	0.0264	0.0049 0.32	263.4	7.1	319	67	760	290	263	7
Zircon_059	633	474	0.75	0.0558	0.0044	0.303	0.026	0.04059	0.00096	0.0105	0.0015 0.38	256.5	6.0	268	20	420	130	257	6
Zircon_061	342	176	0.51	0.0505	0.0040	0.288	0.025	0.04163	0.00078	0.0131	0.0018 0.22	262.9	4.8	256	20	230	120	263	5
Zircon_062	844	539	0.64	0.0701	0.0056	0.375	0.033	0.03911	0.00068	0.0111	0.0015 0.27	247.3	4.3	323	24	930	110	247	4
Zircon_063	539	410	0.76	0.0716	0.0063	0.402	0.037	0.04112	0.00079	0.0147	0.0020 0.06	259.7	4.9	342	27	950	150	260	5
Zircon_064	256	139	0.54	0.0529	0.0045	0.300	0.028	0.04106	0.00069	0.0133	0.0019 0.18	259.4	4.2	266	22	360	110	259	4
Zircon_065	143	75	0.53	0.0762	0.0077	0.418	0.038	0.04060	0.00220	0.0150	0.0022 0.60	257.0	14.0	353	28	1090	130	257	14
Zircon_066	286	166	0.58	0.0530	0.0052	0.299	0.031	0.04060	0.00080	0.0122	0.0017 0.19	256.6	5.0	265	24	340	160	257	5
Zircon_067	74	47	0.63	0.0530	0.0064	0.298	0.038	0.04134	0.00090	0.0133	0.0020 0.25	261.1	5.6	264	31	600	150	261	6
Zircon_068	280	130	0.47	0.0547	0.0045	0.310	0.028	0.04151	0.00083	0.0127	0.0018 0.13	262.2	5.2	274	22	378	84	262	5
Zircon_069	78	62	0.80	0.0616	0.0058	0.348	0.034	0.04155	0.00098	0.0139	0.0020 0.22	262.4	6.1	312	26	690	100	262	6
Zircon_070	1624	757	0.47	0.0523	0.0041	0.301	0.027	0.04153	0.00065	0.0135	0.0019 0.17	262.3	4.0	267	21	290	100	262	4

Notes: U and Th concentrations are calculated employing an external standard zircon as in Paton et al. (2010). 2σ uncertainties propagated according to Paton et al. (2010). $^{207}Pb/^{206}Pb$ ratios, ages and errors are calculated according to Petrus and Kamber (2012). Analyzed spots were 23 micrometers, using an analytical protocol modified from Solari et al. (2010). Data measured employing a Thermo Xseries QICPMS coupled to a Resonetics, Resolution M050 excimer laser workstation.

Table B.1 (continued)

Sample				Corrected Ratios									Corrected Ages (Ma)							
Zircon grain	U (ppm)	Th (ppm)	Th/U	$^{207}Pb/^{206}Pb$	±2σ abs	$^{207}Pb/^{235}U$	±2σ abs	$^{206}Pb/^{238}U$	±2σ abs	$^{208}Pb/^{232}Th$	±2σ abs	Rho	$^{206}Pb/^{238}U$	±2σ	$^{207}Pb/^{235}U$	±2σ	$^{207}Pb/^{206}Pb$	±2σ	Best Age (Ma)	±2σ
IC-46 / Chollay																				
Zircon_036	422	230	0.55	0.0610	0.0027	0.330	0.013	0.03973	0.00056	0.0139	0.0006	0.36	251.2	3.5	289.0	10.0	629	59	251	4
Zircon_037	751	453	0.60	0.0513	0.0019	0.274	0.011	0.03872	0.00050	0.0123	0.0006	0.32	244.9	3.1	245.4	8.9	254	52	245	3
Zircon_038	390	174	0.45	0.0530	0.0018	0.287	0.012	0.03935	0.00044	0.0122	0.0006	0.27	248.8	2.7	255.5	9.1	299	52	249	3
Zircon_039	759	610	0.80	0.0571	0.0025	0.288	0.011	0.03710	0.00082	0.0100	0.0007	0.58	234.9	5.1	257.1	8.6	524	74	235	5
Zircon_040	633	332	0.52	0.0531	0.0021	0.286	0.012	0.03900	0.00037	0.0128	0.0006	0.23	246.6	2.3	255.2	9.3	319	55	247	2
Zircon_041	1466	393	0.27	0.0699	0.0023	0.261	0.012	0.02760	0.00150	0.0160	0.0010	0.86	175.5	9.6	235.3	9.5	917	62	176	10
Zircon_042	1048	433	0.41	0.0547	0.0017	0.237	0.008	0.03147	0.00086	0.0124	0.0006	0.85	199.8	5.4	216.0	6.3	392	47	200	5
Zircon_043	639	235	0.37	0.0518	0.0014	0.280	0.009	0.03942	0.00037	0.0125	0.0007	0.30	249.2	2.3	250.5	6.9	286	31	249	2
Zircon_044	672	294	0.44	0.0580	0.0021	0.312	0.012	0.03920	0.00043	0.0132	0.0007	0.29	247.9	2.7	275.3	9.3	549	48	248	3
Zircon_045	1076	364	0.34	0.0537	0.0012	0.285	0.008	0.03856	0.00042	0.0126	0.0006	0.40	243.9	2.6	254.1	6.1	364	26	244	3
Zircon_046	741	345	0.47	0.0573	0.0018	0.299	0.009	0.03784	0.00063	0.0132	0.0006	0.53	239.4	3.9	265.4	7.2	503	54	239	4
Zircon_047	557	243	0.44	0.0535	0.0014	0.289	0.009	0.03916	0.00042	0.0125	0.0006	0.36	247.6	2.6	257.9	6.9	353	40	248	3
Zircon_048	1032	549	0.53	0.0554	0.0059	0.284	0.019	0.03719	0.00099	0.0125	0.0012	0.40	235.4	6.2	254.0	14.0	430	150	235	6
Zircon_049	502	266	0.53	0.0610	0.0170	0.303	0.021	0.03590	0.00280	0.0127	0.0007	0.91	227.0	18.0	268.0	16.0	660	310	227	18
Zircon_050	890	506	0.57	0.0566	0.0030	0.296	0.011	0.03783	0.00081	0.0121	0.0006	0.58	239.3	5.0	263.3	8.7	492	93	239	5
Zircon_051	568	263	0.46	0.0574	0.0017	0.250	0.009	0.03214	0.00049	0.0121	0.0006	0.41	203.9	3.1	226.7	7.5	509	39	204	3
Zircon_052	488	351	0.72	0.0572	0.0018	0.297	0.011	0.03760	0.00051	0.0089	0.0004	0.37	237.9	3.2	264.0	8.6	481	50	238	3
Zircon_053	663	415	0.63	0.0516	0.0044	0.276	0.011	0.03880	0.00190	0.0123	0.0006	0.95	246.0	11.0	250.0	8.8	280	140	246	11
Zircon_054	400	241	0.60	0.0533	0.0016	0.286	0.009	0.03899	0.00043	0.0118	0.0006	0.34	246.6	2.7	255.2	7.3	364	44	247	3
Zircon_055	606	328	0.54	0.0524	0.0017	0.279	0.010	0.03873	0.00058	0.0123	0.0006	0.42	245.0	3.6	249.8	7.9	318	43	245	4
Zircon_056	302	198	0.66	0.0608	0.0020	0.317	0.012	0.03776	0.00061	0.0132	0.0006	0.43	239.0	3.8	279.2	9.6	623	57	239	4
Zircon_057	1155	493	0.43	0.0574	0.0012	0.294	0.008	0.03707	0.00053	0.0120	0.0006	0.51	234.6	3.3	261.7	6.4	525	29	235	3
Zircon_059	237	153	0.65	0.0556	0.0021	0.303	0.013	0.03905	0.00067	0.0129	0.0006	0.40	246.9	4.2	268.0	10.0	475	45	247	4
Zircon_060	472	297	0.63	0.0607	0.0024	0.284	0.012	0.03393	0.00058	0.0118	0.0006	0.40	215.1	3.6	253.7	9.3	603	51	215	4
Zircon_063	710	608	0.86	0.0666	0.0050	0.277	0.019	0.03047	0.00074	0.0076	0.0006	0.35	193.5	4.6	248.0	14.0	790	130	194	5
Zircon_064	349	131	0.38	0.0515	0.0016	0.279	0.010	0.03921	0.00043	0.0117	0.0006	0.31	247.9	2.7	249.5	7.8	286	44	248	3
Zircon_065	1169	527	0.45	0.0623	0.0017	0.237	0.011	0.02770	0.00130	0.0104	0.0006	0.93	176.1	7.9	215.7	8.5	679	40	176	8
Zircon_066	1236	930	0.75	0.0568	0.0091	0.295	0.020	0.03640	0.00180	0.0115	0.0006	0.73	230.0	11.0	262.0	15.0	480	210	230	11
Zircon_067	723	365	0.50	0.0518	0.0016	0.275	0.009	0.03905	0.00043	0.0121	0.0006	0.32	247.0	2.7	248.0	7.9	272	48	247	3
Zircon_068	342	101	0.30	0.0536	0.0016	0.292	0.010	0.03975	0.00044	0.0139	0.0007	0.32	251.3	2.7	259.8	8.0	368	32	251	3
Zircon_069	941	498	0.53	0.0534	0.0024	0.281	0.013	0.03874	0.00041	0.0123	0.0008	0.23	245.0	2.6	251.0	10.0	325	82	245	3
Zircon_070	549	285	0.52	0.0503	0.0013	0.279	0.009	0.03985	0.00041	0.0123	0.0006	0.34	251.9	2.6	249.4	6.8	244	51	252	3

Notes: U and Th concentrations are calculated employing an external standard zircon as in Paton et al. (2010). 2σ uncertainties propagated according to Paton et al. (2010). $^{207}Pb/^{206}Pb$ ratios, ages and errors are calculated according to Petrus and Kamber (2012). Analyzed spots were 23 micrometers, using an analytical protocol modified from Solari et al. (2010). Data measured employing a Thermo Xseries QICPMS coupled to a Resonetics, Resolution M050 excimer laser workstation.

Table B.1 (continued)

Sample				Corrected Ratios								Corrected Ages (Ma)							
Zircon grain	U (ppm)	Th (ppm)	Th/U	$^{207}Pb/^{206}Pb$	±2σ abs	$^{207}Pb/^{235}U$	±2σ abs	$^{206}Pb/^{238}U$	±2σ abs	$^{208}Pb/^{232}Th$	±2σ abs Rho	$^{206}Pb/^{238}U$	±2σ	$^{207}Pb/^{235}U$	±2σ	$^{207}Pb/^{206}Pb$	±2σ	Best Age (Ma)	±2σ
IC-47 / Chollay																			
Zircon_001	341	286	0.84	0.0535	0.0020	0.284	0.012	0.03876	0.00056	0.0111	0.0006 0.34	245.1	3.6	253.9	9.7	385	51	245	4
Zircon_002	479	228	0.48	0.0549	0.0020	0.292	0.011	0.03823	0.00043	0.0133	0.0006 0.30	241.8	2.7	259.7	8.5	424	49	242	3
Zircon_003	126	99	0.79	0.0595	0.0032	0.329	0.018	0.04013	0.00053	0.0131	0.0007 0.24	253.7	3.3	288.0	13.0	570	77	254	3
Zircon_004	473	337	0.71	0.0548	0.0022	0.283	0.013	0.03810	0.00069	0.0120	0.0006 0.39	241.0	4.3	253.0	10.0	355	49	241	4
Zircon_005	1150	560	0.49	0.0526	0.0013	0.279	0.009	0.03910	0.00059	0.0126	0.0006 0.47	247.3	3.4	249.6	7.0	319	36	247	3
Zircon_006	1008	618	0.61	0.0531	0.0011	0.280	0.008	0.03840	0.00036	0.0120	0.0007 0.34	242.9	2.3	250.7	6.2	317	40	243	2
Zircon_007	807	301	0.37	0.0519	0.0012	0.281	0.008	0.03940	0.00042	0.0124	0.0006 0.36	249.1	2.6	250.9	6.5	286	30	249	3
Zircon_008	405	200	0.49	0.0520	0.0017	0.276	0.010	0.03873	0.00045	0.0123	0.0006 0.32	245.0	2.8	247.4	8.0	330	47	245	3
Zircon_010	491	306	0.62	0.0543	0.0018	0.291	0.011	0.03902	0.00053	0.0123	0.0006 0.36	246.7	3.3	258.9	8.6	386	41	247	3
Zircon_011	1024	479	0.47	0.0524	0.0015	0.279	0.009	0.03882	0.00042	0.0123	0.0006 0.33	245.5	2.6	249.5	7.2	284	41	246	3
Zircon_012	177	90	0.51	0.0554	0.0026	0.291	0.015	0.03834	0.00047	0.0127	0.0006 0.24	242.5	2.9	259.0	11.0	463	61	243	3
Zircon_013	483	272	0.56	0.0566	0.0017	0.305	0.011	0.03922	0.00050	0.0126	0.0006 0.35	248.0	3.1	269.9	8.2	469	43	248	3
Zircon_014	262	148	0.57	0.0542	0.0022	0.295	0.013	0.03933	0.00043	0.0129	0.0006 0.25	248.6	2.7	262.0	10.0	411	44	249	3
Zircon_015	251	116	0.46	0.0525	0.0020	0.282	0.012	0.03921	0.00051	0.0125	0.0006 0.31	247.9	3.2	252.3	9.4	310	51	248	3
Zircon_016	701	406	0.58	0.0539	0.0015	0.280	0.009	0.03830	0.00042	0.0124	0.0006 0.33	242.3	2.6	250.8	7.4	375	35	242	3
Zircon_018	1010	500	0.50	0.0536	0.0012	0.297	0.009	0.03991	0.00045	0.0114	0.0006 0.38	252.3	2.8	263.6	6.9	373	30	252	3
Zircon_019	404	234	0.58	0.0525	0.0018	0.282	0.011	0.03865	0.00046	0.0124	0.0006 0.31	244.5	2.8	251.9	8.4	319	50	245	3
Zircon_020	287	137	0.48	0.0552	0.0022	0.298	0.012	0.03984	0.00049	0.0130	0.0006 0.31	251.8	3.0	270.3	9.6	427	66	252	3
Zircon_021	517	316	0.61	0.0532	0.0016	0.289	0.011	0.03946	0.00044	0.0124	0.0006 0.29	249.5	2.7	257.3	8.4	338	46	250	3
Zircon_022	230	114	0.49	0.0537	0.0022	0.285	0.012	0.03878	0.00046	0.0126	0.0007 0.28	245.3	2.9	254.6	9.3	392	39	245	3
Zircon_023	599	334	0.56	0.0518	0.0015	0.274	0.009	0.03868	0.00044	0.0120	0.0006 0.33	244.6	2.8	245.5	7.5	256	32	245	3
Zircon_024	476	342	0.72	0.0531	0.0016	0.274	0.010	0.03802	0.00045	0.0118	0.0006 0.33	240.5	2.8	245.9	7.9	313	43	241	3
Zircon_025	142	114	0.80	0.0572	0.0072	0.300	0.044	0.03830	0.00074	0.0119	0.0011 0.13	242.3	4.6	265.0	33.0	450	180	242	5
Zircon_026	520	438	0.84	0.0521	0.0018	0.277	0.011	0.03850	0.00045	0.0123	0.0006 0.29	243.5	2.8	247.9	8.4	310	47	244	3
Zircon_027	680	317	0.47	0.0517	0.0014	0.270	0.008	0.03828	0.00037	0.0119	0.0006 0.31	242.1	2.3	242.7	6.7	274	39	242	2
Zircon_028	218	100	0.46	0.0539	0.0026	0.283	0.015	0.03830	0.00054	0.0118	0.0006 0.27	242.3	3.3	253.0	12.0	375	57	242	3
Zircon_029	579	304	0.52	0.0531	0.0015	0.280	0.009	0.03883	0.00035	0.0114	0.0006 0.27	245.6	2.2	252.1	7.2	335	49	246	2
Zircon_030	506	232	0.46	0.0518	0.0015	0.274	0.009	0.03867	0.00046	0.0121	0.0006 0.36	244.6	2.9	245.7	7.2	277	35	245	3
Zircon_031	559	311	0.56	0.0517	0.0016	0.273	0.010	0.03845	0.00040	0.0118	0.0006 0.30	243.2	2.5	244.6	7.5	272	42	243	3
Zircon_032	477	330	0.69	0.0523	0.0015	0.281	0.009	0.03931	0.00058	0.0118	0.0006 0.44	248.5	3.6	251.4	7.4	326	40	249	4
Zircon_033	398	288	0.72	0.0577	0.0018	0.305	0.010	0.03883	0.00040	0.0105	0.0006 0.31	245.6	2.5	270.3	8.1	504	49	246	3
Zircon_034	102	61	0.60	0.0545	0.0030	0.287	0.017	0.03891	0.00052	0.0114	0.0007 0.23	246.1	3.3	258.0	13.0	351	51	246	3
Zircon_035	493	264	0.54	0.0525	0.0019	0.279	0.011	0.03867	0.00042	0.0122	0.0006 0.28	244.6	2.6	249.3	8.6	327	47	245	3

Notes: U and Th concentrations are calculated employing an external standard zircon as in Paton et al. (2010). 2σ uncertainties propagated according to Paton et al. (2010). $^{207}Pb/^{206}Pb$ ratios, ages and errors are calculated according to Petrus and Kamber (2012). Analyzed spots were 23 micrometers, using an analytical protocol modified from Solari et al. (2010). Data measured employing a Thermo Xseries QICPMS coupled to a Resonetics, Resolution M050 excimer laser workstation.

Table B.1 (continued)

Sample				Corrected Ratios									Corrected Ages (Ma)							
Zircon grain	U (ppm)	Th (ppm)	Th/U	$^{207}Pb/^{206}Pb$	±2σ abs	$^{207}Pb/^{235}U$	±2σ abs	$^{206}Pb/^{238}U$	±2σ abs	$^{208}Pb/^{232}Th$	±2σ abs	Rho	$^{206}Pb/^{238}U$	±2σ	$^{207}Pb/^{235}U$	±2σ	$^{207}Pb/^{206}Pb$	±2σ	Best Age (Ma)	±2σ
IC-81 / Chollay																				
Zircon_071	842	528	0.63	0.0526	0.0013	0.266	0.009	0.03714	0.00045	0.0121	0.0006	0.36	235.1	2.8	239.7	7.0	315	45	235	3
Zircon_072	331	190	0.57	0.0517	0.0023	0.273	0.013	0.03831	0.00042	0.0115	0.0006	0.23	242.3	2.6	244.0	10.0	303	67	242	3
Zircon_074	384	212	0.55	0.0525	0.0016	0.276	0.010	0.03835	0.00044	0.0116	0.0006	0.33	242.6	2.8	247.2	7.7	319	33	243	3
Zircon_075	506	263	0.52	0.0520	0.0017	0.273	0.009	0.03821	0.00043	0.0117	0.0006	0.33	241.7	2.7	244.7	7.4	316	40	242	3
Zircon_077	569	380	0.67	0.0535	0.0016	0.286	0.009	0.03957	0.00053	0.0121	0.0006	0.41	250.2	3.3	255.3	7.8	346	46	250	3
Zircon_078	301	147	0.49	0.0509	0.0019	0.280	0.011	0.03997	0.00050	0.0120	0.0006	0.32	252.7	3.1	250.6	8.9	231	43	253	3
Zircon_079	341	176	0.52	0.0512	0.0017	0.294	0.010	0.04203	0.00058	0.0131	0.0007	0.41	265.4	3.6	261.4	8.2	332	49	265	4
Zircon_080	423	297	0.70	0.0505	0.0020	0.277	0.012	0.03963	0.00049	0.0120	0.0006	0.29	250.5	3.1	249.8	9.8	249	56	251	3
Zircon_081	505	250	0.50	0.0517	0.0017	0.282	0.010	0.03968	0.00045	0.0119	0.0006	0.32	250.9	2.8	252.4	8.3	294	47	251	3
Zircon_082	414	234	0.57	0.0516	0.0016	0.284	0.011	0.03966	0.00072	0.0121	0.0006	0.47	250.7	4.5	253.4	9.2	279	38	251	5
Zircon_083	188	154	0.82	0.0502	0.0019	0.272	0.011	0.03945	0.00056	0.0121	0.0006	0.35	249.4	3.4	243.8	8.4	256	44	249	3
Zircon_084	881	347	0.39	0.0506	0.0025	0.275	0.016	0.03950	0.00110	0.0122	0.0008	0.48	249.7	7.0	247.0	12.0	219	39	250	7
Zircon_085	770	416	0.54	0.0531	0.0015	0.297	0.010	0.04098	0.00047	0.0125	0.0006	0.36	258.9	2.9	264.2	7.6	336	41	259	3
Zircon_086	249	144	0.58	0.0573	0.0021	0.306	0.013	0.03952	0.00048	0.0128	0.0007	0.29	249.9	3.0	271.0	10.0	488	60	250	3
Zircon_087	879	394	0.45	0.0519	0.0015	0.274	0.010	0.03820	0.00130	0.0120	0.0006	0.94	241.9	8.1	247.0	8.0	292	42	242	8
Zircon_088	556	433	0.78	0.0528	0.0014	0.276	0.009	0.03836	0.00040	0.0118	0.0006	0.34	242.7	2.5	247.0	6.8	284	51	243	3
Zircon_089	332	198	0.60	0.0512	0.0017	0.267	0.009	0.03826	0.00044	0.0115	0.0006	0.34	242.0	2.7	240.5	7.3	274	46	242	3
Zircon_090	651	337	0.52	0.0541	0.0014	0.277	0.008	0.03689	0.00039	0.0115	0.0005	0.37	233.5	2.4	248.0	6.4	392	37	234	2
Zircon_091	803	701	0.87	0.0517	0.0016	0.271	0.010	0.03812	0.00040	0.0119	0.0006	0.28	241.2	2.5	243.4	7.9	281	63	241	3
Zircon_092	560	343	0.61	0.0515	0.0019	0.290	0.012	0.04103	0.00045	0.0125	0.0006	0.27	259.2	2.8	258.4	9.2	290	63	259	3
Zircon_093	861	322	0.37	0.0535	0.0016	0.282	0.010	0.03821	0.00042	0.0134	0.0007	0.32	241.7	2.6	252.0	7.7	339	58	242	3
Zircon_094	416	177	0.43	0.0514	0.0012	0.282	0.011	0.03967	0.00084	0.0123	0.0006	0.54	250.8	5.2	254.3	8.4	269	38	251	5
Zircon_095	266	171	0.64	0.0516	0.0020	0.292	0.012	0.04113	0.00053	0.0132	0.0007	0.31	259.8	3.3	262.5	9.7	314	38	260	3
Zircon_097	898	477	0.53	0.0521	0.0013	0.279	0.009	0.03927	0.00042	0.0123	0.0006	0.33	248.3	2.6	249.6	7.1	264	29	248	3
Zircon_098	872	355	0.41	0.0520	0.0015	0.277	0.010	0.03908	0.00052	0.0120	0.0007	0.37	247.1	3.2	248.4	7.9	280	36	247	3
Zircon_099	1091	662	0.61	0.0524	0.0015	0.297	0.011	0.04110	0.00081	0.0129	0.0007	0.53	259.6	5.0	264.0	8.6	318	51	260	5
Zircon_100	370	180	0.49	0.0519	0.0014	0.295	0.010	0.04112	0.00055	0.0128	0.0006	0.39	259.8	3.4	262.6	8.1	306	46	260	3
Zircon_102	447	217	0.48	0.0538	0.0023	0.279	0.013	0.03767	0.00088	0.0132	0.0006	0.50	238.4	5.5	258.0	11.0	432	44	238	6
Zircon_103	2770	1526	0.55	0.0528	0.0011	0.307	0.009	0.04262	0.00058	0.0130	0.0007	0.45	269.1	3.6	272.2	7.2	329	28	269	4
Zircon_104	890	419	0.47	0.0532	0.0025	0.297	0.015	0.04060	0.00046	0.0127	0.0010	0.22	256.5	2.9	264.0	12.0	343	83	257	3
Zircon_105	590	394	0.67	0.0511	0.0015	0.280	0.011	0.03936	0.00055	0.0119	0.0006	0.36	248.9	3.4	250.6	8.7	226	55	249	3

Notes: U and Th concentrations are calculated employing an external standard zircon as in Paton et al. (2010). 2σ uncertainties propagated according to Paton et al. (2010). $^{207}Pb/^{206}Pb$ ratios, ages and errors are calculated according to Petrus and Kamber (2012). Analyzed spots were 23 micrometers, using an analytical protocol modified from Solari et al. (2010). Data measured employing a Thermo Xseries QICPMS coupled to a Resonetics, Resolution M050 excimer laser workstation.

Table B.1 (continued)

Sample				Corrected Ratios									Corrected Ages (Ma)							
Zircon grain	U (ppm)	Th (ppm)	Th/U	$^{207}Pb/^{206}Pb$	±2σ abs	$^{207}Pb/^{235}U$	±2σ abs	$^{206}Pb/^{238}U$	±2σ abs	$^{208}Pb/^{232}Th$	±2σ abs	Rho	$^{206}Pb/^{238}U$	±2σ	$^{207}Pb/^{235}U$	±2σ	$^{207}Pb/^{206}Pb$	±2σ	Best Age (Ma)	±2σ
IC-92 / Chollay																				
Zircon_106	187	124	0.66	0.0692	0.0027	0.276	0.014	0.02915	0.00055	0.0107	0.0006	0.37	185.2	3.5	247.0	12.0	899	46	185	4
Zircon_107	100	85	0.85	0.0570	0.0049	0.279	0.026	0.03550	0.00055	0.0113	0.0007	0.17	224.9	3.4	256.0	19.0	510	130	225	3
Zircon_108	91	70	0.77	0.0564	0.0063	0.262	0.031	0.03584	0.00059	0.0117	0.0008	0.14	227.0	3.6	243.0	25.0	690	170	227	4
Zircon_109	99	60	0.60	0.0520	0.0040	0.246	0.018	0.03383	0.00063	0.0104	0.0007	0.25	214.5	3.9	226.0	14.0	351	75	215	4
Zircon_110	130	84	0.65	0.0563	0.0031	0.261	0.015	0.03360	0.00055	0.0105	0.0006	0.28	213.1	3.4	235.0	12.0	509	68	213	3
Zircon_111	149	114	0.76	0.0625	0.0030	0.265	0.013	0.03047	0.00047	0.0092	0.0005	0.31	193.5	2.9	238.0	11.0	700	57	194	3
Zircon_112	102	68	0.67	0.0592	0.0054	0.289	0.027	0.03542	0.00059	0.0118	0.0009	0.18	224.4	3.7	257.0	21.0	564	82	224	4
Zircon_113	101	67	0.66	0.0519	0.0039	0.245	0.019	0.03432	0.00052	0.0102	0.0006	0.20	217.5	3.3	224.0	15.0	384	70	218	3
Zircon_115	141	178	1.26	0.0580	0.0041	0.265	0.019	0.03335	0.00067	0.0100	0.0006	0.28	211.5	4.2	238.0	15.0	560	110	212	4
Zircon_116	75	70	0.93	0.0505	0.0093	0.243	0.074	0.03500	0.00120	0.0099	0.0023	0.11	221.7	7.3	224.0	47.0	420	390	222	7
Zircon_117	93	59	0.63	0.0633	0.0044	0.314	0.022	0.03572	0.00069	0.0131	0.0008	0.28	226.2	4.3	276.0	16.0	760	82	226	4
Zircon_118	53	32	0.61	0.0521	0.0038	0.261	0.018	0.03475	0.00055	0.0119	0.0007	0.23	220.2	3.4	234.0	15.0	408	76	220	3
Zircon_119	172	162	0.94	0.0504	0.0021	0.244	0.012	0.03530	0.00055	0.0111	0.0006	0.32	223.6	3.4	221.6	9.0	246	50	224	3
Zircon_120	73	33	0.46	0.0833	0.0024	2.240	0.110	0.19440	0.00660	0.0571	0.0036	0.69	1144.0	36.0	1189.0	33.0	1269	30	1269	30
Zircon_121	193	235	1.22	0.0576	0.0036	0.254	0.022	0.03160	0.00095	0.0101	0.0007	0.35	200.6	5.9	232.0	17.0	559	91	201	6
Zircon_122	58	39	0.67	0.0497	0.0055	0.245	0.026	0.03510	0.00073	0.0117	0.0007	0.20	222.4	4.5	225.0	21.0	440	110	222	5
Zircon_123	67	46	0.70	0.0604	0.0050	0.295	0.025	0.03548	0.00071	0.0128	0.0008	0.24	224.7	4.4	262.0	19.0	749	83	225	4
Zircon_124	110	109	0.99	0.0511	0.0048	0.245	0.024	0.03420	0.00062	0.0104	0.0007	0.19	216.8	3.8	222.0	19.0	380	120	217	4
Zircon_125	172	191	1.11	0.0516	0.0069	0.246	0.045	0.03461	0.00073	0.0109	0.0011	0.12	219.3	4.5	223.0	32.0	300	210	219	5
Zircon_126	110	73	0.67	0.0521	0.0035	0.246	0.016	0.03429	0.00051	0.0109	0.0006	0.23	217.4	3.2	225.0	13.0	362	67	217	3
Zircon_127	174	149	0.86	0.0533	0.0053	0.248	0.031	0.03389	0.00068	0.0105	0.0010	0.16	214.8	4.2	224.0	22.0	420	120	215	4
Zircon_128	134	152	1.13	0.0538	0.0041	0.250	0.020	0.03394	0.00054	0.0103	0.0005	0.20	215.1	3.4	226.0	16.0	463	80	215	3
Zircon_129	110	66	0.60	0.0588	0.0029	0.294	0.016	0.03584	0.00068	0.0100	0.0007	0.35	227.0	4.3	262.0	12.0	575	60	227	4
Zircon_130	456	519	1.14	0.0537	0.0016	0.275	0.010	0.03715	0.00045	0.0114	0.0006	0.35	235.2	2.8	247.4	7.6	360	48	235	3
Zircon_131	111	74	0.66	0.0623	0.0068	0.279	0.029	0.03267	0.00045	0.0107	0.0010	0.13	207.2	2.8	249.0	22.0	730	150	207	3
Zircon_132	65	49	0.76	0.0530	0.0070	0.248	0.034	0.03390	0.00063	0.0098	0.0008	0.14	214.9	3.9	221.0	27.0	750	170	215	4
Zircon_133	124	127	1.03	0.0487	0.0029	0.234	0.015	0.03429	0.00056	0.0102	0.0005	0.25	217.3	3.5	213.0	13.0	267	61	217	4
Zircon_134	107	70	0.66	0.0565	0.0043	0.270	0.020	0.03504	0.00051	0.0112	0.0007	0.20	222.0	3.2	242.0	16.0	480	85	222	3
Zircon_135	224	306	1.37	0.0561	0.0054	0.256	0.027	0.03343	0.00076	0.0105	0.0007	0.22	212.0	4.7	231.0	21.0	490	130	212	5
Zircon_136	125	97	0.78	0.0620	0.0120	0.284	0.056	0.03202	0.00049	0.0102	0.0012	0.08	203.1	3.1	244.0	39.0	670	240	203	3
Zircon_137	144	123	0.86	0.0609	0.0025	0.287	0.014	0.03457	0.00045	0.0115	0.0006	0.27	219.1	2.8	256.0	11.0	630	36	219	3
Zircon_138	190	225	1.18	0.0543	0.0024	0.250	0.012	0.03348	0.00037	0.0104	0.0005	0.23	212.3	2.3	226.6	9.7	418	59	212	2
Zircon_139	182	171	0.94	0.0585	0.0030	0.276	0.015	0.03438	0.00046	0.0117	0.0006	0.25	217.9	2.9	247.0	12.0	554	59	218	3

Notes: U and Th concentrations are calculated employing an external standard zircon as in Paton et al. (2010). 2σ uncertainties propagated according to Paton et al. (2010). $^{207}Pb/^{206}Pb$ ratios, ages and errors are calculated according to Petrus and Kamber (2012). Analyzed spots were 23 micrometers, using an analytical protocol modified from Solari et al. (2010). Data measured employing a Thermo Xseries QICPMS coupled to a Resonetics, Resolution M050 excimer laser workstation.

Table B.1 (continued)

Sample				Corrected Ratios									Corrected Ages (Ma)							
Zircon grain	U (ppm)	Th (ppm)	Th/U	$^{207}Pb/^{206}Pb$	±2σ abs	$^{207}Pb/^{235}U$	±2σ abs	$^{206}Pb/^{238}U$	±2σ abs	$^{208}Pb/^{232}Th$	±2σ abs	Rho	$^{206}Pb/^{238}U$	±2σ	$^{207}Pb/^{235}U$	±2σ	$^{207}Pb/^{206}Pb$	±2σ	Best Age (Ma)	±2σ
IC-23 / Montosa																				
Zircon_001	133	271	2.05	0.0519	0.0051	0.306	0.032	0.04154	0.00079	0.0129	0.0018	0.04	262.3	4.9	270.0	24.0	390	100	262	5
Zircon_002	454	239	0.53	0.0511	0.0043	0.290	0.026	0.04115	0.00067	0.0124	0.0017	0.18	260.0	4.2	259.0	20.0	264	91	260	4
Zircon_003	374	423	1.13	0.0522	0.0045	0.307	0.030	0.04235	0.00084	0.0128	0.0018	0.08	267.4	5.2	272.0	23.0	290	110	267	5
Zircon_004	512	374	0.73	0.0553	0.0043	0.317	0.027	0.04177	0.00093	0.0124	0.0017	0.61	263.8	5.8	279.0	21.0	410	110	264	6
Zircon_005	486	162	0.33	0.0525	0.0043	0.299	0.027	0.04171	0.00073	0.0134	0.0019	0.24	263.4	4.5	266.0	21.0	330	120	263	5
Zircon_006	469	409	0.87	0.0526	0.0043	0.308	0.026	0.04216	0.00080	0.0128	0.0018	0.22	266.2	5.0	272.0	20.0	340	100	266	5
Zircon_008	318	180	0.57	0.0546	0.0099	0.320	0.065	0.04221	0.00084	0.0137	0.0019	0.35	266.5	5.2	281.0	46.0	370	260	267	5
Zircon_009	158	208	1.32	0.0544	0.0054	0.311	0.034	0.04140	0.00100	0.0122	0.0017	0.39	261.4	6.3	274.0	26.0	470	160	261	6
Zircon_010	210	151	0.72	0.0512	0.0043	0.303	0.027	0.04211	0.00087	0.0130	0.0018	0.36	265.9	5.4	268.0	21.0	250	89	266	5
Zircon_011	125	151	1.21	0.0566	0.0052	0.338	0.033	0.04190	0.00100	0.0137	0.0019	0.20	264.8	6.4	295.0	26.0	490	110	265	6
Zircon_012	83	129	1.55	0.0544	0.0067	0.308	0.038	0.04050	0.00100	0.0123	0.0017	0.12	256.0	6.2	272.0	29.0	430	170	256	6
Zircon_013	313	293	0.94	0.0520	0.0042	0.300	0.026	0.04180	0.00092	0.0125	0.0017	0.32	264.0	5.7	266.0	21.0	304	93	264	6
Zircon_014	152	161	1.06	0.0509	0.0045	0.295	0.030	0.04150	0.00110	0.0129	0.0018	0.43	262.0	6.7	264.0	23.0	340	140	262	7
Zircon_015	224	177	0.79	0.0534	0.0045	0.309	0.029	0.04190	0.00110	0.0130	0.0018	0.42	264.6	6.7	275.0	21.0	400	120	265	7
Zircon_016	176	220	1.25	0.0517	0.0043	0.298	0.027	0.04185	0.00081	0.0128	0.0018	0.07	264.3	5.0	265.0	21.0	267	86	264	5
Zircon_017	294	289	0.98	0.0524	0.0044	0.311	0.028	0.04288	0.00078	0.0128	0.0018	0.20	270.6	4.8	275.0	22.0	270	100	271	5
Zircon_018	238	265	1.11	0.0521	0.0044	0.295	0.027	0.04127	0.00069	0.0120	0.0017	0.18	260.7	4.3	262.0	21.0	300	100	261	4
Zircon_019	149	317	2.13	0.0525	0.0048	0.294	0.029	0.04115	0.00079	0.0121	0.0017	0.29	259.9	4.9	263.0	23.0	329	94	260	5
Zircon_020	870	527	0.61	0.0529	0.0046	0.321	0.030	0.04377	0.00078	0.0136	0.0019	0.63	276.2	4.8	283.0	23.0	330	130	276	5
Zircon_021	146	117	0.80	0.0648	0.0059	0.380	0.035	0.04269	0.00078	0.0147	0.0020	0.12	269.5	4.8	326.0	26.0	790	120	270	5
Zircon_022	191	368	1.93	0.0561	0.0056	0.316	0.033	0.04177	0.00090	0.0130	0.0018	0.21	263.8	5.6	279.0	25.0	470	110	264	6
Zircon_023	754	324	0.43	0.0511	0.0039	0.295	0.024	0.04164	0.00066	0.0128	0.0018	0.16	263.0	4.1	262.0	19.0	240	130	263	4
Zircon_024	1084	542	0.50	0.0502	0.0042	0.299	0.028	0.04320	0.00110	0.0131	0.0018	0.58	272.7	6.8	265.0	21.0	240	100	273	7
Zircon_025	193	217	1.12	0.0560	0.0043	0.334	0.030	0.04370	0.00100	0.0136	0.0019	0.25	275.6	6.1	296.0	23.0	400	150	276	6
Zircon_026	1510	844	0.56	0.0563	0.0046	0.323	0.027	0.04159	0.00085	0.0129	0.0018	0.33	262.7	5.3	284.0	21.0	470	160	263	5
Zircon_027	1287	654	0.51	0.0528	0.0042	0.310	0.026	0.04293	0.00075	0.0133	0.0018	0.25	271.0	4.7	274.0	21.0	330	100	271	5
Zircon_028	203	230	1.13	0.0550	0.0050	0.323	0.030	0.04270	0.00083	0.0129	0.0018	0.21	269.5	5.1	288.0	23.0	430	130	270	5
Zircon_029	204	376	1.85	0.0558	0.0060	0.327	0.041	0.04220	0.00110	0.0135	0.0019	0.30	266.4	6.6	287.0	30.0	540	150	266	7
Zircon_030	280	291	1.04	0.0534	0.0050	0.306	0.030	0.04100	0.00073	0.0121	0.0017	0.18	259.0	4.5	271.0	23.0	350	120	259	5
Zircon_032	543	350	0.64	0.0526	0.0044	0.311	0.028	0.04278	0.00072	0.0124	0.0017	0.43	270.1	4.4	275.0	22.0	330	120	270	4
Zircon_033	825	398	0.48	0.0510	0.0040	0.291	0.025	0.04132	0.00067	0.0126	0.0017	0.09	261.0	4.2	259.0	20.0	223	97	261	4
Zircon_034	592	316	0.53	0.0523	0.0042	0.305	0.026	0.04241	0.00065	0.0132	0.0018	0.24	267.8	4.0	270.0	21.0	320	110	268	4
Zircon_035	483	356	0.74	0.0577	0.0055	0.353	0.039	0.04438	0.00081	0.0153	0.0021	0.43	279.9	5.0	307.0	28.0	510	170	280	5

Notes: U and Th concentrations are calculated employing an external standard zircon as in Paton et al. (2010). 2σ uncertainties propagated according to Paton et al. (2010). $^{207}Pb/^{206}Pb$ ratios, ages and errors are calculated according to Petrus and Kamber (2012). Analyzed spots were 23 micrometers, using an analytical protocol modified from Solari et al. (2010). Data measured employing a Thermo Xseries QICPMS coupled to a Resonetics, Resolution M050 excimer laser workstation.

Table B.1 (continued)

Sample				Corrected Ratios									Corrected Ages (Ma)							
Zircon grain	U (ppm)	Th (ppm)	Th/U	$^{207}Pb/^{206}Pb$	±2σ abs	$^{207}Pb/^{235}U$	±2σ abs	$^{206}Pb/^{238}U$	±2σ abs	$^{208}Pb/^{232}Th$	±2σ abs	Rho	$^{206}Pb/^{238}U$	±2σ	$^{207}Pb/^{235}U$	±2σ	$^{207}Pb/^{206}Pb$	±2σ	Best Age (Ma)	±2σ
IC-99 / Montosa																				
Zircon_001	240	163	0.68	0.0573	0.0029	0.316	0.014	0.03988	0.00091	0.0137	0.0004	0.52	252.1	5.7	279.0	11.0	540	100	252	6
Zircon_002	1001	678	0.68	0.0515	0.0011	0.258	0.008	0.03607	0.00066	0.0111	0.0003	0.03	228.4	4.1	232.8	6.2	270	35	228	4
Zircon_003	1193	2034	1.70	0.0541	0.0011	0.295	0.009	0.03919	0.00073	0.0133	0.0003	0.50	247.8	4.5	263.5	6.4	361	19	248	5
Zircon_004	514	313	0.61	0.0523	0.0014	0.312	0.011	0.04322	0.00090	0.0132	0.0003	0.46	272.7	5.5	275.6	8.9	299	37	273	6
Zircon_005	455	356	0.78	0.0519	0.0015	0.289	0.010	0.04039	0.00080	0.0127	0.0003	0.09	255.2	4.9	257.8	7.6	268	37	255	5
Zircon_006	135	103	0.77	0.0522	0.0044	0.290	0.022	0.04090	0.00100	0.0121	0.0010	0.47	258.4	6.3	258.0	17.0	400	140	258	6
Zircon_007	465	456	0.98	0.0515	0.0015	0.283	0.009	0.03934	0.00073	0.0124	0.0003	0.60	248.7	4.5	253.0	7.0	300	44	249	5
Zircon_008	345	354	1.03	0.0522	0.0013	0.291	0.010	0.04024	0.00075	0.0125	0.0003	0.46	254.3	4.6	259.0	7.6	292	34	254	5
Zircon_010	409	292	0.71	0.0587	0.0024	0.308	0.015	0.03703	0.00080	0.0124	0.0003	0.51	234.4	5.0	272.0	12.0	547	79	234	5
Zircon_011	346	220	0.64	0.0512	0.0016	0.290	0.011	0.04031	0.00091	0.0133	0.0004	0.26	254.8	5.7	258.2	8.4	295	48	255	6
Zircon_012	279	182	0.65	0.0592	0.0018	0.332	0.012	0.03972	0.00076	0.0130	0.0003	0.09	251.1	4.7	291.1	9.1	591	43	251	5
Zircon_013	628	850	1.35	0.0516	0.0013	0.283	0.008	0.03947	0.00076	0.0123	0.0003	0.22	249.5	4.7	253.0	6.5	270	34	250	5
Zircon_014	291	212	0.73	0.0516	0.0022	0.286	0.012	0.04006	0.00077	0.0133	0.0004	0.46	253.2	4.8	257.0	11.0	286	59	253	5
Zircon_015	138	58	0.42	0.0537	0.0035	0.301	0.018	0.04018	0.00099	0.0137	0.0006	0.41	253.9	6.1	267.0	14.0	397	82	254	6
Zircon_016	357	235	0.66	0.0518	0.0016	0.295	0.010	0.04040	0.00110	0.0124	0.0004	0.32	255.4	6.6	263.3	7.6	309	40	255	7
Zircon_017	267	165	0.62	0.0515	0.0020	0.296	0.013	0.04111	0.00087	0.0133	0.0004	0.17	259.7	5.4	263.0	10.0	308	61	260	5
Zircon_018	294	203	0.69	0.0544	0.0021	0.304	0.013	0.04014	0.00077	0.0124	0.0003	0.01	253.7	4.8	269.0	10.0	406	49	254	5
Zircon_020	319	206	0.65	0.0517	0.0016	0.290	0.011	0.04010	0.00087	0.0132	0.0004	0.59	253.5	5.4	258.0	8.8	266	42	254	5
Zircon_021	256	205	0.80	0.0531	0.0025	0.306	0.015	0.04152	0.00087	0.0125	0.0004	0.06	262.2	5.4	271.0	11.0	339	52	262	5
Zircon_022	297	163	0.55	0.0525	0.0020	0.292	0.010	0.04028	0.00095	0.0127	0.0003	0.69	254.6	5.9	259.8	8.1	332	58	255	6
Zircon_023	355	283	0.80	0.0534	0.0021	0.295	0.013	0.03986	0.00084	0.0126	0.0003	0.23	252.0	5.2	262.0	10.0	341	45	252	5
Zircon_024	196	91	0.46	0.0531	0.0032	0.282	0.018	0.03896	0.00085	0.0129	0.0015	0.31	246.4	5.3	252.0	14.0	334	66	246	5
Zircon_025	363	227	0.63	0.0505	0.0016	0.291	0.010	0.04165	0.00081	0.0132	0.0003	0.01	263.0	5.0	259.2	8.2	215	43	263	5
Zircon_026	962	823	0.86	0.0520	0.0012	0.284	0.010	0.03981	0.00091	0.0123	0.0003	0.48	251.6	5.6	253.7	7.9	299	32	252	6
Zircon_027	1838	1351	0.74	0.0518	0.0009	0.299	0.008	0.04194	0.00074	0.0124	0.0003	0.46	264.9	4.6	265.6	5.9	282	22	265	5
Zircon_028	286	222	0.78	0.0518	0.0016	0.284	0.011	0.03987	0.00086	0.0124	0.0003	0.43	252.0	5.3	253.6	8.6	299	44	252	5
Zircon_029	855	940	1.10	0.0519	0.0013	0.285	0.009	0.04017	0.00085	0.0128	0.0003	0.33	253.9	5.3	255.3	6.8	278	29	254	5
Zircon_030	308	214	0.70	0.0511	0.0020	0.287	0.012	0.04098	0.00072	0.0128	0.0003	0.42	258.9	4.5	257.2	9.0	248	57	259	5
Zircon_031	1365	800	0.59	0.0510	0.0011	0.286	0.008	0.04090	0.00076	0.0124	0.0003	0.34	258.4	4.7	255.4	6.3	237	31	258	5
Zircon_032	122	95	0.78	0.0625	0.0061	0.374	0.039	0.04373	0.00095	0.0144	0.0018	0.34	275.9	5.9	322.0	29.0	674	99	276	6
Zircon_033	1464	954	0.65	0.0517	0.0010	0.293	0.008	0.04137	0.00073	0.0123	0.0003	0.09	261.3	4.5	260.8	5.9	258	29	261	5
Zircon_034	561	539	0.96	0.0521	0.0015	0.302	0.011	0.04200	0.00092	0.0134	0.0003	0.13	265.2	5.7	267.6	8.2	306	29	265	6
Zircon_035	249	167	0.67	0.0539	0.0031	0.297	0.017	0.04032	0.00077	0.0126	0.0003	0.33	254.8	4.8	264.0	14.0	380	80	255	5

Notes: U and Th concentrations are calculated employing an external standard zircon as in Paton et al. (2010). 2σ uncertainties propagated according to Paton et al. (2010). $^{207}Pb/^{206}Pb$ ratios, ages and errors are calculated according to Petrus and Kamber (2012). Analyzed spots were 23 micrometers, using an analytical protocol modified from Solari et al. (2010). Data measured employing a Thermo Xseries QICPMS coupled to a Resonetics, Resolution M050 excimer laser workstation.

Table B.1 (continued)

Sample				Corrected Ratios									Corrected Ages (Ma)							
Zircon grain	U (ppm)	Th (ppm)	Th/U	$^{207}Pb/^{206}Pb$	±2σ abs	$^{207}Pb/^{235}U$	±2σ abs	$^{206}Pb/^{238}U$	±2σ abs	$^{208}Pb/^{232}Th$	±2σ abs	Rho	$^{206}Pb/^{238}U$	±2σ	$^{207}Pb/^{235}U$	±2σ	$^{207}Pb/^{206}Pb$	±2σ	Best Age (Ma)	±2σ
IC-102 / Montosa																				
Zircon_071	170	185	1.09	0.0570	0.0039	0.295	0.021	0.03945	0.00094	0.0124	0.0004	0.24	249.4	5.8	262.0	16.0	442	62	249	6
Zircon_072	145	158	1.09	0.0547	0.0033	0.287	0.018	0.03943	0.00080	0.0130	0.0005	0.32	249.3	4.9	256.0	14.0	358	60	249	5
Zircon_073	519	365	0.70	0.0604	0.0031	0.283	0.016	0.03424	0.00085	0.0114	0.0006	0.28	217.0	5.3	253.0	13.0	640	40	217	5
Zircon_074	1343	884	0.66	0.0544	0.0013	0.308	0.010	0.04113	0.00079	0.0130	0.0003	0.41	259.8	4.9	272.5	7.3	388	37	260	5
Zircon_075	103	90	0.87	0.0526	0.0030	0.288	0.016	0.03987	0.00094	0.0126	0.0004	0.01	252.0	5.8	257.0	13.0	367	50	252	6
Zircon_076	424	278	0.66	0.0527	0.0014	0.294	0.010	0.04082	0.00088	0.0125	0.0003	0.31	257.9	5.5	263.8	8.2	316	30	258	6
Zircon_077	319	146	0.46	0.0530	0.0020	0.294	0.013	0.04069	0.00078	0.0131	0.0004	0.54	257.1	4.9	262.0	10.0	343	57	257	5
Zircon_078	813	488	0.60	0.0533	0.0014	0.268	0.009	0.03715	0.00074	0.0118	0.0006	0.37	235.1	4.6	240.6	7.2	327	31	235	5
Zircon_079	243	217	0.89	0.0579	0.0033	0.289	0.018	0.03687	0.00084	0.0121	0.0004	0.46	233.4	5.3	261.0	15.0	545	65	233	5
Zircon_080	67	42	0.63	0.0593	0.0058	0.334	0.036	0.04120	0.00140	0.0143	0.0008	0.20	260.1	8.4	299.0	30.0	650	110	260	8
Zircon_081	253	164	0.65	0.0521	0.0018	0.285	0.012	0.03973	0.00077	0.0127	0.0003	0.19	251.1	4.8	254.4	9.2	318	42	251	5
Zircon_082	592	406	0.69	0.0515	0.0012	0.284	0.009	0.04013	0.00085	0.0127	0.0003	0.54	253.7	5.3	253.7	7.2	274	27	254	5
Zircon_083	179	156	0.87	0.0525	0.0022	0.288	0.013	0.03932	0.00081	0.0122	0.0003	0.11	248.6	5.0	257.0	10.0	369	48	249	5
Zircon_084	382	342	0.90	0.0521	0.0021	0.290	0.012	0.04117	0.00083	0.0127	0.0003	0.07	260.0	5.2	258.7	9.6	281	47	260	5
Zircon_085	176	122	0.69	0.0539	0.0033	0.291	0.018	0.03950	0.00120	0.0124	0.0004	0.12	249.7	7.7	259.0	14.0	370	70	250	8
Zircon_086	127	100	0.79	0.0555	0.0033	0.294	0.019	0.03978	0.00079	0.0125	0.0004	0.17	251.4	4.9	264.0	14.0	417	69	251	5
Zircon_087	194	153	0.79	0.0526	0.0020	0.287	0.011	0.03962	0.00079	0.0122	0.0003	0.02	250.4	4.9	255.7	8.9	353	47	250	5
Zircon_088	112	113	1.01	0.0568	0.0044	0.296	0.024	0.03751	0.00085	0.0121	0.0004	0.28	237.4	5.3	262.0	19.0	530	94	237	5
Zircon_089	120	109	0.91	0.0560	0.0038	0.301	0.022	0.03950	0.00100	0.0123	0.0005	0.36	249.5	6.3	267.0	17.0	529	94	250	6
Zircon_090	201	194	0.96	0.0522	0.0021	0.278	0.012	0.03906	0.00076	0.0124	0.0004	0.02	247.0	4.7	248.7	9.6	285	59	247	5
Zircon_091	1769	1255	0.71	0.0519	0.0009	0.284	0.007	0.03997	0.00070	0.0120	0.0003	0.09	252.6	4.4	253.5	5.7	277	19	253	4
Zircon_092	660	402	0.61	0.0532	0.0018	0.282	0.011	0.03918	0.00086	0.0120	0.0004	0.22	247.8	5.3	252.0	9.0	335	39	248	5
Zircon_093	207	147	0.71	0.0517	0.0044	0.285	0.026	0.04005	0.00096	0.0126	0.0009	0.16	253.2	6.0	254.0	21.0	360	160	253	6
Zircon_094	630	1039	1.65	0.0526	0.0013	0.271	0.009	0.03771	0.00083	0.0115	0.0004	0.68	238.6	5.2	243.0	7.1	330	33	239	5
Zircon_095	180	126	0.70	0.0569	0.0032	0.303	0.018	0.04035	0.00087	0.0127	0.0003	0.36	255.0	5.4	273.0	16.0	458	82	255	5
Zircon_096	159	208	1.31	0.0536	0.0021	0.292	0.012	0.04021	0.00086	0.0122	0.0003	0.52	254.1	5.3	260.9	9.9	346	55	254	5
Zircon_097	360	394	1.09	0.0526	0.0015	0.270	0.010	0.03791	0.00069	0.0118	0.0003	0.30	239.8	4.3	242.7	7.7	303	32	240	4
Zircon_098	180	246	1.37	0.0568	0.0049	0.299	0.025	0.03821	0.00096	0.0118	0.0008	0.03	241.7	6.0	265.0	19.0	490	130	242	6
Zircon_099	175	149	0.85	0.0529	0.0025	0.285	0.014	0.03961	0.00079	0.0125	0.0003	0.41	250.4	4.9	254.0	11.0	341	52	250	5
Zircon_100	225	227	1.01	0.0620	0.0036	0.335	0.020	0.03967	0.00081	0.0126	0.0003	0.12	250.8	5.0	293.0	15.0	643	86	251	5
Zircon_101	667	483	0.72	0.0525	0.0023	0.286	0.012	0.04027	0.00084	0.0124	0.0003	0.07	254.5	5.2	255.4	9.7	305	67	255	5
Zircon_102	109	76	0.70	0.0719	0.0039	0.384	0.022	0.03911	0.00095	0.0145	0.0027	0.28	247.3	5.9	329.0	16.0	983	65	247	6
Zircon_103	182	192	1.05	0.0533	0.0027	0.304	0.016	0.04162	0.00091	0.0137	0.0004	0.42	262.9	5.6	269.0	12.0	386	57	263	6
Zircon_104	282	186	0.66	0.0552	0.0030	0.305	0.020	0.03956	0.00091	0.0126	0.0004	0.11	250.1	5.7	270.0	15.0	434	61	250	6
Zircon_105	389	505	1.30	0.0528	0.0017	0.286	0.010	0.03962	0.00079	0.0116	0.0003	0.60	250.4	4.9	255.1	7.5	328	48	250	5

Notes: U and Th concentrations are calculated employing an external standard zircon as in Paton et al. (2010). 2σ uncertainties propagated according to Paton et al. (2010). $^{207}Pb/^{206}Pb$ ratios, ages and errors are calculated according to Petrus and Kamber (2012). Analyzed spots were 23 micrometers, using an analytical protocol modified from Solari et al. (2010). Data measured employing a Thermo Xseries QICPMS coupled to a Resonetics, Resolution M050 excimer laser workstation.

Table B.1 (continued)

Sample				Corrected Ratios									Corrected Ages (Ma)							
Zircon grain	U (ppm)	Th (ppm)	Th/U	$^{207}Pb/^{206}Pb$	±2σ abs	$^{207}Pb/^{235}U$	±2σ abs	$^{206}Pb/^{238}U$	±2σ abs	$^{208}Pb/^{232}Th$	±2σ abs	Rho	$^{206}Pb/^{238}U$	±2σ	$^{207}Pb/^{235}U$	±2σ	$^{207}Pb/^{206}Pb$	±2σ	Best Age (Ma)	±2σ
IC-106 / Montosa																				
Zircon_106	1395	1249	0.90	0.0556	0.0014	0.324	0.013	0.04250	0.00110	0.0128	0.0003	0.64	268.6	6.6	285.0	10.0	416	47	269	7
Zircon_107	1261	708	0.56	0.0526	0.0012	0.301	0.009	0.04165	0.00076	0.0132	0.0003	0.07	263.1	4.7	266.9	6.7	321	25	263	5
Zircon_108	674	523	0.78	0.0521	0.0017	0.293	0.010	0.04133	0.00083	0.0127	0.0004	0.02	261.1	5.2	262.0	8.4	290	49	261	5
Zircon_109	307	165	0.54	0.0520	0.0021	0.289	0.013	0.03978	0.00081	0.0126	0.0005	0.12	251.4	5.0	257.0	10.0	319	59	251	5
Zircon_110	430	282	0.66	0.0528	0.0019	0.278	0.013	0.03836	0.00079	0.0126	0.0003	0.44	242.6	4.9	249.0	11.0	299	48	243	5
Zircon_111	375	241	0.64	0.0526	0.0026	0.302	0.016	0.04150	0.00086	0.0128	0.0003	0.17	262.1	5.3	270.0	12.0	323	39	262	5
Zircon_112	732	515	0.70	0.0520	0.0022	0.275	0.011	0.03860	0.00100	0.0123	0.0003	0.65	244.4	6.2	246.6	8.7	286	51	244	6
Zircon_113	1005	595	0.59	0.0513	0.0011	0.281	0.008	0.03983	0.00075	0.0127	0.0003	0.47	251.8	4.7	251.5	6.6	264	28	252	5
Zircon_114	763	381	0.50	0.0517	0.0014	0.289	0.011	0.04037	0.00094	0.0125	0.0003	0.55	255.1	5.8	257.3	8.4	275	43	255	6
Zircon_115	780	409	0.52	0.0522	0.0011	0.296	0.009	0.04093	0.00079	0.0130	0.0003	0.60	258.6	4.9	263.4	7.0	316	28	259	5
Zircon_116	604	428	0.71	0.0521	0.0013	0.287	0.009	0.04033	0.00083	0.0122	0.0003	0.37	254.9	5.1	256.4	7.1	308	36	255	5
Zircon_117	578	247	0.43	0.0515	0.0017	0.273	0.011	0.03823	0.00075	0.0121	0.0003	0.35	241.8	4.6	245.2	8.9	269	37	242	5
Zircon_118	901	554	0.61	0.0524	0.0011	0.293	0.009	0.04036	0.00075	0.0127	0.0003	0.32	255.1	4.7	260.6	7.0	290	27	255	5
Zircon_119	354	187	0.53	0.0528	0.0016	0.293	0.011	0.04083	0.00082	0.0130	0.0004	0.14	258.0	5.1	261.1	8.3	321	37	258	5
Zircon_120	299	200	0.67	0.0526	0.0018	0.296	0.012	0.04080	0.00100	0.0131	0.0005	0.19	257.5	6.2	262.8	9.3	349	39	258	6
Zircon_121	1519	2660	1.75	0.0524	0.0014	0.282	0.008	0.03881	0.00076	0.0123	0.0007	0.15	245.5	4.7	251.9	6.6	310	54	246	5
Zircon_122	349	76	0.22	0.0604	0.0027	0.316	0.014	0.03740	0.00075	0.0149	0.0013	0.45	236.7	4.6	278.0	11.0	605	68	237	5
Zircon_123	385	177	0.46	0.0510	0.0020	0.285	0.013	0.04053	0.00097	0.0128	0.0004	0.24	256.1	6.0	256.5	9.5	293	38	256	6
Zircon_124	919	550	0.60	0.0519	0.0013	0.283	0.008	0.03898	0.00073	0.0121	0.0003	0.30	246.5	4.5	252.9	6.3	282	34	247	5
Zircon_125	1260	780	0.62	0.0509	0.0013	0.285	0.010	0.04050	0.00087	0.0128	0.0003	0.60	255.9	5.4	254.6	7.7	244	42	256	5
Zircon_126	358	335	0.94	0.0525	0.0020	0.296	0.012	0.04093	0.00091	0.0127	0.0003	0.02	258.6	5.6	263.4	9.6	326	42	259	6
Zircon_127	1067	636	0.60	0.0516	0.0014	0.286	0.010	0.03968	0.00077	0.0121	0.0003	0.45	250.8	4.8	255.0	7.7	263	32	251	5
Zircon_128	676	772	1.14	0.0562	0.0016	0.312	0.011	0.03986	0.00087	0.0128	0.0003	0.18	252.0	5.4	275.4	8.3	433	41	252	5
Zircon_129	624	326	0.52	0.0518	0.0015	0.275	0.010	0.03832	0.00072	0.0121	0.0003	0.32	242.4	4.5	246.5	7.6	285	35	242	5
Zircon_130	191	98	0.51	0.0532	0.0024	0.309	0.012	0.04175	0.00095	0.0142	0.0004	0.59	263.7	5.9	273.1	9.7	363	66	264	6
Zircon_131	557	620	1.11	0.0526	0.0017	0.293	0.010	0.04037	0.00074	0.0132	0.0003	0.02	255.1	4.6	260.7	8.0	375	67	255	5
Zircon_132	1442	985	0.68	0.0516	0.0011	0.290	0.008	0.04046	0.00075	0.0125	0.0003	0.36	255.7	4.7	258.1	6.4	262	27	256	5
Zircon_133	416	283	0.68	0.0528	0.0021	0.294	0.011	0.04042	0.00097	0.0126	0.0003	0.04	255.4	6.0	261.8	8.9	317	50	255	6
Zircon_134	355	255	0.72	0.0516	0.0014	0.288	0.010	0.04014	0.00081	0.0123	0.0003	0.58	253.7	5.0	256.8	8.1	302	38	254	5
Zircon_135	511	272	0.53	0.0517	0.0014	0.274	0.009	0.03841	0.00073	0.0123	0.0003	0.28	243.0	4.5	246.8	7.8	250	31	243	5
Zircon_136	543	331	0.61	0.0505	0.0016	0.276	0.010	0.03898	0.00079	0.0123	0.0003	0.32	246.5	4.9	247.5	8.1	230	38	247	5
Zircon_137	890	409	0.46	0.0553	0.0022	0.314	0.012	0.04109	0.00088	0.0138	0.0008	0.56	259.6	5.4	276.9	8.9	420	42	260	5
Zircon_138	326	239	0.73	0.0538	0.0018	0.291	0.012	0.03907	0.00080	0.0127	0.0003	0.47	247.1	5.0	259.4	9.7	370	37	247	5
Zircon_139	1056	844	0.80	0.0513	0.0014	0.284	0.009	0.03988	0.00087	0.0127	0.0005	0.40	252.1	5.4	253.7	7.4	270	46	252	5
Zircon_140	430	247	0.57	0.0531	0.0017	0.298	0.010	0.04071	0.00083	0.0133	0.0004	0.14	257.2	5.1	264.8	7.8	339	41	257	5

Notes: U and Th concentrations are calculated employing an external standard zircon as in Paton et al. (2010). 2σ uncertainties propagated according to Paton et al. (2010). $^{207}Pb/^{206}Pb$ ratios, ages and errors are calculated according to Petrus and Kamber (2012). Analyzed spots were 23 micrometers, using an analytical protocol modified from Solari et al. (2010). Data measured employing a Thermo Xseries QICPMS coupled to a Resonetics, Resolution M050 excimer laser workstation.

Table B.1 (continued)

Sample				Corrected Ratios									Corrected Ages (Ma)							
Zircon grain	U (ppm)	Th (ppm)	Th/U	$^{207}Pb/^{206}Pb$	±2σ abs	$^{207}Pb/^{235}U$	±2σ abs	$^{206}Pb/^{238}U$	±2σ abs	$^{208}Pb/^{232}Th$	±2σ abs	Rho	$^{206}Pb/^{238}U$	±2σ	$^{207}Pb/^{235}U$	±2σ	$^{207}Pb/^{206}Pb$	±2σ	Best Age (Ma)	±2σ
RdM-09 / Montosa																				
Zircon_106	190	231	1.22	0.0518	0.0061	0.293	0.037	0.04109	0.00078	0.0140	0.0020	0.51	259.6	4.9	267.0	28.0	320	180	260	5
Zircon_107	557	518	0.93	0.0495	0.0040	0.275	0.025	0.03960	0.00100	0.0132	0.0018	0.80	250.1	6.4	246.0	20.0	180	100	250	6
Zircon_108	150	114	0.76	0.0682	0.0068	0.387	0.040	0.04253	0.00085	0.0152	0.0021	0.17	268.5	5.3	334.0	29.0	830	140	269	5
Zircon_109	162	107	0.66	0.0481	0.0049	0.262	0.027	0.03965	0.00083	0.0118	0.0017	0.20	250.6	5.2	236.0	22.0	250	110	251	5
Zircon_110	125	148	1.19	0.0528	0.0046	0.302	0.031	0.04180	0.00140	0.0125	0.0017	0.29	264.0	8.7	267.0	23.0	360	110	264	9
Zircon_111	168	204	1.21	0.0498	0.0052	0.279	0.030	0.04028	0.00088	0.0119	0.0017	0.20	254.6	5.4	248.0	24.0	251	88	255	5
Zircon_112	205	155	0.75	0.0499	0.0048	0.276	0.027	0.04013	0.00074	0.0122	0.0017	0.19	253.6	4.6	249.0	23.0	410	170	254	5
Zircon_113	790	529	0.67	0.0518	0.0043	0.292	0.026	0.04071	0.00069	0.0130	0.0018	0.37	257.2	4.3	260.0	20.0	302	76	257	4
Zircon_114	286	149	0.52	0.0533	0.0047	0.299	0.028	0.03996	0.00070	0.0134	0.0019	0.19	252.6	4.3	269.0	21.0	410	110	253	4
Zircon_115	227	208	0.92	0.0512	0.0045	0.301	0.028	0.04270	0.00110	0.0139	0.0019	0.28	269.4	6.5	269.0	24.0	310	140	269	7
Zircon_116	659	312	0.47	0.0507	0.0044	0.283	0.027	0.04064	0.00081	0.0126	0.0018	0.73	256.8	5.0	253.0	21.0	210	110	257	5
Zircon_117	292	353	1.21	0.0538	0.0051	0.300	0.033	0.04065	0.00081	0.0131	0.0018	0.22	256.9	5.0	266.0	25.0	420	140	257	5
Zircon_118	2637	685	0.26	0.0567	0.0048	0.323	0.031	0.04126	0.00078	0.0170	0.0024	0.30	260.7	4.8	284.0	23.0	480	150	261	5
Zircon_119	1612	3620	2.25	0.0504	0.0040	0.276	0.023	0.03994	0.00065	0.0118	0.0016	0.07	252.4	4.0	248.0	19.0	200	110	252	4
Zircon_120	251	296	1.18	0.0512	0.0045	0.282	0.027	0.04049	0.00089	0.0123	0.0017	0.44	255.9	5.5	256.0	21.0	290	130	256	6
Zircon_121	1990	2270	1.14	0.0529	0.0045	0.290	0.026	0.03986	0.00061	0.0121	0.0017	0.20	252.0	3.8	258.0	20.0	320	150	252	4
Zircon_122	310	317	1.02	0.0602	0.0058	0.333	0.036	0.04098	0.00074	0.0135	0.0019	0.58	258.9	4.6	291.0	28.0	600	130	259	5
Zircon_123	302	211	0.70	0.0590	0.0050	0.357	0.032	0.04376	0.00075	0.0150	0.0021	0.05	276.1	4.6	310.0	24.0	613	95	276	5
Zircon_124	501	390	0.78	0.0526	0.0043	0.286	0.026	0.04004	0.00098	0.0128	0.0018	0.40	253.1	6.1	255.0	21.0	300	110	253	6
Zircon_125	708	469	0.66	0.0509	0.0042	0.270	0.023	0.03849	0.00067	0.0122	0.0017	0.30	243.4	4.1	244.0	19.0	230	100	243	4
Zircon_126	307	251	0.82	0.0506	0.0043	0.281	0.026	0.04010	0.00076	0.0122	0.0017	0.24	253.5	4.7	251.0	20.0	240	120	254	5
Zircon_127	793	1470	1.85	0.0542	0.0047	0.296	0.028	0.03950	0.00078	0.0123	0.0017	0.52	249.7	4.8	263.0	22.0	400	170	250	5
Zircon_128	241	212	0.88	0.0760	0.0093	0.456	0.061	0.04336	0.00091	0.0186	0.0026	0.16	273.6	5.6	379.0	41.0	1020	180	274	6
Zircon_129	311	99	0.32	0.0659	0.0065	0.364	0.038	0.04030	0.00081	0.0174	0.0025	0.12	254.7	5.0	315.0	28.0	830	130	255	5
Zircon_130	1463	651	0.44	0.0508	0.0041	0.269	0.023	0.03836	0.00061	0.0119	0.0016	0.37	242.6	3.8	242.0	18.0	235	81	243	4
Zircon_131	2290	939	0.41	0.0502	0.0040	0.265	0.023	0.03833	0.00057	0.0121	0.0017	0.17	242.5	3.5	239.0	19.0	220	130	243	4
Zircon_132	143	103	0.72	0.0543	0.0057	0.296	0.031	0.03953	0.00080	0.0128	0.0018	0.19	249.9	5.0	267.0	23.0	420	110	250	5
Zircon_133	165	70	0.43	0.0523	0.0050	0.290	0.029	0.04020	0.00070	0.0131	0.0019	0.23	254.1	4.4	258.0	23.0	320	120	254	4
Zircon_134	1232	721	0.59	0.0498	0.0040	0.273	0.024	0.03988	0.00066	0.0130	0.0018	0.29	252.1	4.1	245.0	19.0	189	87	252	4
Zircon_135	208	157	0.75	0.0702	0.0077	0.394	0.048	0.04172	0.00079	0.0169	0.0024	0.45	263.5	4.9	344.0	33.0	910	140	264	5
Zircon_136	1175	625	0.53	0.0495	0.0039	0.270	0.024	0.03903	0.00073	0.0122	0.0017	0.18	246.8	4.5	242.0	19.0	170	100	247	5
Zircon_137	154	105	0.68	0.0537	0.0052	0.290	0.029	0.03994	0.00079	0.0123	0.0017	0.20	252.4	4.9	257.0	23.0	403	99	252	5
Zircon_138	246	147	0.60	0.0541	0.0052	0.296	0.030	0.03973	0.00075	0.0129	0.0018	0.25	251.2	4.6	263.0	23.0	370	130	251	5
Zircon_139	162	126	0.77	0.0519	0.0051	0.281	0.028	0.03924	0.00080	0.0125	0.0017	0.20	248.1	4.9	251.0	22.0	420	120	248	5
Zircon_140	242	165	0.68	0.0500	0.0045	0.289	0.027	0.04079	0.00073	0.0125	0.0017	0.19	257.7	4.5	257.0	21.0	270	110	258	5

Notes: U and Th concentrations are calculated employing an external standard zircon as in Paton et al. (2010). 2σ uncertainties propagated according to Paton et al. (2010). $^{207}Pb/^{206}Pb$ ratios, ages and errors are calculated according to Petrus and Kamber (2012). Analyzed spots were 23 micrometers, using an analytical protocol modified from Solari et al. (2010). Data measured employing a Thermo Xseries QICPMS coupled to a Resonetics, Resolution M050 excimer laser workstation.

Table B.2 Full geochemical analyses of the Montosa–El Potro Batholith.

Unit		*La Estancilla*	*El Colorado*					*El León*	
Sample		*IC-17*	*IC-14*	*IC-42*	*IC-44*	*IC-51*	*IC-93*	*IC-55*	*IC-56*
wt.%	*d.l.*								
SiO_2	0.01	59.87	68.19	75.89	76.78	73.52	73.54	71.01	73.22
Al_2O_3	0.01	16.46	15.69	12.45	12.18	12.83	13.40	14.43	13.53
Fe_2O_3(T)	0.01	6.68	3.35	1.63	1.68	1.88	1.80	2.28	1.84
MnO	0.001	0.10	0.07	0.03	0.04	0.05	0.03	0.04	0.06
MgO	0.01	3.12	0.95	0.13	0.16	0.07	0.38	0.30	0.54
CaO	0.01	6.14	2.86	0.48	0.33	0.51	1.16	0.96	0.73
Na_2O	0.01	2.73	4.27	3.17	4.05	3.55	3.98	4.55	3.85
K_2O	0.01	1.85	2.66	5.03	4.17	4.74	4.12	3.58	3.90
TiO_2	0.001	0.90	0.48	0.15	0.13	0.24	0.22	0.41	0.27
P_2O_5	0.01	0.14	0.16	0.03	0.04	0.07	0.06	0.10	0.09
LOI		1.89	0.61	1.12	0.78	0.97	1.42	0.87	0.91
Total		99.87	99.28	100.10	100.30	98.42	100.10	98.53	98.94
ppm									
Sc	1	17	6	3	2	3	3	8	5
Be	1	2	2	3	3	4	3	2	3
V	5	156	51	12	11	18	26	23	23
Cr	20	30	<20	<20	<20	<20	<20	<20	<20
Co	1	16	4	<1	<1	1	2	2	2
Ni	20	<20	<20	<20	<20	<20	<20	<20	<20
Cu	10	20	<10	<10	<10	<10	10	<10	<10
Zn	30	60	<30	40	60	<30	<30	50	30
Ga	1	17	17	19	17	16	14	16	15
Ge	0.5	1.7	1.7	1.9	1.1	2.1	2	1.7	1.9
As	5	11	<5	<5	<5	<5	<5	<5	<5
Rb	1	85	89	269	194	284	126	99	166
Sr	2	297	247	37	30	96	115	120	123
Y	0.5	14.8	24.5	47.1	47.9	31.2	16.1	21.2	19.8
Zr	1	139	210	232	193	138	103	303	126
Nb	0.2	5.1	7.4	17.3	14.3	15.8	7.8	8.7	8.4
Mo	2	<2	<2	2	<2	3	<2	<2	<2
Ag	0.5	0.7	1.3	1	0.9	<0.5	<0.5	1.6	<0.5
In	0.1	<0.1	<0.1	<0.1	<0.1	<0.1	<0.1	<0.1	<0.1
Sn	1	1	1	4	2	3	1	<1	2
Sb	0.2	0.3	<0.2	0.3	<0.2	<0.2	<0.2	<0.2	<0.2
Cs	0.1	3.8	1.7	6.8	5.3	12.5	1.9	2.4	3.1
Ba	3	323	818	255	201	379	657	2607	585
La	0.05	17.9	42.1	42.9	30.6	49.3	27.2	55.1	26
Ce	0.05	35.6	77.8	90.9	62.2	98.5	52.1	119	51
Pr	0.01	4.1	8.76	10.8	8.06	10.7	5.8	11.4	5.71
Nd	0.05	15.7	31.8	40.4	30.5	35.3	19.4	41.9	20.7
Sm	0.01	3.28	6.22	8.97	7.29	6.02	3.57	6.87	3.86
Eu	0.005	0.937	1.28	0.38	0.271	0.68	0.628	2.27	0.768
Gd	0.01	3.02	4.96	7.98	7.26	5.02	2.86	4.85	3.38
Tb	0.01	0.48	0.83	1.49	1.41	0.88	0.5	0.74	0.56
Dy	0.01	2.72	4.63	8.82	8.38	5.23	2.79	4.1	3.34
Ho	0.01	0.55	0.89	1.79	1.82	1.1	0.56	0.81	0.72
Er	0.01	1.5	2.59	5.08	5.02	3.35	1.67	2.29	2.11
Tm	0.005	0.254	0.411	0.846	0.871	0.559	0.303	0.38	0.391
Yb	0.01	1.61	2.56	5.41	5.37	3.94	2.01	2.49	2.62
Lu	0.002	0.226	0.338	0.75	0.736	0.571	0.308	0.388	0.402
Hf	0.1	3.2	4.7	6.8	6.1	3.9	2.9	7.1	3.7
Ta	0.01	0.6	0.93	2.34	1.81	1.75	1.2	0.83	1.19
W	0.5	<0.5	<0.5	8	<0.5	3.2	<0.5	<0.5	<0.5
Tl	0.05	0.55	0.57	2.14	2.62	2.2	0.72	0.73	0.96
Pb	5	12	11	22	16	15	10	14	15
Bi	0.1	0.2	<0.1	0.3	<0.1	0.2	0.2	<0.1	<0.1
Th	0.05	8.93	10	31.9	25.2	31.5	11.9	15.6	17.8
U	0.01	2.09	1.42	6.14	4.65	3.25	2.31	1.66	2.04

Notes: Major element oxides and trace elements were analysed by Actlabs Canada.
Mayor elements plus Sc, Be, V, Sr, Zr and Ba were analysed using FUS-ICP and trace elements using FUS-ICPMS.
Total iron as Fe_2O_3; *d.l.* = detection limit.

Table B.2 (continued)

Unit	*El León*			*Chollay*				
Sample	*IC-57*	*IC-58*	*IC-94*	*IC-46*	*IC-47*	*IC-49*	*IC-79*	*IC-81*
wt.%								
SiO_2	70.55	71.23	76.19	78.45	76.19	74.63	70.00	72.07
Al_2O_3	14.70	14.10	12.63	12.03	12.11	12.18	14.17	13.73
Fe_2O_3(T)	3.05	3.18	0.69	1.00	1.57	3.04	3.80	2.91
MnO	0.09	0.06	0.01	0.02	0.04	0.04	0.08	0.06
MgO	0.88	0.88	0.07	0.03	0.19	0.27	0.87	0.55
CaO	2.13	2.26	0.67	0.30	0.87	0.63	2.17	1.46
Na_2O	3.93	3.31	3.70	3.57	2.97	3.60	3.84	3.88
K_2O	3.56	3.98	4.48	4.89	4.89	4.65	4.45	4.57
TiO_2	0.36	0.36	0.11	0.10	0.19	0.20	0.57	0.37
P_2O_5	0.09	0.10	0.04	0.03	0.05	0.08	0.18	0.11
LOI	0.99	0.84	1.02	0.51	1.55	0.58	0.50	0.54
Total	100.30	100.30	99.62	100.90	100.60	99.90	100.60	100.20
ppm								
Sc	8	7	3	2	3	3	9	5
Be	3	2	1	6	4	5	4	4
V	48	52	11	9	13	26	45	29
Cr	20	20	<20	<20	<20	20	<20	20
Co	4	5	<1	<1	1	2	4	3
Ni	<20	<20	<20	<20	<20	<20	<20	<20
Cu	<10	<10	<10	<10	<10	10	<10	<10
Zn	50	40	<30	<30	30	50	50	30
Ga	14	15	12	15	14	19	19	18
Ge	1.7	1.9	1.8	2.2	1.8	2	2.1	2
As	<5	<5	<5	<5	< 5	5	<5	<5
Rb	135	168	132	347	239	251	219	185
Sr	256	199	64	27	40	59	143	140
Y	23	24.9	18	37.1	23.5	48.7	51.4	35.7
Zr	140	137	54	84	115	203	290	225
Nb	5.7	6.8	5.1	25.7	12.3	17.6	23.3	16
Mo	<2	<2	<2	<2	<2	3	<2	2
Ag	<0.5	<0.5	<0.5	<0.5	<0.5	1.1	0.8	0.6
In	<0.1	<0.1	<0.1	<0.1	0.1	<0.1	<0.1	<0.1
Sn	1	2	<1	1	178	11	4	2
Sb	<0.2	<0.2	<0.2	<0.2	<0.2	<0.2	<0.2	<0.2
Cs	3.2	4.1	1.9	5	3.8	3.7	7.1	4.1
Ba	827	793	846	101	365	211	542	559
La	26.5	34.7	16.6	18.2	34.7	51.8	62.4	69
Ce	53.8	68.3	32.7	49.1	65.9	111	127	133
Pr	6.24	7.64	3.72	4.95	7.47	12.7	14.7	14.3
Nd	23.4	26.6	12.9	17.6	25.7	47.2	53.3	47.4
Sm	4.81	5.36	2.73	4.31	4.76	9.84	10.5	7.96
Eu	0.922	0.883	0.388	0.259	0.586	0.361	1.13	1
Gd	4.07	4.45	2.48	4.09	3.87	8.63	9.1	5.93
Tb	0.68	0.75	0.47	0.91	0.69	1.58	1.58	1
Dy	4.02	4.2	2.96	5.85	4.05	8.91	9.01	5.9
Ho	0.83	0.9	0.62	1.35	0.86	1.87	1.83	1.2
Er	2.45	2.6	1.82	4.25	2.53	5.27	5.18	3.52
Tm	0.409	0.45	0.319	0.796	0.46	0.876	0.856	0.628
Yb	2.48	2.86	2.05	5.75	3.01	5.53	5.67	3.91
Lu	0.356	0.423	0.291	0.809	0.429	0.785	0.78	0.572
Hf	3.9	3.9	1.8	3.3	3.5	6.5	7.1	5.6
Ta	0.81	1.12	0.84	5.26	1.77	2.06	2.38	2.01
W	<0.5	7.3	<0.5	0.9	<0.5	<0.5	5.4	<0.5
Tl	1.08	1.16	0.84	2.48	2.73	2.42	1.35	1.24
Pb	14	12	14	19	13	27	18	17
Bi	0.2	0.6	0.3	0.3	0.9	0.7	<0.1	<0.1
Th	10.6	16.9	8.17	38.7	19.7	29.2	35.8	24.9
U	1.79	3.8	1.51	6.49	3.01	5.37	8.08	3.9

Notes: Major element oxides and trace elements were analysed by Actlabs Canada.
Mayor elements plus Sc, Be, V, Sr, Zr and Ba were analysed using FUS-ICP and trace elements using FUS-ICPMS.
Total iron as Fe_2O_3; *d.l.* = detection limit.

Table B.2 (continued)

Unit	*Chollay*			*Montosa*				
Sample	*IC-83*	*IC-91*	*IC-92*	*IC-22*	*IC-23*	*IC-96*	*IC-97*	*IC-98*
wt.%								
SiO_2	76.14	68.80	75.38	68.82	78.31	60.58	56.22	69.62
Al_2O_3	13.00	14.71	12.70	14.88	11.85	17.95	18.34	14.46
Fe_2O_3(T)	1.37	3.76	2.44	4.20	0.97	5.24	6.12	3.83
MnO	0.05	0.06	0.02	0.06	0.01	0.11	0.11	0.06
MgO	0.33	0.98	0.13	1.27	0.14	1.84	1.90	1.16
CaO	0.93	2.58	0.71	3.44	0.68	5.01	7.08	3.44
Na_2O	3.91	3.82	4.41	3.28	2.69	4.30	4.25	3.66
K_2O	4.17	3.69	3.85	3.37	5.40	1.73	1.13	1.58
TiO_2	0.17	0.48	0.25	0.49	0.12	0.64	0.82	0.47
P_2O_5	0.08	0.15	0.06	0.13	0.03	0.21	0.27	0.14
LOI	0.74	1.78	0.78	0.81	0.62	3.05	4.40	0.79
Total	100.90	100.80	100.70	100.70	100.80	100.70	100.60	99.21
ppm								
Sc	4	8	4	10	3	13	15	3
Be	3	3	3	2	<1	2	2	2
V	13	66	20	76	14	99	111	66
Cr	<20	<20	<20	<20	<20	<20	<20	20
Co	1	5	2	6	<1	9	10	6
Ni	<20	<20	<20	<20	<20	<20	<20	<20
Cu	<10	<10	10	<10	<10	10	20	<10
Zn	<30	40	<30	<30	<30	60	70	50
Ga	14	16	17	16	11	19	20	16
Ge	2.1	1.8	1.6	1.7	1.9	1.6	1.5	1.4
As	<5	7	<5	6	<5	<5	<5	<5
Rb	172	133	81	157	106	60	40	69
Sr	89	235	55	245	86	427	427	296
Y	22.8	19.5	22.9	21.7	5.9	17.5	24.7	8.2
Zr	74	184	242	200	76	192	293	161
Nb	6.4	7.2	5.8	7.8	0.8	2.5	4.1	1.1
Mo	<2	<2	<2	<2	<2	<2	<2	<2
Ag	<0.5	<0.5	1	1.1	<0.5	0.6	1.3	<0.5
In	<0.1	<0.1	<0.1	<0.1	<0.1	<0.1	<0.1	<0.1
Sn	1	2	<1	2	<1	<1	2	<1
Sb	<0.2	<0.2	<0.2	0.4	<0.2	<0.2	<0.2	<0.2
Cs	3.7	3.8	1.1	8.3	1.5	3.5	4.2	2.6
Ba	617	727	683	846	1101	935	540	629
La	27	29.7	33	31	33.7	21.4	29.7	71.8
Ce	52.4	63.2	64.7	62.6	60.6	43	60.1	120
Pr	5.81	7.51	7.3	7.1	6.22	5.06	7.14	11.4
Nd	20.3	27.2	25.9	25.6	19.3	19.9	28.3	33.2
Sm	3.96	4.71	4.89	4.87	2.68	3.89	5.7	3.69
Eu	0.644	0.886	0.674	0.982	0.617	1.1	1.67	0.891
Gd	3.41	3.72	4.03	4.04	1.68	3.5	5.02	1.85
Tb	0.62	0.62	0.7	0.68	0.22	0.58	0.83	0.26
Dy	3.78	3.5	4.02	3.83	1.15	3.23	4.51	1.47
Ho	0.81	0.72	0.86	0.76	0.22	0.66	0.89	0.28
Er	2.36	2.09	2.62	2.2	0.63	1.82	2.56	0.88
Tm	0.424	0.368	0.434	0.367	0.104	0.279	0.401	0.152
Yb	2.72	2.39	2.9	2.36	0.82	1.75	2.48	0.94
Lu	0.401	0.349	0.431	0.329	0.128	0.257	0.355	0.146
Hf	2.1	4.5	6	4.6	2.7	4.3	6.5	3.8
Ta	0.98	0.95	0.85	1.21	0.34	0.17	0.66	0.31
W	<0.5	<0.5	<0.5	<0.5	<0.5	<0.5	<0.5	<0.5
Tl	1.21	0.93	0.88	0.86	0.61	0.43	0.28	0.38
Pb	20	17	<5	11	12	8	9	7
Bi	<0.1	<0.1	<0.1	0.1	<0.1	<0.1	<0.1	0.2
Th	14.4	16.6	10.3	18.8	10.6	3.85	5.61	12.4
U	1.62	2.03	2.65	3.86	1.49	1.26	1.39	1.64

Notes: Major element oxides and trace elements were analysed by Actlabs Canada.
Mayor elements plus Sc, Be, V, Sr, Zr and Ba were analysed using FUS-ICP and trace elements using FUS-ICPMS.
Total iron as Fe_2O_3; *d.l.* = detection limit.

Table B.2 (continued)

Unit	*Montosa*								
Sample	*IC-99*	*IC-100*	*IC-101*	*IC-102*	*IC-103*	*IC-104*	*IC-106*	*RdM-07*	*RdM-09*
wt.%									
SiO_2	68.87	71.05	62.90	70.88	59.24	61.99	67.25	74.02	78.46
Al_2O_3	15.06	14.59	17.02	13.07	17.84	17.61	14.64	13.35	11.96
Fe_2O_3(T)	4.31	2.59	4.77	2.40	6.16	5.66	4.25	2.88	1.05
MnO	0.08	0.07	0.09	0.06	0.11	0.09	0.09	0.05	0.03
MgO	1.33	0.88	1.47	0.63	2.21	1.90	1.33	0.48	0.13
CaO	3.81	2.67	4.44	1.68	5.34	3.59	2.44	1.60	0.83
Na_2O	3.94	3.94	4.06	3.78	4.01	5.22	3.77	3.28	3.72
K_2O	1.49	2.56	2.35	3.26	2.01	1.38	2.91	4.14	3.78
TiO_2	0.50	0.30	0.58	0.30	0.79	0.62	0.55	0.34	0.11
P_2O_5	0.18	0.10	0.20	0.09	0.21	0.20	0.15	0.10	0.03
LOI	0.69	0.88	0.74	2.25	0.73	2.14	1.54	0.47	0.26
Total	100.30	99.62	98.64	98.39	98.64	100.40	98.93	100.70	100.40
ppm									
Sc	8	6	10	5	12	14	12	2	1
Be	2	2	2	2	2	2	2	2	1
V	74	39	83	32	126	109	84	33	13
Cr	<20	<20	<20	<20	<20	<20	<20	<20	<20
Co	6	4	7	3	12	9	7	3	<1
Ni	<20	<20	<20	<20	<20	<20	<20	<20	<20
Cu	<10	<10	10	<10	10	10	<10	<10	<10
Zn	60	30	50	<30	80	60	40	<30	<30
Ga	17	16	19	14	21	19	17	14	12
Ge	1.5	1.6	1.6	1.4	1.7	1.3	1.9	1.6	1.7
As	<5	<5	<5	<5	<5	<5	<5	<5	<5
Rb	57	72	75	117	91	49	85	102	69
Sr	303	235	336	65	352	725	338	172	37
Y	9.9	11.5	15.1	21	22.6	18.7	19.1	5.8	5.8
Zr	162	104	207	144	162	167	160	182	72
Nb	0.9	0.6	4.8	6	4.6	3	5.2	<0.2	<0.2
Mo	<2	<2	<2	<2	<2	<2	<2	<2	<2
Ag	<0.5	<0.5	0.9	<0.5	<0.5	<0.5	<0.5	<0.5	1.4
In	<0.1	<0.1	<0.1	<0.1	<0.1	<0.1	<0.1	<0.1	<0.1
Sn	<1	<1	<1	<1	<1	<1	<1	<1	<1
Sb	<0.2	<0.2	<0.2	<0.2	<0.2	<0.2	<0.2	<0.2	<0.2
Cs	1.9	1.3	2.3	2.4	3.7	0.7	2.3	2.1	0.7
Ba	728	964	691	552	604	355	1176	2023	218
La	28.1	18.2	22	32.7	22	18	45.1	53.2	19.9
Ce	49.9	34.2	44.8	63.6	46.3	38.6	84.8	90.8	38.5
Pr	5.21	3.91	5.06	7.11	5.91	4.89	8.87	9.15	4.33
Nd	17.4	13.8	17.3	25	23.6	19.8	30	28.7	14.5
Sm	2.7	2.65	2.92	4.44	4.86	4.22	4.99	3.57	2.38
Eu	0.964	0.655	0.974	0.826	1.29	1.11	1.09	0.593	0.363
Gd	2	2.12	2.39	3.63	4.37	3.77	3.99	1.87	1.64
Tb	0.31	0.36	0.4	0.64	0.71	0.61	0.61	0.18	0.21
Dy	1.74	2.05	2.3	3.66	4.15	3.4	3.44	0.97	1.05
Ho	0.35	0.44	0.51	0.73	0.83	0.66	0.69	0.19	0.21
Er	1.02	1.26	1.59	2.11	2.33	1.99	1.98	0.61	0.59
Tm	0.186	0.19	0.273	0.361	0.374	0.313	0.304	0.112	0.085
Yb	1.16	1.22	1.8	2.36	2.36	2.05	2.07	0.88	0.6
Lu	0.177	0.163	0.264	0.338	0.333	0.282	0.291	0.15	0.092
Hf	3.8	2.6	4.8	4.1	4.1	4.1	4.1	4.8	1.8
Ta	0.25	0.27	0.31	0.89	1.17	0.41	0.52	0.18	0.3
W	<0.5	<0.5	<0.5	<0.5	<0.5	<0.5	<0.5	<0.5	<0.5
Tl	0.34	0.38	0.35	0.61	0.54	0.32	0.45	0.52	0.57
Pb	7	10	10	8	9	5	13	15	16
Bi	<0.1	<0.1	<0.1	<0.1	<0.1	<0.1	<0.1	0.1	<0.1
Th	4.49	3.33	3.53	12.6	5.21	5.4	9.94	11.5	16.1
U	1.3	0.75	0.97	2.32	1.32	1.59	1.85	1.65	0.98

Notes: Major element oxides and trace elements were analysed by Actlabs Canada.
Mayor elements plus Sc, Be, V, Sr, Zr and Ba were analysed using FUS-ICP and trace elements using FUS-ICPMS.
Total iron as Fe_2O_3; *d.l.* = detection limit.

Table B.3 Summarized geochemical classification for all the analysed samples from the Montosa–El Potro Batholith.

Sample	TAS Classification	TAS Classification	SiO_2-K_2O	$(La/Yb)_N$	(Eu/Eu*)	A/CNK	A/NK	S-I-A type
La Estancilla pluton								
IC-17	Tonalite	Diorite	Calc-alkaline	7.6	0.89	0.93	2.53	I-type
Montosa								
IC-22	Granodiorite	Granodiorite	High-K Calc-alkaline	9.0	0.66	0.97	1.65	I-type
IC-23	Afs granite	Granite	High-K Calc-alkaline	28.0	0.83	1.03	1.15	I-type, slightly S-type
IC-96	Qz monzodiorite	Diorite	Calc-alkaline	8.3	0.89	0.99	2.01	I-type
IC-97	Qz monzodiorite	Diorite	Calc-alkaline	8.2	0.93	0.87	2.23	I-type
IC-98	Granodiorite	Granodiorite	Calc-alkaline	52.1	0.92	1.03	1.87	I-type
IC-99	Granodiorite	Granodiorite	Calc-alkaline	16.5	1.21	1.00	1.86	I-type
IC-100	Granodiorite	Granite	Calc-alkaline	10.2	0.81	1.03	1.58	I-type
IC-101	Granodiorite	Granodiorite	Calc-alkaline	8.3	1.09	0.98	1.85	I-type
IC-102	Granite	Granite	High-K Calc-alkaline	9.5	0.61	1.02	1.34	I-type
IC-103	Qz monzodiorite	Diorite	Calc-alkaline	6.4	0.84	0.97	2.03	I-type
IC-104	Qz monzodiorite	Granodiorite	Calc-alkaline	6.0	0.83	1.06	1.75	I-type, slightly S-type
IC-106	Granodiorite	Granodiorite	High-K Calc-alkaline	14.9	0.72	1.06	1.57	I-type, slightly S-type
RdM-07	Granite	Granite	High-K Calc-alkaline	41.2	0.63	1.04	1.35	I-type
RdM-09	Granite	Granite	High-K Calc-alkaline	22.6	0.53	1.02	1.17	I-type
El León								
IC-55	Granite	Granite	High-K Calc-alkaline	15.1	0.63	1.10	1.27	A-type
IC-56	Granite	Granite	High-K Calc-alkaline	6.8	0.62	1.14	1.28	S-type
IC-57	Granite	Granite	High-K Calc-alkaline	7.3	0.54	1.04	1.42	I-type
IC-58	Granite	Granite	High-K Calc-alkaline	8.3	0.45	1.02	1.45	I-type
IC-94	Granite	Granite	High-K Calc-alkaline	5.5	1.14	1.04	1.15	I-type
El Colorado								
IC-14	Granodiorite	Granodiorite	Calc-alkaline	11.2	0.68	1.04	1.58	I-type
IC-42	Granite	Granite	High-K Calc-alkaline	5.4	0.13	1.08	1.17	A-type
IC-44	Afs granite	Granite	High-K Calc-alkaline	3.9	0.11	1.03	1.09	A-type
IC-51	Granite	Granite	High-K Calc-alkaline	8.5	0.37	1.08	1.17	I-type, slightly S-type
IC-93	Granite	Granite	High-K Calc-alkaline	9.2	0.58	1.02	1.22	I-type
Chollay								
IC-46	Afs granite	Granite	High-K Calc-alkaline	2.2	0.19	1.03	1.08	I-type
IC-47	Granite	Granite	High-K Calc-alkaline	7.9	0.40	1.03	1.19	I-type, slightly S-type
IC-49	Granite	Granite	High-K Calc-alkaline	6.4	0.12	1.01	1.11	A-type
IC-79	Granite	Granite	High-K Calc-alkaline	7.5	0.34	0.94	1.27	A-type
IC-81	Granite	Granite	High-K Calc-alkaline	12.0	0.43	0.98	1.21	I-type
IC-83	Granite	Granite	High-K Calc-alkaline	6.8	0.52	1.03	1.19	I-type
IC-91	Granite	Granite	High-K Calc-alkaline	8.5	0.62	0.98	1.43	I-type
IC-92	Granite	Granite	High-K Calc-alkaline	7.8	0.45	1.00	1.11	I-type

Notes: TAS Classification according to Middlemost (1985).
TAS Classification according to Middlemost (1994).
Afs: alkali feldspar.
SiO_2–K_2O classification according to Peccerillo and Taylor (1976).
$(La/Yb)_N$, N: normalized to chondrite, McDonough and Sun (1995).
A/CNK = $Al_2O_3/(CaO+Na_2O+K_2O)$ (molar).
A/NK = $Al_2O_3/(Na_2O+K_2O)$ (molar).
I-, S-, and A-type classification according to Ce+Nb+Zr+Y vs. 10,000×Ga/Al granite discrimination diagram from Whalen et al. (1987). I- and S-type separation according to Chappell and White (2001).

Summarized petrographic descriptions

Generally, units from the Montosa–El Potro Batholith correspond to tonalites with quartz dioritic mafic enclaves, granites and porphyritic rhyolites.

La Estancilla pluton is only represented by sample IC-17 (Fig. B.1), which consists in a white medium- to coarse-grained phaneritic tonalite constituted by plagioclase (55%), quartz (30%), hornblende (10%) and biotite (5%). Accessory minerals (<2%) are apatite, titanite, zircon and opaque. This unit also presents medium-grained phaneritic mafic enclaves composed by plagioclase (50%), hornblende (39%) and biotite (10%), with accessory titanite and opaque. The mafic enclaves can be classified as diorites.

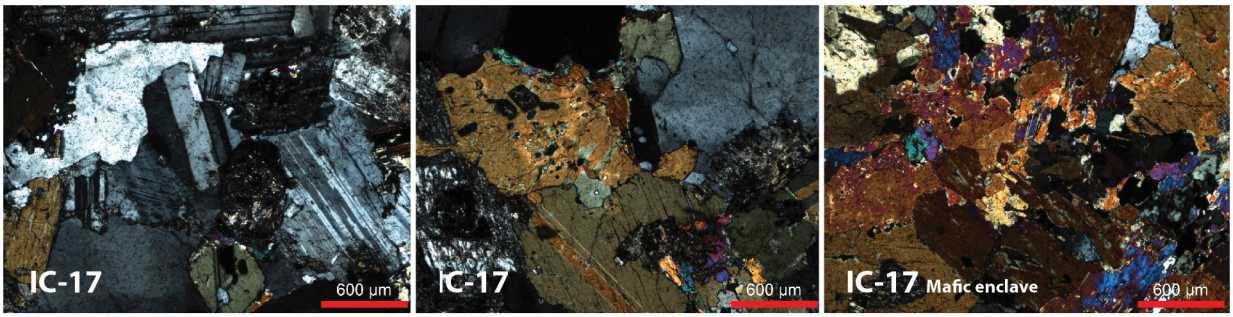

Fig. B.1 Photomicrographs of La Estancilla pluton. Photomicrographs of sample IC-17, classified as tonalite, together with its mafic enclave classified as diorite (5x/XPL).

Montosa unit (Fig. B.2) consists in medium- to coarse-grained white phaneritic rocks constituted by plagioclase (35-67%), quartz (20-55%), K-feldspar (4-15%), biotite (6-10%) and hornblende (1-5%), with accessory apatite, titanite, zircon and opaque. Most rocks can be classified as tonalites with minor granodiorites they also present fine-grained mafic enclaves constituted by plagioclase (49-61%), hornblende (1-30%), biotite (20-25%) and quartz (ca. 15%), with accessory titanite and opaque, and classified as quartz diorites. Tonalites are intruded by pink medium- to coarse- grained phaneritic granites constituted by K-feldspar (20-47%), quartz (25-42%), plagioclase (20-30%), biotite (0-5%) and hornblende (ca. 2%), with accessory apatite, titanite, zircon and opaque; and sometimes microcline. One sample intruding the tonalites was classified as porphyritic rhyolite Some samples present myrmekitic intergrowth and scarce symplektitic texture.

El León unit (Fig. B.3) consists in whitish to pinkish medium- to coarse-grained phaneritic granites (and one quartz monzonite) composed by K-feldspar (30-45%), plagioclase (20-36%), biotite (1-5%) and hornblende (0-2%), with accessory apatite, titanite, zircon and opaques; and sometimes white mica and microcline. Myrmekitic, symplektitic and micrographic textures are seen within this unit.

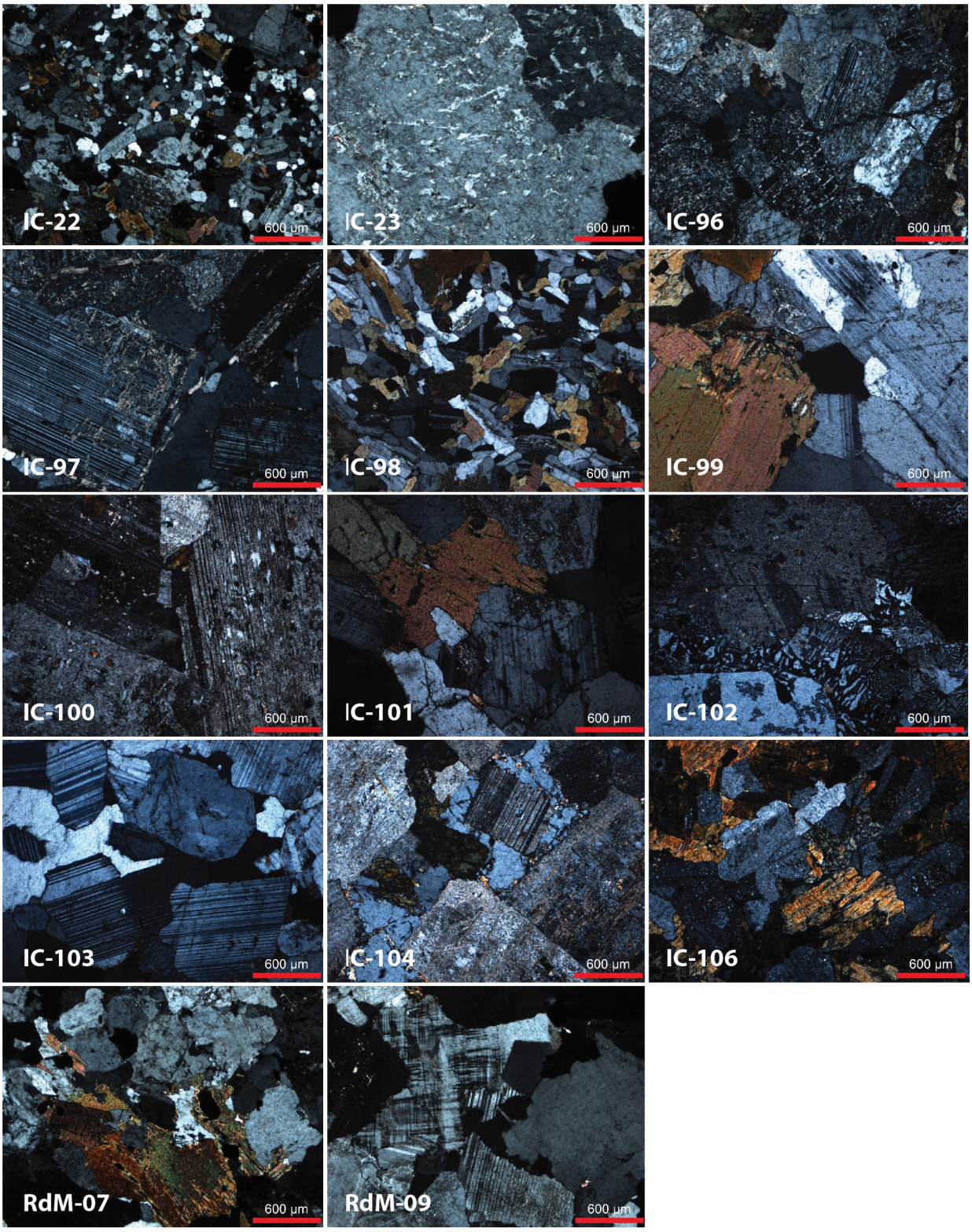

Fig. B.2 Photomicrographs of Montosa unit. Photomicrographs of sample IC-22: hbl-bt tonalite, IC-23: bt syenogranite, IC-96: hbl-bt tonalite, IC-97: hbl-bt tonalite, IC-98: hbl-bt tonalite, IC-99: hbl-bt granodiorite, IC-100: bt monzogranite, IC-101: hbl-bt tonalite, IC-102: bt porhyritic rhyolite, IC-103: hbl-bt granodiorite, IC-104: hbl-bt tonalite, IC-106: hbl-bt granodiorite, RdM-07: bt syenogranite, and RdM-09: bt syenogranite (5x/XPL).

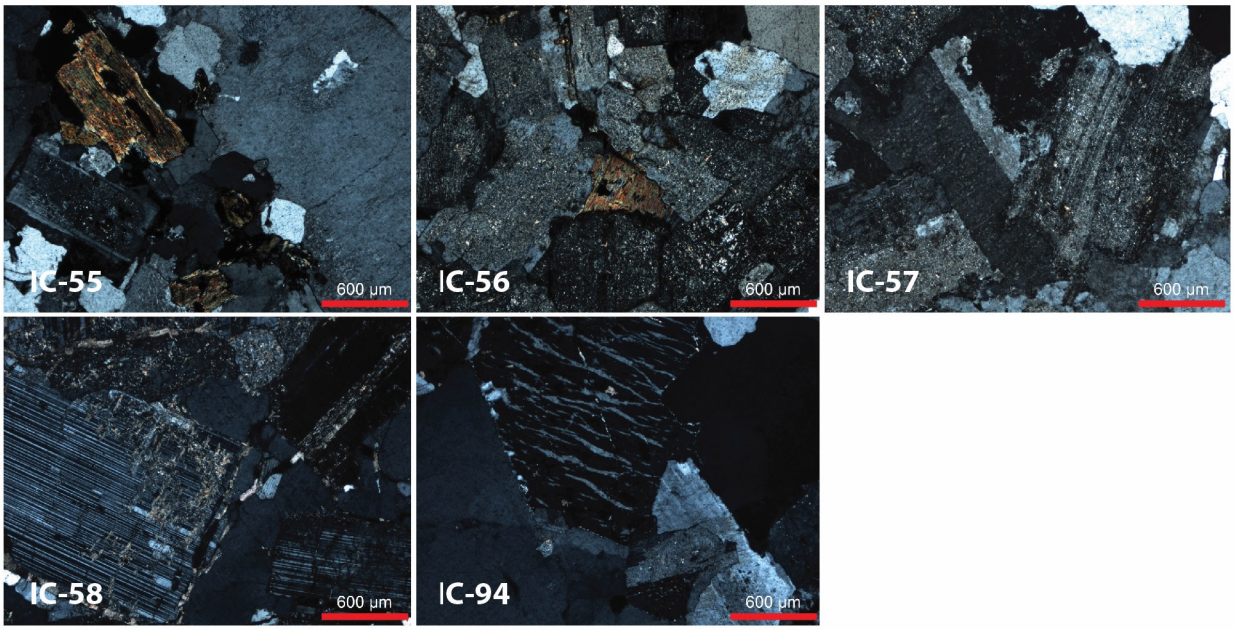

Fig. B.3 Photomicrographs of El León unit. Photomicrographs of sample IC-55: hbl-bt monzogranite, IC-56: bt monzogranite, IC-57: hbl-bt quartz monzonite, IC-58: hbl-bt monzogranite, and IC-94: syenogranite (5x/XPL).

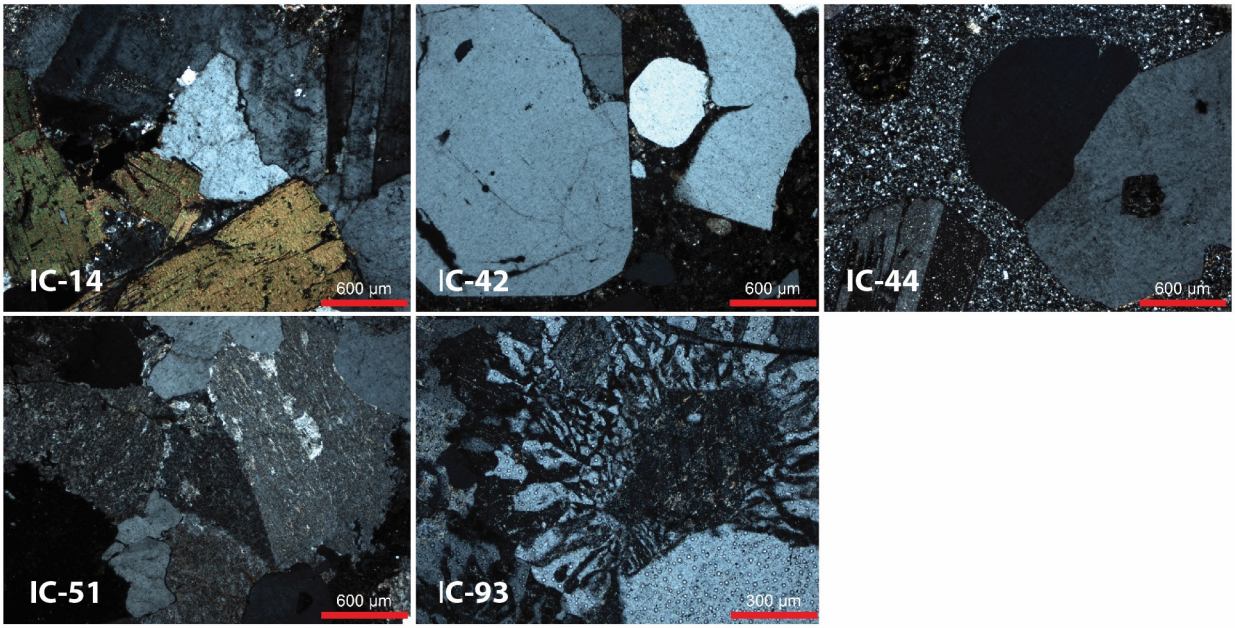

Fig. B.4 Photomicrographs of El Colorado unit. Photomicrographs of sample IC-14: bt monzogranite, IC-42: hbl-bt porphyritic rhyolite, IC-44: hbl-bt porphyritic rhyolite, IC-51: monzogranite, and IC-93: bt syenogranite (5x/XPL).

El Colorado unit (Fig. B.4) corresponds to pink medium- to coarse-grained phaneritic granites constituted by K-feldspar (28-45%), quartz (30-35%), plagioclase (8-30%), biotite (1-5%) and hornblende (0-1%), with accessory apatite, titanite, zircon and opaques; and sometimes microcline. This unit also presents red-brick porphyritic rhyolites, composed by quartz (15-20%), K-feldspar (10-20%),

plagioclase (5-10%) and biotite (0-1%) phenocrysts within a felsitic groundmass (ca. 60%). Myrmekitic and micrographic intergrowth is observed within this unit.

Lastly, Chollay unit (Fig. B.5) corresponds to pink medium- to coarse-grained granites, alkali feldspar granites and granodiorites constituted by K-feldspar (25-53%), plagioclase (10-39%), quartz (30-35%), biotite (1-5%) and hornblende (0-1%), with accessory apatite, titanite, zircon and opaque; and sometimes white mica and microcline. This unit also presents red-brick porphyritic rhyolites and quartz latites composed by K-feldspar (ca. 23%), quartz (10%), plagioclase (7%), biotite (2%) and hornblende (1%), within a felsitic groundmass (ca. 60%). Myrmekitic and micrographic intergrowth is observed within this unit.

On the other hand, practically all samples are weakly altered (ca. 1-15%), regardless of the unit they belong to. In this respect, feldspars (plagioclase and alkali feldspars) are altered to clay and sericite, and mafic minerals (hornblende and biotite) altered to chlorite and epidote. Carbonates and limonites can be seen disseminated along the minerals and filling microveins. Chlorite and epidote can also be seen scarcely disseminated in the entire rocks.

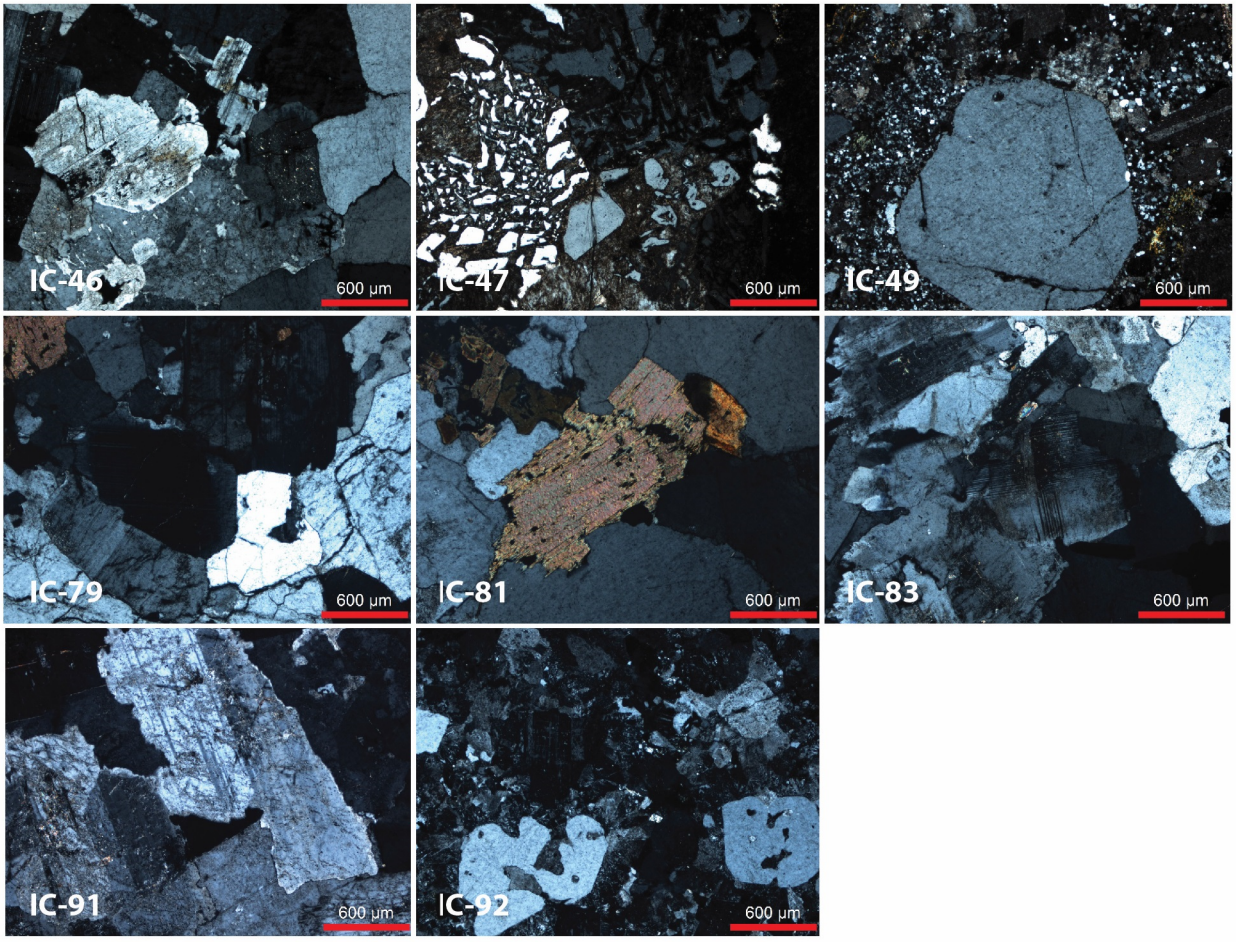

Fig. B.5 Photomicrographs of Chollay unit. Photomicrographs of sample IC-46: bt syenogranite, IC-47: alkali feldspar granite, IC-49: hbl-bt porphyritic rhyolite, IC-79: hbl-bt granodiorite, IC-81: bt monzogranite, IC-83: bt syenogranite, IC-91: hbl-bt syenogranite, and IC-92: porphyritic quartz latite (5x/XPL).

APPENDIX C

Conference abstracts

EGU Poster presentation

European Geosciences Union, General Assembly
Vienna, Austria. 27 April–02 May 2014

Late Paleozoic to Triassic magmatism in the north-central High Andes, Chile: New insights from SHRIMP U–Pb geochronology and O–Hf isotopic signatures in zircon

Á. Del Rey[1], K. Deckart[1], M. Fanning[2], and C. Arriagada[1]
[1]Universidad de Chile, Departamento de Geología, Santiago, Chile (alvherna@ing.uchile.cl)
[2]Research School of Earth Sciences, Australian National University, Canberra, Australia

The Chilean High Andes (28°–31°S) comprises a vast number of late Paleozoic–Triassic granitoids which give information about the last stages of Gondwana assemblage. Particularly, previous studies determined two tectonic configurations during this time: subduction related compressional setting (late Carboniferous–late Permian) and non-subduction post-collisional extensional setting (late Permian–Triassic), as the last stage of Gondwana assemblage. However, new O–Hf isotopic data along new U–Pb SHRIMP ages in zircon have shown that this model should be modified and updated to the new analytical data available. $\delta^{18}O$ values indicate a strong change in the tectonic configuration approximately 270 Ma (earliest middle Permian) and thus, units can be divided into 2 mayor groups: late Carboniferous to earliest middle Permian and middle Permian to Triassic. The oldest group shows slightly low values of εHf_i (ca. +1 to -4) with high $\delta^{18}O$ (ca. >6.5 ‰), indicating an elevated supracrustal component and the addition of less radiogenic continental-like material, which along significant residence time (T_{DM2}: Mesoproterozoic) can be interpreted as magmas formed at depth in a subduction-related continental arc, and contaminated with supracrustal material and/or oceanic sediments transported through the subducted slab to the mantle-wedge. Subsequently, middle Permian–Triassic rocks show a wider range of εHf_i values (ca. +3 to -3) with relatively low, mantle-like $\delta^{18}O$ (ca. 4.5-6.5 ‰), indicating a source of magmas without the addition of supracrustal material for some plutons, whilst for others, a slight input. The higher positive values of εHf_i can be related to the influence of new juvenile material in the source of some magmas. This isotopic data can be interpreted as rocks formed as the result of melting of an old thinned mafic crust (with mantle-like $\delta^{18}O$ values characteristic of this type of rocks) with limited addition of supracrustal material; in agreement with regional models, which postulate an extensional setting during this time, and thus, during the last stages of Gondwana assemblage. Finally, the result for the late Carboniferous to earliest middle Permian group shows almost identical O–Hf signatures compared to those observed in the Chilean Coastal Batholith (33°–40°S) of mid Carboniferous–early Permian age. This suggests a comparable tectonic configuration for the entire magmatism, initiating from south-to-north, with magmatism starting from the south.

Goldschmidt Poster presentation

Goldschmidt Conference
Sacramento, California. 08–13 June 2014

Late Paleozoic to Triassic magmatism in the north-central Frontal Andes, Chile: Records for the last stages of Pangea assemblage

Á. Del Rey[1], K. Deckart[1], M. Fanning[2] and C. Arriagada[1]
[1]Universidad de Chile, Departamento de Geología, Santiago, Chile (alvherna@ing.uchile.cl)
[2]Research School of Earth Sciences, Australian National University, Canberra, Australia

The Chilean Frontal Andes (28°–31°S) comprises a vast number of late Paleozoic–Triassic granitoids which give information about the last stages of Pangea assemblage. Previous studies determined two tectonic configurations during this time: subduction related compressional setting (late Carboniferous–late Permian) and non-subduction post-collisional extensional setting (late Permian–Triassic). However, new O–Hf and Re–Os isotopic data along new U–Pb SHRIMP ages in zircon, and whole rock major and trace geochemistry have shown that this model should be modified. $\delta^{18}O$ values indicate a strong change in the tectonic configuration approximately 270 Ma (earliest middle Permian) and thus, units can be divided into 2 mayor groups: late Carboniferous to earliest middle Permian and middle Permian to Triassic. The oldest group shows slightly low values of εHf_i with high $\delta^{18}O$, indicating an elevated supracrustal component and the addition of less radiogenic continental-like material, which along significant residence time (T_{DM2}: Mesoproterozoic) can be interpreted as magmas formed at depth in a subduction-related continental arc with normal-to-thickened crust, and contaminated with supracrustal material and/or oceanic sediments transported through the subducted slab to the mantle-wedge. Subsequently, middle Permian–Triassic rocks show a wider range of εHf_i values with relatively low, mantle-like $\delta^{18}O$ and low γOs, with some samples caracterized as A-type granites, indicating a source of magmas without the addition of supracrustal material for some plutons, whilst for others, a slight input. This isotopic data can be interpreted as rocks formed as the result of melting of an old thinned mafic crust with limited addition of supracrustal material; in agreement with regional models, which postulate an extensional setting during this time, and thus, during the last stages of Pangea assemblage.

APPENDIX BIBLIOGRAPHY

Bouvier, A., Vervoort, J.D., Patchett, P.J., 2008. The Lu-Hf and Sm-Nd isotopic composition of CHUR: constraints from unequilibrated chondrites and implications for the bulk composition of terrestrial planets. Earth Planet. Sci. Lett. 273, 48–57.

Chappell, B.W., White, A.J.R., 2001. Two contrasting granite types: 25 years later. Aust. J. Earth Sci. 48, 489–499.

Goodge, J.W., Vervoort, J.D., 2006. Origin of mesoproterozoic A-type granites in Laurentia: Hf isotope evidence. Earth Planet. Sci. Lett. 243, 711–731.

McDonough, W.F., Sun, S.S., 1995. Composition of the Earth. Chem. Geol. 120, 223–253.

Middlemost, E.A.K., 1985. Magmas and Magmatic Rocks. Longman, London.

Middlemost, E.A.K., 1994. Naming materials in the magma/igneous rock system. Earth-Science Rev. 37, 215–224.

Paton, C., Woodhead, J.D., Hellstrom, J.C., Hergt, J.M., Greig, A., Maas, R., 2010. Improved laser ablation U–Pb zircon geochronology through robust downhole fractionation correction. Geochemistry Geophys. Geosystems 11.

Peccerillo, A., Taylor, S.R., 1976. Geochemistry of Eocene calc-alkaline volcanic rocks from the Kastamonu area, Northern Turkey. Contrib. to Mineral. Petrol. 58, 63–81.

Petrus, J.A., Kamber, B.S., 2012. VizualAge: A Novel Approach to Laser Ablation ICP-MS U-Pb Geochronology Data Reduction. Geostand. Geoanalytical Res. 36, 247–270.

Söderlund, U., Patchett, J.P., Vervoort, J.D., Isachsen, C.E., 2004. The 176Lu decay constant determined by Lu-Hf and U-Pb isotope systematics of Precambrian mafic intrusions. Earth Planet. Sci. Lett. 219.

Solari, L.A., Gómez-Tuena, A., Bernal, J.P., Pérez-Arvizu, O., Tanner, M., 2010. U-Pb zircón geochronology by an integrated LAICPMS microanalytical workstation: achievements in precision and accuracy. Geostand. Geoanalytical Res. 34, 5–18.

Tera, F., Wasserburg, G., 1972. U-Th-Pb systematics in three Apollo 14 basalts and the problem of initial Pb in lunar rocks. Earth Planet. Sci. Lett. 14, 281–304.

Vervoort, J.D., Blichert-Toft, J., 1999. Evolution of the depleted mantle: Hf isotope evidence from juvenile rocks through time. Geochim. Cosmochim. Acta 63, 533–556.

Whalen, J.B., Currie, K.L., Chappell, B.W., 1987. A-type granites: geochemical characteristics, discrimination and petrogenesis. Contrib. to Mineral. Petrol. 95, 407–419. doi:10.1007/BF00402202

Williams, I.S., 1998. U–Th–Pb geochronology by ion microprobe, in: McKibben, M.A., Shanks, W.C., Ridley, W.I. (Eds.), Reviews in Economic Geology. pp. 1–35.